Proceedings of the Joint MAP D-PHASE Scientific Meeting – COST 731 mid-term seminar

Challenges in hydrometeorological forecasting in complex terrain

19-22 May 2008, Conference Centre of CNR, Bologna, Italy

edited by:

Andrea Montani, Pier Paolo Alberoni, Andrea Rossa,

Mathias W. Rotach, Andrea Buzzi, Silvio Davolio

January 2009

Foreword

The meeting "Challenges in hydro-meteorological forecasting in complex terrain" aimed at bringing together scientists, mainly meteorologists and hydrologists who participate in the MAP D-PHASE project and in the COST Action 731 or are active in the related fields. These two initiatives share the aim of improving the quality and reliability of quantitative precipitation and river discharge / flood forecasting, particularly in mountainous areas. Both are also concerned with important applications related to decision support and societal impact.

The main topics of the meeting were ensemble modelling, challenging the limited atmospheric predictability, high-resolution hydro-meteorological modelling, dealing explicitly with atmospheric convection, nowcasting, uncertainty in observations, assimilation of data into models, model verification and decision support in critical situations.

After the highly successful international R&D Project MAP (Mesoscale Alpine Programme), which was focused on the investigation and understanding of atmospheric processes over the Alps, the World Weather Research Programme (WWRP) proposed to the MAP community to perform a Forecast Demonstration Project. The goal of MAP D-PHASE was decided to be to demonstrate the ability of reliably forecasting orographically influenced precipitation in the Alps and its consequences on the distribution of run-off characteristics. Hence, the acronym D-PHASE stands for Demonstration of Probabilistic Hydrological and Atmospheric Simulation of flood Events in the Alpine region. The D-PHASE Operations Period (DOP) ran from June to November 2007. Participants in D-PHASE are meteorological and hydrological services in the Alps (but also far from the Alps as Canada and United Kingdom), universities, research institutions and, in particular, decision makers (end users) with respect to flood management. The first D-PHASE scientific meeting was held in Fall 2006 in Vienna and was dedicated to scientific planning and coordination of the various activities. After the DOP the second D-PHASE scientific meeting now provided an excellent opportunity to present first results, discuss further plans and create an overview on the impact and possible further developments of the project. The common interests and topics made it a perfect opportunity to jointly hold the meeting with COST 731.

The COST 731 Action was launched in 2005 in the COST Domain Earth System Science and Environmental Management (ESSEM) as a five-year coordinative effort in hydrometeorology. It reflects a common European will to tackle the challenge of enhancing hydrological forecasting by using imperfect, yet not information-void, meteorological data with 20 countries and a majority of operational groups participating. COST 731 addresses the problem of forecasting (heavy) precipitation events and the corresponding hydrological processes in connection with the uncertainty inherent in this task. Hereby the main focus of the Action is the quantification of forecast uncertainty and its propagation through a meteo-hydrological

forecast chain, and is structured in three working groups, which deal with uncertainty cascading from observations (predominantly from radar) into numerical weather prediction (NWP) models, from observations and NWP into hydrological models, and the use of uncertainty as support in decision making. The groups of scientists involved in the Action therefore range from radar meteorology, NWP, hydrological modelling, to as far as sociologists who deal with risk communication. MAP D-PHASE was, at the conception stage, and continues to be an important element of COST 731, while the present conference represented the Mid-term Seminar of the Action.

The meeting was organized jointly by ISAC (Institute of Atmospheric Sciences and Climate) of CNR (National Research Council) and ARPA-SIM, the Hydro-Meteorological Service of the environmental and protection regional agency of the Emilia-Romagna region. These are two of the several institutions (including the local university) where research and operational meteorological and hydrological activities are conducted in Bologna, taking advantage from a consolidated tradition.

The meeting was hosted at the Congress Centre of the Research Area of CNR in Bologna.

Andrea Buzzi, Andrea Rossa and Mathias Rotach

The Programme Committee:

Andrea Buzzi (ISAC-CNR - chairperson), Pier Paolo Alberoni (ARPA-SIM, local organizing committee), Marco Arpagaus (MeteoSwiss), Michael Bruen (UCD), Silvio Davolio (ISAC-CNR, local organizing committee), Manfred Dorninger (Univ. of Vienna), Christoph Hegg (Eidgenssische Forschungsanstalt WSL), Christian Keil (DLR), Andrea Montani (ARPA-SIM, local organizing committee), Thomas Skaugen (NVE), Roberto Ranzi (Univ. of Brescia), Evelyne Richard (CNRS/UPS), Andrea Rossa (ARPA Veneto), Mathias Rotach (MeteoSwiss), Volker Wulfmeyer (Univ. of Hohenheim).

Acknowledgements

We are grateful to several colleagues of ARPA–SIM and ISAC-CNR, who were involved in the preparation stages of the conference and worked hard so as to insure its final implementation. In particular, we are indebted:

- to Barbara Ramponi, Katia Casini, Daniela Ranieri and Sandra Zerbini for assistance in several administrative issues,
- to Barbara Gualandi for providing useful logistic information and valuable suggestions,
- to Francesco Siviero and Paola Cristofanelli for creating, updating, maintaining the database and the web pages of the conference,
- to Fabrizio "Biko" Roccato and Marco Elementi for audio-video supervision during the conference days,
- to Roberta Renati and Valeria Sacchetti for taking charge of the Art Competition,
- to Andrea Malossini for taking patiently the pictures of the hundreds of contributions for the Art Competition,
- to the staff of ARPArivista for the graphical project on the Conference bags.

And last (but not least), we acknowledge the contribution of the following sponsors (rigorously in alphabetical order!) who generously supported the event:

- CAE
- ELDES
- Elsag Datamat
- EURELETTRONICA ICAS
- MED INGEGNERIA
- ProGeA
- SELEX Sistemi Integrati
- Vaisala

The Local Organising Committee:

Andrea Buzzi, Pier Paolo Alberoni,

Silvio Davolio, Andrea Montani

Contents

1.1 Performance of the COSMO–LEPS system during the D–PHASE Operations Period

Andrea Montani, Chiara Marsigli, Tiziana Paccagnella

Hydrometeorological Regional Service ARPA–SIM, Bologna, Italy

Introduction

COSMO–LEPS is the Limited–area Ensemble Prediction System developed and implemented by ARPA–SIM within COSMO (COnsortium for Small–scale MOdelling; the members of the Consortium are Germany, Greece, Italy, Poland, Romania and Switzerland). COSMO-LEPS project aims to generate "short to medium–range" (48–132 hours) probabilistic predictions of severe weather events based on the non–hydrostatic regional COSMO–model, nested on a number of ECMWF EPS members, chosen via a clustering selection technique (Marsigli et al., 2001).

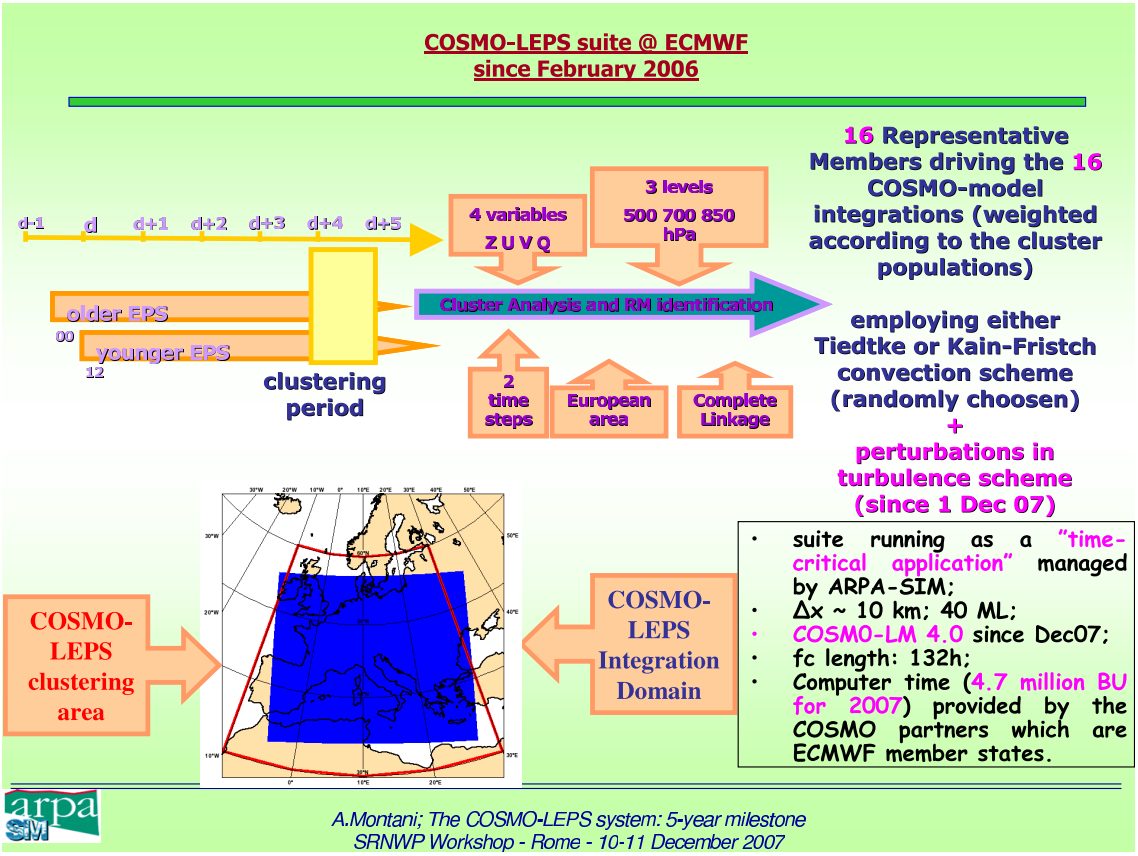

Figure 1.1: Present set–up of COSMO–LEPS operational suite.

The "experimental–operational" COSMO–LEPS suite (following the methodology described by Montani et al., 2003 and Marsigli et al., 2005) was set–up in November 2002 so as to produce probabilistic forecasts over a domain covering all countries involved in COSMO. After 6 years of activity, COSMO–LEPS application has become an "ECMWF member–state time–critical application" managed by ARPA–SIM and its present configuration in shown in Fig. 1.1. COSMO–LEPS is made up of 16 members, running at the horizontal resolution of 10 km with 40 model levels in the vertical. The computer–time to run COSMO-LEPS application on ECMWF supercomputers is provided from allocations to the ECMWF COSMO partners (i.e. Germany, Greece, Italy and Switzerland), whose contributions are joined into a unique "COSMO-account". Perturbations to the initial and boundary conditions are provided by the different EPS members driving the limited–area integrations. In addition to this, the following model perturbations are introduced:

- perturbations to the convection scheme: within each COSMO–LEPS integration, a random choice between Tiedtke or Kain–Fritsche convection scheme is made;
- perturbations in the maximal turbulent length scale;
- perturbations in the length scale of thermal surface patterns.

In this contribution, it is assessed the state–of–the–art of the system, showing its ability to provide warnings of severe weather events (e.g. heavy rainfall, strong winds, cold temperature anomalies).

Results of verification

As already mentioned, COSMO–LEPS has recently passed the 6–year milestone of activity. Therefore, a big verification effort was undertaken so as to assess objectively how the system changed in these years and the extent to which modifications have actually caused an improvement in terms of precipitation forecasts over mountainous areas.

In order to carry on this evaluation, a fix set of SYNOP stations (about 470) was selected, over an area covering the Alps (43-50N, 2-18E) and for the period ranging from December 2002 to August 2008. Precipitation accumulated over 12 hours (18-06 UTC and 06-18 UTC) was verified, comparing the values forecast on the grid–point nearest to each station against the observed values at that station. The other main features of the verification exercise are summarised in Fig. 1.2. Several probabilistic scores were used and the performance of the system was analysed both in terms of monthly and seasonal scores so as to identify the occurrence of possible seasonal variability.
As an example of the obtained results, Fig. 1.3 shows the performance of COSMO–LEPS in terms of the Relative Operating Characteristic (ROC) area, for 4 different thresholds (1, 5,

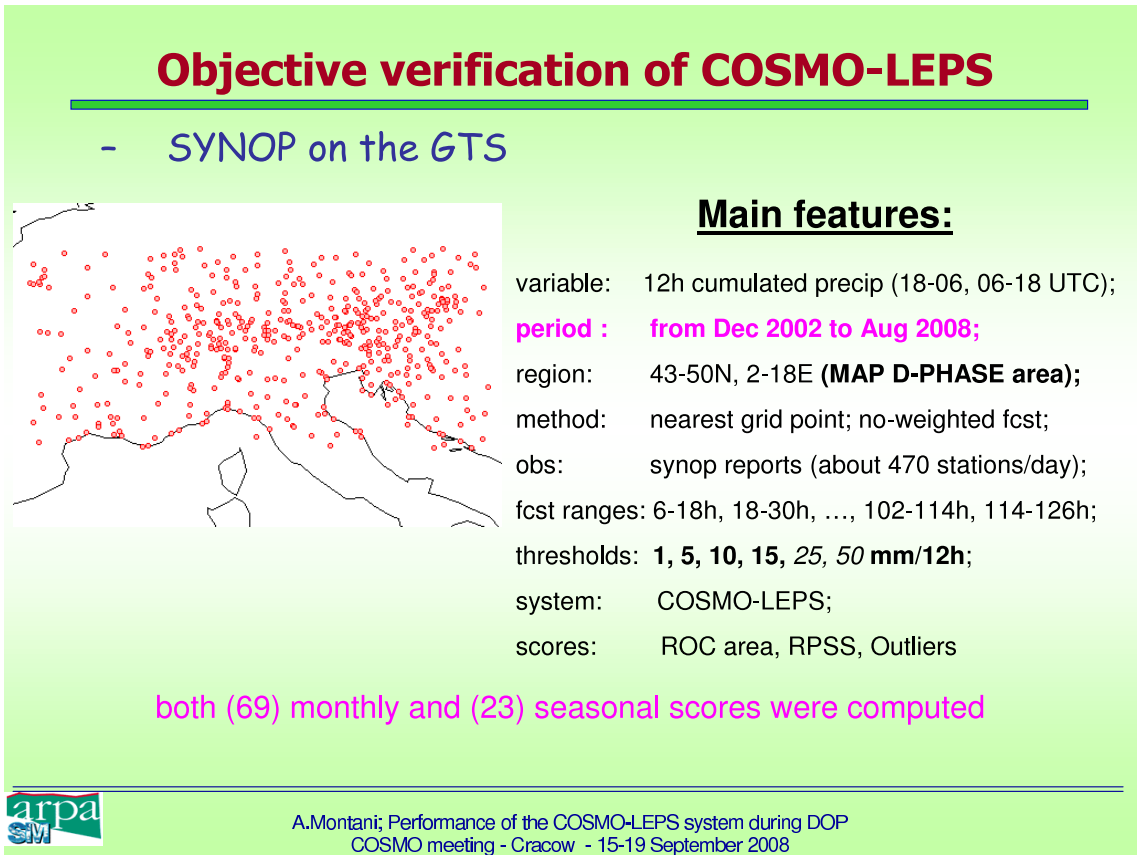

Figure 1.2: Main features of COSMO–LEPS verification.

10, 15 mm/12h) at the 78–90h forecast range. Although the score is computed monthly, the 3–month running mean is actually shown in the plots to increase readability, due a marked month–to–month variability of the score itself. At the beginning of the verification period (early 2003), the ROC area scores (especially for high rainfall thresholds) were close to, or below, the 0.6 line, considered the discriminating value to detect between a useful and a useless forecast. Then, the scores increased for all thresholds starting from summer 2004. The ROC area has been well above 0.6 since spring 2004, for all the thresholds including the highest (15mm/12h). A different behaviour is exhibited in autumn 2006, which was a very dry season: COSMO–LEPS performance is not satisfactory. On the other hand, the ROC area is close to 0.8 during both 2007 and 2008, indicating a skillful system in the prediction of precipitation at the day–4 range. A marked seasonal variability is also evident, the system often performing better in the summer season.

In the overall evaluation of the system performance, it has to be kept in mind that, in addition to the upgrades in the COSMO–model itself, COSMO–LEPS configuration was subject to three major changes during the verification period:

- June 2004: the ensemble members were increased from 5 to 10 and only two EPS instead of three were considered to select the global–model members to drive the COSMO–LEPS integrations;
- February 2006: the ensemble members were increased from 10 to 16 and the vertical

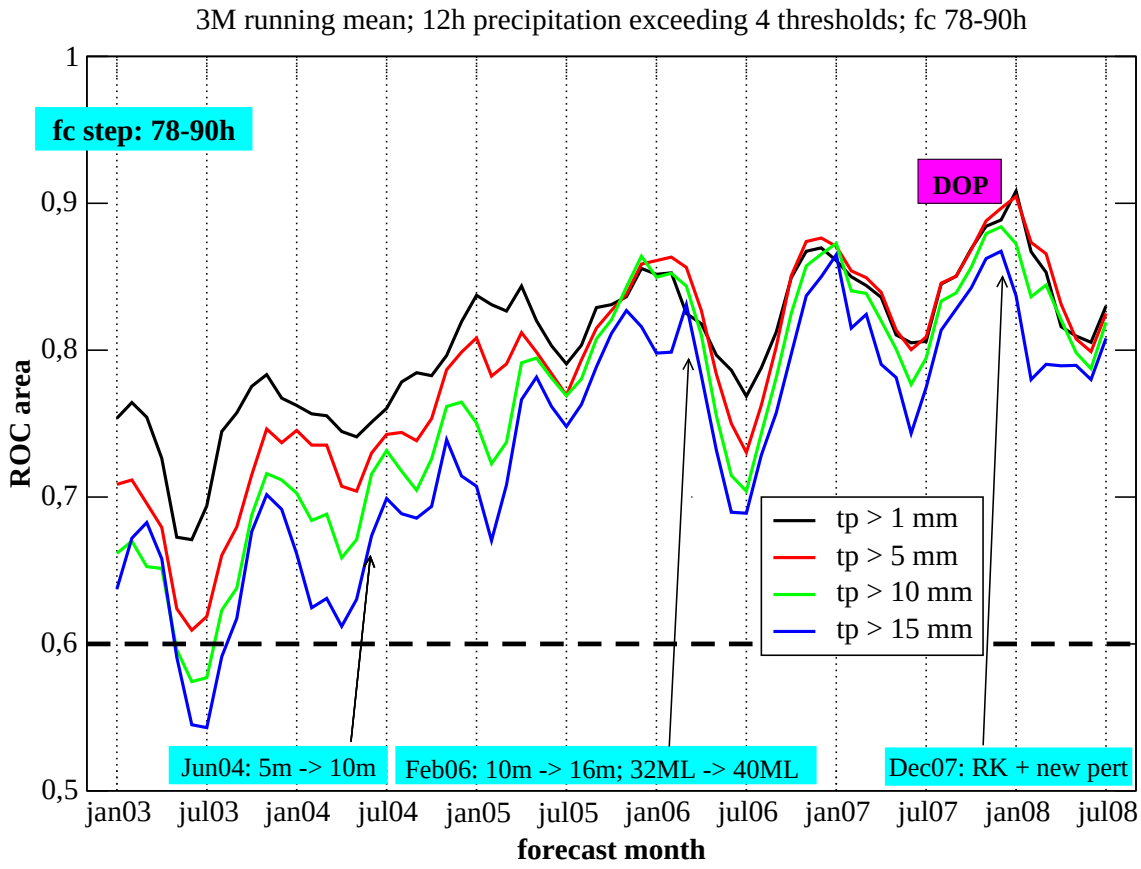

Figure 1.3: ROC area of COSMO–LEPS 12-hour precipitation forecasts for the forecast range 78–90h. The BSS was computed for each month, from January 2003 to July 2008. A 3-monthly running mean was applied to the scores to improve readability.

resolution of COSMO–LEPS integrations from 32 to 40 levels;

- December 2007: it was introduced the Runge–Kutta numerical scheme as well as new perturbations (in the maximal turbulent length scale and in the length scale of thermal surface patterns).

The former change seems to have led to better scores, since an improvement is evident from spring 2004. The impact of the latter change is more difficult to be judged, due to the already underlined problem in autumn 2006. Obn the other hand, a positive trend is well evident in the scores obtained in 2007, especially during the various meteorological experiments which took place during that year (e.g. COPS and MAP D-PHASE). This is also true if other scores, like the Brier Skill Score and the percentage of outliers, are considered (not shown).

As a final remark, it has to be pointed out that nowadays COSMO–LEPS forecast products are well–established in met–ops rooms across COSMO community. They have been recently used with success in EC projects (e.g. Windstorms PREVIEW) as well as in the field campaigns of the above–mentioned meteorological experiments. As future developments, it is planned to introduce more model perturbations, so as to improve the spread–skill relationship of the system, and to develop "calibrated" COSMO–LEPS forecasts.

References

Marsigli C., Montani A., Nerozzi F., Paccagnella T., Tibaldi S., Molteni, F., Buizza R., 2001. A strategy for high–resolution ensemble prediction. Part II: limited–area experiments in four Alpine flood events. *Quart. J. Roy. Meteor. Soc.*, **127**, 2095–2115.

Marsigli C., Boccanera F., Montani A., Paccagnella T., 2005. The COSMO-LEPS mesoscale ensemble system: validation of the methodology and verification. *Nonlin. Proc. Geophys.*, **12**, 527–536.

Montani A., Capaldo M., Cesari D., Marsigli C., Modigliani U., Nerozzi F., Paccagnella T., Tibaldi S., 2003. Operational limited–area ensemble forecasts based on the 'Lokal Modell'. ECMWF Newsletter No. 98. Available from: ECMWF, Shinfield Park, Reading RG2 9AX, UK.

1.2 The COSMO-SREPS ensemble for the short-range: system analysis and verification on the MAP D-PHASE DOP

Chiara Marsigli, Andrea Montani, Tiziana Paccagnella

Hydrometeorological Regional Service ARPA–SIM, Bologna, Italy

System description

The COSMO-SREPS (COSMO Short-Range Ensemble Prediction System) ensemble system is based on 16 integrations of the limited-area non-hydrostatic COSMO model at about 10 km of horizontal resolution, with 40 vertical levels.

This system has been built to fulfil some needs that have recently arisen in the COSMO community:

- to have a short-range mesoscale ensemble to improve the support especially in situations of high impact weather
- to have a very short-range ensemble for data assimilation purposes
- to provide boundary conditions for the COSMO-DE-EPS convection-resolving ensemble, currently under development at DWD.

Therefore, the ensemble had to be designed to describe the uncertainty affecting the short-range predictions of surface weather parameters at a high spatial resolution. Aiming at this purpose, the strategy to generate the mesoscale ensemble members proposed by this project tried to take into account as many as possible sources of uncertainty which affect the scales of interest in the weather forecast at the short time range, in order to model many of the possible causes of the relevant forecast errors. Hence, perturbations have been applied both in the driving model and in the mesoscale model. The driving model error is described by means of a multi-analysis multi-boundary approach. Initial and boundary condition perturbations are applied by driving the 10-km COSMO runs with the four 25-km COSMO members of the Multi-Analysis Multi-Boundary SREPS system of INM. These four lower resolution COSMO runs, nested on four different global models (IFS, GME, GFS, UM) which use independent analyses, are provided by INM for this purpose. A representation of the smaller scale uncertainty is accomplished by applying limited-area model perturbations as well: the values of a number of parameters included in the sub-grid process parametrisation schemes

are randomly changed (within their range of variability) in the different ensemble members. The set-up of the 16 runs is summarised in Table 1. The MAP D-PHASE DOP was chosen

Member	Driving model of the LM-INM run	P1	P2	P3	P4
1	IFS	tiedtke=.T.	kainfri=.F.	tur_len=-1	pat_len=500
2	IFS	tiedtke=.F.	kainfri=.T.	tur_len=-1	pat_len=500
3	IFS	tiedtke=.T.	kainfri=.F.	tur_len=1000	pat_len=500
4	IFS	tiedtke=.T.	kainfri=.F.	tur_len=-1	pat_len=10000
5	GME	tiedtke=.T.	kainfri=.F.	tur_len=-1	pat_len=500
6	GME	tiedtke=.F.	kainfri=.T.	tur_len=-1	pat_len=500
7	GME	tiedtke=.T.	kainfri=.F.	tur_len=1000	pat_len=500
8	GME	tiedtke=.T.	kainfri=.F.	tur_len=-1	pat_len=10000
9	NCEP	tiedtke=.T.	kainfri=.F.	tur_len=-1	pat_len=500
10	NCEP	tiedtke=.F.	kainfri=.T.	tur_len=-1	pat_len=500
11	NCEP	tiedtke=.T.	kainfri=.F.	tur_len=1000	pat_len=500
12	NCEP	tiedtke=.T.	kainfri=.F.	tur_len=-1	pat_len=10000
13	UKMO	tiedtke=.T.	kainfri=.F.	tur_len=-1	pat_len=500
14	UKMO	tiedtke=.F.	kainfri=.T.	tur_len=-1	pat_len=500
15	UKMO	tiedtke=.T.	kainfri=.F.	tur_len=1000	pat_len=500
16	UKMO	tiedtke=.T.	kainfri=.F.	tur_len=-1	pat_len=10000

Table 1. Main features of the 16 runs which constitute the ensemble.

for an extensive testing of the system. During the DOP, 99 full runs of the COSMO-SREPS system were performed, covering not continuously the period, 50 in summer (JJA) and 49 in autumn (SON). Each full run (made up of 16 COSMO-model integrations at 10 km) started at 00UTC. The lack of continuity in the runs was mainly depending on the availability of initial and boundary conditions.
Different data-sets have been used for the evaluation:

- *high-res alpine:* a dense network of stations covering Northern-Central Italy and Switzerland, providing precipitation data accumulated over 24h, from 06 to 06 UTC (about 1400 stations)
- *high-res Italy:* a dense network of stations covering Northern-Central Italy, providing precipitation data accumulated over 6h (about 900 stations) and 2m temperature data (about 600 stations)
- *synop alpine:* the SYNOP stations covering approximately the same area (43-48 N 6-14 E, 218 stations)

The main issues which have been addressed in the system evaluation are: 1) if the system shows a good spread/skill relationship, representative of the capability of the ensemble in

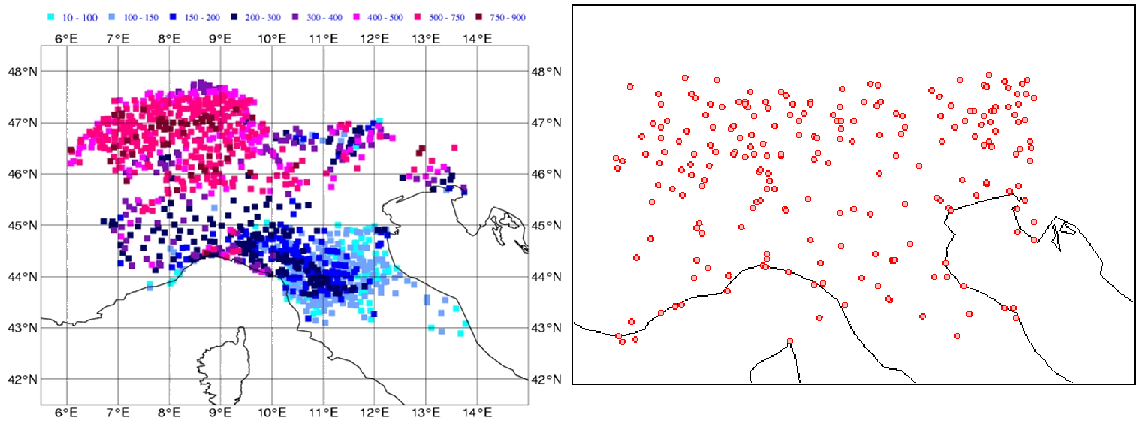

Figure 1.1: The *high-res alpine* dataset (left panel) and the *synop alpine* dataset (right panel). The *high-res Italy* dataset is made up by the Italian part only of the *high-res alpine* one.

describing the forecast error 2) how the different perturbations contribute to the spread and to the skill of the system 3) which is the ensemble skill in the forecast of surface weather parameters.

Some results of the system performances during the DOP

The evaluation of the spread-error relationship shows that the system still tends to be under-dispersive. The gap between the spread and the error has been observed for a number of meteorological variables, both surface and upper-air (2m temperature, mean-sea-level pressure, precipitation, temperature at 850 hPa, geopotential height at 500 hPa). Moving from towards upper-air variables, the gap decreases, but it is still detectable.

In Figure 1.2, the root-mean-square error of the ensemble mean and the root-mean-square spread of the ensemble (or ensemble standard deviation) are compared for the two seasons, in terms of 2m temperature. The error is computed by comparing forecasts interpolated on station points belonging to the synop alpine dataset with the corresponding observations, the spread is computed using these same interpolated forecast values, for homogeneity reasons.

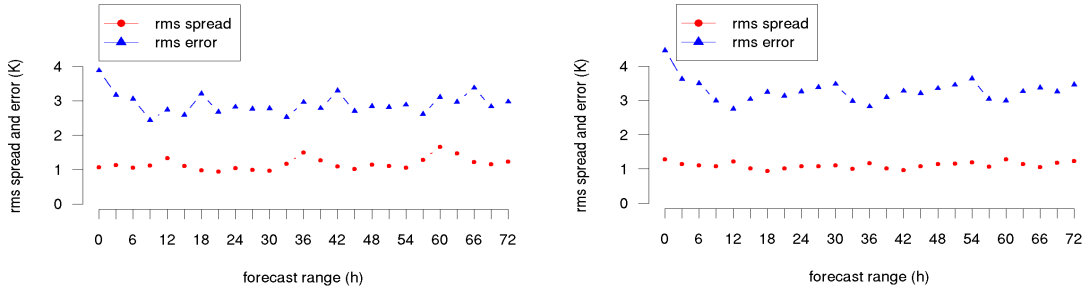

Figure 1.2: COSMO-SREPS spread (red) and error (blue) in terms of 2m temperature for summer (left) and autumn (right) 2007. Data are from the *synop alpine* dataset.

The ensemble spread is bounded between 1 and 2 K in the summer season (Fig. 1.2, left panel), increasing with the forecast range and exhibiting a diurnal cycle, with values peaking at noon. In autumn (right panel) the spread stays close to 1 K throughout the whole forecast range. In both seasons the ensemble mean error is quite larger than the spread, remaining below the 3 K value in summer, with peaks grater than 3 K at 18 UTC, while being generally above the 3 K value in autumn. The gap between the two measures is due to both the underdispersion of the ensemble system and to the COSMO model systematic error, which should not be removed by ensemble techniques, but only by model improvement.

In order to assess the contribution to the skill of the system provided by the different ensemble members, depending on their initial and boundary conditions and physics set-up, it has been analysed how the scores vary according to two different methods used to group the ensemble elements. The 16 members can be subdivided into 4 groups of 4 elements each, in 2 different ways:

- considering groups of elements homogeneous in terms of initial and boundary conditions, but distinct for the model parameterisations;
- considering groups of elements homogeneous in terms of the model parameters, but distinct in terms of initial and boundary conditions.

Each group is referred to after the common feature of their members, e.g. the group named *ecmwf* contains all the run driven by the ECMWF global model, which have different parameter perturbations, while the group named *p1* contains all the run with the same physics perturbation No 1, which have different initial and boundary conditions. Considering 24h precipitation forecast, the ensemble scores have been computed for each of the 4 groups of 4 elements, in order to assess how the different forecast characteristics in terms of driving model and parameter contribute to the skill. The ROC area of the 4-member sub-ensembles are shown in Figure 1.3 for the both seasons for the alpine area.

The light blue line of each panel represents the ROC area of the full 16-member ensemble, which gives an indication of the COSMO-SREPS skill in forecasting precipitation for that period and in that particular area.
In the left panels, the other lines show the ROC area values of the 4-member ensembles made up by the 4 members nested on one particular global model. The 4 members are differentiated only in terms of the set-up of the physical parameterizations. Therefore, these represent the skill of ensembles, which are only model-perturbed, having the same initial and boundary conditions. Apart from the decrease in skill evident when passing from a 16-member to a 4-member ensemble, which is expected, it is worth pointing out that the different 4-member ensembles have different skill, which varies with the considered threshold and also with the forecast range (not shown).

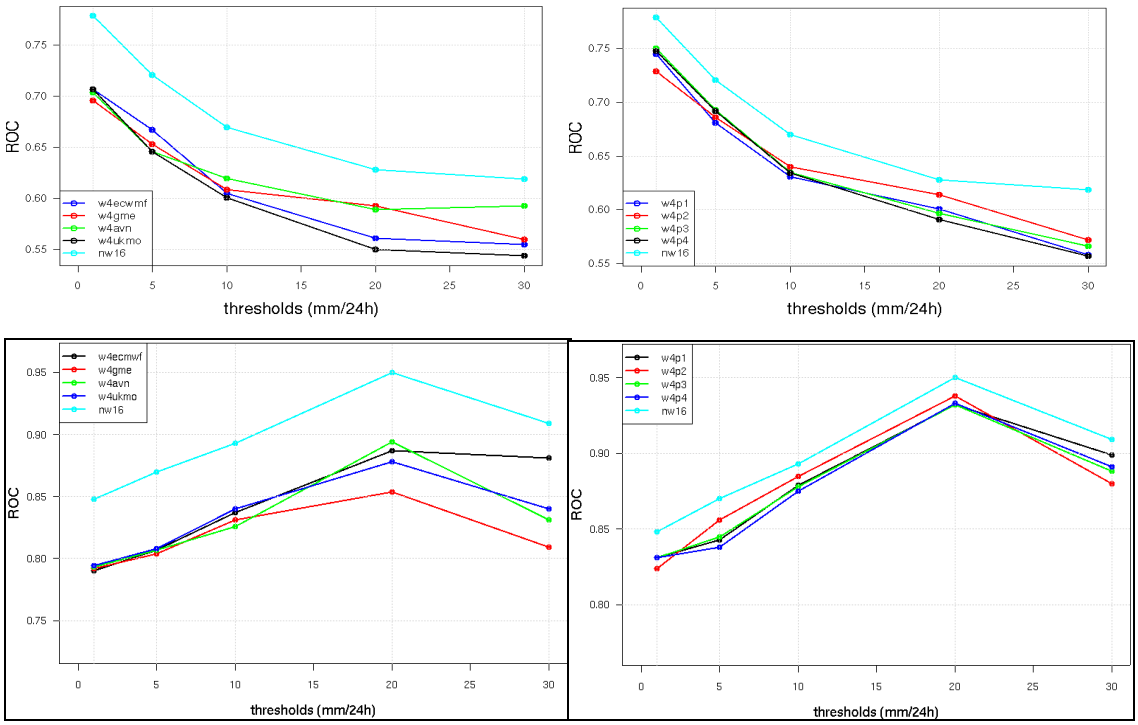

Figure 1.3: ROC area as a function of threshold for 24hr accumulated precipitation in the alpine area (high-res alpine data set) for the summer season (upper panels) and for the autumn season (lower panels). Left panels: full 16-member COSMO-SREPS (light blue line) vs. 4-member ensembles with identical driving run (black: ECMWF, red: GME, green: GFS, blue: UKMO). Right panels: full 16-member COSMO-SREPS (light blue) vs. 4-member ensembles with identical physical perturbation (black: p1, red: p2, green: p3, blue p4). The scores are for the +30 h forecast range.

In the right panels, the 4-member ensembles made up from identical physics perturbations are shown. Therefore, these represent the skill of ensembles, which are perturbed in the initial and boundary conditions only, but have the same model set-up. Comparing each right panel with the corresponding left one suggests that perturbation of initial conditions generally yields more skilful performance than physical perturbation only. This is an indication of the fact that, the higher degree of diversity among members introduced by perturbing initial and boundary conditions determines a greater amount of skill with respect to the smaller-scale diversity introduced by the physics perturbations. As for the role of the different parameterizations, the 4-member ensemble where model perturbation p2 (Kain-Fritsch convection scheme) is applied to each member (red line on the right panels) turns out to be more skilful that other 4-member ensembles.

Finally, it appears that scores for the autumn season are quite higher than those relative to the summer season, but the general features are the same.

Conclusions

Some conclusions can be drawn:

- **spread-skill relationship:** a correlation between error and spread exists, but the system is under-dispersive. Hence a better representation of model error is needed
- the **different driving models** contribute differently to the ensemble skill, but there is a strong dependence on forecast range, season, verification area
- the **different perturbations** can contribute differently to the ensemble skill as well

The analysis over the is still on-going. In particular, a comparison of COSMO-SREPS with the other mesoscale ensemble systems running during the DOP will be carried on.

1.3 Development of an ensemble prediction system on the convective scale with the COSMO-DE

Christoph Gebhardt[(1)], Susanne E. Theis[(1)], Tanja Winterrath[(1)], Marcus Paulat[(1)], Peter Krahe[(2)],Volker Renner[(1)]

[(1)] *Deutscher Wetterdienst (DWD), Offenbach, Germany,*

[(2)] *Bundesanstalt für Gewässerkunde (BfG), Koblenz, Germany*

Introduction

The Deutscher Wetterdienst (DWD) has developed the convection-resolving limited-area model COSMO-DE (COSMO: Consortium for Small-Scale Modelling, Doms and Förstner 2004) with the aim to improve the very short-range forecast of severe weather triggered by deep moist convection and interaction with small-scale topography. The COSMO-DE has a very small grid spacing of 2.8 km on 50 vertical levels which explicitly allows to simulate small-scale processes such as deep convection. An important advance of the model is the assimilation of radar information. The model is in operational phase since April 2007 with 18 hours forecast range started every 3 hours. The model domain covers mostly Germany. Compared to observations by rain-gauges and radar-estimates, the precipitation forecasts of COSMO-DE look much more realistic than those of the 7 km model COSMO-EU with respect to spatial structure and precipitation patterns. The bias of the diurnal cycle of precipitation is reduced and the assimilation of radar data has positive impact in the first 4 to 6 hours.

Since the predictability of the relevant processes acting on the resolved scales of COSMO-DE can be limited to very short forecast lead times, the quantification of forecast uncertainty and the production of probabilistic forecasts are necessary to guarantee the benefical use of COSMO-DE in warning and decision-making processes. Therefore, the DWD decided to develop an ensemble prediction system (EPS) on the 2.8 km scale. This development explores a new field of research because existing ensemble approaches mainly focus on larger spatial scales (e.g. Molteni et al. 1996, Toth and Kalnay 1997, Lefaivre et al., 1997, Montani et al., 2003, Bowler et al. 2008). The DWD has initiated two closely linked projects to develop an EPS using the COSMO-DE. The first project ('EELMK') is a joint effort of DWD and the Bundesanstalt für Gewässerkunde (BfG) with the aim to run an experimental atmospheric ensemble with focus on hydrological applications. In the second project ('COSMO-DE-EPS'), an EPS for operational weather forecasting is currently under development. Project activities comprise the generation, verification, statistical postprocessing and visualization of the ensemble forecasts. The plan is to run the COSMO-DE-EPS in pre-operational mode

in 2009 with an approximate number of 20 members differing in physics parameters, lateral boundary conditions and initial conditions. Operational implementation with about 40 members is envisaged to start in 2011.

The COSMO-DE-EPS will estimate and quantify inherent uncertainties due to imperfect representation of atmospheric processes and initial conditions in the numerical predictions as well as uncertainties introduced by lateral boundary conditions of the model domain. In the current state of development, we focus on uncertainties in the model itself and in the boundary conditions. The model uncertainties are represented by non-stochastic perturbations of the physics parameterizations. The uncertainty in boundary conditions is estimated by nesting the COSMO-DE in an ensemble chain where uncertainty is propagated from global to resolved scales. The perturbation of initial conditions is part of future tasks and is neglected in this paper keeping in mind that initial uncertainty is important to set up a complete EPS.

In the following, we first introduce the methodologies of perturbation used in COSMO-DE-EPS. Then we present experimental results to describe some general characteristics of the COSMO-DE-EPS. This is followed by a brief outlook.

Model uncertainties

The uncertainty in model formulation can be highly relevant in short-range mesoscale prediction, e.g. when large-scale forcing is weak. Important contributors to model uncertainty are parameterizations of processes acting on the unresolved scales of the model. These parameterizations sum up the mean effect of the sub-scale by functions depending on the resolved scales. These functions depend on parameters which are often empirically estimated under highly idealized conditions. The values of these parameters under real atmospheric conditions are therefore quite uncertain. We incorporate this uncertainty in the COSMO-DE-EPS by perturbing parameters of the parameterization schemes. This is done in a non-stochastic way, i.e. the perturbations are kept constant over the entire forecast range and each member is characterized by one or more perturbed parameters. Up to now, we have tested the perturbation of 13 parameters that are expected to have significant impact on forecast results. These parameters are related to the parameterizations of boundary layer processes, turbulence, cloud microphysics as well as the interaction of soil and vegetation with the atmosphere. Each parameter is perturbed within its full range of physically reasonable values. With such a perturbation approach we generate ensemble members which are systematically different and the ensemble consists of several slightly different model versions. This has the advantage that forecast peturbations can be traced back to the physics perturbations which can be an important feedback for model developers. The disadvantage is that the members are not equally likely which complicates the processing of the results.

Uncertainties in lateral boundary conditions

Depending on the synoptic situation the forecast of a limited-area model can by significantly influenced by the inflow at the lateral boundaries. This inflow is commonly simulated by nesting the limited-area model into a model covering a larger domain with coarser grid size. This nesting implies several sources of uncertainty, i.e. the interpolation to the finer scale, differences in the resolved processes on the different scales or other systematic differences between the nesting and the nested model.
The COSMO-DE-EPS estimates this uncertainty by nesting the COSMO-DE in members of a coarser scale EPS which itself is one link of an ensemble chain which propagates uncertainty across different scales. The coarsest scale of this ensemble chain is the AEMet-SREPS (Garcia-Moya et al. 2007) of the Spanish Meteorological Service. In this EPS, five regional models with 25 km grid size are nested into four global models. The regional COSMO-SREPS (Marsigli et al. 2006) uses four members (COSMO regional model nested in all four global models) of AEMet-SREPS as boundary conditions and applies physics perturbations to produce 16 members at 10 km grid size. The COSMO-SREPS members provide boundary conditions for COSMO-DE-EPS. It is assumed that the differences between these COSMO-SREPS members are representative for the uncertainty of boundary conditions.

Ensemble forecasts

We run an ensemble with 20 members. We selected those five physics perturbations which deviated the most from the unperturbed control run in test experiments and combined them with four different COSMO-SREPS boundary conditions to get 20 members. Each member represents one physics perturbation. The four COSMO-SREPS members where chosen such that each of the four global models entering the AEMet-SREPS is represented in the ensemble. The ensemble was started at 00UTC for most days of August 2007 with a forecast range of 24 hours. Figure 1.1 shows 12 hours accumulated precipitation for four selected members of the ensemble. These members representatively demonstrate the different spatial scales of forecast perturbations due to model and boundary uncertainties. Members with different physics perturbations but identical boundary conditions differ on the small scale while members with different boundary conditions but identical physics differ also on larger scales. This holds for 2m-temperature as well (not shown).
To demonstrate the effect of perturbations in physics and boundary conditions on forecasts of hourly precipitation and 2m-temperature we show in Figure 1.2, the mean behaviour of these variables for each member depending on forecast range. The results are averaged over the model domain and the period 8^{th}–16^{th} August 2007. Looking at the precipitation, it is obvious that the members are grouped by identical boundary conditions and that there is more variability between these groups than within the groups. Thus precipitation variability

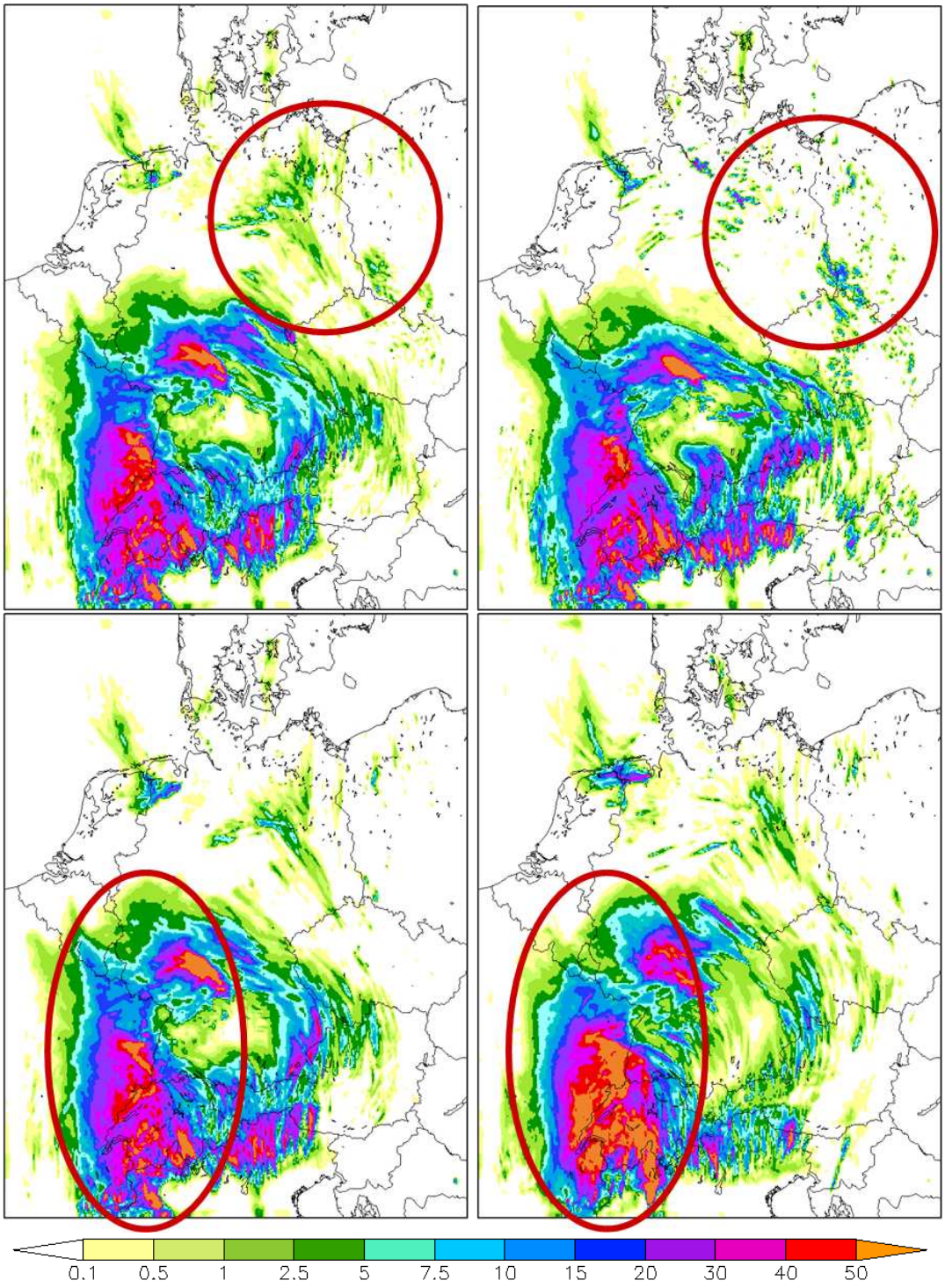

Figure 1.1: Forecast of 12-24UTC accumulated precipitation on 8^{th} August 2007. Top: Members with identical boundary conditions but different physics perturbations. Bottom: Members with different boundary conditions but identical physics perturbations.

is dominated by the variability introduced by the boundary conditions. In contrast, the 2m-temperature forecasts are more grouped by identical physics perturbations and there is more variability due to model uncertainty.

Subensembles are investigated to analyse the characteristics of the ensemble variability more closely. Figure 1.3 shows the mean member range of hourly precipitation and the ensemble

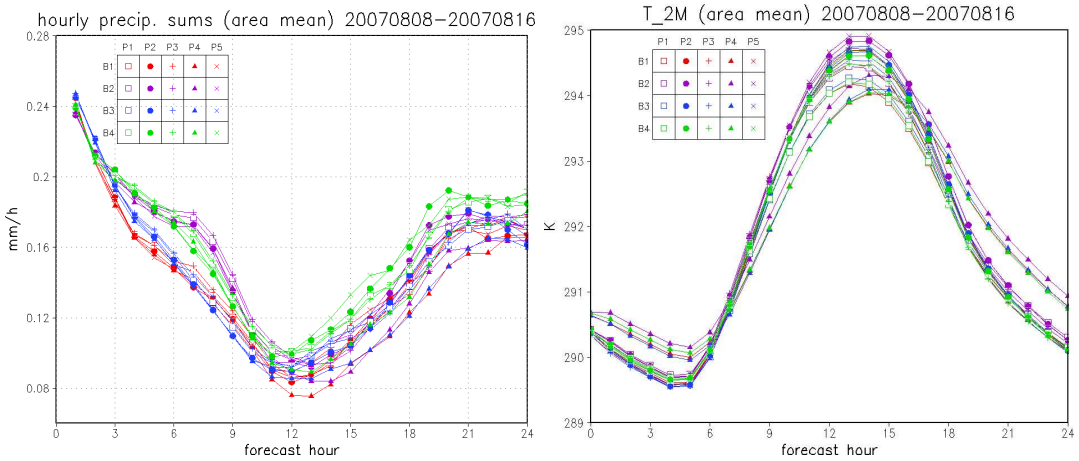

Figure 1.2: Spatial and temporal mean of precipitation (left) and 2m-temperature (right) depending on forecast lead time for all members. Identical colours represent identical boundary conditions, identical symbols represent identical physics perturbations.

spread for 2m-temperature each calculated for subensembles with either fixed boundary conditions or fixed physics perturbations. The member range is defined at each grid point as the difference between the member with the largest value and the member with the smallest value. The results are averaged over the whole model domain and the period 8^{th}–16^{th}

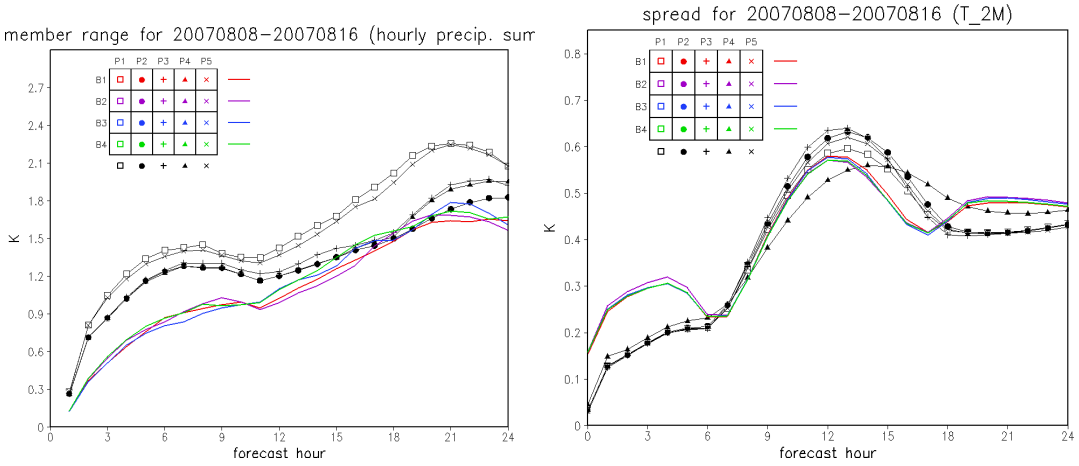

Figure 1.3: Spatial and temporal mean of member range of hourly precipitation (left) and spread of 2m-temperature (right) depending on forecast lead time calculated for subensembles. Identical colours represent identical boundary conditions, identical symbols represent identical physics perturbations.

August 2007. The plot on the left shows that the member range of precipitation is larger in subensembles with varying boundary conditions compared to ensembles with varying physics. This is again an expression of the relative importance of boundary uncertainty for precipitation forecast uncertainty. It can also be seen that the black lines are more divergent than the colored lines. This means that precipitation variability in subensembles with varying boundary conditions depends on the applied physics perturbation. But this

dependence is weaker the other way round. For 2m-temperature, the spread of boundary and physics subensembles is of similar magnitude for all but the first 5 forecast hours. At the beginning of the forecast, the ensemble spread is dominated by the variability due to model uncertainties. In general, black and colored lines are close together and there is no such dependence of boundary ensemble spread on physics perturbation as observed for precipitation.

Outlook

There are four major tasks for the further development of COSMO-DE-EPS. First, it is necessary to run experiments for longer periods to build a sound basis for verification and calibration purposes. While the verification software is already established, appropriate methods for calibration needs to be tested. This calibration is the second task and will focus on precipitation, 2m-temperature and 10m-wind. Challenges in calibration may arise from the very small spatial scale of the ensemble. A further task is the combination of more than one perturbed physics parameter in a single member. This will come along with some tuning and redefinition of the existing perturbations. Furthermore, there is the very important task of perturbing the initial conditions in COSMO-DE-EPS. The plan is to use an ensemble transform Kalman filter in the long run which will be developed in the COSMO priority project KENDA. But inbetween, more ad hoc methods will be tested for the quantification of initial uncertainties.

References

Bowler, N.E., Arribas, A., Mylne, K.R., Robertson, K.B. and S.E. Beare, 2008: The MOGREPS short-range ensemble prediction system. Q. J. R. Met. Soc., 134, 703–722.

Doms, G. and J. Förstner, 2004: Development of a kilometer-scale NWP-system: LMK. COSMO Newsletter, No. 4, 168–176

Garcia-Moya, J.A., Callado, A., Santos, C., Santos-Munoz, D. and J. Simarro, 2007: Predictability for short-range forecast: a multi-model approach. Submitted to Monthly Weather Rev.. Available from Agencia Estatal de Meteorologia, Madrid, Spain.

Lefaivre, L., Houtekamer, P.L., Bergeron, A. and R. Verret, 1997: The CMC Ensemble Prediciton System. Proc. ECMWF 6^{th} Workshop on Meteorological Operational Systems, Reading, U.K., ECMWF, 31–44.

Marsigli, C., Montani, A. and T. Paccagnella, 2006: The COSMO-SREPS project. Newsletter of the 28^{th} EWGLAM and the 13^{th} SRNWP meetings, 9–12 October 2006, Zurich, Switzerland, 269–274.

Molteni, F., Buizza, R., Palmer, T.N. and T. Petroliagis, 1996: The ECMWF ensemble

prediciton system: methodology and validation. Q. J. R. Met. Soc., 123, 1007–1003.

Montani, A., Capaldo, M., Cesari, D., Marsigli, C., Modigliani, U., Nerozzi, F., Paccagnella, T., Patruno, P. and S. Tibaldi, 2003: Operational limited-area ensemble forecasts based on the 'Lokal Modell', ECMWF Newsletter, 98, 2–7.

Toth, Z. and E. Kalnay, 1997: Ensemble forecasting at NCEP and the breeding method. Monthly Weather Rev., 125, 3297–3319.

1.4 Warning system of extreme precipitation for the Dutch Water Boards

Kees Kok and Daan Vogelezang

Royal Netherlands Meteorological Institute

Introduction

About half of the Netherlands is below sea level and the majority of the inhabitants is living there. But the country is not only jeopardized by surges along the coast but also by extreme precipitation events. All excessive amounts of water have to be drained eventually to large rivers, like the Meuse and Rhine, to the IJssel Lake and the North Sea. The possibility to do so depends strongly on the respective river and surge levels. An additional threat is therefore posed by heavy precipitation events upstream in the Meuse and Rhine catchments.

Water management in the Netherlands is organized in 25 so-called water boards. One of their main tasks is to prevent fields and cities from flooding in times of extreme precipitation, and if necessary to get rid of excess water as soon as possible. But they also have to keep the water at a minimal level even in cases of extreme drought.

In order to warn the water boards in cases of potential threats due to meteorological conditions a warning system was developed by the Royal Netherlands Meteorological Institute (KNMI) in cooperation with the Union of Water Boards. KNMI is only allowed to issue warnings with respect to extreme conditions; forecasts are not intended to be used for day-to-day operation. The warning system is operational since 2003. Currently 14 water boards have subscribed to the system (see figure 1.1).

Risk Profiles

The "extremity" of the meteorological conditions depends strongly on local circumstances, and is different for every water board. The amount of precipitation a water board can handle depends e.g. on its geography, canal system, soil type, and of course on its pumping and storage capacity. The pumping capacity is not constant but may strongly be affected by strong winds from certain directions (e.g. when winds push the water away from the pumping station), in particular for larger water boards.

The storage capacity depends among other things on the amount of rain in the last couple of days (soil saturation) and on time of the year (vegetation). For some of the most densely

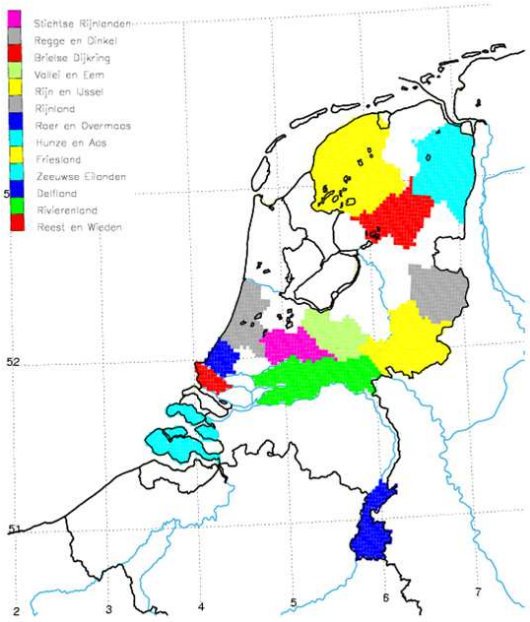

Figure 1.1: Water boards subscribed to the warning system

populated water boards in the western part of the country the storage capacity is quite low and precipitation amounts in the order of 15mm (area averaged) in 24 hours can be critical already, whereas other water boards can handle up to three times as much in favorable conditions.

Water boards have a rather good notion of what their critical precipitation thresholds are, as a function of a large variety of meteorological and initial conditions. We have to bear in mind that it is usually not that important to know the accumulated amount of rain falling between fixed times in the future but it may be much more important to know whether there will be a lot of rain falling in a very short period of time somewhere in the next coming days. In addition, not only excessive rain but also the absence of rain over long periods can cause large economic losses. Therefore also the occurrence of long dry spells can be regarded as an extreme (critical) situation.

Once these critical thresholds are expected to exceed water boards should take precautionary measures to avoid or mitigate the consequences. These measures may comprise early start of pumping, installing extra pump capacity, notifying third parties, change planning, etc., all the way up to evacuation of the endangered area. The time needed for preparing and taking these measures range from several hours to several days.

But since meteorological forecasts are inherently probabilistic water boards also have to assess at what probability level action will be taken. This is the most difficult part. At best the determination of the probability threshold is more or less based on a heuristic cost-loss analysis. If the costs of taking precautionary actions are low compared to the losses incurred when no action is taken then a water board is inclined to take those precautionary actions at

low probabilities already. On the other hand, if the precautionary actions are very expensive relative to the losses incurred then the probability threshold will be relatively high.

So a large number of possible critical situations can be specified together with their probability level above which precautionary actions are profitable. Also the time in advance the water board would like to be warned must be specified in order to give them ample time to take the necessary actions. These are called risk profiles. All participating water boards have been consulted to establish their risk profiles. The typical number of risk profiles for each water board is in the order of 10 to 15 (including different levels for different seasons).

The event thresholds are essentially based on an impact assessment of possible adverse weather situations / scenarios, but they are usually taken somewhat on the safe side to account for the variability of the precipitation within the water board area since locally the situation may be critical while the area averaged threshold is not exceeded. This is also true for the probability threshold; a few extra false alarms are preferred over having no warning at all. Besides, not all risk profiles are intended to take immediate action upon. Many risk profiles, especially for longer lead times, mainly serve to raise the awareness that something might happen.

Description of the present status of the warning system

In order to provide water boards with warnings in case of .extreme. weather conditions an automatic warning system has been developed which checks every hour all risk profiles of all participating water boards and issues a warning if at least one of the critical thresholds is exceeded. As indicated in the previous section it has to consist of a historic part and a prediction part. Since soil saturation and diminished storage capacity is important for the amount of (additional) precipitation a water board can handle, the warning system must include an estimate of this each time the risk profiles are checked. As a proxy for this we take the history of (area averaged) precipitation over the last couple of days (to a maximum of 5 days). The length of this .history. period again depends on local circumstances and is different for each water board. Some water boards can restore normal situation much faster than other water boards. The precipitation record is constructed from radar observations over all pixels covering the water board area, but calibrated using online rain gauge measurements from stations within the particular area (Holleman, 2006). The radar pixels have recently been changed from 2.5x2.5 km to approximately 1x1 km.

The meteorological prediction part consists of a deterministic and a probabilistic part. The deterministic part is optional. It is limited to a maximum of 36 hours (starting from the issuance time) and is obtained from the local Hirlam model that runs 4 times a day with a resolution of 11km. The first two hours of the deterministic forecast are replaced by a “radar extrapolation” in which the observed radar field at time zero is advected using the model

winds at that time, and the precipitation is summed over the area of the water board (Rudolf van Westrhenen, pers. comm.). The probabilistic part comes directly from the ensemble prediction system (EPS) of ECMWF; no calibration or post-processing is performed. The forecasts used are mainly precipitation but also combinations with winds and other variables are possible (see the example in the next section). EPS forecasts are available twice a day with a forecast range of 15 days. If water boards have risk profiles extending into the probabilistic forecast range (i.e. beyond 36 hours), they can choose to incorporate (part of) the deterministic forecast into the evaluation of the risk profile. In that case the deterministic value at the predetermined lead time is simply subtracted from the event threshold in the particular risk profile.

Also probabilistic water level forecasts for several sites along the Dutch coast are available in the alert system. These are produced by the WAQUA/DCSM storm surge model (de Vries, 2008) driven by ECMWF EPS forecasts for wind and mean sea level pressure, and are updated twice daily as well.

This means that water boards can define risk profiles that may be combinations of all kinds of meteorological and surge conditions up to lead times of 15 days. The precipitation amount of up to 5 days in the past can be taken into account. The number of risk profiles is virtually unlimited but most water boards have risk profiles in the order of 10-15. As mentioned above the system is updated every hour, and every hour all risk profiles are checked. If at least one of the thresholds is exceeded an automatic mail will be send to the water board with all relevant information regarding the forecast and precipitation record. There is also some graphical support available to the water boards by means of a web site with restricted access. Finally, in cases of doubt or if further consultation is needed KNMI forecasters can be phoned 24 hours a day.

Example

In order to construct more tailor-made risk profiles including a less subjective basis of event as well as probabilistic thresholds we are performing an experiment with one of the water boards. It is water board Fryslan which is located in the NE part of Holland. Excess water has to be drained through a system of canals and small lakes to the North Sea in the north and to the IJssel Lake in the west (see figure 1.2).

In normal circumstances water board Fryslan can handle at least 40mm of precipitation but it runs into trouble if there is a strong persistent wind from west or north west resulting in relatively high water levels in the canals in the south east and relatively low levels in western parts. In extreme situations this difference in water level may be almost 50 cm. Situations are even worse if this happens in combination with high surges along the coast, which is usually the case in a northwesterly flow regime, since part of the water has to be drained

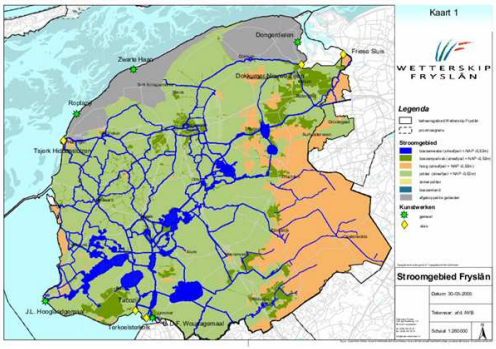

Figure 1.2: Water Board Fryslan

towards the north sea by opening sluices at low tides. In these conditions it is expected that a precipitation amount of 25 mm accumulated over 48 hours may be critical already. The water board may wish to receive an alert at least 3 days in advance if the probability is at least 25% that a situation like this will occur. In figure 1.3, a forecast is shown based on the 12UTC run of EPS on the 15th of November 2007. The probability of having a surge along the coast of more than 1.5 meter above normal is indicated in blue, the probability of a wind speed of at least 10 m/s from the NW averaged over the last 24 hours is given in green and the probability of more than 25 mm of rain in red. The combined probability (given in black) exceeds the 25% threshold in 4.5 days time. This 25% ideally comes from an estimate of the cost-loss ratio as outlined previously but is still a matter of further investigation.

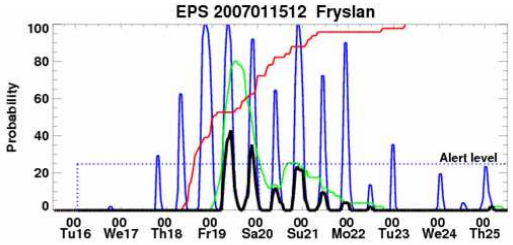

Figure 1.3: red: probability of accumulated precipitation of $\geq$ 25mm; green: prob. of sustained ff $\geq$ 10m/s from the NW; blue: sea level $\geq$ 1.5 meter +NAP; black: combined probability (if $\geq$ 25% then alert)

Concluding Remarks

The automatic alert system for the Dutch water boards is a rather flexible one. It can accommodate almost all meteorological and surge situations for all water boards. The acceptance of the warnings being based on probabilistic in stead of deterministic information is quite good, although determining probabilistic thresholds in the risk profiles is still somewhat troublesome. By tailoring the profiles more closely to critical conditions that are combinations of several meteorological parameters, including possibly surge levels, we hope to improve the

use and usefulness of the system even more.

In the near future the system will be updated to include probabilistic river level forecasts. These are very important for some of the water boards for the amount of precipitation they can handle. Furthermore, work is in progress to replace the deterministic short range forecasts by probabilistic ones. Probabilities obtained from EPS do not show enough spread and are therefore not reliable (Wilks, 2006). The method we plan to use is Bayesian Model Averaging (BMA) performed on several operational NWP models available at KNMI.

References

Holleman, I., 2006: Bias adjustment of radar-based 3-hour precipitation accumulations. KNMI Technical Report, TR-290.

de Vries, J.W., 2008: Probability forecasts for water levels at the coast of the Netherlands. ECMWF Newsletter No. 114, 23-29.

Wilks, D.S., 2006: Statistical methods in the atmospheric sciences, 2nd Ed., Academic Press, 627 pp.

1.5 Experiences in the operational flood forecasting service with MAP D-PHASE products

Stephan Vogt

Federal Office for the Environment FOEN, Hydrology Department, 3003 Bern, Switzerland

Introduction

For more than two decades the Hydrology division of FOEN has been running an operational hydrological forecasting service for the High Rhine basin. Initially forecasts were only issued for the most downstream gauging station Rhein-Rheinfelden. Over the last years additional forecasts for the main tributaries have been set up. Today forecasts for 11 gauging stations are issued to regional authorities and private customers.

The increased frequency of flood events over the past years in Switzerland and in neighboring countries sensitized the public as well as media and led to increased expectations of the hydrological forecasting service.

Especially the flood event in August 2005 and the resulting event analysis showed the need for improvements in various respects. Among other points the consideration of uncertainty as well as frequently updated high resolution forecasts as input in the hydrological model were identified as key factors.

The project MAP D-PHASE provided an excellent opportunity to benefit from the latest developments in the field of numerical weather prediction and to test new products.

Current operational flood forecasting system at FOEN

In the present operational forecasting system the hydrological model HBV is coupled with COSMO7 from MeteoSwiss; deterministic ECMWF is used as backup. Hourly data from SwissMetNet as well as from the discharge gauging network of FOEN is used for data assimilation. The integration of all components is realized in the Flood Early Warning System FEWS.

FEWS as it is currently set up at FOEN is a stand-alone system. This means that forecast runs are triggered manually by the forecaster. Under normal conditions one forecast run is carried out on working days in the morning. Under flood conditions forecasts are produced more frequently up to every two hours also during weekends. In consequence flood forecasts do not have regular initial times.

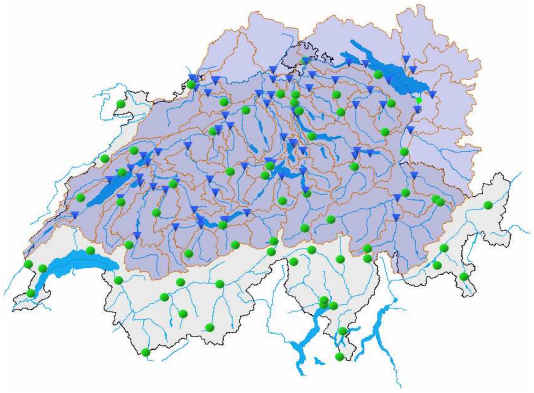

Figure 1.1: Area covered by flood forecasting systems at FOEN

Experimental setup of FEWS during MAP D-PHASE

COSMO2, a refined version of COSMO7, COSMO-LEPS and SRNWP-PEPS were tested during the DOP of MAP D-PHASE. COSMO7 and the deterministic version of ECMWF were already used for the operational hydrological forecasting service, these models were also considered for the experimental setup. All models are in use in the operational forecasting service at MeteoSwiss which means that assistance for the interpretation was available.

In collaboration with DeltaRes an experimental version of FEWS was set up parallel to the existing forecasting system. Like the operational system it is a stand-alone system which has to be run manually. This is done once a day under normal conditions and more frequent during flood situations if the operational service allowed it.

Direct model output was disseminated to the MAP D-PHASE visualisation platform. More than 30 persons in 12 different institutions participated as end users and were informed actively by E-Mail in case of an exceedance of MAP D-PHASE warning level 2 (mHQ - σ).

Because of the great benefit of the use of MAP D-PHASE products for the hydrological forecasters as well as for the end users the experimental setup of FEWS MAP D-PHASE has been prolonged beyond the DOP. Plans to carry over the experimental setup into an operational status are discussed below.

Flood event from August 8 and 9, 2007

On August 8 and 9 extraordinary flood peaks were observed especially in the central and northwestern parts of Switzerland. Return periods of more than 100 years have been estimated for several gauging stations.

For river Kleine Emme, a hindcast experiment has been carried out using all available COSMO2 forecasts as input for HBV instead of only one as it is done under normal conditions.

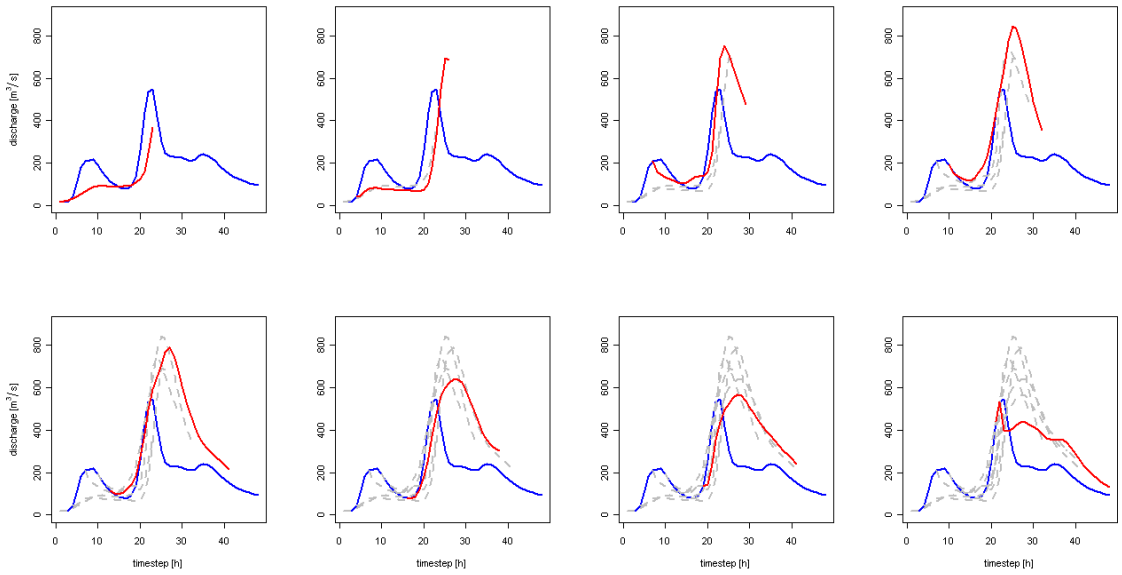

Figure 1.2: hindcast experiment with COSMO2 coupled with HBV for Kleine Emme-Littau. Blue line: measured discharge. Red line: actual initialisation. Gray lines: previous initialisations. t_0 = August 08, 2008, 00 CEWT

The large overestimation of the magnitude of the flood peak in the first runs was reduced to an acceptable level while the timing of the peak was too late. All runs can be considered as time-lagged ensemble, the measured flood peak is within the ensemble spread.

COSMO-LEPS coupled with HBV from the same day in the same basin shows clear indices for a rise of discharge above MAP D-PHASE warning level 2. The rise above warning level 3 has been indicated only with a very low probability. The timing of the flood peak tends to be too late.

Follow-up projects triggered by MAP D-PHASE

Automatisation of forecasting system: It was clear after a short time working which different meteorological model input that switching back to the deterministic one-model-world is not an option. Since the stand-alone version of FEWS does not allow to use the full potential of frequently updated high-resolution models, a project for a fully automated client-server system has been set up. A testing system will be available in early 2009.

Verification of MAP D-PHASE forecasts: In collaboration with MeteoSwiss, WSL and DeltaRes a project for a sound evaluation of the MAP D-PHASE forecasts is set up. Verification will be done with WMO standard methods, an adaptation is needed to hydrological questions, e.g. flood volume and timing of peak. Three different approaches will be pursued:

- As mentioned above, forecasts were started and disseminated to end users with irregular

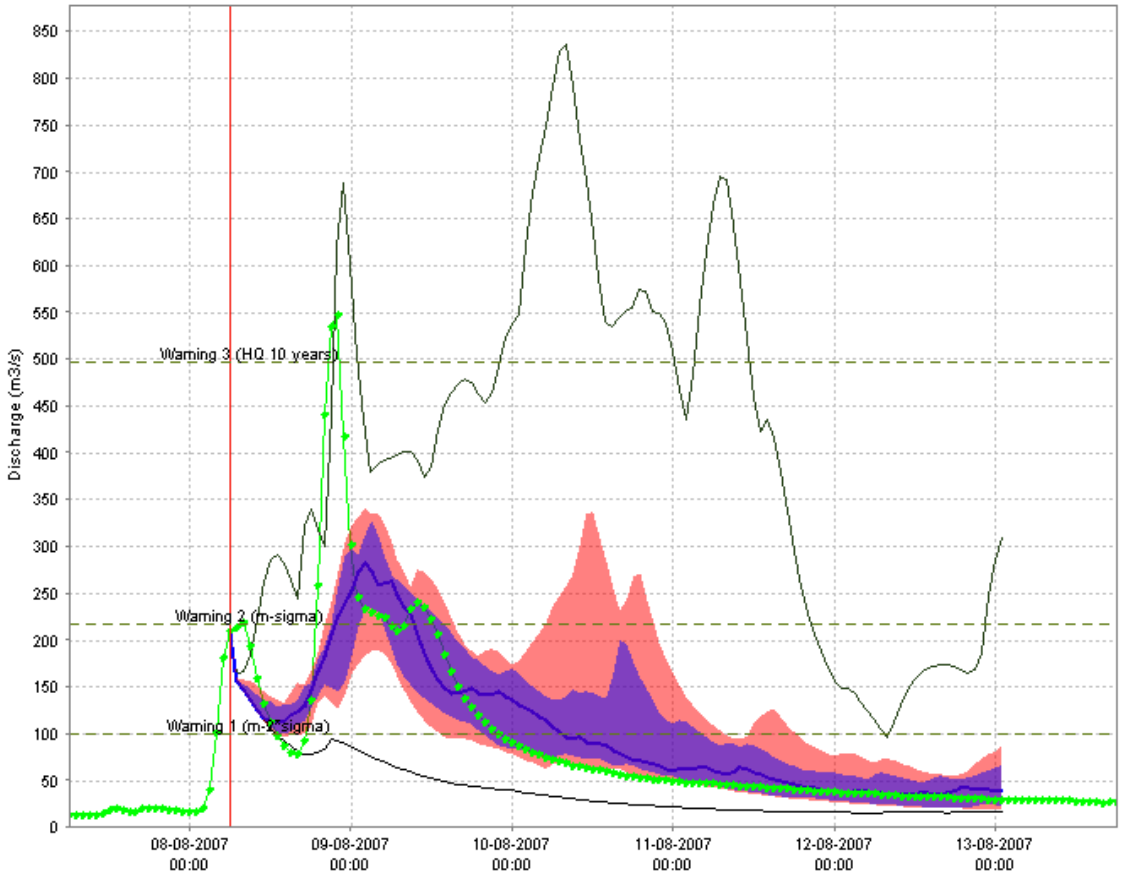

Figure 1.3: Operational flood forecast based on COSMO-LEPS/HBV for Kleine Emme-Littau.

initial times. In order to judge the possible benefit for end users, these operational MAP D-PHASE forecasts are examined.

- Complete hindcasts series for all driving models and all available initial times will be verified. This will help to judge the full potential of frequently updated forecasts.
- For special events (e.g. flood August 8 + 9, 2007) detailed analyses are carried out.

Using only the forecasts from the DOP results in a very small data basis, therefore the test forecasting period has been extended to June 2008. On the basis of the methodology used for the MAP D-PHASE verification it is planned to develop an operational real-time verification tool.

Conclusions

Working with more than one meteorological model and especially with ensemble models as driving input for hydrological models has been a paradigm shift in operational flood forecasting in Switzerland. This includes the perspective of the hydrological forecaster as well

as the perspective of the end user who has to take a decision upon ambiguous information. Therefore, the following statements may be trivial for met forecasters and modelers but are important for the hydrological community:

- Subjective experience from the forecasting service shows that the best input for flood forecasting does not exist and using one model is not enough.
- In case of longer reaction times (>48h) decisions have to be made on the basis of mid-range forecasting models (ECMWF, COSMO-LEPS). The accuracy may be relatively low especially in small, fast responding catchment. On the other hand this information is very helpful to raise the awareness and to think in scenarios. For shorter reaction times (<24h) frequently updated forecasts (COSMO2) should be drawn on for the judgment of the development.
- Guidance from the meteorological forecaster is essential. They have the knowledge of typical behavior of meteorological models in certain weather situation and can provide add-benefit to the hydrological forecaster.
- Forecasting is interpretating, weighting and judging of different models, based on the forecasters experience, knowledge and intuition. While this is undisputed in meteorology, this has been the practice for many years in hydrological forecasting. The whole bunch of different model output can be very complex for many (not all!) end users. This model output should not be kept back from the end user but has to be completed with the forecaster's interpretation.
- Due to the previous practice end users are used to look and focus on the hydrograph. Therefore training of customers and sharing of experience and knowledge between end users and forecasting center is important. The forecasting service has the challenge to prepare and communicate the products in the easiest way possible. On the other hand it's the end user's duty to be prepared to learn how to work with uncertainty.

References

WWRP/WGNE Joint Working Group on Verification, 2008: Forecast Verification - Issues, Methods and FAQ.
http://www.bom.gov.au/bmrc/wefor/staff/eee/verif/verif_web_page.html, last checked: October 30, 2008

1.6 Quantification of radar rainfall estimates uncertainty and propagation into a distributed hydrological model

Kai Schröter [1], Xavier Llort [2], Carlos Velasco-Forero [2],
Manfred Ostrowski [1], Daniel Sempere-Torres [2]

[1] *IHWB, TU-Darmstadt, Petersenstr.13, 64287 Darmstadt, Germany;*

[2] *GRAHI-UPC, C/Gran Capita 2-4, 08034 Barcelona, Spain*

Introduction

Radar based quantitative precipitation estimates (QPE_{rad}) available in real time at high spatial and temporal resolution are promising information to adequately simulate the dynamics of hydrological systems. Though, remarkable progress has been achieved in measuring precipitation fields these data remain an important source of uncertainty in hydrological model predictions. On the one hand, uncertain precipitation input propagates through the hydrological model contributing directly to the uncertainty of model predictions. On the other hand, uncertain input data affect hydrological model parameter estimates as they tend to compensate for erroneous input data during inverse parameter estimation procedures. Biased parameter estimates, in turn, influence the reliability of model predictions.

Objectives

The objective of this work is to statistically analyse spatial and temporal characteristics of uncertain QPE_{rad} and to conceive an appropriate probabilistic model to describe this uncertainty. The capability of the probabilistic model to explain the uncertainty present in the input data is evaluated both in precipitation terms and in hydrological terms.

Methodology

The quantification of QPE_{rad} uncertainty builds on a relative comparison of different QPE methods. QPE_{rad}, which are available for operational hydrological modelling applications in real time, are compared against a benchmark precipitation field (QPE_{bm}) which represents the best ex post attainable estimate of the precipitation field. QPE_{bm} assimilates all available information, including data records which are not accessible in real time, and allows for a thorough post-processing and expert analysis.

This approach does not resolve uncertainties related to both unknown errors and known but unaccounted errors in the benchmark field. Still, this method deepens insight into the

structure of QPE_{rad} uncertainty and is suitable to evaluate the relevance of different input uncertainty characteristics in a hydrological modelling context. The error field resulting from the comparison is statistically analysed to infer the parameters of the probabilistic input uncertainty model. Following Germann et al. (2006) and Lee et al. (2007) a multiplicative error definition is adopted. The error is defined in equation 1.6 as the ratio in logarithmic scale between QPE_{bm} and the QPE_{rad} field.

$$E_{(t)} = LOG_{10} \cdot \frac{QPE_{bm_{(t)}}}{QPE_{rad_{(t)}}} \qquad (1)$$

A threshold value is applied to identify actual occurrence of rainfall and to cut off error values outside the definition domain of the logarithm. For each error field, the relative frequency distribution, the mean ($\mu_{(t)}$) and standard deviation ($\sigma_{(t)}$) as well as the spatial auto-correlation of error pixel values are determined. The analysis of spatial auto-correlation resorts to the String of Beads model proposed by Pegram and Clothier (2001), which applies spectral analysis of the field. Fast Fourier Transformation (FFT) is used to quantify the degree of spatial auto-correlation in terms of the slope ($\beta_{(t)}$) in the Fourier power spectrum, (Llort et al. 2008).

Perturbation fields are generated for each time step from the input uncertainty model by means of a stochastic sampling process using the temporal mean values ($\overline{\mu}$, $\overline{\sigma}$ and $\overline{\beta}$) of the parameters identified in the analysis of the error fields. The probabilistic simulation process starts with the generation of a white noise field. This field is transformed according to the actual mean and standard deviation of the error sample. Next, spatial correlation is superimposed using FFT. Along these lines an arbitrary number of perturbation fields (ϵ^i) with identical statistical properties is produced. For the preparation of the precipitation input ensemble the error term in equation 1.6 is replaced by a realisation of the perturbation field (ϵ_i). Reorganising (1) results in the definition for the computation of an input ensemble member (QPE_{ENS}) as given in equation 1.6.

$$QPE_{ENS_t^i} \; = \; QPE_{rad_{(t)}} \cdot 10^{\frac{\epsilon^i_{(t)}}{10}} \qquad (2)$$

QPE_{ENS} are used to force the hydrological model. Forward propagation of uncertain input reveals the sensitivity of model predictions to input uncertainty. The impact on hydrological model parameter estimates is analysed in terms of changes in the posterior parameter distribution using a Bayesian inference approach. To exclude other sources of uncertainty, a set of reference model parameters are used. In combination with QPE_{bm} this parameter set is used to generate reference hydrographs to study the implications of QPE_{rad} and the performance of QPE_{ens} .

Application Study

For the analysis a distributed hydrological model (WBrM) (Lempert, M. 2000) is applied to the Bess basin (1024 km, near Barcelona, Spain). Soil and land use patterns as well as precipitation input are represented on a 1 km grid resolution. Data from the C-Band radar of the Spanish Institute of Meteorology (INM) at Corbera de Llobregat are used. QPE_{rad} data have a resolution of 1 km and are available in 10 minutes intervals. Further, there are 31 remote data transmitting rain-gages of the SAIH network (Hydrological Information and Alert System) within the region of interest reporting in 10 minute intervals, refer to Berenguer et al. (2005) for details on the data processing algorithms applied.

Four parameters are used to calibrate the hydrological model, being, the degree of imperviousness (DI), total porous volume (TPV), saturated hydraulic conductivity (kf) and initial soil moisture (iniSM).

Results

A selected single rainfall-runoff event is used to demonstrate the procedure of the methodology proposed. The QPE_{rad} and the QPE_{bm} data yield hyetographs of the mean areal precipitation (MAP) that largely show a similar development in time. As a mayor difference the volumetric information provided by QPE_{rad} overestimates rainfall depth by 16 %. The corresponding hydrological responses using the WBrM are shown in Figure 1.1 in terms of the hydrographs at the basin outlet. The thick solid and dashed black lines correspond to the model response using QPE_{bm} and QPE_{rad} respectively. This plot shows that overestimation of rainfall depth by QPE_{rad} consistently leads to an overestimation of discharge volume and peak discharges.

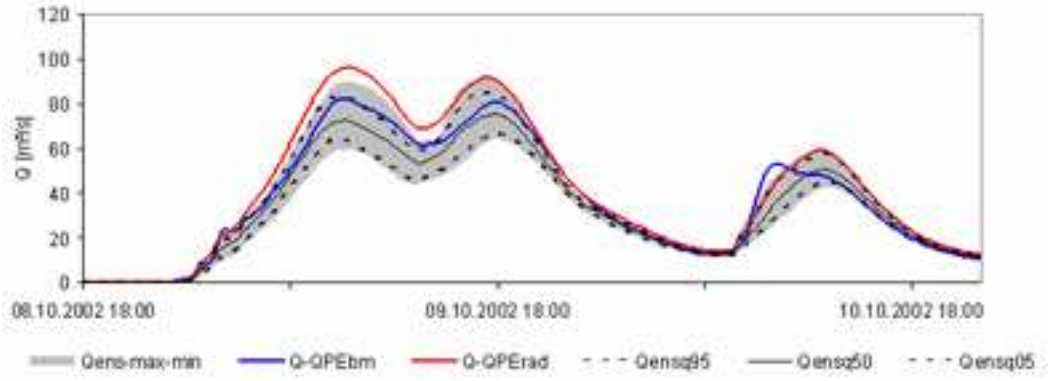

Figure 1.1: Simulated hydrographs using different input data for the hydrological model WBrM.

The histogram of errors resulting from the statistical analysis of the QPE data according

to equation 1.6 resembles a normal distribution (not shown). The variation of μ_t , σ_t and β_t within the different error fields of the event is small, see Llort et al. (2008) for details. An ensemble with 100 members has been generated. The hyetographs of the QPE_{ens_i} have been compared to the (QPE_{bm}) field in order to assess whether it adequately describes the uncertainty inherent to the (QPE_{rad}) field. The range of ensemble hyetographs almost entirely embraces (QPE_{bm}). However the volumetric correction is too strong (not shown).

The grey shaded area in Figure 1.1 contains the range of minimum and maximum responses produced by the input ensemble using the hydrological model. The slim solid and the dotted black lines mark the 50%, 10% and 90% quantiles of the model output ensemble. In general, the dynamics of the ensemble hydrographs follow the QPE_{rad} simulation results. The ensemble range in great parts approximates the benchmark hydrograph. With regard to the magnitude of simulated peaks and the discharge volume, the findings of the analysis in precipitation terms are consistently reflected in the hydrographs. Overall, the discharge ensemble too strongly corrects for the volume differences and most members slightly underestimate the peak values.

Model parameter and parameter uncertainty estimation has been carried out using a sub set of 10 members of the entire ensemble (100 members). These members have been selected in view of capturing the variation in accumulated MAP as well as extreme occurrence of precipitation intensity. The normalised parameter values obtained from a repeated (10 repetitions) estimation process based on the minimisation of the error variance are shown in Figure 1.2 using different input data. For comparison the reference parameter values are also given in the chart. Overall, the parameters identified using QPE_{ENS} are closer to the reference values than obtained by calibration using QPE_{rad}. The degree of imperviousness and initial soil moisture show the tendency to increase the runoff volume in order to compensate for the volumetric differences in comparison to QPE_{bm} data. Similar observations have been made for the mode of the posterior parameter distributions using a Monte Carlo Markov Chain inference approach which cannot be discussed in detail here. Refer to Schröter (2008) for a full discussion of this approach.

Conclusions

These first results presented demonstrate that it is possible to condense the uncertainty inherent to radar based input uncertainty in a probabilistic model and to map this uncertainty to the response of a hydrological model by means of an input ensemble. The statistical analysis does not resolve all aspects of input data uncertainty. Uncertainty with regard to volumetric information has been found to be highly relevant. Further it has been shown that the explicit quantification of input uncertainty adds additional information to the parameter estimation process and can be beneficially exploited. The evaluation of the approach has to

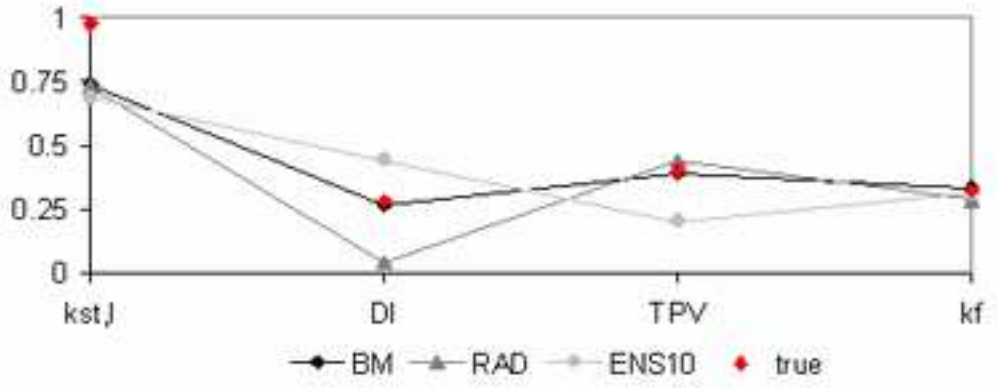

Figure 1.2: Reference parameter values and parameter estimates using different input data.

be deepened and extended in order to analyse further characteristics of input uncertainty more in detail, such as temporal auto-correlation, maximum precipitation intensity as well as the space time distribution. In this context, the analysis in hydrological terms has to be conducted at different internal sites of the catchment. Another issue of interest concerns the generality and transferability of the parameter values of the probabilistic input uncertainty model to different events.

Acknowledgements: Parts of the work have been elaborated within the frame of the EU project EWASE, contract no. 02NH0810, which is embedded in the ERA-NET CRUE integrated project, supported by the European Comission under FP6. Further support has been granted by COST Action 731 by means of Short Term Scientific Mission.

References

Berenguer, M., C. Corral, R. Sanchez-Diezma and D. Sempere-Torres (2005). "Hydrological validation of a radar-based nowcasting technique." Journal of Hydrometeorology 6(4): 532-549.

Corral, C., M. Berenguer, D. Sempere-Torres and I. Escaler (2002). Evaluation of a conceptual distributed rainfall-runoff model in the Bess catchment in Catalunya using radar information. 2nd European Conference on Radar in Meteorology and Hydrology, Munich.

Germann, U., M. Berenguer, D. Sempere Torres, and G. Salvad, 2006: Ensemble radar precipitation estimation - a new topic on the radar horizon. Fourth European Conference on Radar in Meteorology and Hydrology, Barcelona.

Lee, G., A. W. Seed, and I. Zawadzki, 2007: Modeling the variability of drop size distributions in space and time. Journal of Applied Meteorology and Climatology, 46, 742-756.

Lempert, M., 2000: Ein GIS-gekoppeltes rasterbasiertes Modell zur Berechnung des Wasserhaushaltes kleiner Einzugsgebiete, Inst. fr Wasserbau und Wasserwirtschaft, Technische Universitt Darmstadt, 183.

Llort, X., C. Velasco-Forero, J. Roca-Sancho and D. Sempere-Torres (2008). Characterization of Uncertainty in Radar-Based Precipitation Estimates and Ensemble Generation. Fifth European Conference on Radar in Meteorology and Hydrology, Helsinki.

Pegram, G. G. S. and A. N. Clothier, 2001: High resolution space-time modelling of rainfall: the "String of Beads" model. Journal of Hydrology, 241, 26-41.

Schröter, K., Llort, X., Velasco-Forero, C., Muschalla, D., Ostrowski, M., Sempere-Torres, D. (2008). Accounting for uncertain radar rainfall estimates in distributed hydrological modelling. International Symposium on Weather Radar and Hydrology, Grenoble, France.

Schröter, K. (2008). A contribution to the uncertainty analysis of distributed hydrological models, PhD Thesis, Inst. fr Wasserbau und Wasserwirtschaft, Technische Universitt Darmstadt, submitted.

1.7 Can time–lagged precipitation forecasts improve hydrological predictions?

Jonas Olsson, Göran Lindström

Research & Development (hydrology)

Swedish Meteorological and Hydrological Institute (SMHI), 601 76 Norrköping, Sweden

Introduction and objective

The concept of time-lagged deterministic forecasts has been explored in different meteorological applications. Forecasts with different initialisation times but with the same verification time are pooled to generate a small (poor-mans) forecast ensemble. This ensemble may be used directly to produce probabilistic forecasts but it has also been used to create perturbed initial conditions for EPS. For both short- and medium-range forecasting, the time-lagging has been showed to improve the forecast accuracy. Evaluation has however generally focused on free-atmosphere variables (geopotential height, temperature, wind speed, etc.) and less on the hydrologically more important precipitation at surface level.

The objective of the study is to investigate whether previously issued forecasts of 24-h accumulated catchment precipitation can be used to enhance the current forecast in different respects. The predictand is accumulated precipitation between t and t+24. The current forecast is denoted f_t and the previous forecasts considered f_{t-24} and f_{t-48}. Two approaches are tested: (1) weighting of the forecasts and (2) probabilistic forecasts from a mini-ensemble.

Methodology and evaluation

One previously attempted strategy is to use a weighted combination. An adjusted weighted forecast $f_t^{'}$ may be generated according to

$$f_t^{'} = w_t * f_t + w_{t-24} * f_{t-24} + w_{t-48} * f_{t-48},$$

where w are constants (weights).

The three forecasts f_t, f_{t-24} and f_{t-48} form a mini-ensemble. From this ensemble, forecast probabilities can be estimated according to:
p_{max}=p(obs¿f_{max}) with f_{max}=max(f_t,f_{t-24},f_{t-48})
p_{min}=p(obs¡f_{min}) with f_{min}=min(f_t,f_{t-24},f_{t-48}),
where p() denotes probability.

The two approaches were evaluated using 2 years of daily precipitation observations (gauge-derived averages) and categorical forecasts (PMP, combining HIRLAM and ECMWF forecasts) for 77 Swedish catchments, representing different sizes as well as geographical/climatological conditions. Forecast accuracy was assessed in terms of average value (Avg), standard deviation (Std) and mean absolute error (MAE). For approach 1 the constants were optimised by multiple linear regression. For approach 2 the empirical values of p_{max} and p_{min} were estimated.

Results and discussion

In the original forecast, the mean value is overestimated by $\sim$ 20%, the standard deviation by $\sim$ 10% and MAE is 1.48 mm.

On average, the contribution to the weighted forecast is 52% from f_t, 22% from f_{t-24} and 13% from f_{t-48}. The weights are almost always positive, but in some catchments w_{t-48} is negative. The fact that the sum of the average weights is below unity may reflect the overestimated mean value in the original forecast. The resulting mean value, however, becomes slightly underestimated (4%) but more accurate than in the original forecast. MAE is 1.22 mm, which means an 18% improvement compared with the original forecast. The weighting procedure naturally has a smoothing effect on the forecasts, which is reflected in an underestimated standard deviation (20%).

If the three forecasts are evenly distributed over the probability space, f_{max} defines the upper quartile (75% probability of non-exceedance) and f_{min} the lower quartile (25%). Thus 25% of the observations should fall above f_{max} and 25% below f_{min} ($p_{min} = p_{max} = 25\%$), i.e. 50% outside the entire range (f_{min}-f_{max}). On average, however, only 36% of the observations fall outside the range, indicating that the spread obtained from the latest three forecasts is larger than the interquartile range. There is in reality on average a 20% probability of getting precipitation above f_{max} and a 16% probability of getting precipitation below f_{min}. The values are rather similar for different catchments.

Conclusions and future work

The results indicate that the current forecast of daily catchment precipitation may be improved by simple functions of previous forecasts or information derived from them. Overall, the attainable gain in accuracy was found to be 10-20% when all days are considered. The result from the mini-ensemble evaluation indicated relatively stable values of p_{max} and p_{min}, with rather limited variation between catchments. This suggests that the maximum (minimum) of the three most recent forecasts may be used as a rough estimate of the precipitation value with a 15-20% probability of exceedance (non-exceedance). Possible future extensions

of the study include the incorporation of older forecasts than f_{t-48} as well as evaluation focusing on large (observed and/or forecasted) rainfall events. Finally, the ultimate aim of the work is improved hydrological forecasts. Hydrological modelling with adjusted precipitation forecasts is required to assess the hydrological significance of the improvements obtained for the precipitation forecasts.

1.8 Point process statistical analysis for meteorological ensemble predictions

Fabrizio Nerozzi

Servizio Idro–Meteo–Clima ARPA Emilia–Romagna, Italy

(e–mail address: fnerozzi@arpa.emr.it)

Introduction

Ensemble forecasting appears to be the only feasible method to predict the evolution of the atmospheric probability distribution function (PDF) beyond the range in which error growth can be prescribed by linearized dynamics (Molteni *et al.*, 1996). The contained large amount of information can be hardly managed in the whole, and two different strategies, clustering and tubing, are adopted at the ECMWF for reducing the 51 EPS forecasts to few alternative scenarios (Molteni *et al.*, 2001; Marsigli *et al.*, 2001).

For clustering, "similar" EPS forecasts are collected in clusters and averaged to constitute new forecasts, whose probability of occurence are provided by the cluster sizes. At present clustering is performed on the 500 hPa forecast and a quadratic norm is adopted for evaluating the similarity degree between two forecasts. One of the principal shortcomings of the clustering technique is the empirical distribution of the ensemble members: a large spread in the ensemble does therefore not necessarily lead to more clusters, nor does a small spread necessarily lead to fewer.

The tubing technique averages all ensemble members close, in term of RMS again, to the ensemble mean, while the excluded members are grouped together in a number of tubes. Each tube is represented by its most extreme member and not by an average of members belonging to it. Although tubing allows a better visualization of the most different scenarios in the ensemble, tubes are not intended to serve as probability alternatives, but only to give an indication of what is not included in the central cluster.

In order to provide a different way to condense information, which tries to overcome the shortcomings related to the empirical distribution of ensemble members, it is here exploited the possibility to represent ensemble forecasts as point processes in the plane, i.e. as a finite set of random points distributed in plane or in space. The subject of point process statistics is to define some methodologies for establishing whether random points do not exhibit any kind of interaction (homogeneous distribution pattern) or, instead, among them there is a tendency to the clustering or a regular distribution. Usually, it is useful to compare

an unknown point process against other point processes, considered as reference models (Stoyan et al., 1987; Cressie, 1991). Hereafter, it is tested the hypothesis according to which EPS point processes can be treated statistically equivalent to one of these reference models: Poisson, Gaussian and Poisson cluster processes.

The Principal Component Analysis

The Principal Component Analysis (PCA) is a very useful tool in the treatment of meteorological and climatological data, because it enables to transform a data set, characterized by a large number of variables in a new one, where the number of variables is highly reduced. Because of the strong correlation between original variables, a few of these new variables may explain the most part of variance of the original data set. The new variables are calculated as the eigenvectors of the covariance matrix and they are orthogonal among them (Preisendorfer, 1988).

The freedom degree number of an ensemble of forecasts is very large, because related to the grid point number, where meteorological fields are defined, and to the ensemble size. For the whole winter season 2006–2007 PCA has been therefore applied to the 5 to 7 day ECMWF EPS forecasts of 500 hPa geopotential height, defined over a regular grid at 1 degree of resolution and covering the European clustering area. Let Z represent the 51 ensemble anomalies respect to the ensemble mean. The covariance matrix is given by $S = ZZ^T$, and the eigenvectors $E = [e_1, ..., e_m]$ are obtained by the following equation system:

$$SE = E\Lambda$$

The analysis equation, representing the principal components matrix, is hence defined as

$$A = Z^T E$$

Because number of grid points is larger than the ensemble size, it is more useful to compute A as

$$Z^T SE = Z^T(ZZ^T)E = (Z^T Z)Z^T E = Z^T E\Lambda = A\Lambda$$

while EOFs having norm equal to 1 are given by

$$E = \frac{1}{\sqrt{n}} ZA\Lambda^{-1/2}$$

The variance explained by the first two eigenvectors ranges from 46% to 69% of the total variance.

The point–process statistics

The 90 Winter 5 to 7 day ECMWF EPS forecasts are reduced to point patterns in a plane by the first two Empirical Orthogonal Functions (EOF). In such case every point, say event, represents a single ensemble member, whose coordinates are provided by the first two Principal Components. A point process obtained projecting ensemble members over the plane of the first two EOFs, is reported in figure 1.1, as an example.

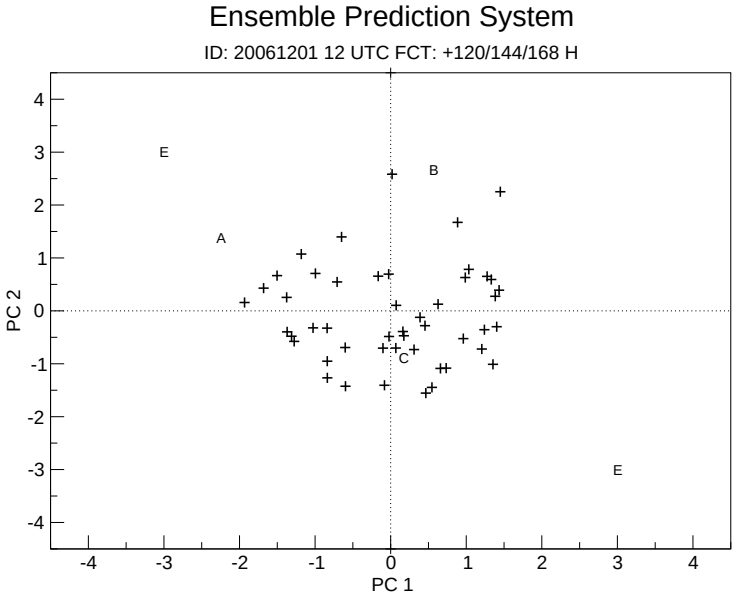

Figure 1.1: 5 to 7 day ECMWF ensemble forecasts starting from the 1^{st} December 2006 12 UTC. The sign (+) represent the ensemble perturbed forecasts, the capital letter A, B represent the two most distant members from the ensemble mean, whereas C show the control forecast position. The letters E indicate the positions of two possible extreme events, outside ensemble.

Three kinds of point processes are here used as reference models:

(i) a stationary Poisson point process with intensity λ equal to 51, whose events are uniformly distributed over a quadratic box of side equal to 4;

(ii) a Gaussian point process with the same intensity, whose events are distributed according to a standardized normal probability distribution function;

(iii) a Poisson cluster process, realized as a combination of two point processes: at first, a random number of parent events, ranging from 1 to 6, is generated in the quadratic

box of side 4 according to a Poisson point process. Then, in the neighbours of the parent events, taken as new centers, other random events are generated according to a Gaussian point process until a number of 51 events is reached.

Two different point–processes can be compared by the nearest–neighbour distribution function and by the reduced second order momentum, so called K function, or its derivative L. The nearest–neighbour distribution function $D(r)$ describes the probability the distance from a randomly chosen event to its nearest event is less than or equal to $r > 0$. Theoretical calculations show that for a homegeneous Poisson process, with intensity λ, the distribution function of the distance from an event to the nearest event in $\Re^2$ is (Stoyan *et al.*, 1987):

$$H(r) = 1 - e^{-\lambda \pi r^2}$$

This function can be euristically estimated from the observed pattern:

$$\hat{D}(r) = \frac{\sum_{i=1}^{n} I(r_{i,A} \leq r, d_i > r)}{\sum_{i=1}^{n} I(d_i > r)}$$

where d_i denotes the distance of the event from the nearest boundary of the closed set A and $r_{i,A}$ is the distance from the nearest event in A (Cressie, 1991).

The K functon uses information in the pattern over a wide range of scales than the nearest–neighbour distribution function. Its definition is related to the number of extra events within distance r from an arbitrary event. For a homogeneous point process in the plane, the reduced second order momentum $K(r)$ is given by the formula (Stoyan *et al.*, 1987):

$$K(r) = \pi r^2$$

Estimating of K from an observed pattern in a bounded $A \subset \Re^2$ is complicated by edge effects. Here the Ripley's edge–corrected estimator is considered (Cressie, 1991):

$$\hat{K}(r) = \frac{1}{n\lambda} \sum_{i=1}^{n} \sum_{j=1'}^{n} w(\mathbf{s}_i, \mathbf{s}_j)^{-1} I(\|\mathbf{s}_i - \mathbf{s}_j\| \leq r)$$

Let $u = \|\mathbf{s}_i - \mathbf{s}_j\|$ and let d_1 and d_2 be, respectively the distances of $\mathbf{s}_i$ from the edges of A; $w(\mathbf{s}_i, \mathbf{s}_j)$ is the weighting factor computed as a function from u, d_1 and d_2. The estimator $\hat{K}$ is approximately unbiased provided that the n events are approximately independent.

Estimating of the derivative of the K function, $\hat{L}(r)$, are computed by the formula (Stoyan *et al.*, 1987):

$$\hat{L}(r) = \sqrt{\frac{\hat{K}(r)}{\pi}}$$

When $\hat{L}(r)$ is approximatively linear, events tend to be distributed in a homogeneous manner; positive deviations from the linearity indicate a tendency to a clustering, whereas negative deviations are representative of a regular distribution of the points.

Results

The objective of the present study is to apply some mathematical tools of the point process statistics for finding out typical behaviours of the 90 Winter 5 to 7 day ECMWF EPS predictions, represented by the principal component analysis as point processes. For pursuing this objective, a comparison based on the similarity degree of the nearest–neighbour distribution function and the derivative of K function among the ensemble point processes and the other processes is perfomed. In particular, in the figure 1.2 the shaded area represents the confidence interval relative to the minimum and maximum values obtained by 99 simulated Poisson point processes. The median is also indicated and in this case it follows quite well the theoretical curve. At the same time it is also reported the inteval of the minimum and maximum values for the 90 ensemble point processes. It is evident on the left side the increasing displacement between the two nearest–neighbors distribution function. Similarly, a large deviation is also evident on the right side of the figure, for the second order momentum derivative.

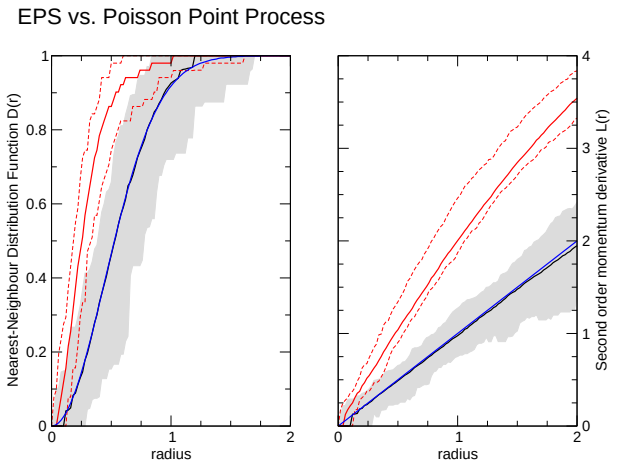

Figure 1.2: Ensemble point process vs. Poisson point process: nearest–neighbour distance distribution function (left side) and the derivative of the reduced second order momentum (right side): grey shaded area represents the confidence interval for 99 stochastic point processes, black solid line indicates the median value, while the blue solid line is the theoretical one. Red dashed lines represent the minimum and maximum values of the ECMWF EPS point process distribution, whereas the red continuos line is the median.

A good agreement between the median curves is evident for the case of gaussian point processes (fig. 1.3). In fact, for both functions the confidence interval of the ensemble point processes is contained in the shaded area. However, it is important to highlight on the right side of the figure a slight overestimation of the median for the second order momentum derivative.

For the case of Poisson cluster processes the median relative to the nearest–neighbor distribution function lies under the ensemble median as evident on the left side of the figure 1.4. Moreover, all the confidence interval of the ensemble point processes is placed in the region over the median for the second order momentum derivative.

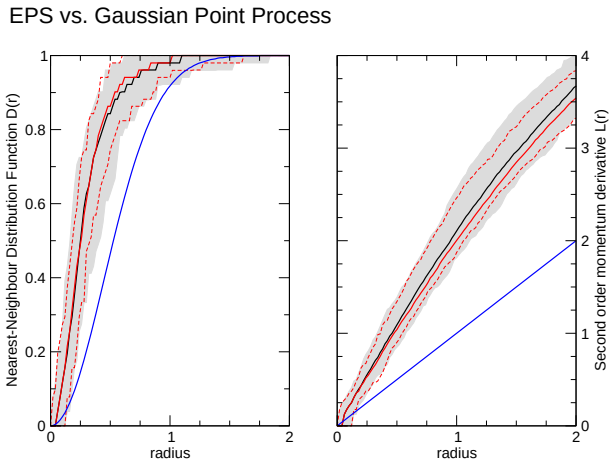

Figure 1.3: Ensemble point process vs. Gaussian point process: as in figure 1.2.

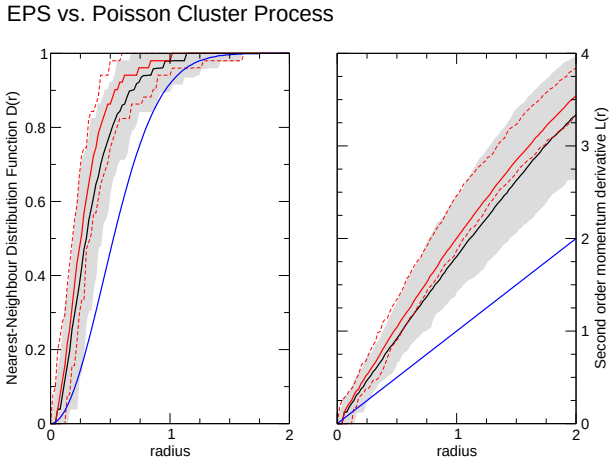

Figure 1.4: Ensemble point process vs. Poisson cluster process: as in figure 1.2.

Summary and Outlook

The possibility of applying mathematical tools of point–process statistics to the ECMWF Ensemble Prediction System (EPS) has been exploited in this work, in order to find a different way to condense the large amount of ensemble information. It has been proved the first two empirical orthogonal functions enable to represent about, or more, the 50% of the ensemble spread as point processes in a plane. These planar representations have been therefore compared to other three point patterns, obtained by a Monte Carlo method and considered as reference models. The estimations of the nearest–neighbour distribution function and of the reduced second order momentum function for point processes relative to the ensemble predictions are in good agreement with the correspondent estimations of gaussian point processes. At the same time, the behaviour of ensemble forecasts represented as point processes appears to be biased respect to a Poisson cluster processs.

On the basis of these results, it appears reasonable assign a probability to each ensemble member calculated by the standardized normal distribution function, proportionally to the distance of the event from the origin in the plane.

References

Cressie, N. 1991: Statistics for spatial data. Eds. J.Wiley & Sons.

Marsigli, C., A. Montani, F. Nerozzi, T. Paccagnella, S. Tibaldi, F. Molteni, R. Buizza, 2001: A strategy for high–resolution ensemble prediction. Part II: Limited–area experiments in four Alpine flood events. Q. J. R. Meteorol. Soc. in press.

Molteni, F, R. Buizza, T.-N. Palmer, T. Petroliagis, 1996: The ECMWF Ensemble Prediction System: Methodology and validation. Q. J. R. Meteorol. Soc. 122, 73–119.

Molteni, F., R. Buizza, 1999: Validation of ECMWF Ensemble Prediction System using empirical orthogonal function. Q. J. R. Meteorol. Soc. in press.

Molteni, F., R. Buizza, C. Marsigli, A. Montani, F. Nerozzi, T. Paccagnella, 2001: A strategy for high–resolution ensemble prediction. Part I: Definition of Representative Members and Global Model Experiments. Q. J. R. Meteorol. Soc. in press.

Preisendorfer, R.-W., 1988: Principal component analysis in meteorology and oceanograpy. Eds. Curtis D. Mobley.

Stoyan, D., W.-S. Kendall, J. Mecke, 1987: Stochastic geometry and its applications. Eds. J. Wiley & Sons.

2.1 Assessment of cloud cover and precipitation forecasts obtained with MESO-NH in summertime

Jean-Pierre Chaboureau and Evelyne Richard

Laboratoire d'Aérologie, Université de Toulouse and CNRS, Toulouse, France

Introduction

Clouds and their potential outcome - precipitation - are sensible weather elements that it is crucial to forecast. Despite the importance of the water cycle for human activities, skill in forecasting cloud cover on a day-to-day basis has been little explored. Satellite observations, with their good coverage in time and space, can provide a basis for assessing such skills. In this study, we adopted a model-to-satellite approach, in which satellite brightness temperature (BT) images were directly compared to BTs computed from predicted model fields. This approach offers the advantage that the satellite data are used in an objective way, without being combined with any ancillary data. The verification of the cloud cover forecast combined the model-to-satellite approach with the calculation of scores and was carried out over the series of daily 30-h simulations performed with the MESO-NH model, driven with ECMWF analyses and forecasts during the D-PHASE period. We essentially used the BT at 10.8 μm from hourly MSG observations, which is mainly affected by cloud-top heights. The cloud forecast assessment was also examined in comparison with the results of a more classical precipitation verification method based on rain gauge observations. The overall method provides a framework for assessing the cloud cover and precipitation forecasts together and quantifying their predictability with respect to weather regimes

Model setup and experimental design

The forecasts were made with the anelastic non-hydrostatic mesoscale model, MESO-NH (Lafore et al. 1998). The two-way interactive grid-nesting method (Stein et al. 2000) enabled simultaneous running of several models on the same vertical levels but with different horizontal resolutions. The forecasts were made using triply nested models with horizontal grid spacings of 32, 8, and 2 km, the inner model covering the COPS area. The vertical grid had 50 levels up to 20 km with a level spacing of 60 m close to the surface, rising to 600 m at high altitude. A sponge layer was installed from 14 to 20 km in order to damp the upward propagating gravity waves. The lateral boundary conditions were given by large-scale operational analyses for the outermost model and they were provided by the outer models

for the inner models at each time step. The individual forecasts were initialized with 00 UTC European Centre for Medium-Range Weather Forecasts (ECMWF) or ARPEGE analyses. From 1 July to 31 August 2008, two sets of 62 daily 30-hour forecasts were run. For the two coarser-resolution grids (32 and 8 km), the subgrid-scale convection was parameterized by a mass-flux convection scheme. For the inner grid (2 km), explicit deep convection was permitted and the convection scheme was switched off. The microphysical scheme included the three water phases with five species of precipitating and non-precipitating liquid and solid water. The turbulence parameterization was based on a 1.5-order closure. The radiative scheme was the one used at ECMWF including the Rapid Radiative Transfer Model (RRTM) parameterization. The surface scheme was the Interactions between Soil, Biosphere and Atmosphere (ISBA) soil scheme.

Cloud cover assessment

Synthetic brightness temperatures (BT) corresponding to the MSG observations were computed off line using the Radiative Transfer for Tiros Operational Vertical Sounder (RTTOV) code version 8.7 and compared against observations following Chaboureau et al. (2000, 2002). We used the BT at 10.8 μm from hourly MSG observations as it is mainly affected by cloud-top heights. The method provided a framework for assessing the cloud cover forecast. In particular it has been used to investigate the predictability of convective systems with synoptic forcing over West Africa (Söhne et al. 2008).

Time evolution Systematic errors in the representation of the cloud cover were first examined through the time evolution of the mean observed and forecasted BTs and the associated biases (Fig. 2.1 left). The mean BT range was between 240 and 300 K. The low BT values that persisted for several hours corresponded to fronts travelling across the simulation domain (on 2, 3, 8, 20, 23, and 30 July and 1-2, 7-8, 21, and 29-30 August). The high BT values characterized the hot weather periods around 14 July and 5 August. Intermediate BTs that presented a high variability during daytime characterized convective periods, e.g. on 16-19 July or 12-20 August. Note that longer periods of convection occurred in July than in August. On the other hand, the bias varied between 0 and 5 K (Fig. 2.1b). The largest values were found in the transition periods when the observed mean BT was around 260 K. As the two sets of forecasts showed a similar time evolution of the bias, the latter could be attributed to a systematic fault in the model.

BT distribution The systematic error in BT was further investigated using observed and forecasted BT distributions over the whole period (Fig. 2.1 right). All the distributions showed a maximum for the 290-295 K bin and a shape skewed towards the lower values. The frequency of forecasted BTs was overestimated in the maximum bin, which counterbal-

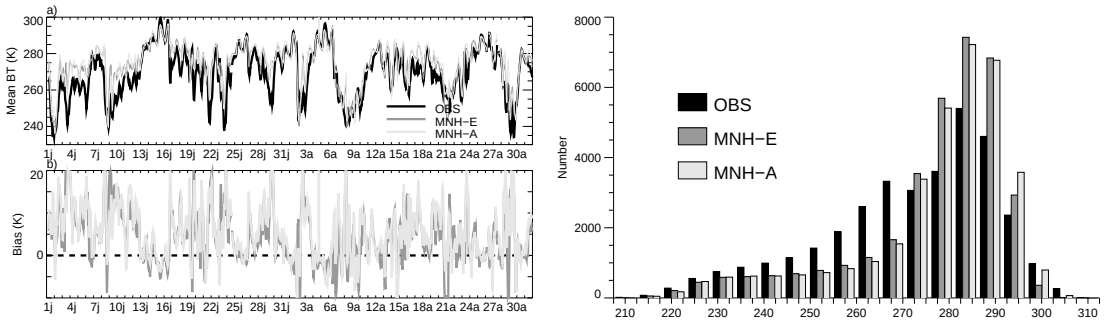

Figure 2.1: (left) Time evolution of mean BT and bias (a) mean BT from (black) the MSG observation and (grey) the Meso-NH forecasts. (b) bias between the Meso-NH forecasts and the MSG observation. The time axis is indicated by the day; j, July; a, August. (right) BT distribution from MSG observation and forecasts.

anced the underestimation in the occurrence between 300-315 K and between 235-270 K. In the upper range the discrepancy pointed out an understimation of the highest surface temperature during hot weather conditions, the discrepancy being more pronounced for the MESO-NH-E forecasts than for the MESO-NH-A ones. In the lower range, the lack of intermediate BTs can be attributed to a limitation in the physics, in particular to our choice of using explicit microphysics only (the use of shallow convection parameterization might have been a beneficial option).

Scores BTs at 10.8 μm were used to characterize the cloud patchiness (Schroeder et al. 2006) using 260 K as the threshold below which BTs were associated with high clouds. The observed patchiness linked to periods of cloudy days was reasonably well forecasted (Fig. 2.2a). However, the forecasted cloud systems were too patchy, indicating a lack of organized cloud systems. The skill in forecasting cloud cover as measured using the Fractions Skill Score (FSS, Roberts and Lean 2008) was rather high. The highest scores, close to 1, the perfect skill, were achieved during overcast periods, particularly in August (Fig. 2.2b).

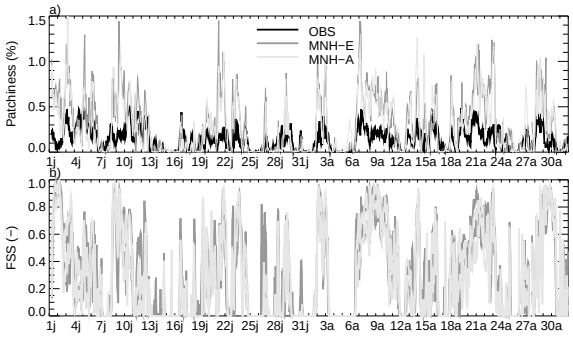

Figure 2.2: (a) Time evolution of the patchiness from (black) the MSG observation and (grey) the Meso-NH forecasts. (b) Time evolution of the FSS between the Meso-NH forecasts and the MSG observation. The time axis is indicated by the day; j, July; a, August.

Spatial distribution Another question concerned the location of the errors in the cloud cover forecasts. A simple diagnosis was obtained by averaging the observed BTs during the two-month period and computing the associated biases in forecasts (Fig. 2.3). The mean observed BT showed a small range, between 268 and 273 K, with lower BTs over the mountains, especially over the Alps, and higher BTs in the valleys (Fig. 2.3a). This pattern can be explained by the sensitivity of BT to both the surface temperature under clear conditions (with lower temperatures over the mountains) and the cloud top temperature under cloudy conditions (with more frequent clouds over the orography). The mean difference between forecasts and observations pointed out some systematic errors (Fig. 2.3b, c). For both sets of forecasts, the biases were the lowest on the crests (<2 K), in particular over the Alps and highest (>5 K) over the Rhine valley. From the two sets, the MESO-NH-A forecasts showed the largest bias extending from the Vosges to the German plain.

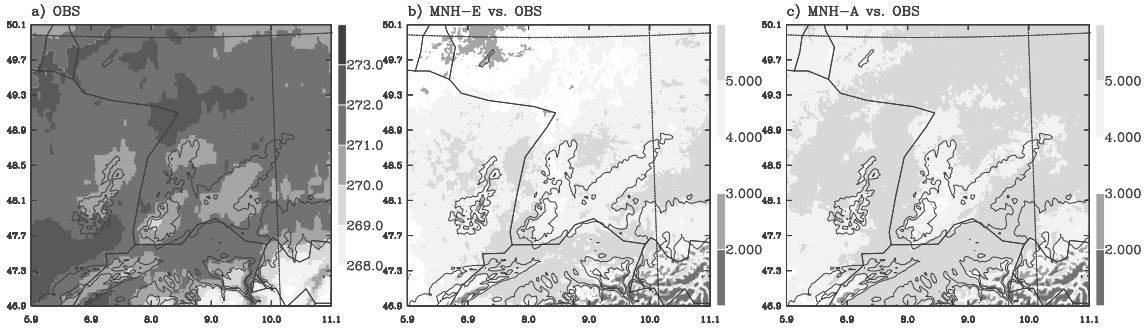

Figure 2.3: a) Mean BT (K) from observation and the associated BT bias (K) for b) MESO-NH-E and c) MESO-NH-A. The black lines indicate the topographic heights of 600 and 900 m.

Precipitation assessment

Precipitation measurements were taken by rain gauges. Here we used 24-h daily accumulated rain from 06 UTC on a particular day to 06 UTC the next day. Each rain gauge was compared with the nearest model grid point. In addition, the comparison with rain gauges was extended to the forecasts from two Meteo-France models, ALADIN, the current operational model using a grid-mesh of 10 km, and AROME, the future operational model running with a 2.5-km grid mesh. Both models use initial conditions from the global analysis ARPEGE. As AROME shares the same physics with MESO-NH, the present comparison exercise could help to document some systematic errors due to modelling issues other than the physics. On the other hand, comparison with ALADIN allowed discussion of the added value provided by Cloud-Resolving Models (CRMs) compared to the previous generation of models.

Time evolution An overview of the model skill is given with the time evolution of the 24-h accumulated rain spatially averaged over the COPS area (Fig. 2.4 left). Both MESO-

NH and AROME represented the time evolution well. In particular, the occurrence of the forecasted rain peaks followed the observations closely, but with some disagreements in their intensity. It is interesting to note that the two models gave different peaks. This can be attributed to the different initial conditions used by the models. On the other hand, there was no systematic bias, but the CRMs presented a larger amplitude. This was to be expected because, as seen next, the largest values predicted by the CRMs can lead to larger errors than the ALADIN forecasts.

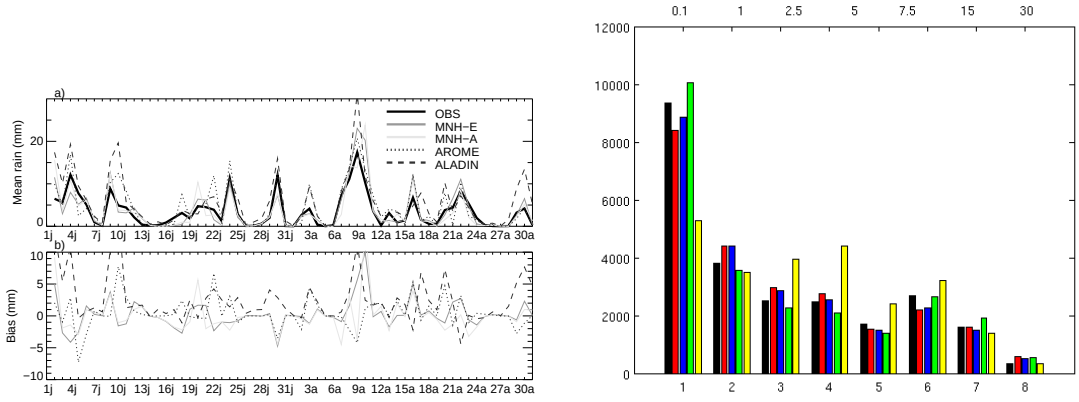

Figure 2.4: (left) Time series of (a) the 24-h accumulated rain from observation and forecasts and (b) their associated bias. The time axis is indicated by the day; j, July; a, August. (right) Distribution of the 24-h accumulated rain from observation and forecasts.

Rain distribution The observed rain distribution over the whole period exhibited a decrease in frequency with the increase in accumulated rain (Fig. 2.4 right). The CRMs reproduced the rain distribution well. They slightly overestimated the cases with more than 30 mm of rain. Remarkably, there is no outstanding difference between MESO-NH and AROME. This result suggests that the difference in initial conditions and in modelling other than physics did not affect the rain distribution significantly. In contrast, ALADIN showed some departures from the observed rain distribution: the frequency of light rain (less than 0.1 mm) was underestimated by a factor 2 while intermediate rain amounts were overestimated.

Scores The Heidke Skill Score (HSS) characterizes the ability of a model to forecast rain over a certain threshold. It is shown for all the models (Fig. 2.5 left). As expected, a lower skill is achieved for heavy rain as these events are less frequent in time and space. On the other hand, ALADIN shows higher skill except for small amounts of rain. The poorer results for the CRMs can be attributed to the double penalty effect. This arises when an observed small scale feature is realistically forecast but is misplaced. The CRM is penalized twice, once for missing the actual feature and again for forecasting it where it is not. The forecast skill was further analyzed by differentiating the HSS (Fig. 2.5 right) between July

and August (left column) and between the Vosges and the Black Forest (right column). Results show higher scores in August, when conditions were less convective, and over the Vosges, i.e. upwind.

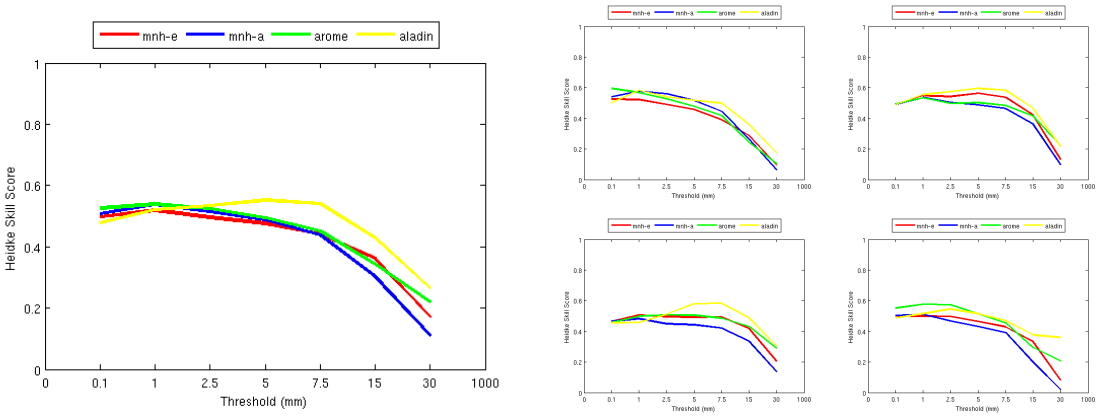

Figure 2.5: HSS as function of the rain threshold. Results (right) for the whole period and (left) for (a) July and (c) August and between (b) the Vosges and (d) the Black Forest.

Spatial distribution The dependency of the skill on location was examined with the mean observed rainfall and the associated biases for the two sets of MESO-NH forecasts (Fig. 2.6). Observations showed heavy rain upwind and on the crests with up to 7 mm of rain. In particular, the mean rainfall was larger over the Vosges than the Black Forest. The bias between MESO-NH-E and the observation showed good agreement over the Vosges, but a larger bias over the Black Forest. This was also the case for MESO-NH-A, but with some reduced values in bias downwind of the Black Forest. This difference in the two sets of forecasts is consistent with the higher BT forecasted by MESO-NH-A.

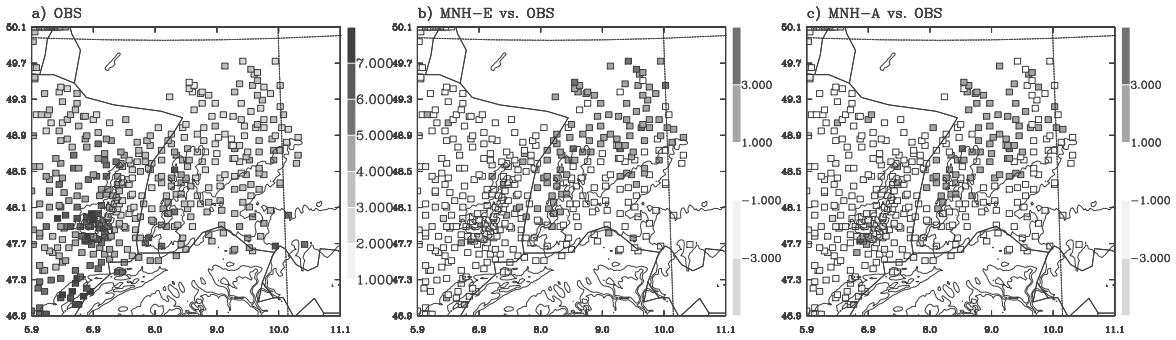

Figure 2.6: a) Observed mean rain (mm) from rain gauges and the associated biases (mm) for the b) MNH-E and c) MNH-A forecasts. The black lines indicate the topographic heights of 600 and 900 m.

Summary and Outlook

The paper has presented an assessment of the MESO-NH forecasts made in July and August 2007 in the framework of the COPS and MAP-D PHASE programmes. The evaluation was

made using BT at 10.8 μm observed from MSG and 24-h accumulated rain measured by rain gauges. A general consistency between the variables is found. The highest scores are obtained during the least convective periods (i.e. in August) and upwind (i.e. over the Vosges). The comparison with BTs points out too patchy a structure in cloud cover as well as a lack of intermediate BTs. This could be attributed to the choice of not using any subgrid cloud scheme.

In addition, the evaluation with rain forecasted by AROME and ALADIN has shown the dependency of skill on the spatial scale. When using a classical score such as the HSS, better skill is obtained for the 10-km forecasts compared to the 2-km forecasts. However, the rain distribution is better represented by the CRMs. This underlines the necessity of designing scores for the scale of the CRMs.

Acknowledgement

This study was funded by ANR (COPS France). MSG observations were obtained from SATMOS (Météo-France/CNRS). The Meso-NH forecasts were made on the Laboratoire d'Aérologie PC cluster. Thanks are due to Juan Escobar and Didier Gazen for their computer support, to Yann Seity for providing us with the ALADIN and AROME forecasts, and to Delphine Sulmont for her contribution during a Master's training period.

References

Chaboureau, J.-P., J.-P. Cammas, P. Mascart, J.-P. Pinty, C. Claud, R. Roca, and J.-J. Morcrette, 2000: Evaluation of a cloud system life-cycle simulated by Meso-NH during FASTEX using METEOSAT radiances and TOVS-3I cloud retrievals. Quart. J. Roy. Meteor. Soc., 126, 1735–1750.

Chaboureau, J.-P., J.-P. Cammas, P. Mascart, J.-P. Pinty, and J.-P. Lafore, 2002: Mesoscale model cloud scheme assessment using satellite observations. J. Geophys. Res., 107(D17), 4301, doi:10.1029/2001JD000714.

Lafore, J.-P., et al., 1998: The Meso–NH Atmospheric Simulation System. Part I: adiabatic formulation and control simulations. Scientific objectives and experimental design. Ann. Geophys., 16, 90–109.

Roberts, N. M. and H. W. Lean, 2008: Scale-selective verification of rainfall accumulations from high-resolution forecasts of convective events. Mon. Wea. Rev., 136, 78–97.

Schröder, M., et al., 2006: Comparison of model predicted low-level cloud parameters with satellite remote sensing observations during two days of the BALTEX Bridge campaigns. Atmos. Res., 82, 83–101.

Söhne, N., J.-P. Chaboureau, and F. Guichard, 2008: Verification of cloud cover forecast

with satellite observation over West Africa. Mon. Wea. Rev., 136, 4421–4434.

Stein, J., E. Richard, J.-P. Lafore, J.-P. Pinty, N. Asencio, and S. Cosma, 2000: High-resolution non-hydrostatic simulations of flash-flood episodes with grid-nesting and ice-phase parameterization. Meteorol. Atmos. Phys., 72, 203–221.

2.2 Forecasting summer convective activity over the Po Valley: insights from MAP D-PHASE

S. Davolio, O. Drofa and P. Malguzzi

ISAC - CNR, Bologna, Italy

Introduction

The Po Valley is an area prone to convective storms often associated with severe weather conditions, such as hail and strong winds, especially during spring and summer. The large and flat valley is surrounded on three sides by orographic chains (Alps and Apennines) that remarkably affect its weather, modifying the large scale flow and contributing to generate favourable mesoscale conditions for deep convection. Moreover, the valley is a semi-closed basin in which the low-level wind circulation is generally sluggish (Morgan, 1973). During summer, this facilitates heating and humidification of low-level air, thus producing favourable (unstable) conditions for convection development.

In the past, numerous studies were devoted to investigate different aspects of this phenomenon, such as climatological distribution (Bossolasco, 1949; Morgan, 1973; Cacciamani et al., 1995), physical mechanisms, dynamic and thermodynamic characteristics (Buzzi and Alberoni, 1992; Costa et al., 2001). The passage of frontal structures and the development of orographic cyclones on the lee (southern) side of the Alpine chain turned out to be the synoptic scale features most favourable for the occurrence of thunderstorms. Moreover, convection over the Po Valley resulted often organized and associated with mesoscale circulation induced by direct or indirect topographic effects.

The climatological analysis of Bossolasco (1949) clearly showed the Po Valley as one of the area of Italy mostly affected by thunderstorms, which are more frequent in the region north of the Po river. The sesonal distribution is characterized by a peak during the summer months, in particular between May and August.

During the summer period of MAP (Mesoscale Alpine Programme) D-PHASE, that is between June and August 2007, a number convective systems affected the Po Valley. The D-PHASE offered a unique opportunity to assess, at least qualitatively at this stage, the capability of state-of-the-art high-resolution, convection-resolving models in predicting thunderstorms over the Po Valley. In the present study a preliminary evaluation of short-range forecasts issued by several fine-scale models, operational during the project, is presented.

Experiment setup

In order to evaluate the performance of the high-resolution models in predicting the development and evolution of convective episodes, forecast precipitation is compared with available radar data. In particular, the attention is focused on the region covered by the San Pietro Capofiume radar, located in Emilia Romagna region about 40 km north east of Bologna and managed by ARPA-SIMC (HydroMeteorological Service of the Emilia-Romagna Regional Agency for Environmental Protection). In order to avoid problems in radar precipitation estimates connected with the presence of orography, mountainous area (above 200 m a.s.l) are not considered in the analysis. Moreover, radar data are upscaled in order to fit models' resolution. The radar domain (Fig. 2.1) cover almost entirely the eastern part of the Po Valley.

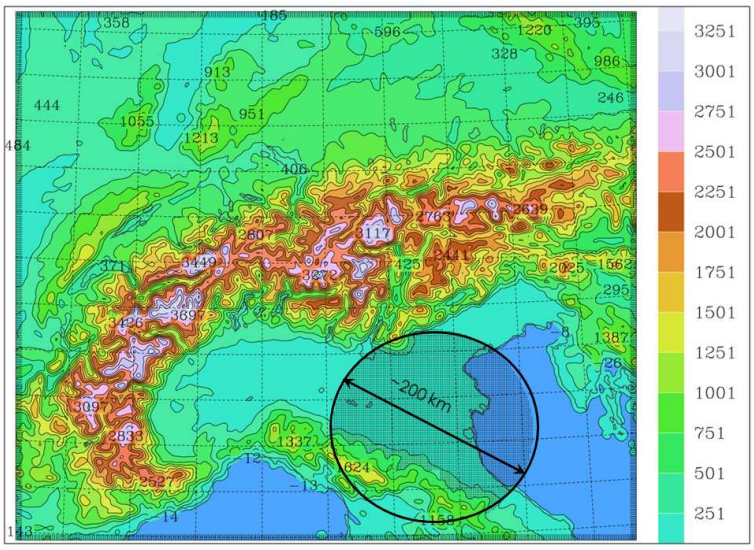

Figure 2.1: Orography of northern Italy and the area covered by the San Pietro Capofiume radar. The grid-points over the orography (see text) are not considered in the analysis.

Among the high-resolution operational models employed in the D-PHASE project, only three of them were run on a domain that besides the whole Alpine region suitably cover the area of interest: MOLOCH (run in two different configurations), AROME and COSMOCH2, for a total of four daily forecasts (see Table 2.1 for details).

MOLOCH model (Malguzzi et al., 2006) was run at ISAC-CNR using two different initial and boundary conditions data set, provided by ECMWF and GFS global model, respectively. The run driven by the 00 UTC, GFS analysis/forecasts (named ISACMOL) started at 09 UTC and lasted for 39 hours, while the run driven by the 18 UTC ECMWF analysis/forecasts (named ISACMOL2) started at 00 UTC and lasted for 48 hours. MOLOCH was not directly nested in the global model, but an intermediate nesting step, performed using the hydrostaic

model BOLAM (Zampieri et al., 2005), was needed. AROME (Bouttier and Roulet, 2008) forecasts were performed daily by the CNRM of Meteo-France, starting at 00 UTC. The forecasts, driven by the non-hydrostatic ALADIN-France model which was itself nested in the ARPEGE global spectral model, covered a 30-hour period. COSMOCH2 (for a complete description see the COSMO (COnsortium for Smallscale MOdelling) web site www.cosmo-model.org) was run by MeteoSwiss several times a day, driven by the ECMWF global model analysis/forecasts. In the present analysis only the 24-hour run starting at 00 UTC is considered.

The time series of maximum and mean (areal averaged) hourly precipitation for the three month period of June, July and August obtained from radar data and model forecasts are compared. The model time series have been obtained using consecutive forecasts. Concerning the two MOLOCH runs, the forecast range has been selected so as to maintain the same time interval from the global model initial condition. Therefore for ISACMOL the forecast range between +3 and +27 hours has been selected, while for ISACMOL2 the interval is from +6 to +30 hours. The same forecast range (+6 to +30) has been chosen for AROME, while for COSMOCH2 the entire 24-hour run has considered.

Results

Figure 2.2 shows the comparison among the time series of the maximum hourly precipitation computed from the radar data and model forecasts for the entire three-month period. It has to be intended as a temporal correlation and not a spatial coincidence since at every hour the maximum rainfall pattern may be located anywhere within the region covered by radar (Fig. 2.1). From a qualitatively point of view, the forecast precipitation correlates quite well with the observation and the number of false alarm (that is forecast precipitation missing in the reality) is remarkably low. The COSMOCH2 model displays the less intense precipitation and seems to miss some of the events. The behaviour of the two MOLOCH runs is quite similar in terms of number of forecast episodes, but there are differences in the intensity

MODEL	**Resolution [km]**	**Initial time (UTC)**	**Forecast range [h]**	**IC - BC**
AROME	2.5	00	30	ALADFR ARPEGE (00 UTC)
COSMO_CH	2.2	00	24	COSMOCH7 ECMWF (00 UTC)
MOLOCH_GFS (ISACMOL)	2.2	09	39	BOLAM GFS (00 UTC)
MOLOCH_ECMWF (ISACMOL2)	2.2	00	48	BOLAM ECMWF (18 UTC)

Table 2.1: Main characteristics of model configurations.

of the precipitation concerning the single events. Finally, AROME forecasts more intense precipitation in June, but in general its forecasts do not differ significantly from those of MOLOCH.

The evolution of the areal averaged hourly precipitation (Fig. 2.3) provides information about the amount of rainfall affecting the area. In the process of averaging, isolated maxima, which may be due to anomalous propagation that affect radar measurements especially during the evening and the night, are filtered out, while wide-spread convective activity is highlighted. Therefore, the comparison among areal average quantities provides more robust results.

From the analysis of the mean rainfall time series shown in Fig. 2.3, it can be see that the AROME model provides the "wettest" forecasts, while COSMOCH2 is affected by a clear underestimation of convective activty over the area.

Despite the large differences between radar and model data (in term of intensity) we attempt also a quantitative comparison, computing the anomaly correlation coefficient (ACC) and the root mean square error (RMSE), between forecasts and radar (see Tab. 2).

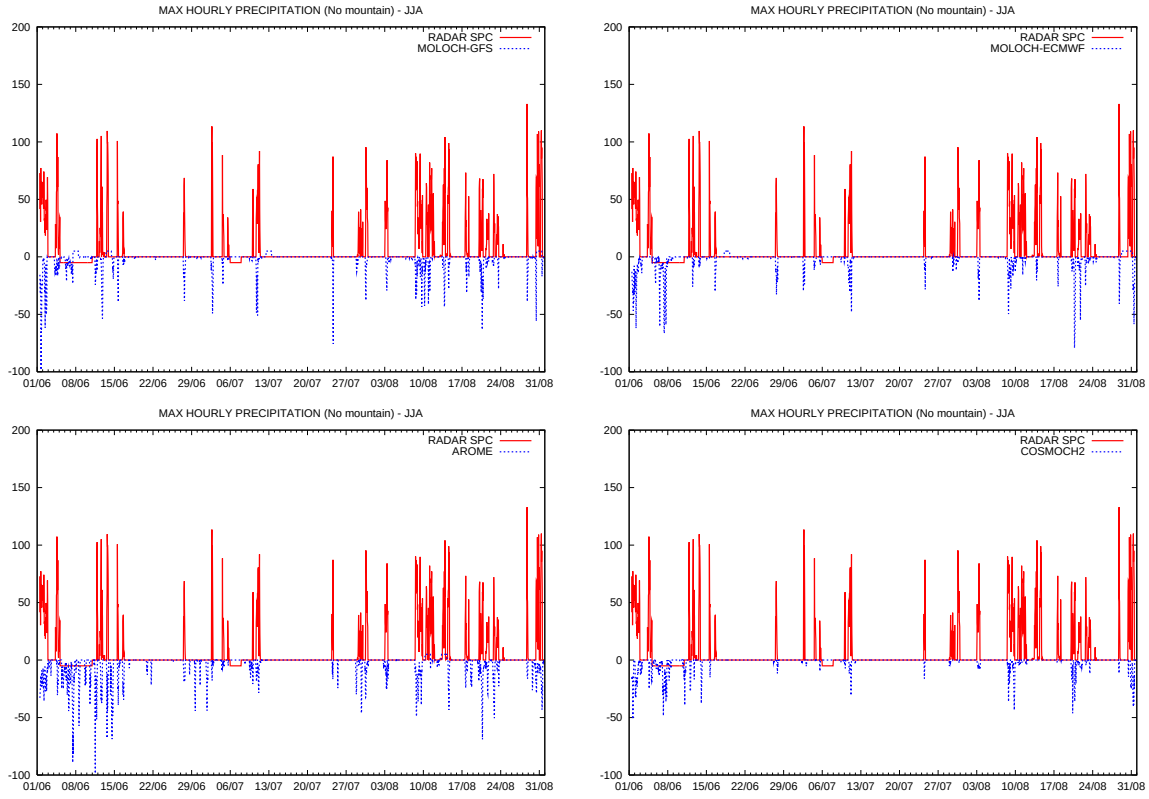

Figure 2.2: Time series of the maximum hourly rainfall (mm) for the 3-month period June-July-August 2007. The red line corresponds to radar data, the blue line to model forecast. ISACMOL (top-left), ISACMOL2 (top-right), AROME (bottom-left), COSMOCH2 (bottom-right). Model time series are plotted as negative in order to facilitate the comparison. Negative (positive) values in the radar (model) time series indicate missing data.

MODEL	Anomaly Correlation Coefficient	Root Mean Square Error
AROME	0.46	0.48
COSMOCH2	0.44	0.49
ISACMOL	0.54	0.44
ISACMOL2	0.62	0.44

Table 2.2: ACC and RMSE computed by comparing the models' forecasts with radar data.

MOLOCH model outperforms both AROME and COSMOCH2.The same analysis computed on the hourly maximum precipitation turned out to be remarkably affected by the presence of isolated intense rainfall patterns due to anomalous propagation, and therefore are not shown here.

Finally, the distribution of rainfall intensity has been computed by kernel estimation using a smoothing parameter of 5 mm/h. The results are shown in Fig. 2.4.

The forecast maximum hourly precipitation follows an esponential distribution, with maximum occurrence for low rainfall intensity. The distribution computed with the radar data is quite different, displaying a much higher occurrence of intense precipitation (above 30 mm/h) and a lower frequency for weak rainfall. The lack of the probability maximum in the radar data is due to the fact that hourly precipitation values below 5 mm/h are excluded from this analysis. However, if we consider the unfiltered radar data, the probability maximum at low

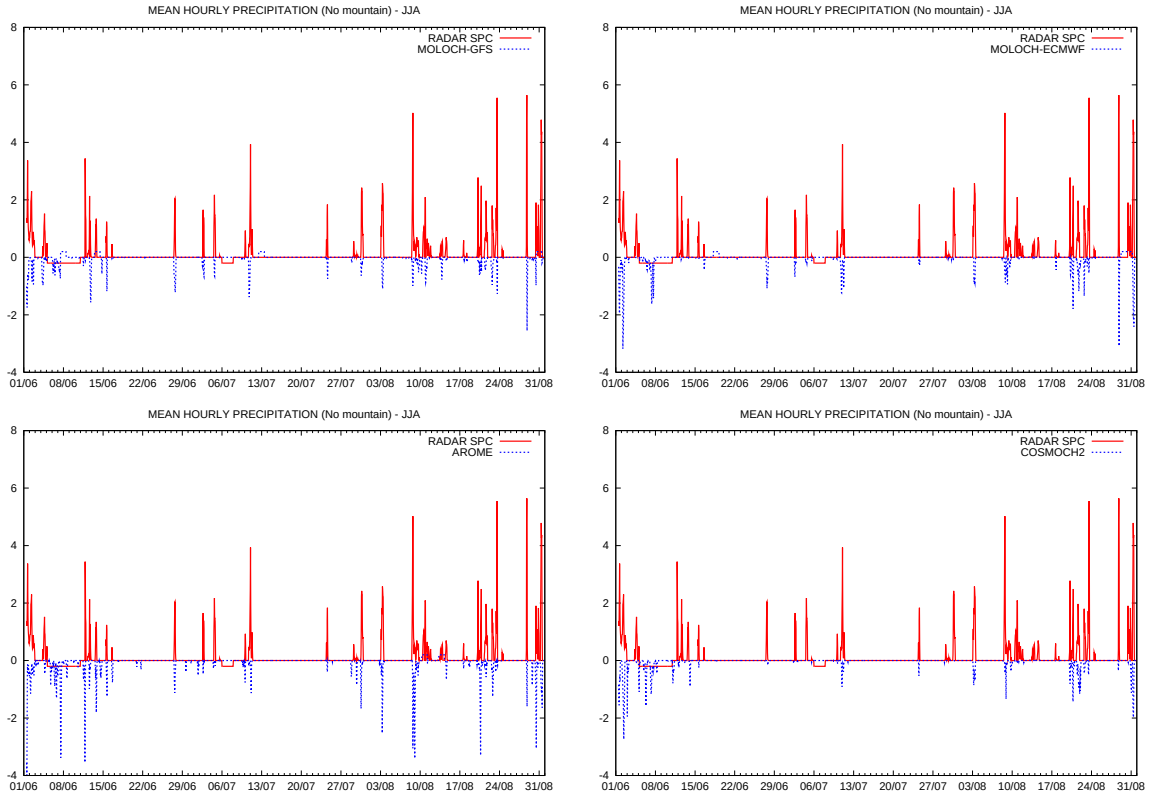

Figure 2.3: As in Fig. 2.2, but for mean (areal averaged) precipitation.

precipitation rates is recovered.

Summary and Outlook

During the MAP D-PHASE, for the first time a number of high-resolution, non-hydrostatic, convection-resolving models have been operated over the whole Alpine area. This offered an unique opportunity to evaluate their skill in forecasting thunderstorms during the summer season in particular over an area prone to intense and organized deep convection such as the Po Valley. The analysis has been undertaken by comparing forecast precipitation with radar data. The results show a quite satisfactory correlation between the hourly rainfall series with a small number of false alarms.

A more detailed analysis of selected episodes of deep convection, occurred over the region during the investigated period, has confirmed the general behaviour of the models outlined here. Moreover, from this analysis we conclude that better forecasts are generally attained when convection is embedded in mesoscale flows having some degree of predictability.

Acknowledgments

The authors are grateful to Dr. Anna Fornasiero and Dr. Pier Paolo Alberoni (ARPA-SIMC) for having provided radar data and for the discussion of the results.

References

Bossolasco, M., 1949: La distribuzione dei temporali in Italia. Energia. Elettro. XXVI(11-12), 3-15.

Bouttier, F. and B. Roulet, 2008: Arome, the new high resolution model of Meteo-France.

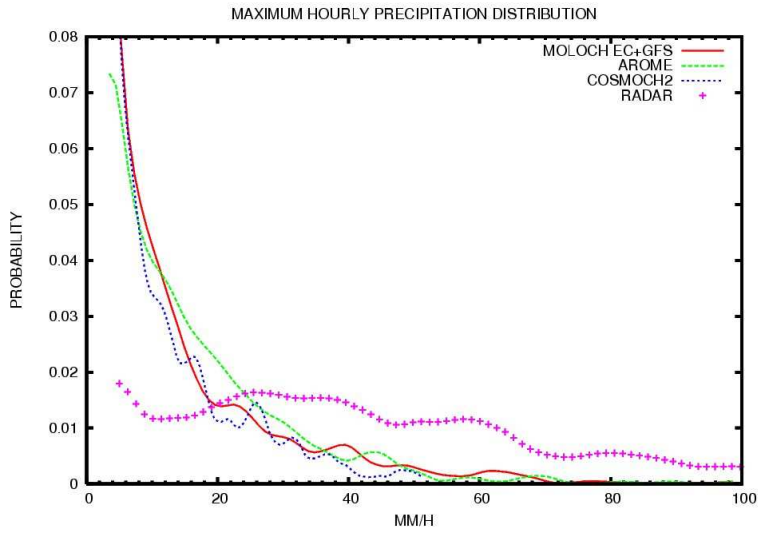

Figure 2.4: Probability distribution of the hourly maximum precipitation. Crosses correspond to radar data, red line to MOLOCH, green line to AROME and blue line to COSMOCH2 forecast.

The European forecaster - Newsletter of the WGCEF (Printed by Meteo-France), 13, 27-30.

Buzzi, A. and P. P. Alberoni, 1992: Analysis and numerical modelling of a frontal passage associated with thunderstorm development over the Po Valley and the Adriatic Sea. Meteorol. Atmos. Phys., 48, 205-224.

Cacciamani, C., F. Battaglia, P. Patruno, L. Pomi, A. Selvini and S. Tibaldi, 1995: A climatological study of thunderstorm activity in the Po Valley. Theor. Appl. Climatol., 50, 185-203.

Costa, S., P. Mezzasalma, V. Levizzani, P. P. Alberoni and S. Nanni, 2001: Deep convection over northern Italy: synoptic and thermodynamic analysis. Atmos. Res., 56, 73-88.

Malguzzi, P., G. Grossi, A. Buzzi, R. Ranzi and R. Buizza, 2006: The 1966 'century' flood in Italy: A meteorological and hydrological revisitation. J. Geophys. Res., 111, D24106, doi:10.1029/2006JD007111.

Morgan, G. M., 1973: A general description of the hail problem in the Po Valley of northern Italy. J. Appl. Meteor., 12, 338-353.

Zampieri, M., P. Malguzzi and A. Buzzi, 2005: Sensitivity of quantitative precipitation forecasts to boundary layer parameterization: a flash flood case study in the Western Mediterranean. Nat. Hazard Earth Sys. Sci., 5, 603-612.

2.3 The flood event near Venice of 26 September 2007: was it forecast by the D-PHASE models?

D. Mastrangelo[1], A. Buzzi[2], and S. Davolio[2]

[1]*Dep. of Environmental Sciences, Parthenope University of Naples;* [2]*ISAC-CNR, Bologna, Italy*

Introduction

The strong impact that heavy precipitation events have on human activities and environment have led to a great effort devoted to improve numerical weather prediction models, that are the main tool for quantitative precipitation forecasting (QPF). Heavy precipitation events are usually related to deep moist convection whose occurrence is tied to various processes acting on different scales, and to their complex interactions. Small errors in initial conditions or in simulating the involved processes can cause large error in QPF. Moist convection is an intrinsic source of forecast uncertainty, therefore limiting predictability of heavy precipitation events (Walser et al., 2004).

The increase of model horizontal resolution, allowed by the raised computing power, has been introduced as one of the possible strategies to improve short-range QPF. Several recent studies were performed to analyse the ability of high-resolution models in reproducing heavy precipitation events and to verify benefits brought by increased horizontal resolution. Buzzi et al. (2004) analyzed three cases of heavy orographic precipitation; they argued that the high horizontal resolution allowed to resolve physical processes, different from those reproduced through parameterization, leading to a more realistic representation of precipitation fields. Anquetin et al. (2005) statistically evaluated the performance of different models in forecasting a flash flood event: high-resolution models (with horizontal grid resolution ranging from 6 to 2 km) showed better results than lower-resolution models, but still retaining their drawbacks in terms of precipitation amount bias and location. Richard et al. (2007) compared four convection-resolving models run over the same domain with the same horizontal resolution (2 km) for the most intense orographic precipitation episode occurred over the southern flank of the Alps during the Mesoscale Alpine Programme (MAP) Special Observing Period: large variability in precipitation forecasts was found but high-resolution models showed more intense precipitation and better objective scores than coarser-resolution models.

In this context, we compare precipitation forecasts of four high-resolution models, operational during the MAP D-PHASE project. We consider a heavy convective precipitation event

occurred over the flat area adjacent to the Venice Lagoon, on 26^{th} September 2007. This work aims at showing the overall performance of the different selected models.

The event

During the morning of 26 September, a mesoscale convective system (MCS) affected the flat area west of the Venice Lagoon causing floods in the nearby towns of Marghera and Mestre. Satellite image (Fig. 2.1(a)) shows the wide V-shaped cloud shield of the MCS and different convective cells over the southern side of the Alpine range, indicating that the large-scale environment was favourable to deep and widespread convection.

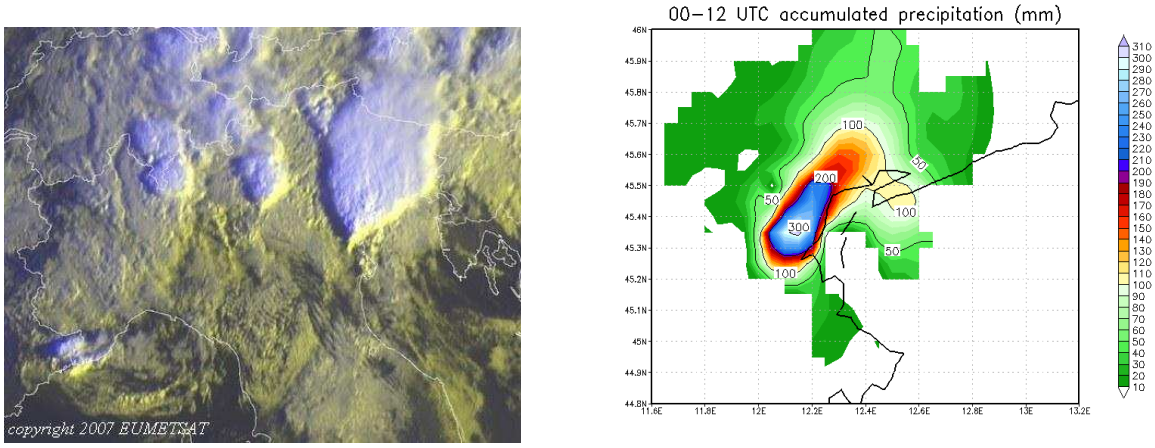

Figure 2.1: Left: Satellite image at 06:00 UTC. Right: observed accumulated precipitation for the 12-h period from 00 UTC to 12 UTC, 26 Sep. 2007

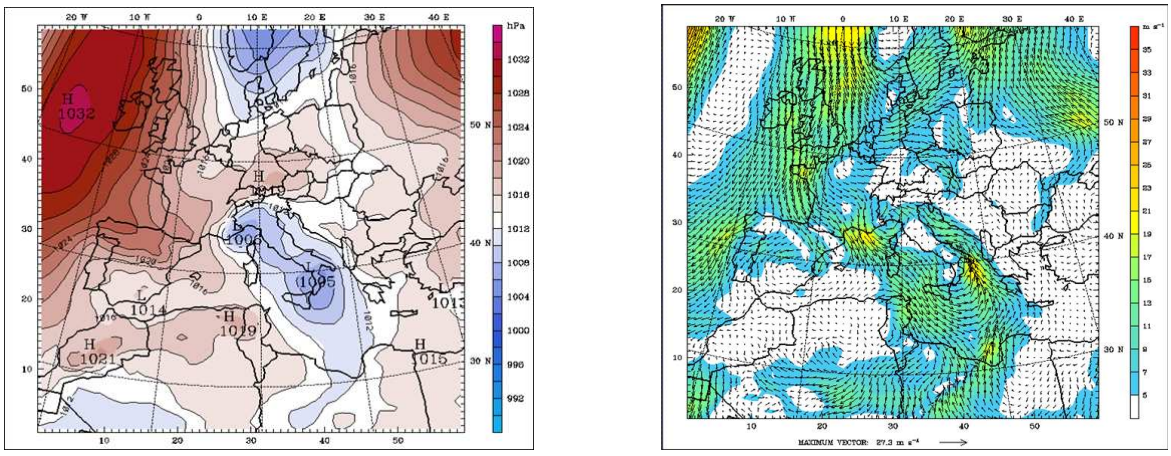

Figure 2.2: NCEP-GFS analyses of 00 UTC, 26 Sep. 2007, at 925 hPa. Left: mean sea level pressure (hPa). Right: wind vectors and speed (m/s)

The approaching of a mid-tropospheric trough towards the western Alpine region favoured a lee cyclogenesis over the Gulf of Genoa that, together with a minimum previously located

over Tunisia, contributed to generate a wide low-pressure area over central Mediterranean and northern Italy (Fig. 2.2). The resulting cyclonic circulation strengthened the pre-existing south-easterly flow that affected the eastern Po valley coming from the Adriatic sea, advecting moist and unstable air. Colder air was already present over the central and eastern Alps, associated with a cold front moving slowly to the south east. As typical, cold air was turning anticyclonically around the eastern Alps, while west of them the cold outbreak had already penetrated over the Mediterranean as Mistral flow.

Some scattered convective cells were observed over the central and eastern Po Valley after about 02 UTC. Two hours later, a MCS started developing along a line roughly oriented from southwest to northeast in the area between Venice and the Prealps. Observed surface rainfall and wind data recorded by 49 automatic stations in the area indicate that convective cells organized in a zone of low-level convergence between the more intense south-easterly wind, blowing from the sea, and a weaker north to north-easterly wind, blowing over inland plain (Fig. 2.3(b)). Rain gauges data show that intense precipitation (rain-rate $>$ 40 mm/hr) affected the same area for almost 5 hours. A peak of hourly rainfall amount of about 126 mm in one hour was recorded around 06 UTC.

The surface wind configuration and related convergence zone persisted throughout the MCS activity, suggesting that the moist south-easterly flow had a relevant role in feeding convection. The MCS then slowly moved eastward, over the sea. After about 10 UTC, the north-easterly flow, following the MCS translation, invaded the area previously affected by the south-easterly wind. The 12-hour accumulated precipitation, from 00 to 12 UTC of 26 September is reproduced in Fig. 2.1(b), which shows a narrow area of high rainfall amounts, oriented from southwest to northeast, with a maximum of 324 mm, of which almost 250 mm fell in 3 h. This event produced the highest rainfall amount observed during the D-PHASE Operations Period.

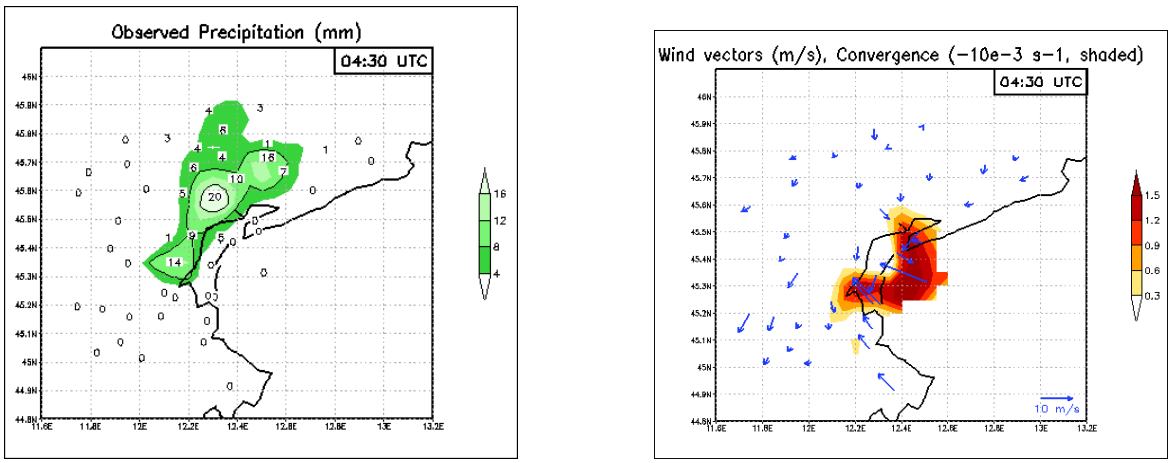

Figure 2.3: Left: 30-min accumulated precipitation (mm) at 04:30 UTC. Right: observed surface wind vectors (m/s) and convergence ($-10^{-3}s^{-1}$) at the same time

	Resolution [km]	Initial time (UTC) [h]	Forecast range [h]	IC - BC (run)
AROME*	2.5	00, 26 Sep	30	ALADFR* ARPEGE (00, 26 Sep)
COSMO_CH	2.2	00, 26 Sep	24	COSMOCH7* ECMWF (00, 26 Sep)
MOLOCH_GFS	2.2	09, 25 Sep	39	BOLAM GFS (00, 25 Sep)
MOLOCH_ECMWF	2.2	00, 26 Sep	48	BOLAM ECMWF (18, 25 Sep)

Table 2.1: Main characteristics of models configurations. *Indicates models that use an assimilation scheme

The high-resolution models

We selected the forecasts provided by 3 models, namely AROME, COSMO_CH and MOLOCH, whose domains suitably covered the area of interest. The modelling chain comprising the MOLOCH model was run with 2 different initial and boundary conditions so that a total of 4 forecasts were analysed in this work. Main characteristics of model setup are summarized in Table 1. The AROME forecasts were performed daily by the CNRM of Meteo-France. Each run started at 00 UTC and covered a period of 30 hours; numerical integrations were computed on a three-dimensional grid with horizontal resolution of 2.5 km and 41 levels. Initial and boundary conditions were provided every 3 hours by the non-hydrostatic ALADIN-France model implemented on a domain with horizontal mesh-sizes of 9.5 km and 46 levels. Such model was initialized and updated every 3 hours using the ARPEGE global spectral model outputs.

The selected COSMO_CH simulation was performed by MeteoSwiss that implemented a modelling chain based on initial and boundary conditions derived from the European Centre for Medium-Range Weather Forecast (ECMWF) global model forecasts initialized at 00 and 12 UTC. The COSMO_CH model was run on two 1-way nested domains with horizontal resolution of 7 and 2.2 km respectively. Two runs per day, with a forecast range of 72 hours, were performed on the outermost domain. Outputs from these runs were used to initialize every 3 hours a new forecast performed on the high-resolution domain, with a time step of 20 sec. The selected run, with forecast range of 24 hours, was initialized at 00 UTC of 26 September.

The MOLOCH model, developed at the Institute of Atmospheric Sciences and Climate - National Research Council (ISAC-CNR) in Bologna, produced two forecasts per day: one using NCEP-GFS analysis and 3-hourly forecast at 0.5 degree resolution, the other using ECMWF analysis and 3-hourly forecast at 0.25 degree resolution. The modelling chain employed at ISAC was based both on the hydrostatic model BOLAM and the non-hydrostatic model MOLOCH, nested in BOLAM. BOLAM was run with a horizontal resolution of 0.11

degree and 40 levels. The MOLOCH run using GFS data (MOLOCH_GFS, indicated also as ISACMOL in the D-PHASE database) started at 09 UTC each day, i. e. at the 9th forecast hour of the BOLAM run. The MOLOCH run using ECMWF data (MOLOCH_ECMWF, indicated also as ISACMOL2) started at 00 UTC each day, i.e. at the 6th forecast hour of the BOLAM run. MOLOCH was implemented with a horizontal resolution of 0.02 degree and 50 levels. We selected the MOLOCH forecasts obtained through the BOLAM runs initialized with 18 UTC ECMWF analysis of 25 September and with 00 UTC GFS forecast of 25 September, respectively.

Results

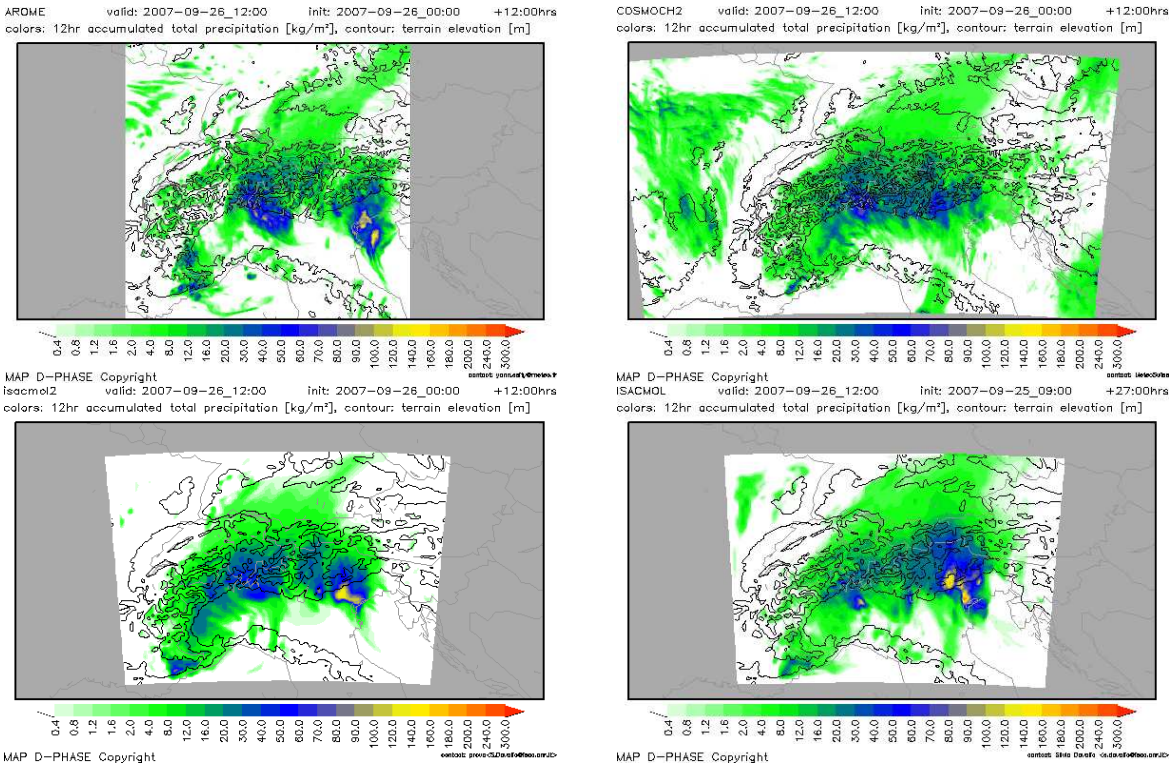

Figure 2.4: 12-h accumulated precipitation (mm) at 12 UTC, 26 Sep. 2007, as forecasted by AROME (top-left), COSMO_CH (top-right), MOLOCH_ECMWF (bottom-left) and MOLOCH_GFS (bottom-right)

Precipitation fields, predicted by the different models over the time interval from 00 UTC to 12 UTC 26 September, are analysed and compared with the corresponding observed rainfall. Fig. 2.4 shows the spatial distribution of the 12-h accumulated precipitation forecast by the four different runs. The AROME forecast (Fig. 2.4(a)) produces a relevant portion of precipitation over the Adriatic sea with a maximum of about 160 mm. The northernmost precipitation peak, of about 140 mm, is reproduced over the coastal area adjacent to the eastern tip of the Venice Lagoon. Amounts of about 60 mm in 12 h are forecast over the Prealps north of the flat region of interest. The COSMO_CH model (Fig. 2.4(b))

produces the smallest precipitation amount among the selected models. Some scattered peaks of about 40 mm are simulated over the coastal area east of the Lagoon; the most intense precipitation is located over and at the foothills of the Prealps northwest of the focus area, with a peak of about 80 mm. The MOLOCH_ECMWF run (Fig. 2.4(c)) shows a precipitation pattern covering the region extending from the Lagoon area to the Prealps. The most intense precipitation is located over the flat area in between, with a maximum of about 150 mm. Rainfall up to 120 mm is reproduced over the area where most intense precipitation was observe, while weak rainfall affects the sea. The MOLOCH_GFS run (Fig. 2.4(d)) provides the highest precipitation amount among the four forecasts. Intense precipitation is reproduced over the sea facing the area of interest and the adjacent flat region: a maximum of about 240 mm is located close to the observed one. A wide area of intense simulated precipitation also hits the mountainous region with a secondary maximum of 180 mm in 12 h.

The largest amounts of precipitation simulated in the four runs are located along a direction roughly from southeast to northwest, that is from the coastal to the mountainous region (Fig. 2.5(a)), indicating the occurrence of different lifting mechanisms, due to low-level convergence zones over the flat terrain and over the sea, and to orography near the Alps. The time evolution of the convective available potential energy (CAPE) computed upstream of the Lagoon (not shown) indicates that sensibly lower values of CAPE were simulated in the COSMO_CH run, suggesting a possible reason for the smaller amount of precipitation of this model. A key-role for the generation and maintenance of the MCS was played also by the surface south-easterly flow that developed over the Adriatic sea, in the form of a low level jet (LLJ), induced mainly by the synoptic scale environment. Model differences in the simulation of the dynamical and thermodynamic properties associated with this LLJ and its interaction with other currents, especially the north-easterly flow south of the Alps, seem to account for the main differences in forecasting precipitation amount and location.

The hourly series of observed and modelled precipitation, averaged on a domain centred on the study area, are presented in Fig. 2.5, in order to evaluate the main temporal features of the simulated rainfall evolution (see in particular Fig. 2.5(b)). All the models except COSMO_CH reproduce a distinct rainy phase starting and culminating during the first 12 hours of 26 September. The AROME model shows the best results in terms of timing and rainy spell length. The absolute maximum is forecast one hour before the observed one, while an unobserved but significant peak is reproduced four hours after precipitation started. Such evolution is caused by the activity of several convective cells affecting the area at different times of the analysed period. For example, at the beginning of the most intense hourly precipitation peak (06 UTC), the high-level cloud cover simulated by AROME (Fig. 2.6(a)) indicates the presence of a convective cell over the area of interest and smaller cells over the adjacent sea. A different evolution is depicted in time series derived from

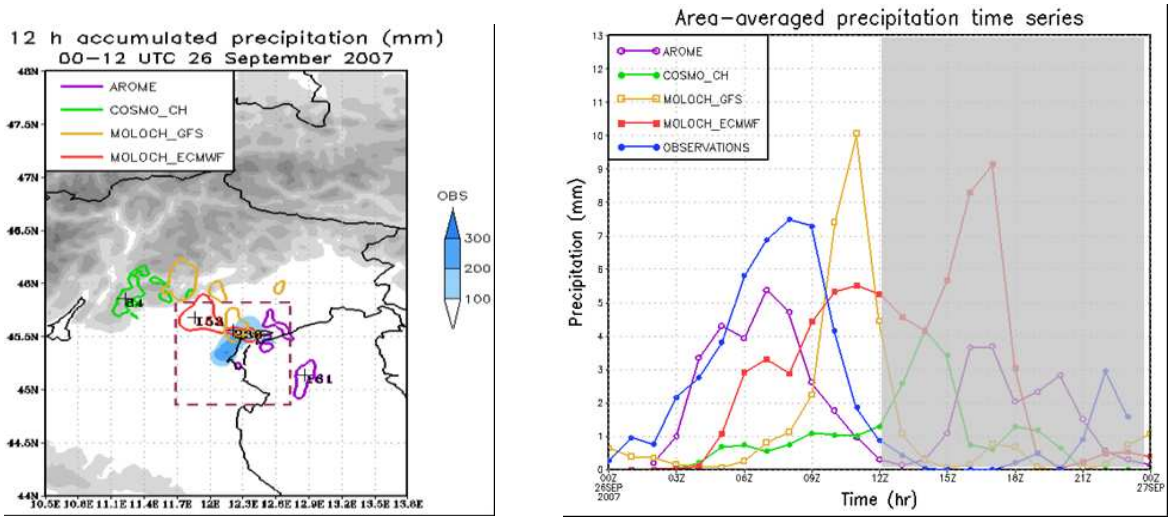

Figure 2.5: Left: 12-h observed (shaded) and simulated accumulated precipitation (mm), showing maximum amounts: 100 mm isoline for AROME and MOLOCH, 50 mm isoline for COSMO_CH. Right: hourly precipitation time series averaged over the 1°x1° domain depicted in the left panel

the two MOLOCH runs: in both simulations, most of precipitation is accumulated during a rainy spell produced by an intense convective structure that affects the area for at least four hours. In the MOLOCH_ECMWF run, the most intense convective activity occurs after a period of weaker precipitation beginning at about 04 UTC and lasting for about four hours. The maximum is underestimated and reproduced three hours later than observed; the subsequent precipitation decay is less marked than in the observed evolution. However, the resulting overall trend realistically captures the length of the rainy period even if it is delayed by about three hours. The MOLOCH_GFS run starts to simulate significant rainfall by 06 UTC, later than the other runs. The shorter rainy spell is associated with a strong convective structure that produces, three hours later than in the observations, the highest hourly area-averaged precipitation amount, even somehow overestimating the observed peak. As shown in Fig. 2.6(b), during the period of most intense hourly precipitation (10-11 UTC), MOLOCH develops a realistic V-shape cloud shield, resembling the observed MCS (Fig. 2.1(a)), with convection regenerating over the area next to the vertex.

Conclusions

An intense MCS, that affected the Venice Lagoon area during the morning of the 26 September 2007 with very intense precipitation and flood of nearby towns, has provided the opportunity to evaluate the performance of a subset of the short-range, high-resolution deterministic forecasts produced during the MAP D-PHASE Operation Period.

Spatial and temporal precipitation characteristics varied significantly among the four model forecasts. All models underestimated the observed accumulated maximum amount. How-

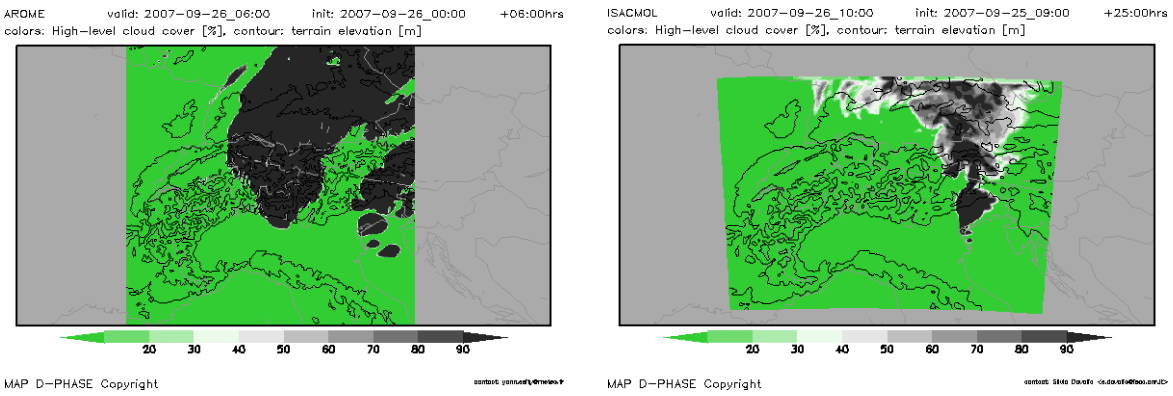

Figure 2.6: Simulated high level cloud cover (%). AROME at 06 UTC (left), MOLCOH_GFS at 10 UTC (right), 26 Sep. 2007

ever, three models reproduced quite clearly the convective nature of the precipitating MCS, predicting intense precipitation, ranging from about 120 to 240 mm, within an area very close to the one where the MCS was actually observed. Therefore, the short-range, high-resolution operational forecast of the analysed convective event can be considered at least moderately successful, also considering that the forecast range varied between 24 and 48 hours.

Various factors acting on different scales contributed to this result, like the presence of a moderate low over the Gulf of Genoa (lee cyclone), the CAPE distribution, the northeasterly flow over the Veneto plains, south of the Alps, and the intensity of a low level jet over the central and northern Adriatic sea. The modelled convective activity appeared to depend to a large extent on the considered model. In spite of the different initialization data, and the lack of mesoscale assimilation, both MOLOCH runs reproduced the most intense and long-lasting convective structures, resembling the observed MCS and differing from the rather scattered convection reproduced by the AROME model. The noticed space variability of precipitation was mainly related to differences in modelling the mesoscale evolution of the moist and unstable south-easterly flow over the Adriatic mentioned above. It appeares to constitute the main mesoscale feature directly involved in triggering and maintaining the convective activity. This indicates that, through the set up of a low-level cyclone and associated circulation, the large scale environment drove the convective event consequently favouring its reatively high degree of predictability.

Acknowledgments

The authors are grateful to ARPA Veneto, Comune di Venezia and the ISMAR-CNR for having provided observational data.

References

Anquetin, S., E. Yates, V. Ducrocq, S. Samouillan, K. Chancibault, S. Davolio, C. Accadia, M. Casaioli, S. Mariani, G. Ficca, B. Gozzini, F. Pasi, M. Pasqui, A. Garcia, M. Martorell, R. Romero and P. Chessa, 2005: The 8 and 9 September 2002 flash flood event in France: a

model intercomparison. Nat. Hazards Earth Syst. Sci., 5, 741-754.

Buzzi, A., S. Davolio, M. D'Isidoro and P. Malguzzi, 2004: The impact of resolution and of MAP reanalysis on the simulations of heavy precipitation during MAP cases. Meteologische Zeitschrift, 13, 91-97.

Richard, E., A. Buzzi and G. Zängl, 2007: Quantitative precipitation forecasting in the Alps: The advances achieved by the Mesoscale Alpine Programme. Q. J. R. Meteorol. Soc., 133, 831-846.

Walser, A., D. Lüthi and C. Schär, 2004: Predictability of precipitation in a cloud-resolving model. Mon. Wea. Rev., 132, 560-577.

2.4 Hydro-meteorological chain for flood forecasting in the Toce basin: a multi-model comparison

A. Ceppi,[1] G. Ravazzani,[1] D. Rabuffetti[2] and M. Mancini[1]

[1]*Politecnico di Milano - D.I.I.A.R., Piazza Leonardo da Vinci, 32, 20133 Milano, Italy*
[2]*A.R.P.A. Piemonte - Via Pio VII 9, 10135, Torino, Italy*

Correspondence to: alessandro.ceppi@mail.polimi.it

Abstract

This study is part of the international MAP-D-PHASE Project, whose main objective is to demonstrate the benefits in forecasting heavy precipitation and related flood events, by coupling atmospheric and hydrological models. The analysis is focused on the River Toce, a middle-size alpine basin, in North-West of Italy. The hydro-meteorological chain includes both probabilistic forecasts based on ensemble prediction systems with lead time of a few days and short-range forecasts based on high resolution deterministic atmospheric models. The hydrological model used to generate the runoff simulations is the rainfall-runoff distributed FEST-WB model, developed at Politecnico di Milano. The observed data to run the control simulations were supplied by ARPA-Piemonte. A re-analysis for two precipitation events, affecting the Toce river basin at half June and at the end of November 2007, is shown.

Introduction

In recent years, the interest in the prediction and prevention of natural hazards related to hydrometeorological events has grown, due to the increased frequency of extreme rainstorms (Rabuffetti et al. 2005a). Several research projects have been developed to test hydrometeorological models for flood forecasting, like HYDROPTIMET Project (Rabuffetti et al., 2005b), and AMPHORE Project (Rabuffetti et al., 2008 and Amengual et al., 2008), two recent Interreg IIIB EU Programmes. Despite these improvements, forecasting of highly localized and severe events is still a challenging problem in many areas, particularly where orographic feature and mesoscale structures cannot be properly represented by Global Circulation Model - Ensemble Prediction System (GCM-EPS) because of its coarse horizontal resolution (Federico et al., 2006). For this reason the challenge for numerical weather modelling, in particular for limited area models, is to improve the Quantitative Precipitation Forecasts (QPFs) for hydrological purposes. Following this goal, many research bodies participated during the summer and autumn 2007 at MAP-D-PHASE Project. D-PHASE stands for Demonstration of Probabilistic Hydrological and Atmospheric Simulation of flood

Events in the Alpine region and is a Forecast Demonstration Project (FDP) of the WWRP (World Weather Research Programme of WMO). It aims at demonstrating some of the many achievements of the Mesoscale Alpine Programme (MAP). The MAP FDP will address the entire forecasting chain ranging from limited-area ensemble forecasting, high-resolution atmospheric modelling (km-scale), hydrological modelling and nowcasting to decision making by the end users, i.e., it is foreseen to set up an end-to-end forecasting system. The D-PHASE Operations Period (DOP) was from 1 June to 30 November 2007. In this framework two non-hydrostatic meteorological limited area models are used to predict such phenomena at local scale: one with a spatial resolution of 10 km, supported by the powerful ensemble prediction system (Cosmo-Leps model) and the other with a finer grid, but with one deterministic output only (Moloch model). The hydrological model (FEST-WB), developed at Politecnico di Milano, was forced with observed weather data and QPF data coming from the meteorological models used. The state variables of the model are updated daily by A.R.P.A. - Piemonte that runs the same model with weather observations. The aim of this work is to reproduce a hindcast for two precipitation events, affecting the Toce river basin, the Western watershed of Maggiore Lake basin in North-West of Italy, at half June (convective event) and at the end of November 2007 (stratiform event), in order to estimate how the uncertainty of meteorological forecasts influences the quality of hydrological forecasts and the whole hydrometeorological alert system for a midsize catchment.

Case study

The Toce basin (Figure 2.1) is a midsize watershed located between North-West of Italy (90 %) and South of Switzerland (10 %). The area, closed at Candoglia, covers 1534 km^2 and it is basically an Alpine basin with maximum altitude of 4635 m a.s.l. (East face of Mount Rosa) and minimum altitude of 193 m a.s.l. (height of Maggiore Lake). The lag time of Toce river is about 9 hours.

During the MAP-D-PHASE period three warning codes were adopted to highlight different alert thresholds from a meteorological and hydrological point of view. As shown in Figure 2.2 the yellow line points out a discharge (306 m^3/s) with a return period of at least 60 days, the orange line points out a discharge (694 m^3/s) with a return period of at least 180 days and the red line a discharge (1588 m^3/s) with a return period of at least 10 years.

Meteorological models

The hydrometeorological chain includes both probabilistic forecasts based on ensemble prediction systems with lead time of a few days and short-range forecasts based on high resolution deterministic atmospheric models, in order to predict the QDF (Quantitative Discharge Forecast). The probabilistic forecast was supplied by Cosmo-Leps model (COnsortium

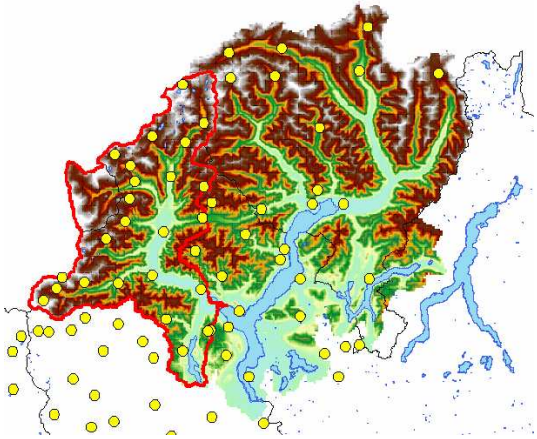

Figure 2.1: Geographical map with the raingauge stations located in the Maggiore Lake basin. The red line bounds the Toce basin.

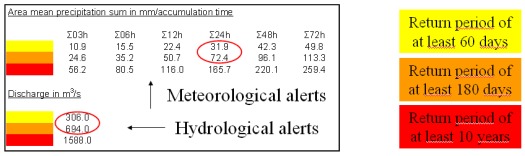

Figure 2.2: Warning codes used for Toce basin at Candoglia during the DPHASE period.

for Small-scale Modelling - Limited-Area Ensemble Prediction System) of A.R.P.A. Emilia-Romagna (Marsigli et al., 2005, Montani et al., 2008). The spatial resolution is 10 km (0.09), while the temporal resolution is 3 h, with 40 vertical levels, 16 ensemble members nested on ECMWF EPS (European Centre for Medium Range Forecast - Ensemble Prediction System) and 5 days as lead-time; the run starts every day at 12:00 UTC, while the hydrological simulation begins 12 hours later at 00:00 UTC. The deterministic forecast was supplied by Moloch model of I.S.A.C. - C.N.R. (Davolio et al., 2007). The spatial resolution is 2.2 km (0.02), while the temporal resolution is 1 h, with 50 vertical levels, nested on BOLAM, based on ECMWF and 2 days as lead-time; the run starts every day at 00:00 UTC, at the same time of the hydrological simulation.

Hydrological model

The hydrological model used to generate the runoff simulations is the rainfall-runoff distributed FEST-WB model, developed at Politecnico di Milano. FEST-WB computes the main process of the hydrological cycle: evapotranspiration, infiltration, surface runoff, flow routing, subsurface flow and snow dynamics. The computation domain is discretized with a mesh of regular square cells, within which water fluxes are calculated. The models needs spatially distributed meteorological forcing. The observed data at ground stations are interpolated to a regular grid using IDW technique, considering the effect of topography such as elevation, aspect and shadow (Rabuffetti et al., 2008). Runoff is computed according to a modified SCS-CN method extended for continuous simulation where the potential maximum retention, S, is updated at the beginning of storm as a linear function of the degree of saturation (Ravazzani et al., 2007). The actual evapotranspiration, ET, is computed as a fraction of the potential rate tuned by a function that, in turn, depends on soil moisture content (Montaldo et al., 2003). The estimation of ETP is computed with Priestley and Taylor

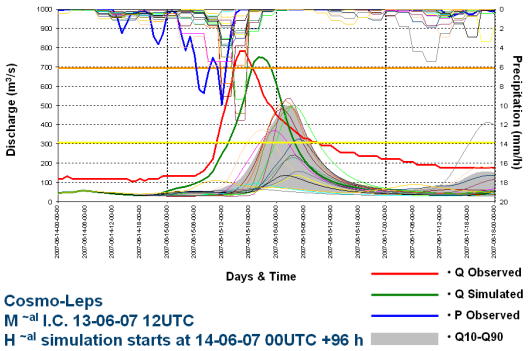

Figure 2.3: Ensemble QDF for Cosmo-Leps model from 14 June to 17 June 2007.

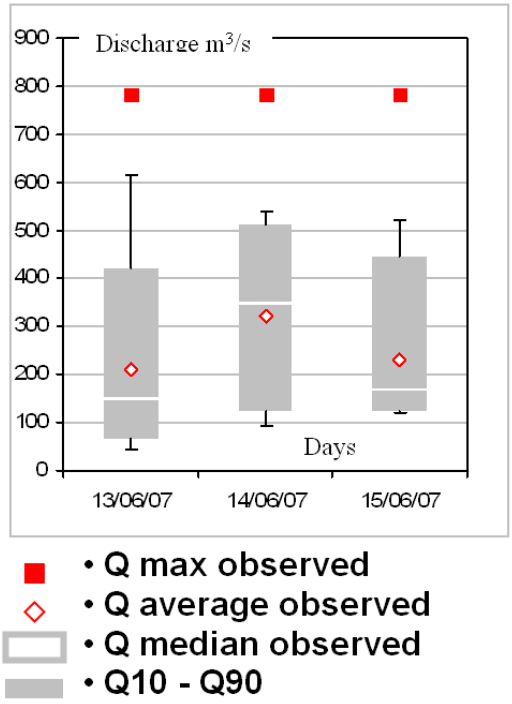

Figure 2.4: Box-Whisker plot for Cosmo-Leps. The date is referred to the day of the initial hydrological simulation.

(1972) equation. The surface and subsurface flow routing is based on the Muskingum-Cunge method in its non-linear form with the time variable celerity (Montaldo et al., 2007). The snow model includes the snow melt and the snow accumulation dynamics. The snow melt simulation is based on the degree day concept (Martinec et al., 1960). The melt rate is proportional to the difference between air temperature and a predefined threshold temperature (Saladin et al., 2004).

13-15 June 2007 event

The synoptic analysis over Europe showed a low depression located South-West of the British Isles with cold air moving eastward over the Po Valley, triggering convective cells on the southern edge of the Alps (about 100 mm of total rain over Toce basin in about 48 hours). The hydrological simulation (green line), done by FEST-WB model, has reached a peak of 750.7 m^3/s and it presents 3 hours of delay as peak time error compared to the observed discharge (red line) of 783.2 m^3/s. The QPF predicted by Cosmo-Leps model shows a general underestimation in all three days of simulations for all 16 members. This affects the forecasted discharge (Figure 2.4) that has never exceed the second alert threshold as shown in Figure 2.3.

The Moloch model, instead, has predicted, one day in advance, the peak discharge, exceeding the second threshold like the observed and simulated discharge, even if there is an evident

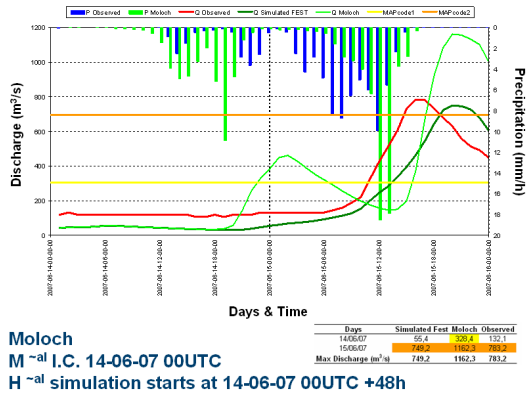

Figure 2.5: QDF for Moloch model (light green curve) from 14 June to 15 June 2007.

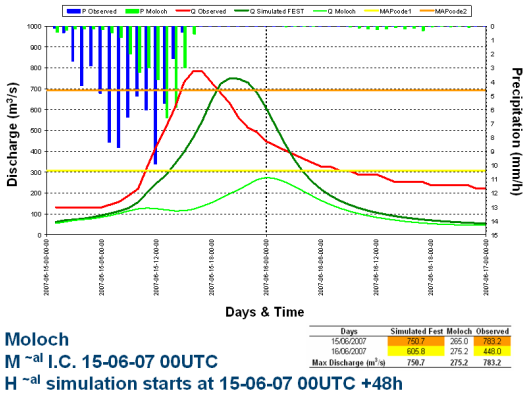

Figure 2.6: QDF for Moloch model (light green curve) on 15 June 2007.

error in time and volume as shown in Figure 2.5. On the contrary, on the same day of the peak event, the QPF was totally underestimated and the discharge has not exceeded even the first alert threshold (Figure 2.6).

21-23 November 2007 event

The synoptic analysis over Europe showed a typical autumn pattern with a deep depression on Atlantic Ocean, bringing moist flow from South-West towards the Italian Alps (about 80 mm of rain on Toce basin, after a long dry period of two months). First of all the FEST-WB discharge simulation with real data has been completely underestimated on 21 (Figure 2.7) and 22 November, due to a not correct initial value of river discharge. Data assimilation of observed discharge, not used in FEST-WB, may provide better results. Therefore, even if Moloch and Cosmo-Leps models have shown a general overestimation of rainfall in terms of volume and intensity, the forecasted discharges remained underestimated. Only on the peak flow day (23 November), after two days of precipitation, a perfect synchrony between the observed and forecasted precipitation (Figure 2.8) and discharges peak is pointed out both for Cosmo-Leps (Figure 2.9) and Moloch model (Figure 2.10). Anyway the observed, simulated and forecasted discharge has never exceeded the first threshold (306 m^3/s) in any model, i.e. no alert was issued for this event.

Conclusions

This analysis has shown the results of the hydro-meteorological chain with a multi-model comparison, using the weather models output (Cosmo-Leps and Moloch) as input into the hydrological model (Fest-WB) to predict a QPF (Quantitative Precipitation Forecast) and a QDF (Quantitative Discharge Forecast). The proposed hydro-meteorological forecasting system has been implemented in a real-time configuration, in order to provide useful information concerning the discharge peak (magnitude and timing). High resolution meteorological

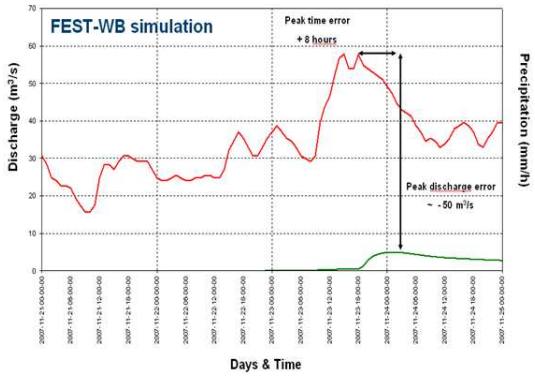

Figure 2.7: Observed (red line) vs simulated discharge by FEST-WB model with initial conditions start on 21 November.

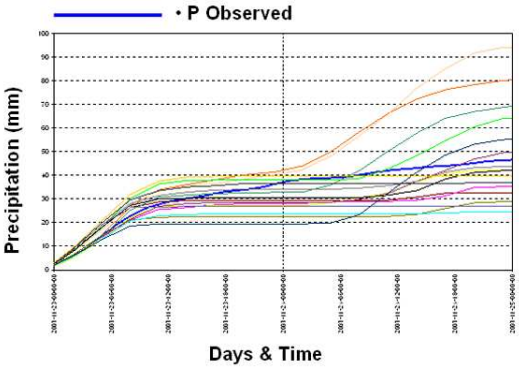

Figure 2.8: Forecasted mean area accumulated precipitation by Cosmo-Leps model on 21 November.

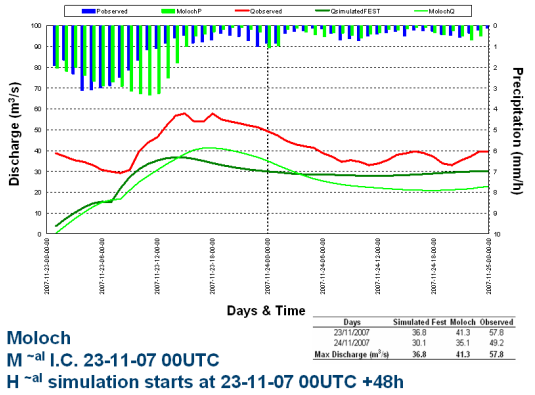

Figure 2.9: QDF for Moloch model (light green curve) on 23 November 2007.

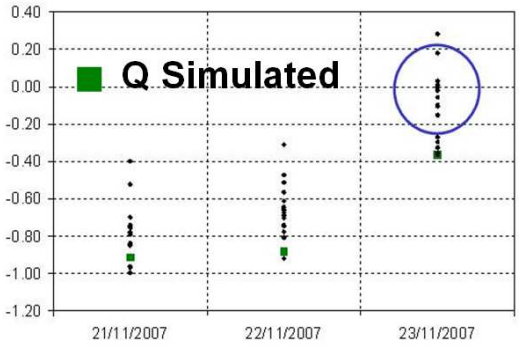

Figure 2.10: QDF error for Cosmo-Leps ensemble members (black dots) and FEST-WB (dark green dot).

model seems to show greater reliability on the prediction of flood on complex topography, but the number of investigated flood events is too small to draw conclusions. Future studies could be addressed to better evaluate the temporal and spatial scale for the total rainfall volume, above all for the convective events. For stratiform events further analyses could be carried out on snow melt temperature which affects the liquid precipitation and therefore the forecasted runoff, like in November event where the snow melt limit was very changeable.

Acknowledgments

Thanks to ARPA Emilia-Romagna (A. Montani) for his contribute in providing COSMO-LEPS model data and to ISAC-CNR (S. Davolio) for MOLOCH model data.

References

Amengual, A., Diomede, T., Marsigli, C., Martin, A., Morgillo, A., Romero, R., Papetti, P. and Alonso, S.: 2008. A hydrometeorological model intercomparison as a tool to quantify

the forecast uncertainty in a medium size basin. Nat. Hazards Earth Syst. Sci., 8, 819-838.

Davolio, S., Buzzi, A., and Malguzzi, P.: 2007. High resolution simulations of an intense convective precipitation event. Meteorol. Atmos. Phys., 95, 139-154.

Federico, S., Avolio, E., Bellucci, C., Colacino, M. and Walko, L.: 2006. Application of the LEPS tecnique for a Quantitative Precipitation Forecasting (QPF) in Southern Italy: a preliminary study. Nonlin. Processes Geophys., 13, 53-66.

Marsigli C., Boccanera F., Montani A., Paccagnella T.: 2005. The COSMO-LEPS mesoscale ensemble system: validation of the methodology and verification. Nonlin. Proc. Geophys., 12,527-536.

Martinec, J.: 1960. The degree-day factor for snowmelt runoff forecasting, proceedings of general assembly of Helsinki commission on surface waters, IAHS Publ. 51, 1960.

Montaldo, N., Ravazzani, G. and Mancini, M.: 2007. On the prediction of the Toce alpine basin floods with distributed hydrologic models, Hydrol. Processes, 21, 608-621.

Montaldo, N., Toninelli, V., Albertson J. D., Mancini, M. and Troch P. A.: 2003. The Effect of Background Hydrometeorological Conditions on the Sensitivity of Evapotranspiration to Model Parameters: Analysis with Measurements from an Italian Alpine Catchment, Hydrol. Earth Syst. Sci., 7, 848-861.

Montani, A. Marsigli, C., Paccagnella, T.: 2008. Five Years of Limited-Area Ensemble Activities at ARPA- SIM: The COSMO-LEPS system, Cosmo Newsletter n.8.

Priestley, C. H. B. and Taylor, R. G.: 1972. On the assessment of surface heat flux and evaporation using large scale parameters. Mon.Weather Rev., 100, 81-92.

Rabuffetti, D. and Barbero, S.: 2005a. Operational hydro-meteorological warning and real time flood forecasting: the Piemonte Region case study. Hydrology and Earth System Sciences, 9(4), 457-466.

Rabuffetti, D. and Milelli, M.: 2005b. The hydro-meteorological chain in Piemonte region, North Western Italy - analysis of the HYDROPTIMET test cases. Natural Hazard and Earth System Sciences, 5, 845-852.

Rabuffetti, D., Ravazzani, G., Corbari, C., and Mancini, M.:2008. Verification of operational Quantitative Discharge Forecast (QDF) for a regional warning system - the AMPHORE case studies in the upper Po River. Nat. Hazards Earth Syst. Sci., 8, 161-173.

Ravazzani, G., Mancini, M., Giudici, I., and Amadio, P.: 2007. Effects of soil moisture parameterization on a real-time flood forecasting system based on rainfall thresholds, in: Quantification and Reduction of Predictive Uncertainty for Sustainable Water Resources Management, edited by: Boegh, E., Kunstmann, H.,Wagener, T., Hall, A., Bastidas, L.,

Franks, S., Gupta, H., Rosbjerg, D., and Schaake, J., IAHS Publ. 313, 407-416, 2007.

Salandin, A., Rabuffetti, B., Barbero, S., Cordola, M., Volonte, G. and Mancini, M.: 2004. Il lago effimero sul ghiacciaio del Belvedere: monitoraggio e simulazione numerica del fenomeno finalizzata alla previsione e gestione dell'emergenza, Neve e Valanghe, 51, 58-65, 2004.

Tarboton D. G., Chowdhury T. G., Jackson Thomas H.: 1994. A Spatially Distributed Energy Balance Snowmelt Model, Utah Water Research Laboratory.

2.5 Flood forecasting and rating curve maintenance on Lambro river in Lombardy

Cislaghi M. and M. Russo

ARPA della Lombardia, U.O. Idrografia

m.cislaghi@arpalombardia.it; m.russo@arpalombardia.it

Introduction

U.O. Idrografia, the hydrology office of ARPA Lombardia, is in charge of river and lake monitoring, discharge measuring, rating curve development and updating. ARPA also co-operates with the Civil Protection Department of Regione Lombardia in flood forecasting and monitoring. The Lambro river runs in the Po valley with a north-south orientation and crosses the city of Milan in the east area (Figure 2.1). Milan has a very high population density and the authorities are aware of the flood risk coming from the river.

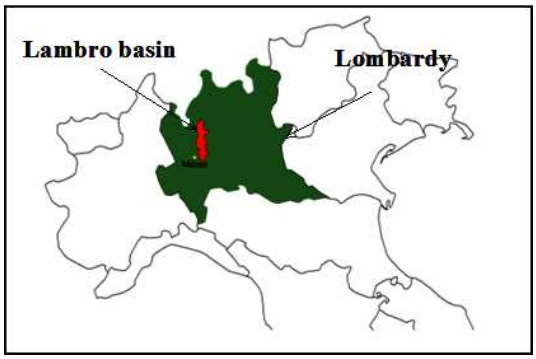

Figure 2.1: The Lambro basin has an area of 562 Km^2.

Medium-small catchments, like Lambro closed at the Milan via Feltre section (Figure 2.2), have fast response that makes difficult to alert the population with a proper advance or to plan discharge measures at high hydrometric levels. For all these reasons the Civil Protection Department of Regione Lombardia developed a semi-distributed hydrological model of the Lambro river. Coupled with meteorological models and observed rainfall data, the hydrological model may give an appropriate flood forecast. The scientific community has been working on coupling meteorological and hydrological models since the 1990s (Yu Z. at al., 1999) and the quantitative precipitation forecast was immediately found as the main source of uncertainty in the whole process. Recently Arduino G. et al (2005) underlined the importance of a high spatial resolution of meteorological models in order to resolve small scale phenomena such as the convective events or the orographic effects (Bartholmes J. at al., 2005). Other authors (Davolio S. et al., 2008; Coulibaly P., 2003; Taschner S. et al., 2000)

observed that the precipitation forecast differs model by model and developed a multi-model or ensemble approach for their studies. In the MAPDPHASE project ARPA Lombardia - U.O. Idrografia applied the multi-model approach to the Lambro basin: the precipitation fields, from four meteorological models (Table 1), have been used as input of one hydrological model. Possible interactions or feedbacks between meteorological and hydrological models (Verbunt M. et al, 2006; 10 Jasper K. et al., 2002) are here neglected.

The hydrological model

The Lambro basin is characterized by different orography and land use: the northern area is mountainous and rural while the southern part is plain and very urbanized. Rural and urbanized areas have different response time and infiltration capacity, then Civil Protection Department divided the Lambro basin into 44 sub-basins and described them with 44 rainfall-runoff lumped models. The runoff from each sub-basin is the input of a hydraulic model that computes the discharge propagation and the water level at the cross-sections.

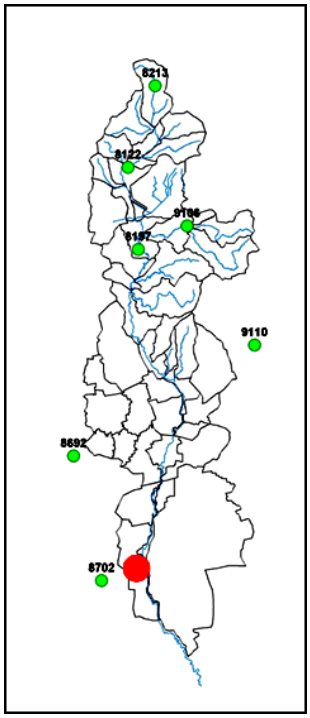

Figure 2.2: The Lambro basin divided into the 44 sub-basins. Milan via Feltre section (red circle), raingauges (green cricles).

The meteorological model

The Lambro basin is characterized by different orography and land use: the northern area is mountainous and rural while the southern part is plain and very urbanized. Rural and urbanized areas have different response time and infiltration capacity, then Civil Protection

Department divided the Lambro basin into 44 sub-basins and described them with 44 rainfall-runoff lumped models. The runoff from each sub-basin is the input of a hydraulic model that computes the discharge propagation and the water level at the cross-sections.

Table 1: Meteorological models

MODEL	AGENCY	GRID RES (km)	TIME RES (h)	FORECAST TIME
CLEPS	ARPA Emr	10.00	3	132 h
LAMI28	ARPA Emr	2.08	1	48 h
ISACMOL	ISAC CNR	2.02	1	39h
ARPALMOL	ARPA Liguria	2.02	3	36 h

Case Studies

Here two interesting rainfall-runoff events are analyzed: the convective event on September 17th 2007 and the frontal event on November 23rd 2007. The convective event on September 17th was very short (6 hrs) and intense. None of the meteorological models forecast the event and neither precipitation nor runoff were given in output. Anyway, using observed precipitation as input, the hydrological model well reproduced the observed discharge (Figure 2.3).

On the contrary, the frontal event of November 23rd has been forecast four days in advance by the CLEPS model (Figure 2.4a). Looking at the forecast made on November 22nd, three out of four meteorological models forecast either temporal or spatial behavior of the precipitation (Figure 2.5). The hydrological model well simulated the temporal behavior of the event (Figure 2.4b), even if it overestimated the actual discharge because of the too high soil moisture initial conditions.

The event has been forecast four days in advance, this allowed U.O. Idrografia to plan a discharge measure on November 23rd. On November 22nd three meteorological models confirmed the rainfall event and the hydrological model predicted the peak time around midday: an U.O. Idrografia team had enough time to setup the instrumentation at Milan via Feltre section, waited for the peak and measured it (Figure 2.6a). In Figure 2.6b the rating curve and the discharge measure are shown. Since the discharge value is very close to the line, it confirmed the rating curve.

Conclusions

Meteorological models well simulated frontal precipitation events but the convective ones are not completely reproduced yet. The time behavior of the flood event is well reproduced by the hydrological model, even if initial soil-moisture conditions affect the actual discharge. A

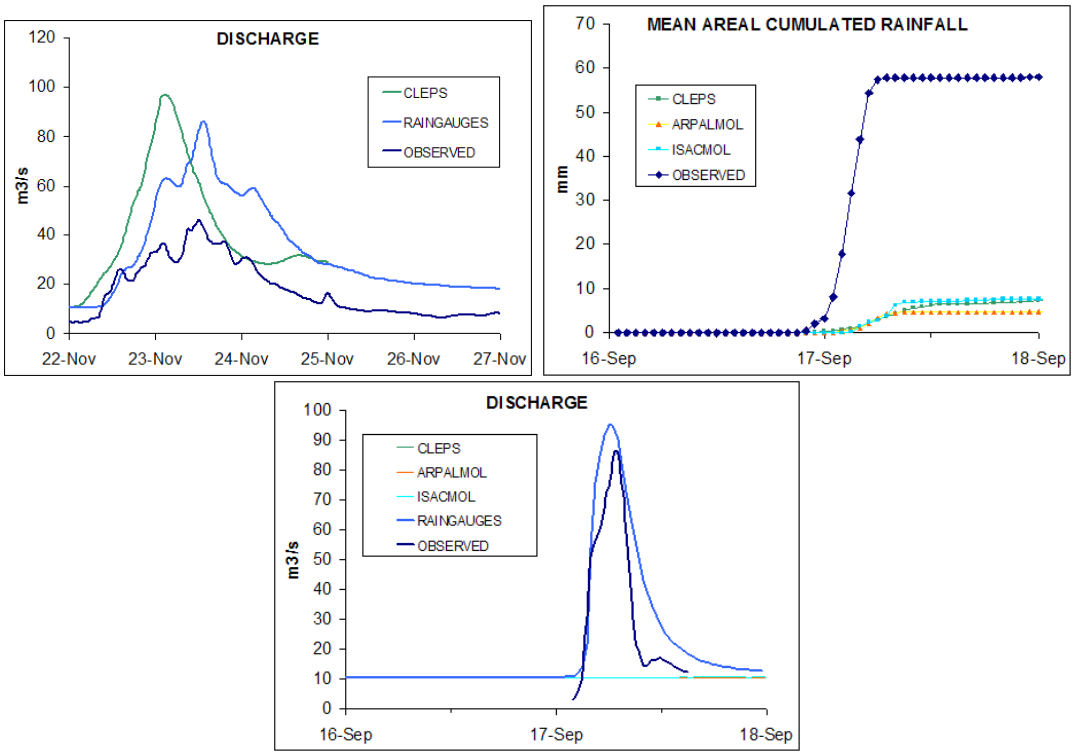

Figure 2.3: Forecast made on September 16th: Mean areal rainfall intensity (a) and cumulated rainfall over the Lambro basin, (b): the convective event is not resolved by any model. Discharge at Milan via Feltre (c): using observed rainfall from raingauges the hydrological model (light blue line) well simulated the observed discharge (dark blue line).

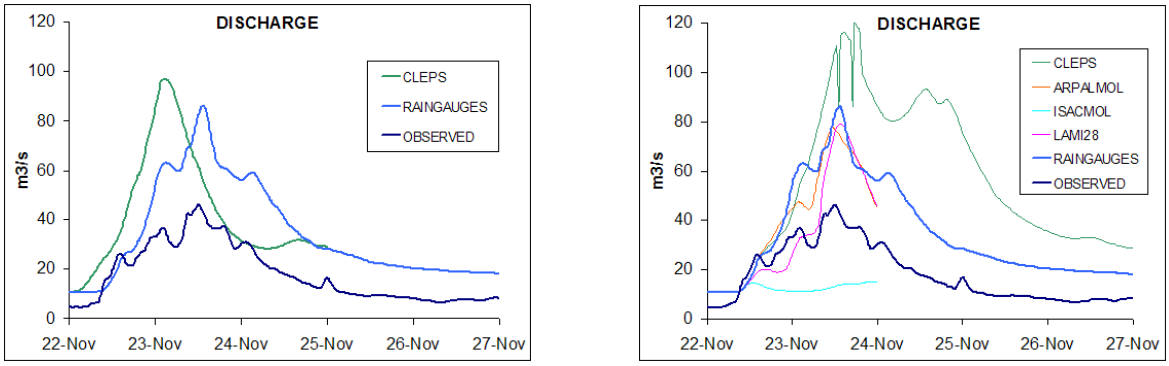

Figure 2.4: Discharge forecast made on Novenber 19th (a): the chain CLEPS-hydrological model forecast a discharge event on November 23rd; comparing the observed discharge (dark blue line) with the simulation using observed rainfall (light blue line), the hydrological model overestimated discharge because of the too high soil moisture initial conditions. Discharge forecast made on November 22nd, (b): ARPALMOL and LAMI28 chains well reproduced the simulation using observed rainfall, the simulated peak time matches with the observed one.

frontal rainfall event and the occurrence time of the flood peak have been forecast 4 days in advance. This allowed ARPA Lombardia - U.O. Idrografia to plan and carry out a discharge measure right during the flood peak. Then the rating curve of Milan Via Feltre section has been validated.

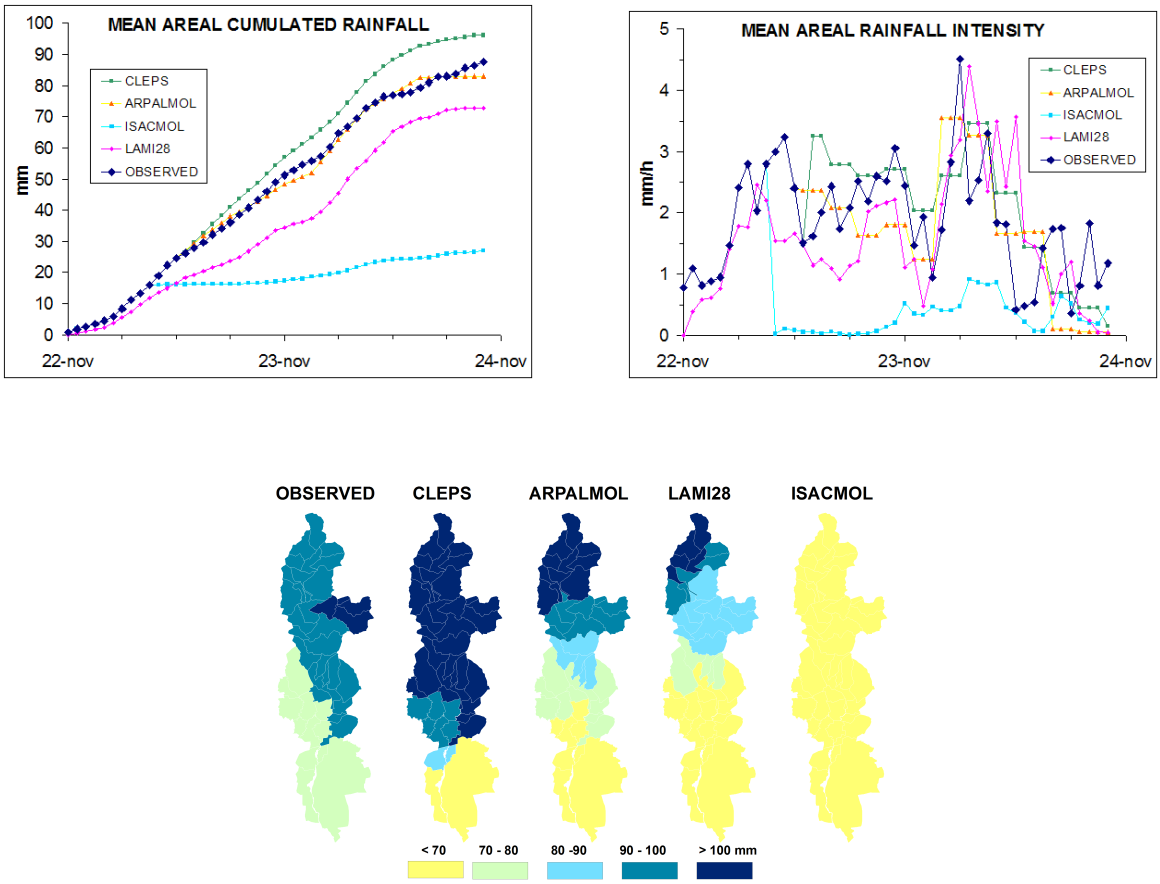

Figure 2.5: Forecast made on November 22nd: Mean areal rainfall intensity (a) and cumulated rainfall over the Lambro basin, (b): the frontal event is well resolved by CLEPS, ARPALMOL and LAMI28. Spatial distribution of cumulated rainfall over Lambro basin (c): the orographic effect is simulated by CLEPS, ARPALMOL and LAMI28.

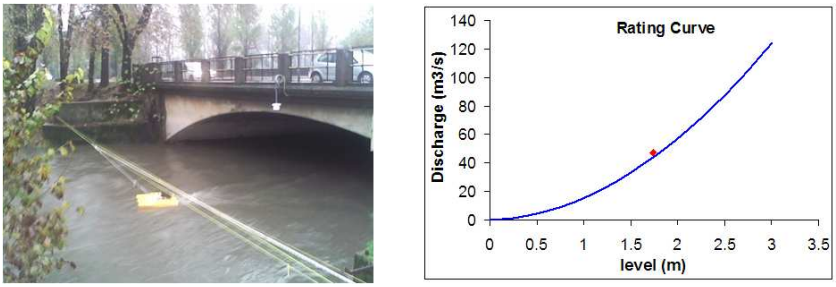

Figure 2.6: (a) Discharge measure at Milan via Feltre on November 23rd, (b) the measured discharge (red point) well fits with the rating curve.

Further developments

With the MAPDPHASE project ARPA Lombardia experienced the efficacy of coupling meteorological and hydrological models. U.O. Idrografia is now testing the methodology on some mountainous basins using simple hydrological lumped models. The basins are shown in Figure 2.7 and are of great interest from a hydrological point of view. If positive results will be achieved, as in the MAPDPHASE project, U.O. Idrografia will have a very useful

help for planning discharge measures.

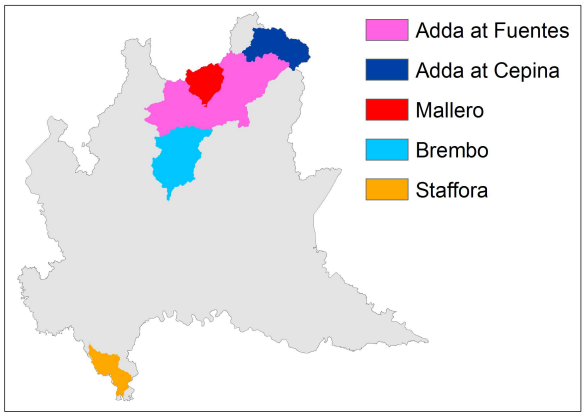

Figure 2.7: ARPA Lombardia - U.O. Idrografia is testing MAPDPHASE approach on some mountainous basins for flood forecasting.

Acknowledgements

ARPA Lombardia - U.O. Idrografia thanks Molari Maurizio (Civil Protection Department of Regione Lombardia), Montani Andrea (ARPA Emilia Romagna), Cesari Davide (ARPA Emilia Romagna), Corazza Matteo (ARPA Liguria), Davolio Silvio (ISAC CNR) for their support and for the models made available during the MAPDPHASE project.

References

Arduino G., P. Reggiani, E. Todini, 2005: Recent advances in food forecasting and flood risk assessment. Hydrology and Earth System Sciences, 9(4), 280-284.

Bartholmes J., E. Todini, 2005: Coupling meteorological and hydrological models for flood forecasting. Hydrology and Earth System Sciences, 9(4), 333-346.

Coulibaly P., 2003: Impact of meteorological predictions on realtime spring flow forecasting. Hydrological Processes, 17, 3791-3801.

Davolio S. M., Miglietta M., Diomede T., Marsigli C., Morgillo A. and Moscatello A., 2008: A meteo-hydrological prediction system based on a multimodel approach for precipitation forecasting. Natural Hazards and Earth System Sciences, 8, 143-159.

Jasper K., J. Gurtz, H. Lang, 2002: Advanced flood forecasting in Alpine watersheds by coupling meteorological observations and forecasts with a distribuited hydrological model. Journal of Hydrology, 267, 40-52.

Taschner S., R. Ludwig, W. Mauser, 2000: Multi-scenario Flood Modeling in a Mountain Watershed Using Data from a NWP Model, Rain Radar and Rain Gauges. Physics and Chemistry of the Earth, Part B: Hydrology, Oceans and Atmosphere, Volume 26, Number

7, 2001, pp. 509-515(7).

Verbunt M., M. Zappa, J. Gurtz, P. Kaufmann, 2006: Verification of a coupled hydrometeorological modelling approach for alpine tributaries in the Rhine basin. Journal of Hydrology, 324, 224-238.

Yu Z., M.N. Lakhtakia, B. Yarnal, R.A. White, D.A. Miller, B. Frakes, E.J. Barron, C. Duy, F.W. Schwartz, 1999: Simulating the river-basin response to atmospheric forcing by linking a mesoscale meteorological model and hydrologic model system. Journal of Hydrology, 218, 72-91.

2.6 The flood event near Venice of 26 September 2007: uncertainty in high resolution forecasting using the MOLOCH model

A. Buzzi and P. Malguzzi

ISAC-CNR, Bologna, Italy

Abstract

The quantitative precipitation and other meteorological fields obtained from a number of different simulations made using the ISAC MOLOCH model, nested in BOLAM as in the configuration applied during the D-PHASE experiment, are presented for the heavy precipitation event that affected the area of Venice on the 26^{th} September 2007. In order to assess to what extent the event was predictable, and how sensitive the QPF is to different initial conditions and model parameters, the model chain setup differs from that of the D-PHASE in some aspects. Simulations based on initial and boundary conditions derived from GFS and ECMWF global forecasts at different times before the event are compared. Although the intense precipitation event is expected to have low predictability due to its convective nature, and in spite of the high spread of QPF obtained, the forecasts of explicit convection made more than 24-30 hours in advance indicate that the larger scale environment driving the event dynamics (as the formation of an Alpine lee cyclone, the presence of a low level jet over the Adriatic Sea and of a cold outbreak over the Veneto inland areas) played an important role in favouring predictability. Results of different sensitivity experiments are shown.

The event and the model setup

In the early morning of 26 September 2007, several thunderstorms developed over the southern side of the Alps and over the plains of northern Italy, in association with the formation of a moderate mesoscale lee cyclone over the Gulf of Genoa and a deepening of an upper level trough west of the Alps (see Fig. 2.6a below). Heavy precipitation was recorded near Milano, but the most prominent intense rainfall event, which seems to have produced the maximum accumulated precipitation over 12-24 hours during the entire D-PHASE project period (Arpagaus et al, 2008), affected an area 10-20 km to the west of Venice, near the town of Marghera (Fig. 2.1), as described in detail in Barbi et al (2007). The absolute precipitation maximum exceeding 300 mm was mostly due to the heavy rainfall occurred in the period 5:00 - 11:00 UTC. The consequence was extensive flooding of the flat area.

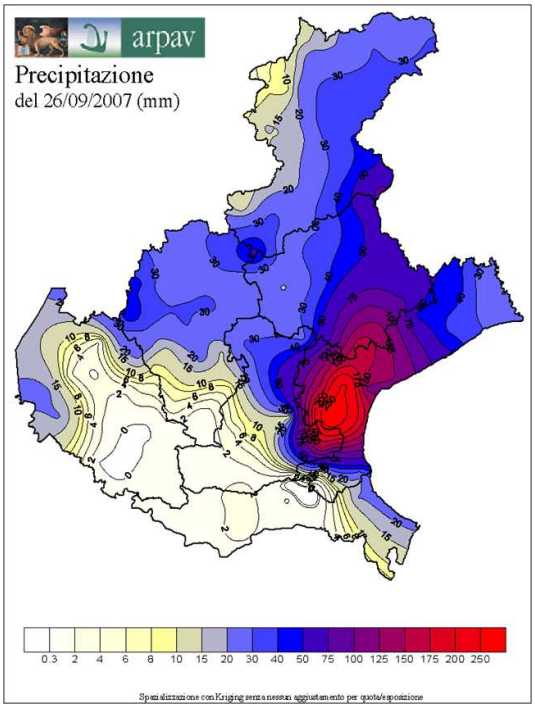

Figure 2.1: Accumulated precipitation of 26 Sep. 2007 (courtesy of ARPAV, Teolo, Padova)

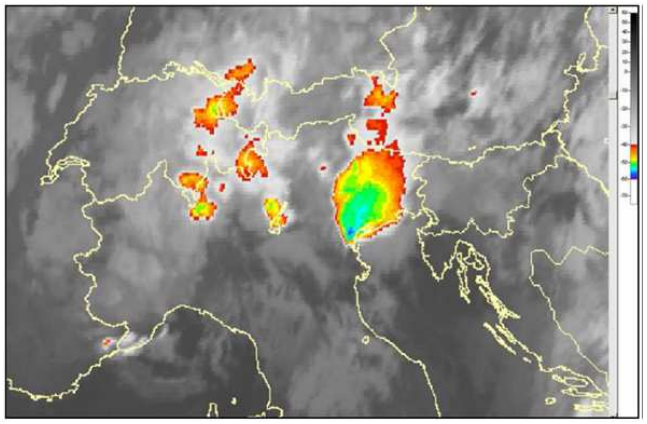

Figure 2.2: MET-9 IR image at 07:00 UTC, 26 Sep. 2007 (EUMETSAT copyright - courtesy of ARPAV, Barbi et al, 2007)

Different convective cells formed in the area located between the Veneto Prealps and the Venice Lagoon, starting around 2:00 UTC. Deep convection developed 3-4 hours later into a MCS that formed about 20 km to the west of Venice and insisted over the region for more than 6 hours, before moving slowly to the east, over the Adriatic sea. The MCS was characterized by a distinct V-shaped cloud top, oriented SW-NE, and was deep (top temperature $\sim$ -55 C, corresponding to a height of about 12 km - see Fig. 2.2).

The operational MOLOCH (Malguzzi et al, 2006) forecast (ISACMOL) of D-PHASE based on 00 UTC GFS/NCEP analysis of 25 September (24-36 hour range) essentially captured the event, predicting a precipitation maximum of 242 mm, located about 20 km north and

2-3 hours late compared with observations.

This case has been chosen to assess the sensitivity of the forecasts to various factors. The MOLOCH resolution is the same as for the D-PHASE (2.2 km), but with a smaller domain (250x250 in place of 340x290 grid points), centred over the area of interest. The MOLOCH runs considered here, always starting at 01 UTC of 26 September, are nested into BOLAM (Zampieri et al, 2005) runs initiated at different times, as specified in the following section.

Experiment results

Sensitivity to the initial conditions

The various experiments have been run starting with ECMWF analyses at September 25-00, 25-12 and 26-00, and GFS analyses at 25-00 and 26-00, respectively. Figure 2.3 shows the two runs starting at 25-00. The two cases produce similar precipitation maxima, but the GFS-based run, as in the DPHASE case, gives the best localization. All the other simulated forecasts initialized at later times (not shown) produce smaller precipitation and with larger geographical errors (except for the ECMWF run starting at 25-00).

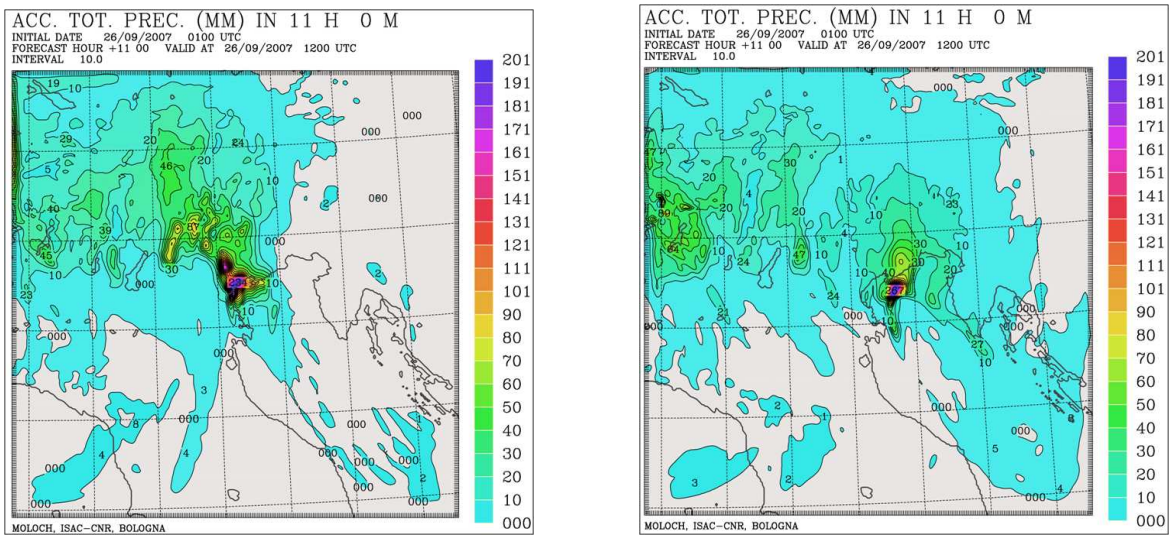

Figure 2.3: Accumulated precipitation as forecast by the MOLOCH model, in the period 01-12 UTC of 26 Sep. 2007. Left: from GFS/NCEP analysis. Right: from ECMWF analysis

The position and intensity of the precipitation maxima obtained in the five experiments are summarized in Fig. 2.4, superimposed on the model orography. Different colours indicate precipitation ranges: blue: $>$ 200 mm; red: 150-200 mm; yellow: 100-150 mm. The arrow points to the position of the observed precipitation maximum. The red circle, having a radius of 40 km, encompasses all the precipitation maxima resulting also from other sensitivity experiments. In the following, the forecast starting with the GFS analysis of 25-00 is named as "control" case.

Multicell structure and V-shape MCS

One of the distinctive features that characterize the "successful" forecasts among those considered here, which produce realistic amounts of precipitation, is related to the vertical penetration and degree of organization of the simulated MCS. The observed MCS was preceded by a multi-cellular stage, before developing into a V-shape structure. The MOLOCH "control" simulation reproduces both stages of development (see the vertical velocity at 500 hPa at 09 - Fig. 2.5a - and 11 UTC - Fig. 2.5b - respectively). Figure 2.5b shows the V-shape feature of the mid-high tropospheric updraft. This figure reflects the shape of the anvil visible in Fig. 2.2.

Role of the orography

The MCS developed during a lee cyclogenesis process: at 26-00 a distinct geopotential minimum is present at 850 hPa over the Ligurian Sea, as indicated by the 850 hPa geopotential in Fig. 2.6a as obtained in the BOLAM model forecast. The lee cyclone circulation induces, together with the direct barrier effects of the Alps but also of the Apennines and the Dinaric Alps, a strong low-level flow confluence/convergence over the area where the severe convection is initiating, as indicated schematically by the arrows in Fig. 2.6a. Over the Adriatic, a SE low level jet (LLJ, indicated by the red arrow) advects warm and moist air, while a NE cold flow (partly a barrier wind, indicated by the blue arrow) is present more to the north, over the Veneto plains. In the case the BOLAM run is performed after the model orography height has been arbitrarily reduced to one fourth of its original amplitude (Fig. 2.6b), the lee cyclone and related convergence are suppressed, the cold front moves smoothly to the SE and severe convection does not develop in the model experiment.

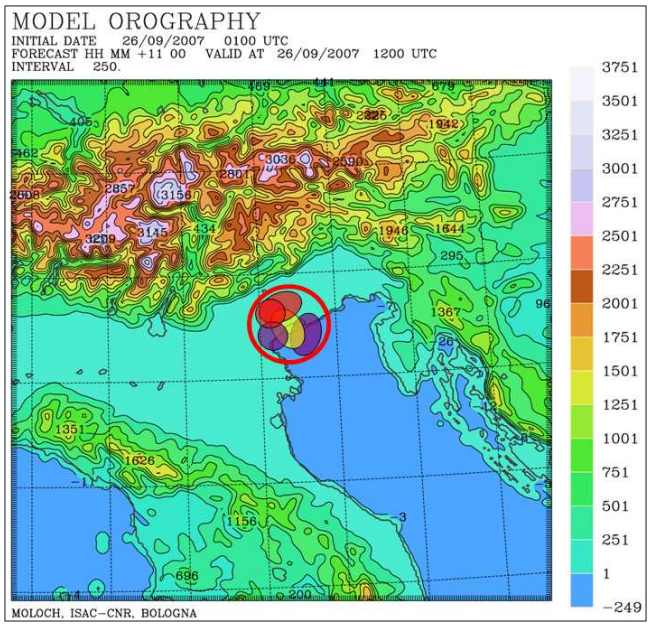

Figure 2.4: Position and intensity of precipitation maxima obtained using different global initial conditions (see text)

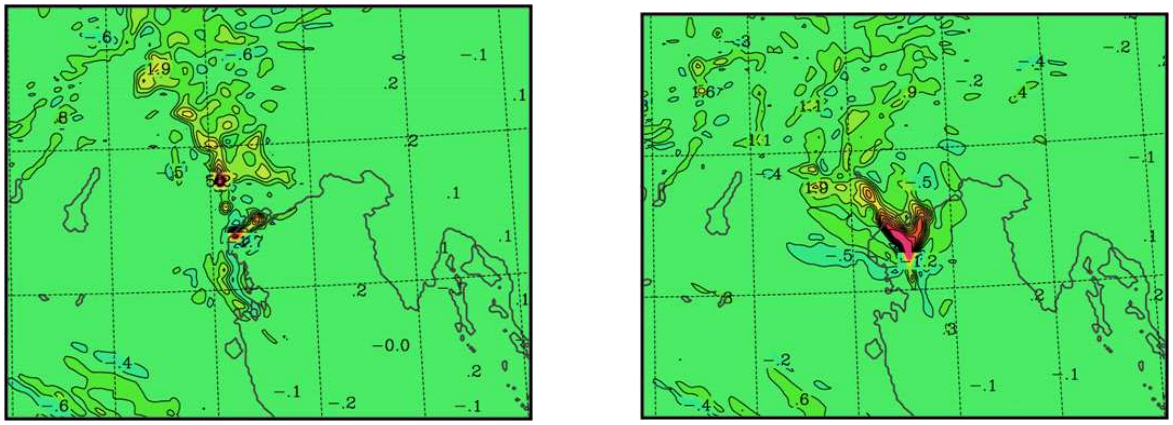

Figure 2.5: Vertical velocity w at 500 hPa, at 00 UTC (left panel) and 11 UTC (right panel), 26 Sep. 2007, as reproduced by the MOLOCH forecast experiment

Conclusions

The results of the D-PHASE project allow us to evaluate to what extent organized convection can be predicted, in the short range, by convection-resolving models, also in association with the capability of forecasting the mesoscale phenomena that determine location and timing of thunderstorm activity. The intense convective precipitation event that affected an area near Venice on September 26 constitutes an interesting case-study.

The MOLOCH model, which produced the more realistic QPF in real time for this event, has been used to evaluate heuristically the forecast uncertainty in the range from 6 to 36 hours in advance. A large number of MOLOCH *a posteriori* forecasts were performed, changing initial conditions, model chain setup (including the intermediate BOLAM model), model parameters, and physical and dynamical schemes. The results are sensitive to the

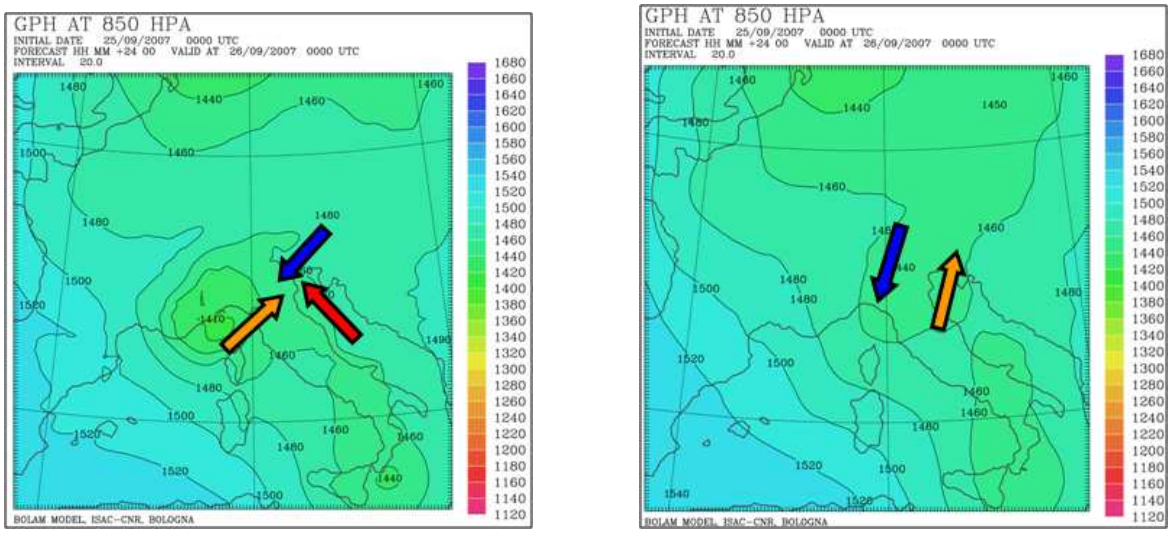

Figure 2.6: BOLAM forecast at +24h, verifying at 00 UTC of 26 Sep. 2007; Left: with full orography; Right: for a orography height reduced to 1/4

convective parameterization scheme applied in the lower resolution model, extension of the inner domain, time at which the fine resolution model is initiated, and spatial resolution. However, in all cases, the MCS developed in the model within the circle depicted in Fig. 2.4 and produced maximum rainfall in the range between 140 and 290 mm.

The above results indicate that forecasting severe convective events and associated quantitative precipitation in advance of one day or so is feasible in cases in which convection is embedded in mesoscale flows having sufficient predictability. This result is consistent with the recent finding of Weisman et al (2008), regarding the forecast application of the non-hydrostatic, convection-permitting WRF model over the North America, nested in the Eta model. In fact they conclude that "perhaps the most notable result is the overall strong correspondence between the Eta and the WRF-ARW guidance..., suggesting the overriding influence of the larger scales of forcing on convective development in the 24-36-h time frame. ... The relative success in forecasting seemingly unpredictable phenomenon such as convection out to 36h seems most directly related to its strong connection to identifiable and more predictable synoptic or subsynoptic features, which establish the mesoscale environment favourable for the convection as well as serving as the primary triggering agent". The event described here has precisely the characteristics identified in the former sentence, which seem to give higher predictability to a phenomenon like convection that is intrinsically poorly predictable.

References

Arpagaus, M., P. Ambrosetti, F. Ament, C. Appenzeller, H. S. Bauer, F. Bouttier, A. Buzzi, M. Corazza, S. Davolio, M. Denhard, M. Dorninger, F. Fontannaz, J. Frick, F. Fundel, U. Germann, T. Gorgas, C. Hegg, A. Hering, C. Keil, M. A. Liniger, C. Marsigli, R. McTaggart-Cowan, A. Montani, K. Mylne, R. Ranzi, E. Richard, A. Rossa, M. W. Rotach, D. Santos-Muñoz, C. Schär, Y. Seity, M. Staudinger, M. Stoll, H. Volkert, A. Walser, Y. Wang, J. Werhahn, V. Wulfmeyer and M. Zappa, 2008: The Forecast Demonstration Project MAP D-PHASE. Verffentlichungen der MeteoSchweiz, 77 (available from http://www.meteoschweiz.admin.ch).

Barbi, A., G. Formentini, M. Monai, F. Rech and F. Zardini, 2007: Analisi meteo-climatica dell'evento pluviometrico del 26 settembre 2007 nel veneziano. ARPAV, Dipartimento Regionale Sicurezza del Territorio, Centro Meteorologico di Teolo, Padova.

Malguzzi, P., G. Grossi, A. Buzzi, R. Ranzi and R. Buizza, 2006: The 1966 "century" flood in Italy: A meteorological and hydrological revisitation. J. Geophys. Res., 111, D24106, doi:10.1029/2006JD007111.

Weisman, M. L., C. Davis, W. Wang, K. W. Manning and J. B. Klemp, 2008: Experiences with 0-36-h explicit convective forecasts with the WRF-ARW model. Wea. Forecasting, 23,

407-437.

Zampieri, M., P. Malguzzi and A. Buzzi, 2005: Sensitivity of quantitative precipitation forecasts to boundary layer parameterization: a flash flood case study in the Western Mediterranean. Nat. Hazard Earth Sys. Sci., 5, 603-612.

2.7 QBOLAM: The APAT contribution to the MAP D-PHASE forecasting activity

Marco Casaioli[(1)], Stefano Mariani[(1)], Alexandre Lanciani[(1)] and Simona Flavoni[(1,2)]

[(1)] *National Agency for Environmental Protection and Technical Services (APAT), now Institute for Environmental Protection and Research (ISPRA), Rome, Italy*

[(2)] *University "Roma Tre", Rome, Italy*

Introduction

Forecasting activities performed during the Demonstration Operational Period (DOP, June to November 2007) represent the core of the World Weather Research Programme (WWRP) Forecast and Development Project (FDP) MAP D-PHASE ($http://www.map.meteoswiss.ch/map-doc/dphase/dphase\_info.htm$). A wide range of numerical models has been run in operational configuration by the project partners, providing real-time forecast and post-processing products (*e.g.*, maps and alerts) over two target areas, namely, the D-PHASE and the Convective and Orographically-induced Precipitation Study (COPS) domains. Data were stored daily on a common database (CERA–World Data Center for Climate) and published on a web-based Visualization Platform (VP).

The APAT (now ISPRA) contribution to DOP is presented here. An improved version of the 10-km, hydrostatic, atmospheric Quadrics BOlogna Limited Area Model (QBOLAM; Mariani *et al.*, 2005; Speranza *et al.*, 2004, 2007) has been run, operationally as well, during DOP. QBOLAM is operational at APAT since 2000 as a part of the Hydro-Meteo-Marine forecasting System ("Sistema Idro-Meteo-Mare", hereinafter SIMM; $http://www.apat.gov.it/pre\_meteo/$), on a domain covering the whole Mediterranean basin, implemented on a parallel platform. The improvement consists mainly in the implementation of a more accurate convection scheme, that is, the Kain and Fritsch (1990, 1993) convective parametrization scheme (hereinafter KF).

As an example of the results of this activity, the 23–25 November 2007 case study is simulated with both the two model versions. The impact of the cumulus convection scheme change on the rainfall forecast is evidenced. As a first attempt of verification, model results are qualitatively compared to the METEOSAT satellite images.

SIMM and its recent evolution

SIMM is an integrated meteo-marine forecasting system formed by a cascade of four numerical models, telescoping from the Mediterranean basin to the Venice Lagoon (Fig. 2.1). These are: QBOLAM; the wave model WAM over the whole Mediterranean Sea; a shallow-water version of the Princeton Ocean model (POM) for sea elevation forecast on the Adriatic Sea; and a finite-element version of the same model (VL-FEM) on the Venice Lagoon (aimed to forecast the "acqua alta" events). The system was designed primarily to achieve a suitable resolution (*i.e.*, 10 km grid step) on the entire Mediterranean area in order to resolve simultaneously the whole range of scales involved in the complex phenomenology of this region.

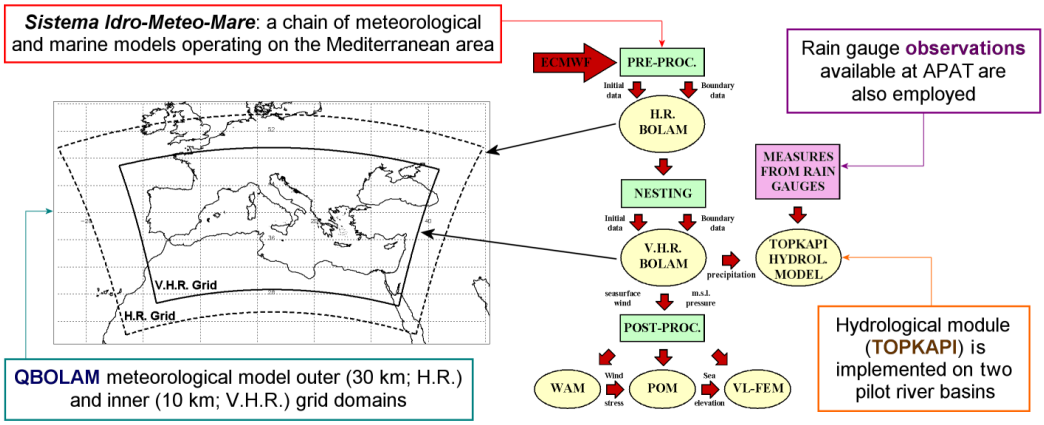

Figure 2.1: An outdraw of SIMM; QBOLAM inner and outer domains are also displayed.

QBOLAM is in turn a parallel version of the hydrostatic model BOLAM, developed at ISAC–CNR (Bologna, Italy), originally designed for the massively parallel supercomputer Quadrics. Initial and boundary conditions from ECMWF global model drive the model on the two nested domains shown in Fig. 2.1. Due to the Quadrics synchronous (SIMD) architecture, model code implementation was subject to severe constraints, especially concerning radiation and convection parametrization. Specifically, the simple Kuo (1974) convection scheme was used in place of the original, and more accurate KF.

Recent developments include porting the system on a new parallel platform (SGI ALTIX) and, on 2007, under the project WERMED of the INTERREG IIIB MEDOCC programme, the acquisition from ISAC–CNR of the up-to-date date serial BOLAM code. Parallelization of the updated code, to be completed during next year, also employing this project's results, will overcome the above-described lacks in parametrization schemes, and implement the recent code improvements, too. In the meanwhile, an intermediate BOLAM version – namely, the old QBOLAM with the KF scheme – has been parallelized on the ALTIX platform and used for research purposes. These include the creation of a multi-annual (2000–2006)

reforecasting database and the participation to the DOP activities.

As a first use, the reforecasting database was employed for objective verification of precipitation forecast improvement due to KF. In fact, QBOLAM forecast verification activity performed in APAT from 2000 (Accadia et al., 2005) evidenced as a critical point in the QBOLAM precipitation forecast the tendency to overpredict convection over the mountains on summer. So, two-years rainfall forecast series (Oct. 2000–Oct. 2002) from both the original (Kuo) and the reforecast (KF) series of the model have been verified over all Italy using categorical scores and skill scores, and the bootstrap method to provide confidence intervals to models' score differences (Mariani et al., 2007; Mariani 2008). Results show a significant increase of forecast quality using KF, with a dramatic decrease of the excessive categorical bias (BIAS) at the highest verification thresholds, and a correspondent, statistically significant increase in the equitable threat score (ETS). Such an improvement is comparatively more pronounced on the summer season, when QBOLAM displayed most of false alarms.

The APAT activity during DOP

Our work, needed to provide suitable, real-time QBOLAM products during the 6-month DOP, required the following steps:

1. Inserting a daily run of the intermediate code (the one using KF), after the operational one, in the system scheduling procedure.
2. Automatic launching of scripts for model output post-processing (selection of variables, cropping the D-PHASE and COPS domains, GRIB encoding, etc.).
3. Automatic launching of a script for the GRADS procedure which generate alerts and images (see an example in Fig. 2.2) and for the FTP-based upload on the CERA archive and VP (in collaboration with the D-PHASE providers).

Our contribution to the MAP D-PHASE allows a further verification of the intermediate QBOLAM with respect to the previous version. A case-study approach has been adopted, choosing the 22–25 November 2007 event. This was the most intense event occurred south of the Alps during DOP (Dr. Andrea Buzzi, *personal communication*). Results are presented in the following section.

Verification of QBOLAM on the 22–25 November 2007 case study

The event provided a test bed for verifying the improvement in the APAT model chain due to the implementation of the KF scheme. The forecast of this model version has been

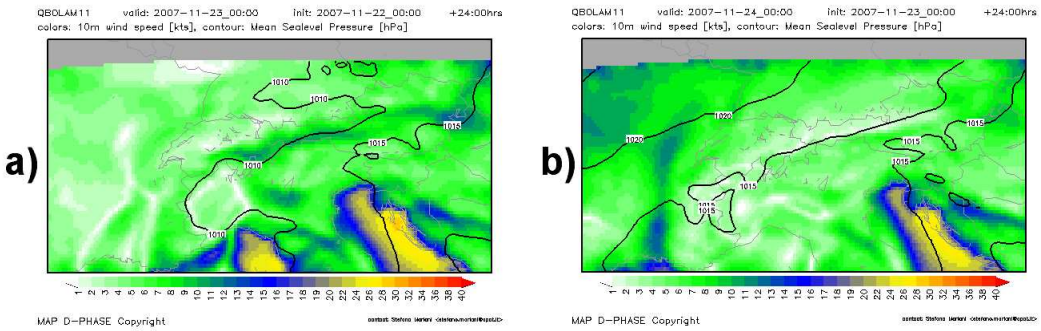

Figure 2.2: Example of QBOLAM plot displayed into the D-PHASE VP: mean sea-level pressure and 10m wind forecast for a) Nov. 23, 0000 UTC; b) Nov. 24, 0000 UTC.

subjectively intercompared with the forecast of the older version, with respect to the 24h-accumulated precipitation analysis. Further verification will be the object of future work.

From 21 to 25 November 2007, an elongated upper-level trough moved slowly above western Europe, while a high was stationary on the Balkans. While south-westerly advection over the Alps was present aloft, several shallow lows developed on the western Mediterranean (Figs. 2.3a and 2.3c), then being slowly advected eastwards (Figs. 2.3b and 2.3d). Intense rain hit northern Italy on days 22–24 November. Many synoptic and sub-synoptic features depicted on the maps are recognizable onto water vapor (WV) satellite images (Figs. 2.3c and 2.3d), along with precipitating clouds: see, in particular, organized convection over the Genoa Gulf in Fig. 2.3d.

Rain-gauge observations over northern Italy (courtesy of the Italian regional and autonomous province environmental agencies of Valle d'Aosta, Liguria, Lombardia, Piemonte, Emilia-Romagna, Friuli-Venezia Giulia, Veneto, Marche, Trento, and Bolzano) have been employed for subjective quantitative precipitation forecast verification. Gridded analyses (Figs. 2.4a and 2.4b) are obtained through a two-pass Barnes (1964) algorithm (no-data areas are blank in figure).

Despite the lack of observation over the sea prevents us to verify most of the predicted rainfall field, subjective verification evidences that both the model versions are able to reproduce the gross structure of the event (Fig. 2.4 refers only to days 24 and 25 Nov.). However, shifting in local structures is visible, and several rainfall peaks are underestimated or overestimated.

Anyway, the QBOLAM version using KF (hereinafter KF forecast) seems more able to catch these features than the QBOLAM version using Kuo (hereinafter Kuo forecast). For instance, on day 23 both QBOLAM versions underestimate rainfall maxima observed in the eastern (Liguria) and southern (eastern Alps) part of the rainy area (Fig. 2.4a), whereas precipitation is overestimated in the center of the rainy zone. Actually, the KF forecast (Fig. 2.4c) predicts more rainfall than the Kuo one (Fig. 2.4e) over Liguria and the eastern Alps. Something

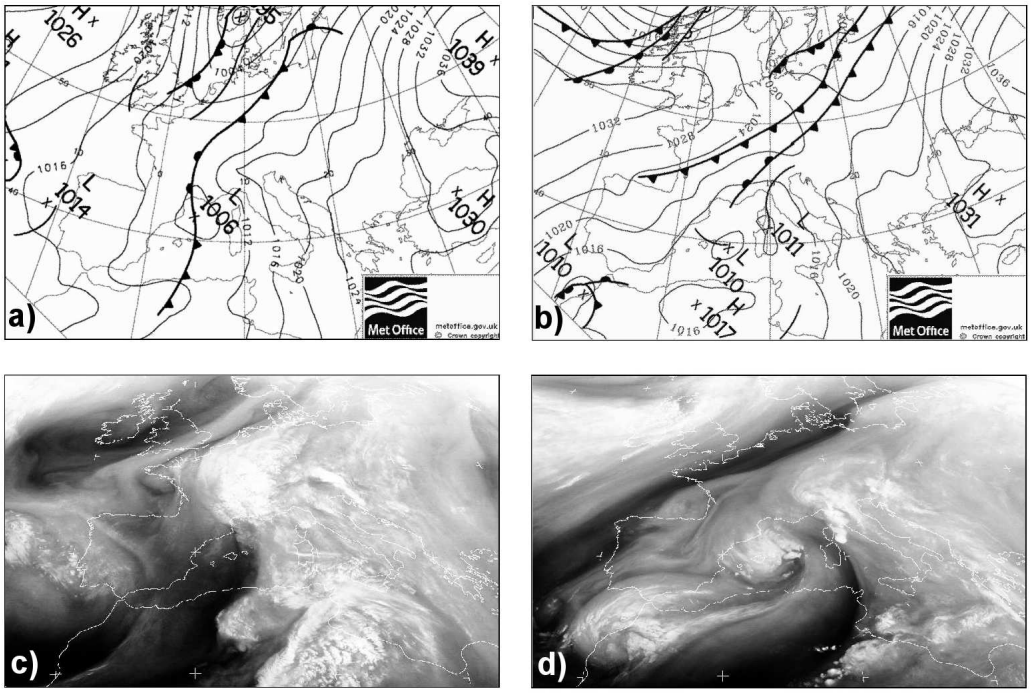

Figure 2.3: The November 2007 event. Surface charts at 0000 UTC for a) 23 Nov.; b) 24 Nov. (courtesy of the UK Met Office). METEOSAT–8 channel 5 (WV) images at 0000 UTC for: c) 23 Nov.; d) 24 Nov. (courtesy of EUMETSAT).

similar happens on day 24 November. Also in this case, rainfall peaks are predicted over the south-western and the north-eastern edges of the observed rain band (Fig. 2.4b). On those areas, the KF forecast (Fig. 2.4f) appears more in agreement with the observations than the Kuo one (Fig. 2.4d). On the contrary, the long rain band predicted by both the models along 9° latitude seems not to be present in the observations, although such an assessment is questionable due to the absence of observations over the Ligurian Sea (actually, it could be associated with the cloud system visible over the same area in Fig. 2.3d).

Summary and Outlook

The APAT activity during DOP gives an opportunity to evaluate the forecast improvement due to the implementation of the Kain-Fritsch convection scheme in the QBOLAM model, in place of the previously-used Kuo scheme. First qualitative results, presented here, suggest an increased ability in predicting rainfall location and intensity. Not surprisingly, the choice of the convection scheme does not affect the ability in predicting structures on a larger scale (*e.g.*, the occurrence of a rain band); rather, it affects the rainfall distribution inside such structures (*e.g.*, shift or underestimation of rainfall peaks).

These results are encouraging in view of the implementation, on a parallel platform, of the

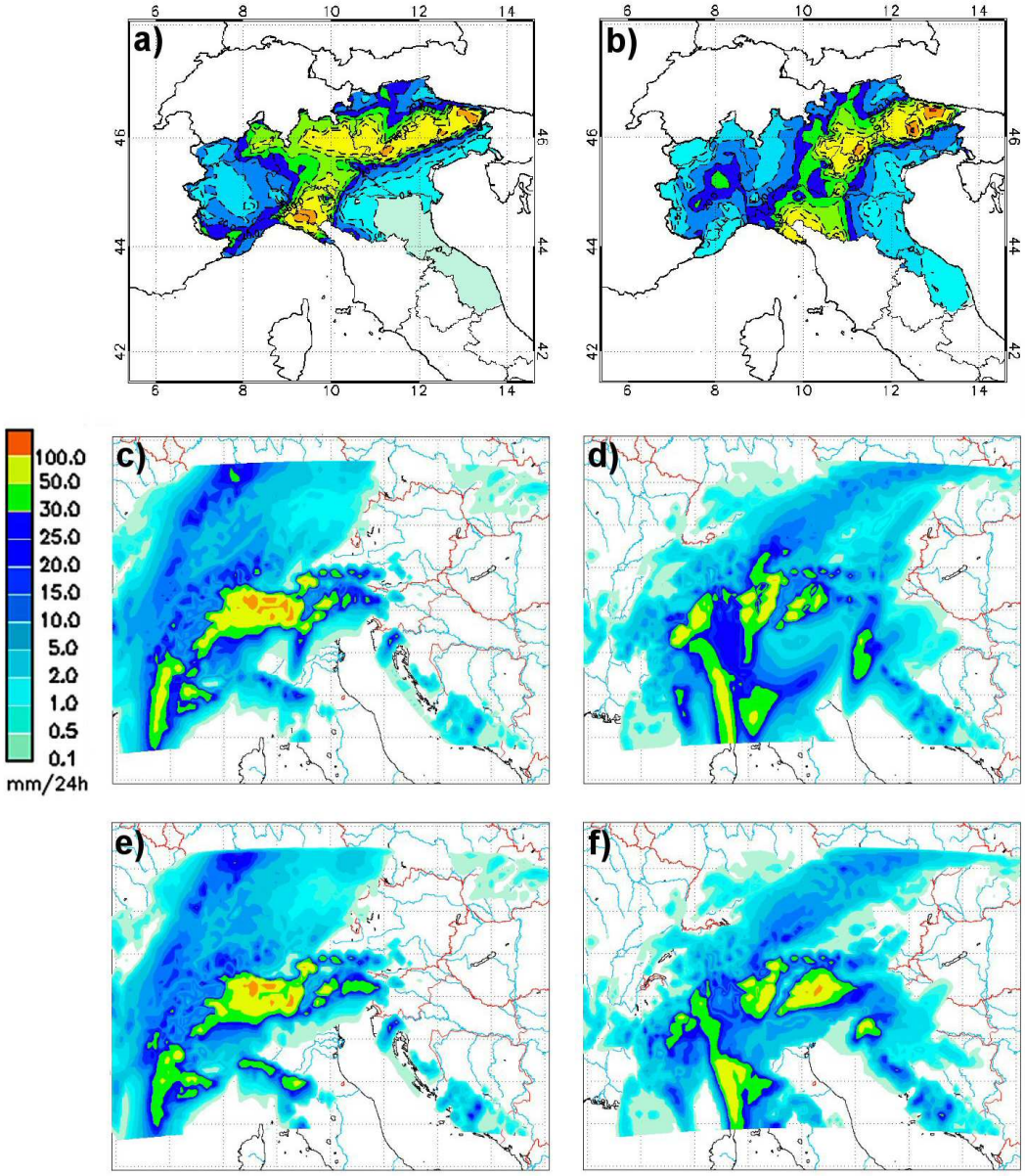

Figure 2.4: Subjective verification of the 22–25 November 2007 event. Left and right column display 24-h accumulated precipitation on 23 November and 24 November, respectively. a) and b): rain gauge analysis; c) and d) QBOLAM–Kuo forecast; e) and f): QBOLAM–KF forecast.

fully updated BOLAM version (to be performed during 2009). By the way, this verification work has been quite useful in order to design the SIMM upgrade, and to plan the related activity. The completion of the verification of the intermediate QBOLAM version, into the D-PHASE framework, will constitute a basis for future verification of the upcoming forecasting system.

References

Accadia, C., S. Mariani, M. Casaioli, A. Lavagnini and A. Speranza, 2005: Verification of Precipitation Forecasts from two Limited Area Models over Italy and comparison with ECMWF Forecasts using a Resampling Technique. Wea. Forecasting, 20, 276–300.

Barnes, S. L., 1964: A technique for maximizing details in numerical weather map analysis. J. Appl. Meteor., 3, 396–409.

Kain, J. S. and J. M. Fritsch, 1993: Convective parameterization for mesoscale models: The Kain-Fritsch scheme. In The Representation of Cumulus Convection in Numerical Models, edited by American Meteorological Society (AMS), Boston, USA, 165–70.

Kain, J. S. and J. M. Fritsch, 1990: A one-dimensional entraining/detraining plume model and its application in convective parameterization. J. Atmos. Sci., 47, 2784–2802.

Kuo, H. L., 1974: Further studies of the parameterization of the influence of cumulus convection on large scale flow. J. Atmos. Sci., 31, 1232–1240.

Mariani, S., 2008: Methodologies in Research and Operational Contexts for Numerical Precipitation Forecast Verification, Ph.D. Thesis, University of Ferrara.

Mariani, S., M. Casaioli, C. Accadia, M. C. Llasat, F. Pasi, S. Davolio, M. Elementi, G. Ficca and R. Romero, 2005: A limited area model intercomparison on the "Montserrat-2000" flash-flood event using statistical and deterministic methods. Nat. Hazards Earth Sys. Sci., 5, 565–581.

Mariani, S., M. Casaioli, C. Accadia, A. Lanciani, N. Tartaglione, A. Speranza and G. Monacelli, 2007: A two-year verification study over italy using reforecast data of the QBOLAM limited area model in the frame of the HYDROCARE project, oral presentation at the 7$^{\text{th}}$ European Meteorological Society Annual Meeting, San Lorenzo de El Escorial, Spain.

Speranza, A., C. Accadia, M. Casaioli, S. Mariani, G. Monacelli, R. Inghilesi, N. Tartaglione, P. M. Ruti, A. Carillo, A. Bargagli, G. Pisacane, F. Valentinotti and A. Lavagnini, 2004: POSEIDON: An integrated system for analysis and forecast of hydrological, meteorological and surface marine fields in the Mediterranean area, Il Nuovo Cimento, 27C(4), 329–345.

Speranza, A., C. Accadia, S. Mariani, M. Casaioli, N. Tartaglione, G. Monacelli, P. M. Ruti and A. Lavagnini, 2007: SIMM: An integrated forecasting system for the Mediterranean Area. Meteorol. Appl., 14, 337–350.

2.8 The flood event near Venice of 26 September 2007: results of simulations using MM5 and WRF high resolution models

D. Mastrangelo[(1)], M. M. Miglietta[(2)], A. Buzzi[(3)]

[(1)] *Department of Environmental Sciences, Parthenope University of Naples,*
[(2)] *ISAC-CNR, Padova, Lecce,*
[(3)] *ISAC-CNR, Bologna*

Introduction

The forecasting of moist convection, especially when associated with heavy precipitation events, is a major challenge for current numerical weather prediction models. The correct reproduction of the different processes involved in moist convection, occurring on different scales, and of their complex mutual interactions, is a difficult task for limited area models. Moreover, errors in the initial conditions, associated with large-scale features, may negatively affect the smaller scales and increase the precipitation forecast uncertainties. The growing computing power and the improvements in model formulation have recently allowed to increase the horizontal resolution of numerical models: the explicit reproduction of the processes associated with deep convection and the finest resolution of the modelled orography can produce positive impacts on the precipitation forecast. In this context, the objective of the present study is to evaluate the performance of two convection-resolving models in forecasting a mesoscale convective system (MCS) occurred over the flat area close to the Venice Lagoon on 26 September 2007 and to give a first insight into the main mesoscale features responsible for the occurrence of heavy rain.

The event and numerical experiments

During the morning of 26 September 2007, a deep mesoscale convective system affected the western side of the Venice Lagoon. More than 320 mm of precipitation were recorded in a 12-hour period, with a peak of almost 250 mm in 3 hours. Precipitations were initially caused by scattered convective cells and subsequently by the organized convection related to the MCS that produced the most intense rainy spell from about 05 to 09 UTC. The resulting precipitation pattern was oriented from SW to NE (Fig. 2.1a).

The severe convective event was associated with a lee cyclogenesis occurring over the Ligurian Sea. The related low-level cyclonic circulation induced a moist and unstable south-easterly flow that entered the area of interest from the Adriatic Sea. The convergence between the

unstable flow and the weaker north-easterly flow inland favoured the triggering of convective activity (Fig. 2.1b).

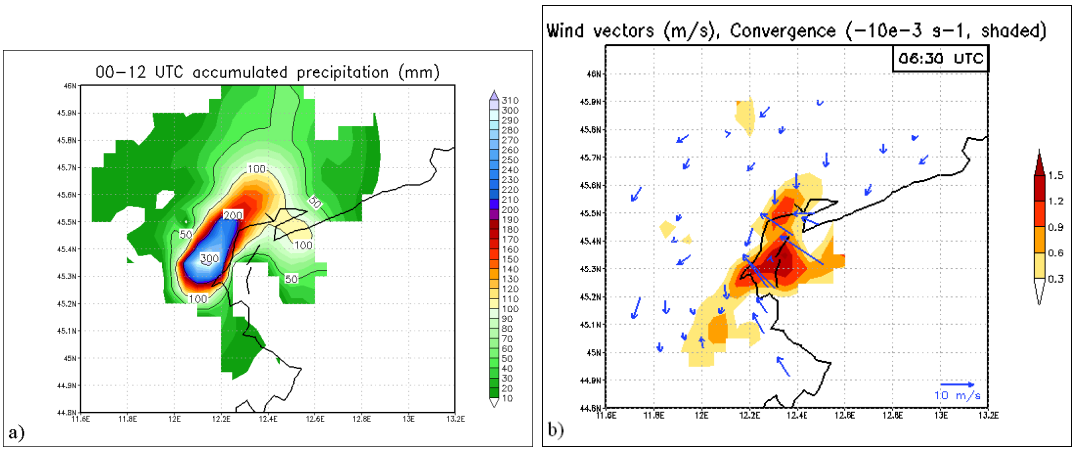

Figure 2.1: (a) 12-h period accumulated precipitation at 12 UTC of 26 September 2007; (b) observed surface wind vectors and wind field convergence (shaded, -10^{-3} s^{-1}) at 06:30 UTC, during the most intense precipitation period.

We used the WRF model (Skamarock et al., 2005) and the PSU-NCAR MM5 model (Grell et al. 1995) to produce high-resolution simulations of the event. The WRF setup includes 2 two-way nested domains and 30 vertical levels while 3 two-way nested domains and 27 vertical levels were used in MM5 runs. Different global forecast data (NCEP-GFS, ECMWF) were used as initial and boundary conditions, and different convective schemes (Grell, 1993, and Kain-Fritsch, 1990, 2004) were activated in the lower-resolution domains. In this way a multi-model multi-analysis modelling scheme was developed to test the predictability of the event. Further details on the different simulations are shown in Table 1.

Experiment name	Model	IC-BC	Grid spacing (Km)	nX x nY of inner domain	Cumulus scheme
W_ECMWF25	WRF	ECMWF Fc 00 UTC 25	16 - 4	185 x 185	Kain-Fritsch
W_GFS26	WRF	GFS Fc 00 UTC 26			Kain-Fritsch
W_GFS25	WRF	GFS Fc 00 UTC 25			Kain-Fritsch
W_GFS25Gr	WRF	GFS Fc 00 UTC 25			Grell
M_GFS25	MM5	GFS Fc 00 UTC 25	22.5 - 7.5 - 2.5	112 x 112	Kain-Fritsch
M_GFS25Gr	MM5	GFS Fc 00 UTC 25			Grell

Table 1: summary of numerical experiments and model set up. The Kain-Fritsch scheme used in WRF runs is described in Kain (2004); the Kain-Fritsch scheme used in MM5 runs is described in Kain-Fritsch (1990).

Results

The 12-h accumulated precipitation, simulated from 00 to 12 UTC of 26 September in the different runs, is shown in Fig. 2.2.

Among the simulations initialized with 00 UTC 25 September GFS forecast (GFS25), only

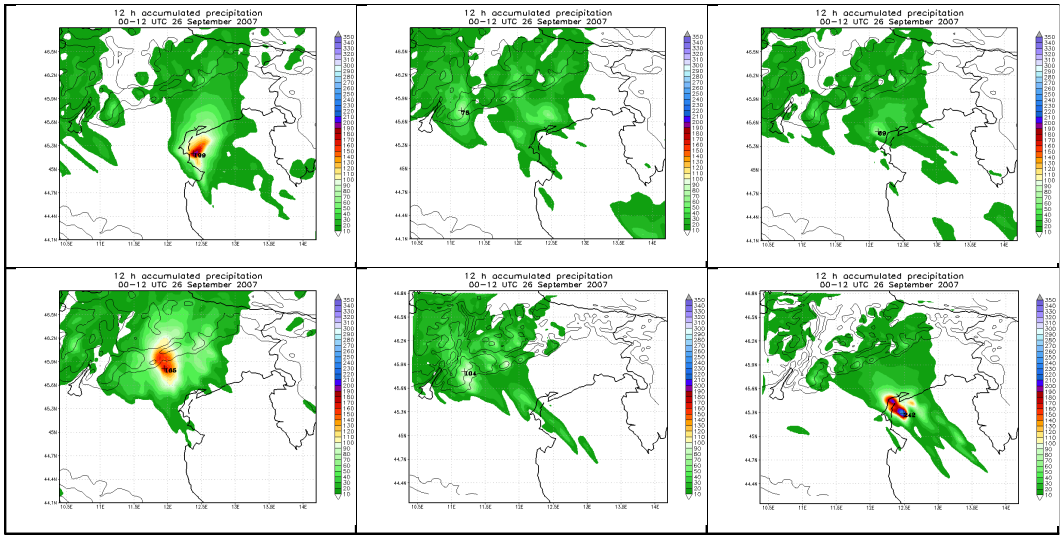

Figure 2.2: 12 hour accumulated simulated precipitation at 12 UTC of 26 September. First row, left to right: W_ECMWF25, W_GFS25Gr and W_GFS25 experiment; second row, left to right: W_GFS26, M_GFS25, M_GFS25Gr experiment. WRF outputs are plotted over a zoomed area of the inner domain.

M_GFS25_Gr was able to predict realistically large rainfall amounts. Also, the maximum rainfall simulated in M_GFS25_Gr is located next to the area actually affected with precipitation, but the pattern is oriented from SE-NW, thus with a different orientation compared with the observations (Fig.2.2d vs. Fig. 2.1). The M_GFS25 experiment misses most of the observed precipitation: maxima of about 100 mm are reproduced downstream, on the pre-alpine area. The WRF experiments initialized with GFS25 are characterized by a strong underestimation of the precipitation, independently of the implemented convective scheme. The precipitation maximum computed in the W_GFS26 run, even if more intense than the W_GFS25 maximum, is predicted over the pre-alpine region, therefore with a large location error. The best prediction in terms of pattern orientation, timing and location is reproduced in the WRF run using ECMWF forecasts starting at 00 UTC, 25 September: in fact, the areas affected by the largest amount of precipitation show a pattern similar to the observations. The maximum is located a few tenths of km to the south of the area actually affected by the most intense precipitation. The overall precipitation pattern is oriented from S to N, thus much closer to the observed patterns than all the other runs, suggesting a more correct representation of the mid-tropospheric currents. The analysis of the simulations reveals that a major mesoscale feature related to the triggering and maintenance of convection was the confluence of the low-level south-easterly flow, associated with the orographic cyclone over the Ligurian Sea, with north-easterly flow. Differences in this feature significantly impact the simulated precipitation. The comparison between Fig. 2.2a and Fig. 2.3a shows that the precipitation simulated in the most realistic run (W_ECMWF25) is associated with low-level convergence of the south-easterly unstable flow with weaker winds inland. Such a feature is not reproduced by the W_GFS26 experiment (Fig. 2.3b): the south-easterly flow impinges directly on the pre-alpine area where most of the precipitation is simulated (Fig. 2.2d). In

order to better understand the characteristics of the air converging with the southerly flow, we estimated the value of the unsaturated Froude number Fr=hN/U (where h is the mountain height, N the Brunt-Vaisala frequency, U the environmental wind speed), at 00 UTC of 26 September, in the lower 1.5 Km layer above the region the flow comes from. As the wind above the ground is prevalently from the east-northeast, we calculate the Froude number based on the section of the mountain crossed by this flow component. The resulting value of Fr 2 indicates the occurrence of a "flow-around" regime (Miglietta and Buzzi, 2001): the easterly wind over Friuli, before the beginning of the convective event, was deviated by the orographic barrier to the left and the southern side of the jet converges with the south-easterly wind over the Venice lagoon.

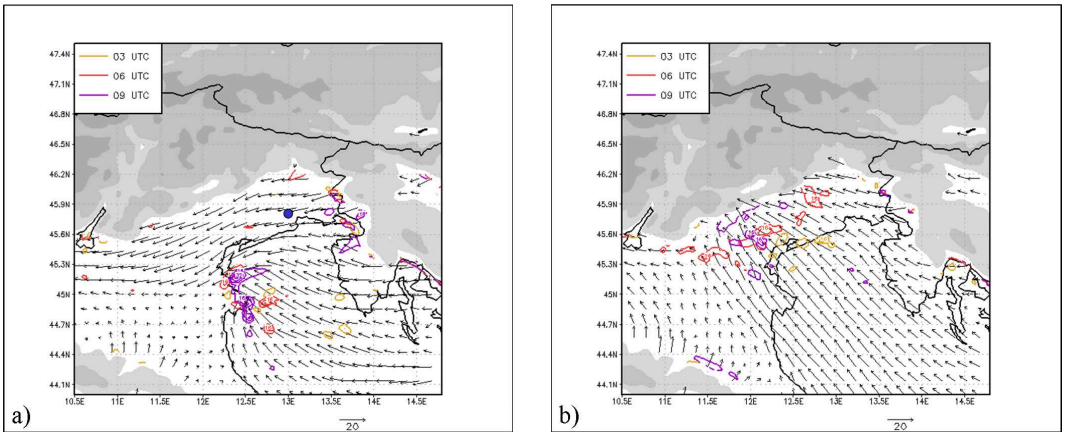

Figure 2.3: 950 hPa wind (vectors) at 09 UTC and 950 hPa wind convergence (contour interval $[8 \cdot (-10)^{-4}]$ s^{-1}) at 03, 06, 09 UTC for (a) W_ECMWF25 and (b) W_GFS26 experiments. The blue dot in (a) indicates the location where the Froude number has been evaluated.

Summary

Several runs have been performed using the MM5 and WRF convection-resolving models to reproduce a flood event occurred over a flat coastal area on 26 September 2007. A general delay and underestimation in most of the model simulations have been found. The simulated quantitative precipitation fields showed strong sensitivity to the different forecast data used as initial and boundary conditions and to the convective parameterisation schemes active on the lower resolution domains. Using similar setups, simulated precipitation depends on the used model as well. Initialization data had the most relevant impact on WRF simulations, with the most realistic run obtained using ECMWF global forecasts starting the day before the event (00UTC, 25 September). Using the same initial conditions (GFS25), a weak sensitivity to the convective scheme has been found in WRF simulations, while the MM5 model showed a stronger sensitivity. The analysis of the most realistic run indicates that important differences in precipitation location and amount are related to the simulation of the mesoscale flow convergence between the low-level flow driven by a large scale minimum

over Liguria and a north-easterly flow that was deviated by the Alpine chain. The fact that the large-scale dynamics controlled to some extent the mesoscale event favoured the predictability of its evolution. Further investigation will be performed to deeply assess the respective influence of initialization data and convective schemes.

Acknowledgements

The authors are grateful to ARPA Veneto, Comune di Venezia, ISMAR-CNR for having provided observational data.

References

Grell, G. A., 1993: Prognostic evaluation of assumptions used by cumulus parameterization. Mon. Wea. Rev., 121, 764787.

Grell, G., J. Dudhia and D. Stauffer, 1995: A Description of the Fifth-Generation Penn State/NCAR Mesoscale Model (MM5). NCAR Tech Notes 398+STR, NCAR, Boulder/CO.

Kain, J. S.: The Kain-Fritsch convective parameterization: an update, J. Appl. Meteorol., 43, 170181, 2004.

Kain, J. S., and J. M. Fritsch, 1990: A one-dimensional entraining/detraining plume model and its application in convective parameterization. J. Atmos. Sci., 47, 27842802.

M.M. Miglietta, A. Buzzi, 2001: A numerical study of moist stratified flows over isolated topography, Tellus, 53A, 481-499, DOI: 10.1111/j.1600-0870.2001.00481.x.

Skamarock, W. C., Klemp, J. B., Dudhia, J., Gill, D. O., Barker, D. M., Wang W., and Powers, J. G.: A description of the Advanced Research WRF Version 2. NCAR Tech. Note 468STR, 88 pp., 2005.

3.1 A multi-method approach for quantitative precipitation forecast verification within the MAP D-PHASE project

Stefano Mariani[(1)], Alexandre Lanciani[(1)], Marco Casaioli[(1)], Christophe Accadia[(2)] and Nazario Tartaglione[(3,4)]

[(1)] *National Agency for Environmental Protection and Technical Services (APAT), now Institute for Environmental Protection and Research (ISPRA), Rome, Italy*
[(2)] *European Organisation for the Exploitation of Meteorological Satellites (EUMETSAT), Darmstadt, Germany*
[(3)] *Department of Physics, University of Camerino, Camerino, Italy*
[(4)] *Meteorology and Climate Centre, School of Mathematical Sciences, University College Dublin, Dublin, Ireland*

Introduction

In the framework of the Mesoscale Alpine Programme (MAP), a Forecast Demonstration Project (FDP) of the World Weather Research Programme (WWRP) of WMO, called "*Demonstration of Probabilistic Hydrological and Atmospheric Simulation of flood Events in the Alpine region*" (D-PHASE), has been launched aimed at demonstrating the benefits in forecasting heavy precipitation and related flooding events in the Alpine region using high-resolution numerical weather prediction (NWP) models, ensemble prediction systems (EPSs), atmospheric–hydrological coupled systems, and real-time nowcasting tools.

During the D-PHASE Operations Period (hereafter DOP), from June to November 20007, the participating institutions provided meteorological simulation over the D-PHASE and the Convective and Orographically-induced Precipitation Study (COPS[1]) domains and hydrological simulations over target river basins. Within the MAP D-PHASE Working Group Verification (WG VER), an intercomparison study of the precipitation fields forecast by several deterministic NWP models over the DOP period has been set-up and started at the beginning of 2008.

The northern Italian regions (Fig. 3.1a) have been considered as test bed for the implementation of a multi-method approach (see Mariani et al., 2008, Lanciani et al., 2008) based on multi-scale (power spectrum analysis), objective (skill scores and contiguous rain area analysis) and subjective methods. On the one hand, multi-scale methods are a methodological necessity since traditional skill scores, measuring point-to-point match, are sensitive to small displacement errors such as those due to the double penalty effect. Higher order moments should be studied to assess whether the fields to compare are defined on grids with the same

[1] A Research and Development Project (RDP) within the WMO WWRP Programme.

real resolution and whether they have the same amount of small-scale detail. On the other hand, objective techniques can provide a quantitative basis to subjective verification, which in turn can suggest physical interpretations to the objective verification findings.

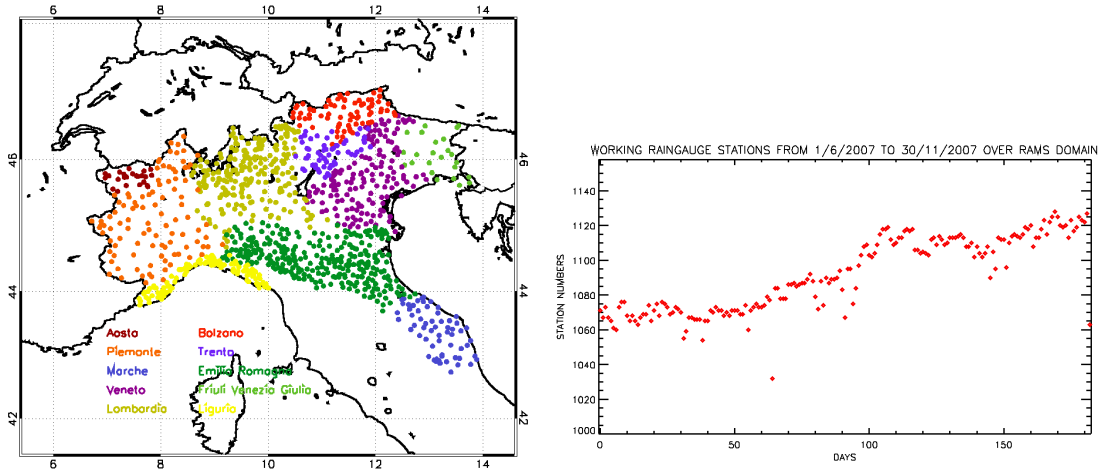

(a) Spatial distribution.

(b) Temporal distribution.

Figure 3.1: Spatial and temporal distribution of the rain gauges available during DOP over the Italian regions considered for the set-up of the multi-method approach. Rainfall data courtesy of the Italian Regional and Autonomous Provincial Environmental Agencies.

Moreover, skill score differences between "competing" models can be statistically assessed by means of a bootstrap-based hypothesis test. Finally, it has been considered the possibility to combine the different deterministic forecasts in order to provide a single multi-model forecast.

The paper is organized as follows. The problem of how to make forecasts and observations "comparable", that is, how to take into account the representativeness of the meteorological fields to be compared, is addressed in the following section. The subsequent section is devoted to the presentation of the methodologies employed for forecast verification multi-method approach. The exposition of this approach is supported by means of preliminary results over the test bed area. Finally, summary and outlook of the future studies, in particular the application of the multi-method approach over the entire D-PHASE domain, are reported in the last section.

Rain Gauges *vs.* NWP Forecasts: What Are We Actually Comparing?

Traditional surface weather instruments, such as rain gauges, provide the more accurate, although localized, estimate of the observed weather, usually referred to as the observational "truth". On the contrary, NWP forecasts should be instead considered, in general, as areal mean quantities (see, *e.g.*, Haltiner and Williams, 1980). Thus, when comparing a numerical

approximation of the atmosphere *vs.* a good estimation of the "true" weather state, we are actually comparing two different quantities. The representativeness of the fields compared – observations *vs.* a single forecast and/or observations *vs.* several "competing" forecasts – need to be addressed before applying any kind of verification.

Consequently, in order to have as much as possible a fair comparison (or intercomparison when verifying "competing" forecasts), it has been decided to make a selection of the NWP models[2] to be verified, and compared against to observations, among the ones available during DOP (see Table 3.1) and to "optimally interpolate" both observations and forecasts at the same scale. Moreover, as reported in Table 3.1, models have been subdivided in two quasi-homogeneous categories, namely the **Very High Resolution** (hereafter VHR), in which models have a grid horizontal spacing of about 2–3 km, and the **High Resolution** (hereafter HR), in which models have instead a grid spacing of about 7–10 km. Each one of these sub-groups can be also considered as a sort of "poor man's ensemble" group. Thus, according to the procedures presented by Ebert (2001), four deterministic ensemble forecasts can been obtained and considered in the verification study:

- AVE: the simple arithmetic ensemble forecast mean;
- MED: the ensemble median precipitation forecast;
- PAV: the probability matched forecast based on AVE;
- PMD: the probability matched forecast based on MED.

Table 3.1: List of the NWP models considered for the study, categorized with respect to the grid size of the native grid. Acronyms (and providers) as reported in the IP document.

Very High Resolution (grid size $\sim$ 2–3 km)	**High Resolution (grid size $\sim$ 7–10 km)**
	ALADAT (ZAMG)
AROME (Météo France)	ALADFR (Météo France)
COSMOCH2 (Meteo Swiss)	COSMOCH7 (Meteo Swiss)
LAMI28 (ARPA SIM)	LAMI7 (ARPA SIM)
LMK (DWD)	LME (DWD)
LMITA (CNMCA)	LMEURO (CNMCA)
ISACMOL2 (ISAC-CNR)	MESONH8 (Univ. Paul Sabatier)
	QBOLAM11 (APAT)

Therefore, for the quantitative precipitation forecast (QPF) verification, the VHR precipitation forecasts have been integrated from their native grids to two common verification grids of 0.05° and 0.1°, respectively; whereas the HR precipitation forecasts have been integrated

[2]The main characteristics of the NWP models analyzed here are summarized in the MAP D-PHASE Implementation Plan (IP) available online at
$http://www.map.meteoswiss.ch/map-doc/dphase/ip-export_v3.2_20070815.zip$.

from their native grids to three common verification grids of 0.1°, 0.3° and 0.5°, respectively. The transfer of the analyzed forecasts from native to verification grid has been performed by means of a simple nearest-neighbour average method, usually referred as remapping (Baldwin, 2000; Accadia et al., 2003). This post-processing procedure is applied as follows. First, each verification grid box is subdivided into n × n sub-boxes. Then, to each sub-grid point is assigned the value of the nearest native grid point. Finally, the average of these sub-grid point values produces the remapped value of the verification grid point.

Rainfall measurements collected within the project from the networks of the Italian Regional and Autonomous Provincial Environmental Agencies have been considered for the implementation of this multi-method approach procedure (see Fig. 3.1). A two-pass Barnes scheme (Barnes, 1964, 1973; Kock et al., 1983) has been used to produce the observational analyses for the DOP period over the four aforementioned verification grids (see, *e.g.*, Fig. 3.2). The

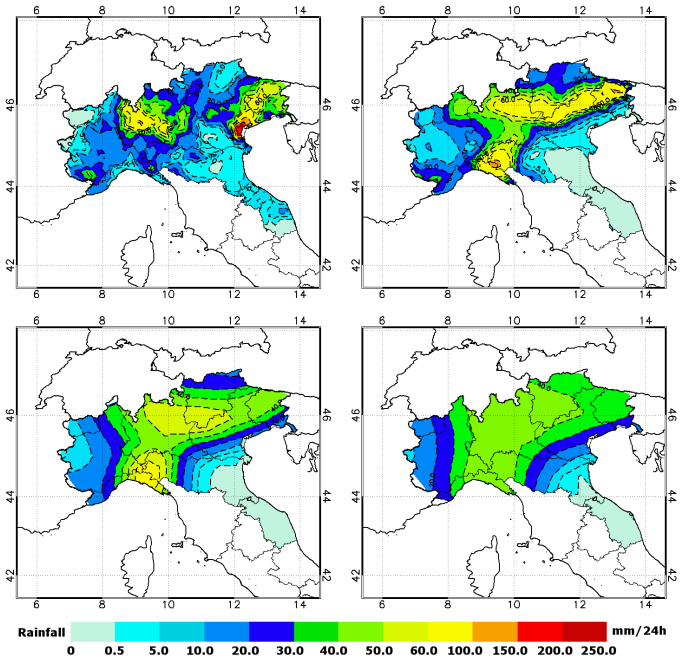

Figure 3.2: Contours, in mm $(24\text{h})^{-1}$, of the precipitation analyses on 23 November 2007 obtained by using the two-pass Barns procedure over the four verification grids: (a) 0.05° grid; (b) 0.1° grid; (c) 0.3° grid; (d) 0.5° grid.

Barnes scheme is a Gaussian weighted-averaging technique that produces a gridded observational analysis by assigning a weight to each rain gauge observation in x_k, averaged spaced Δn, as a function of the distance between the gauge and the grid box center x:

$$w_k = \exp\left[\frac{|x - x_k|^2}{4\kappa}\right], \tag{3.1}$$

where $\kappa \propto \Delta n^2$ is the shape parameter. By iterating the method, it is possible to restore the small details suppressed in the first application. The two-pass version employed here is a

modified version designed to rapidly and sufficiently achieve the convergence of the method by using for the second iteration a modified shape parameter $\kappa' = \gamma\kappa$, where $\gamma \in [0.2, 0.4]$. Then, the observational analyses are obtained as follows:

$$f_A^{(1)}(x) = f_A^{(0)}(x) + \sum_{k=1}^{K} w_k \left[f_0(x_k) - f_A^{(0)}(x_k) \right], \tag{3.2}$$

where $f_0(x_k)$ is the precipitation measured at the k-th gauge and $f_A^{(0)}(x) = \sum_k w_k f_0(x_k)$ is the first-guess precipitation analysis.

For the rainfall verification, 24-h accumulation has been chosen as the temporal scale. Thus, both the gridded observation fields and the remapped forecast fields have been accumulated on a daily basis, starting from 0000 UTC.

Methodologies

As anticipated in the introduction, the approach followed to study the NWP models in Table 3.1 is based on different methodologies, each one focusing on a particular aspect of the forecast performance. A subjective verification limited to particular events occurred during DOP (*e.g.*, 22–25 Nov. 2007) can be useful to provide a physical interpretation of the quantitative verification findings or, more in general, to give some hint about the performance of a particular model with respect to observations and the other models considered in the study. The eyeball comparison is usually employed for this task. However, simulations of satellite observed fields (METEOSAT-7 Water Vapour channel) can be also employed, for instance to check qualitatively the impact of initialization on model error growth.

Categorical scores and skill scores are primarily involved in the QPF objective verification. Verification is then based on a categorical dichotomous "yes/no" statement by considering whether the precipitation forecast exceeds or not a pre-defined threshold. The same kind of statement is also true for the rainfall observational analyses. The combination of paired forecast and observed events above or below the thresholds gives origin to the 2×2 contingency tables. Since different scores evaluate different aspects of the forecast performance, it should be preferable to applied more that one score in each verification study. Thus, comparison between BIAS, ETS, HK, FAR, etc. (Wilks, 1995 and references therein) can provide useful information on the models' performance over the DOP period (see Fig. 3.3). However, to discriminate statistically significant differences between scores of two "competing" models, an hypothesis test should be also applied. The bootstrap-based hypothesis test introduced by Hamill (1999) is applied here in order to assign confidence intervals to score differences.

In the present example, the AVE forecasts is compared to the ISACMOL2 forecasts. Results show that, for the lower thresholds, AVE overforecasts[3] the frequency of the yes observed.

[3]BIAS $>$ 1: it indicates that the considered model overestimates the frequency of the events above a

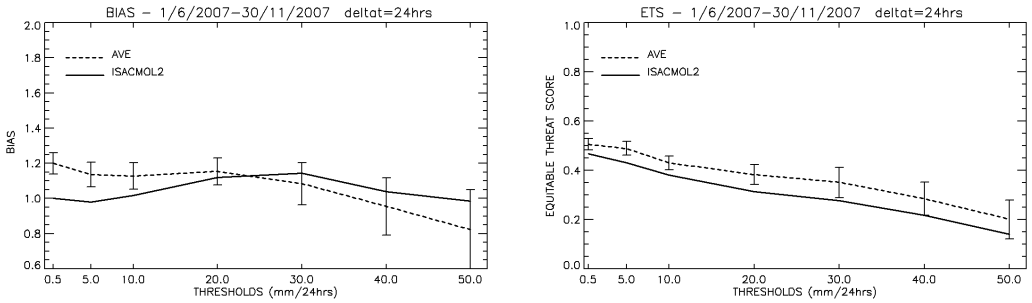

(a) BIAS. (b) ETS.

Figure 3.3: An example of the 24-h accumulation scores calculated for DOP over northern Italy for AVE and ISACMOL2 on the 0.05° grid. The bootstrap confidence intervals are referenced to AVE scores, indicating the 2.5^{th} and the 97.5^{th} percentiles of the resampled distributions.

The BIAS differences are also statistically significant for those thresholds, whereas differences are not statistically significant for the medium-high thresholds. The ETS values are quite close to each other, nevertheless, differences are statistically significant for all thresholds. To assess whether the differences in skill scores between two competing models ("competitor" & "reference") are the result of an actual different forecast capability, the BIA adjustment method (Hamill, 1999) is employed. The method is based on the introduction of a different threshold for the forecasts[4] in order to get similar BIA values for the two competing models. However, the BIA adjustment method does not remove the ambiguity that may still exist in model intercomparison. In other word, how to consider the structure of the fields compared?

In fact, since the score calculation is sensitive to small displacement errors, higher order moments (power spectrum analysis) must be studied to evaluate whether the fields being compared are defined on grids with the same resolution and whether they have the same amount of small scale detail (see, *e.g.*, Lanciani et al., 2008). Moreover, attention should be given to spatial forecast error, as well. A correct simulated event, misplaced with respect to observations, is penalized twice in terms of skill scores: once for missing the event in the correct position, and once for producing a false alarm where the event is not observed (the double penalty effect). Thus, the contiguous rain area analysis (CRA; Ebert and McBride, 2000) can be employed to evaluate the magnitude of the displacement error (and of its component sources, *e.g.*, volume, pattern and displacement errors). This object-oriented technique quantify the displacement (in terms of grid points, and consequently, in terms of km) by translating in latitude and longitude (until a maximum number of grid points – shifting value *sv*) the forecast rainfall entity (a precipitation area delimited by a chosen

threshold. The models could have too many false alarms, so that related skill scores could be negatively affected compared with those related to a model with a lower BIAS. Relative high differences in the BIA measure among competing models may result in an erroneous or ambiguous evaluation of the score differences.

[4]To have the competitor BIA similar to the reference BIA, the competitor contingency tables are recalculated by adjusting the forecast precipitation threshold, while keeping the observation threshold unchanged.

isohyet) over the observed entity, until a best-match criterion is satisfied. Patter-matching can be obtained, for instance, by minimizing the MSE or maximizing the correlation between the forecast and the observed areas. To diagnose systematic spatial forecast errors (see, *e.g.*, Tartaglione et al., 2008), the CRA analysis should be used on the entire DOP period. By repeating the CRA analysis over a set of N events, and giving $ns(i,j)$ the number of times in which the gridded forecast entity need to be shifted i-grid points eastward and j-grid points northward, it is possible to calculate the CRA mean shift (CSM) as:

$$CSM = \sum_{i=-sv}^{sv} \sum_{i=-sv}^{sv} F_{i,j} w_{i,j}, \tag{3.3}$$

where $F_{i,j} = ns(i,j)/N$ is the frequency associated to the shift in (i,j) and $w_{i,j} = \sqrt{i^2 + j^2}$ is the weight that measures the distance between the position (i,j) and the no-shift (*i.e.*, forecast correctly simulated in space) position (0, 0).

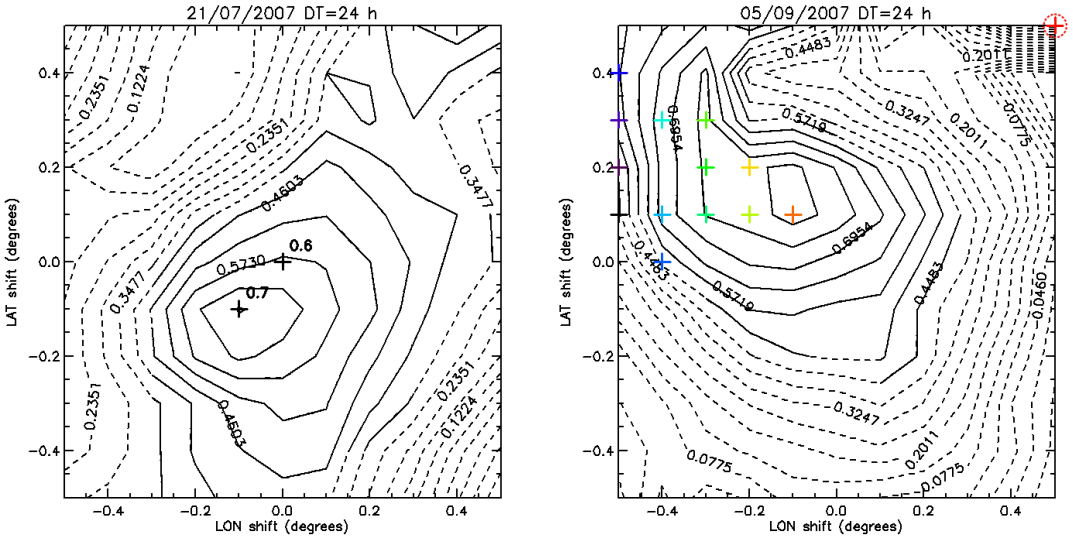

(a) 21 July 2007.

(b) 05 September 2007.

Figure 3.4: The 2-D shift analysis, maximizing correlation, of CRA between the 0.1° QBOLAM11 forecast and the precipitation analysis, using an isohyet equal to 0.5 mm $(24\text{h})^{-1}$. Solid lines indicate statistically significant shifts, whereas dashed lines indicate statistically nonsignificant shifts. On panel (b), maximum values found during CRA are indicated with a cross symbol. The colorscale, from black to red, indicates the progressive order in which these values are found. The suspicious final shift is indicated with a red dashed circle.

Two examples of CRA applied on QBOLAM11 forecasts are reported in Fig. 3.4. As shown in panel (b), quality tests can be also applied to verify whether the best-match found is obtained by chance (*i.e.*, it is not reliable) or it is the result of a reasonable physical match. For the event analyzed, the suspicious final shift in the top-right corner of the 2-D CRA analysis is a localized isolated correlation maximum, whereas the relative second maximum, located in the middle-up left side of the 2-D analysis, is a more robust result.

Summary and Outlook

The present document shows an overview of the multi-method approach implemented within WG VER in order to allow a complex characterization of the forecasts' performance of the NWP models provided during DOP. The approach has been initially applied on a test bed area, the northern Italy, but it is ongoing its application over a wider area, within the D-PHASE domain, selected by taking into account the intersection of the domains of all the models in Table 3.1. First results over this area are foreseen for the beginning of 2009.

References

Accadia, C., S. Mariani, M. Casaioli, A. Lavagnini and A. Speranza, 2003: Sensitivity of precipitation forecast skill scores to bilinear interpolation and a simple nearest-neighbor average method on high-resolution verification grids. Wea. Forecasting, 18, 918–932.

Baldwin, M. E., 2000: Quantitative Precipitation Forecast Verification Documentation. Available online at
http://wwwt.emc.ncep.noaa.gov/mmb/ylin/pcpverif/scores/docs/mbdoc/pptmethod.html.

Barnes, S. L., 1964: A technique for maximizing details in numerical weather map analysis. J. Appl. Meteor., 3, 396–409.

Barnes, S. L., 1973: Mesoscale objective analysis using weighted time-series observations. NOAA Tech. Memo. ERL NSSL–62, National Severe Storm Laboratory, Norman, OK, 60 pp. [NTIS COM–73–10781.]

Ebert, E. E., 2001: Ability of a Poor Man's Ensemble to predict the probability and distribution of precipitation. Mon. Wea. Rev., 129, 2461–2480.

Ebert, E. E. and J. L. McBride, 2000: Verification of precipitation in weather systems: Determination of systematic errors. J. Hydrol., 239, 179–202.

Haltiner, G. J. and R. T. Williams, 1980: Numerical Prediction and Dynamic Meteorology. John Wiley & Sons, New York (USA).

Hamill, T. M., 1999: Hypothesis tests for evaluating numerical precipitation forecasts. Wea. Forecasting, 14, 155–167.

Koch, S. E., M. desJardins and P. J. Kocin, 1983: An interactive Barnes objective map analysis scheme for use with satellite and conventional data. J. Climate Appl. Meteor., 22, 1487–1503.

Lanciani, A., S. Mariani, M. Casaioli, C. Accadia and N. Tartaglione, 2008: A multiscale approach for precipitation verification applied to the FORALPS case studies. Adv. Geosci., 16, 3–9.

Mariani, S., M. Casaioli, A. Lanciani, N. Tartaglione and C. Accadia, 2008: A Multi-method intercomparison approach for precipitation fields modelled by LAMs in the Alpine Area: Two FORALPS case studies. Meteor. Atmos. Phys., in press.

Tartaglione, N., S. Mariani, C. Accadia, S. Chr. Michaelides and M. Casaioli, 2008: Objective verification of spatial precipitation forecasts. In Precipitation: Advances in Measurement, Estimation and Prediction, Springer-Verlag, New York (USA), pp. 453–472.

Wilks, D. S., 1995: Statistical methods in the atmospheric sciences: An introduction. Academic Press, San Diego (USA).

3.2 Feature-based verification of deterministic precipitation forecasts with SAL during COPS

Matthias Zimmer[1] *, Heini Wernli[1], Christoph Frei[2] and Martin Hagen[3]

1) Institute for Atmospheric Physics, University of Mainz
2) Federal Office of Meteorology and Climatology, MeteoSwiss Zürich
3) Institute for Atmospheric Physics, DLR Oberpfaffenhofen

Introduction

Verification is a central aspect of quantitative precipitation forecasts (QPFs) to assess their shortcomings and problems. The MAP D-PHASE dataset offers a unique opportunity to investigate the QPF performance of different deterministic regional numerical weather prediction (NWP) models. Due to the complex nature of precipitation fields the verification of QPFs is very challenging. Also for current high-resolution NWP models, including models without parameterization of deep convection, it is difficult to accurately capture observed convective rainfall events in time and space. When using classical grid-point based verification measures, errors in the timing and/or location of the events lead to the so-called "double penalty" problem. In order to measure the skill of QPFs in a more reasonable way, a feature-based or fuzzy verification technique is required. (See *Casati et al. (2008)* for a review of recently proposed verification approaches.) One of the newly developed QPF quality measures, referred to as SAL *(Wernli et al. 2008)*, will be used in the present study.
The goal of this study is to reveal the differences in the QPF performance of various NWP models that, among other factors differ in terms of horizontal resolution, treatment of deep convection and the influence of assimilated data. QPFs are taken from the MAP D-PHASE dataset during Summer 2007, when the COPS (Convective and Orographically-induced Precipitation Study) field experiment took place (*Wulfmeyer et al. 2008*). The area of interest is the German Part of the COPS region (see Fig. 3.1).

Data and methods

(a) Observations and model data

The observational precipitation field was obtained from about 150 rain gauges in the COPS Germany region, provided by the German Weather Service. These daily accumulated station values were transformed to a grid with a horizontal resolution of 7 km, using the gridding

*zimmerm@uni-mainz.de

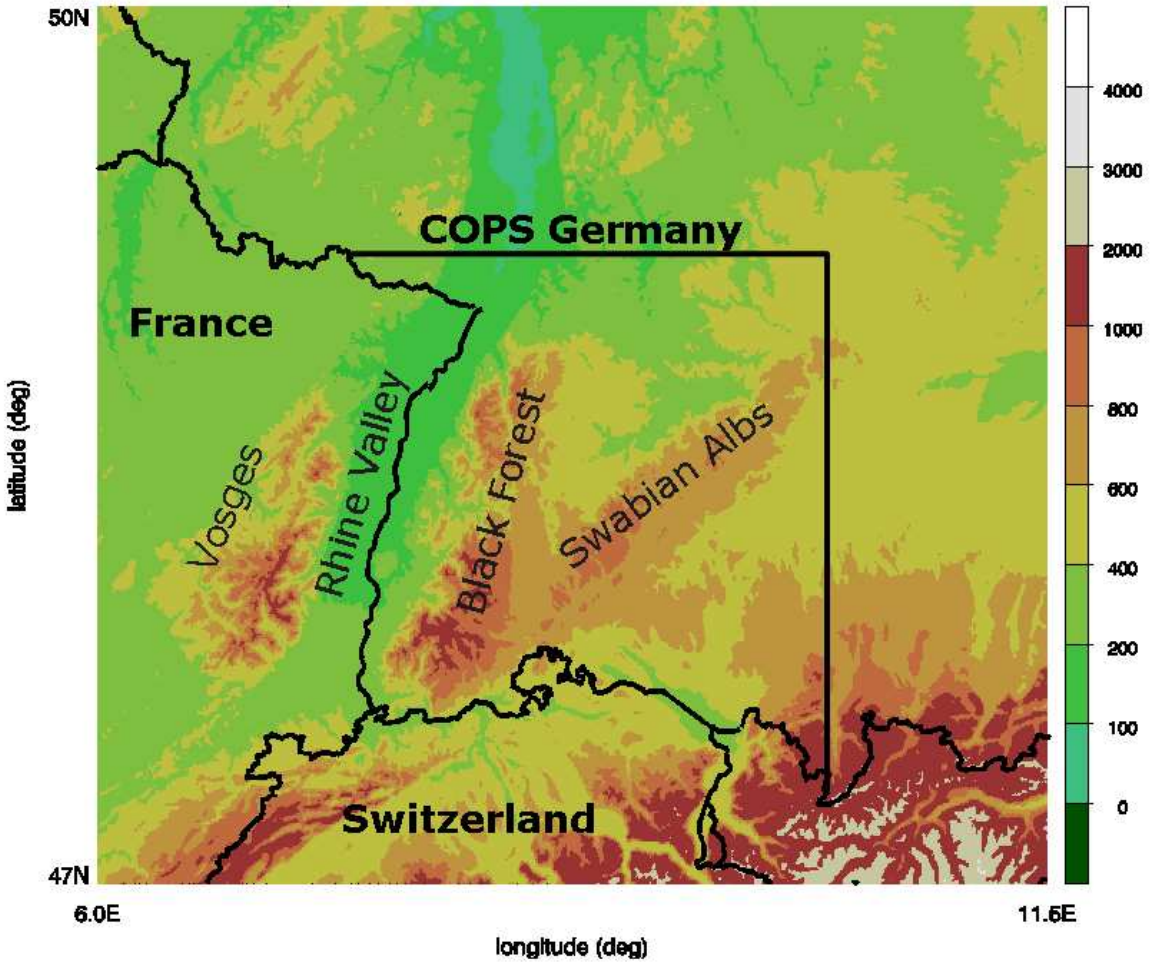

Figure 3.1: Topography of the German part of the COPS region (referred to as "COPS Germany") with the Black Forest, the Swabian Alb and the upper Rhine valley.

technique of *Frei and Schär (1998)*. More information about the gridding of the German rain gauge data can be found in *Paulat et al. (2008)*.

For this study, 19 deterministic models have been extracted from the D-PHASE "model zoo" (see Table 1), which can be divided into three categories: global models (1), medium-resolution local area models (LAMs) with parameterized deep convection (10), and high-resolution LAMs (7) where deep convection is explicitely calculated.

To calculate daily precipitation sums (from 06 to 06 UTC on the following day), the simulations started at 00 UTC (except for COSMO-DE and COSMOCH2 for which the forecasts starting at 00 and 12 UTC had to be combined) were used. Due to the fact that the 19 NWP models have different horizontal resolutions ranging from 2 to 60 km (see Table 1), the forecasts were transformed onto the same grid as the observations with a horizontal resolution of 7 km.

(b) The SAL technique

For the assessment of the QPFs of the 19 NWP models, the recently developed feature-based verification technique SAL (*Wernli et al. 2008*) has been used. SAL contains three indepen-

model	horizontal resolution	parameterization of deep convection	model category
ECMWF	∼30 km	yes	global
MM5_60	60 km	yes	medium-resolution
MM5_15	15 km	yes	medium-resolution
QBOLAM11	11 km	yes	medium-resolution
ALADAT	9,6 km	yes	medium-resolution
ALADFR	9,5 km	yes	medium-resolution
MESONH8	8 km	yes	medium-resolution
COSMO-EU	7 km	yes	medium-resolution
COSMOCH7	7 km	yes	medium-resolution
LMEURO	7 km	yes	medium-resolution
LAMI7	7 km	yes	medium-resolution
COSMO-DE	2,8 km	no	high-resolution
LMITA	2,8 km	no	high-resolution
AROME	2,5 km	no	high-resolution
COSMOCH2	2,2 km	no	high-resolution
MESONH2	2 km	no	high-resolution
MM5_CT	2 km	no	high-resolution
MM5_4D	2 km	no	high-resolution
ISACMOL2	2 km	no	high-resolution

Table 1: List of the 19 models with their horizontal resolution (Δx in km), information about the parameterization of deep convection and the corresponding model category.

dent components measuring the quality of the (S)tructure, (A)mplitude and (L)ocation of the QPF.

The structure component S investigates the size and shape of precipitation objects. It is defined in the range $[-2 \cdots + 2]$, where negative values correspond to too small and/or too peaked objects, while positive values indicate too large and/or too flat simulated precipitation objects. Corresponding to SAL, a value $S = 0$ indicates a perfect structure of the QPF.

The amplitude component A evaluates the total amount of precipitation in a predefined region. The values of A are within $[-2 \cdots + 2]$, where 0 represents again the perfect value. Negative values of A correspond to too little and positive values to too much predicted precipitation, respectively.

The location component L quantifies the displacement of observed and simulated precipitation objects, relative to their overall centers of mass. The values of L are within $[0 \cdots + 2]$ and also here 0 denotes the perfect value.

(c) An example for the application of SAL

To illustrate the working of SAL, an example is shown in Fig. 3.2 for southwestern Germany. The observations are shown on the left-hand side with a couple of distinct precipitation objects. The upper right panel shows the simulation from model I with intense and widespread precipitation. This leads to high positive values of $S = 1,3$ and $A = 0,6$, i.e. the amount of precipitation is overestimated as well as the typical size of the precipitation objects.

The
preci
unde

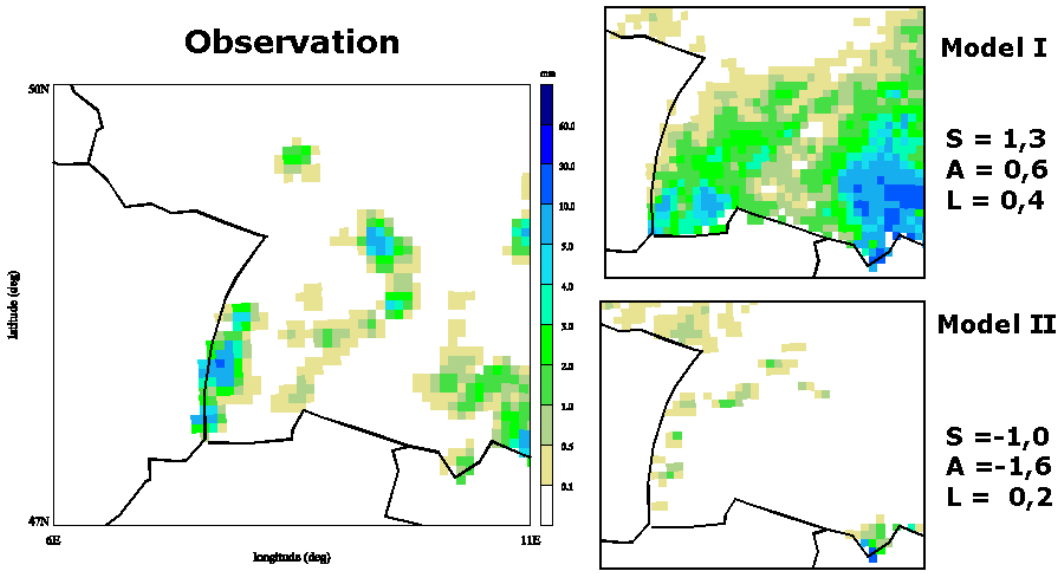

Figure 3.2: An example for the application of SAL. The left panel shows the observations in mm/day and the right panels show two forecasts, which score different in terms of SAL.

Results

For concisely representing the results of all 19 models, the interquartile range (IQR) is plotted against the median in Fig. 3.3 for the SAL components S and A determined for all 92 QPFs in JJA 2007. In this diagram, a perfect model is represented by a point at the origin (median=0, IQR=0). In contrast, a random forecast, generated by using a "Monte-Carlo" approach to the set of observed precipitation fields (*Wernli et al. 2008*), has a median of zero with a high IQR (> 2).

For S, the results for the three model categories are well separated: The medium-resolution models (blue) show a tendency to predict too large and/or too flat rain objects (median of $S \geq 0$), while the high-resolution models (red) simulate too small and/or too peaked rain objects (median of $S \leq 0$). Most of the high-resolution models have a significantly smaller IQR than the medium-resolution models. The global model produces the largest median of S, but a fairly small IQR.

The picture for the A component (Fig. 3.3b) is less systematic, but three particular aspects are apparent. The first one (dark green) is related to the performance of the COSMO model driven by different global models. The COSMO model driven by the GME (global model from the German Weather Service) simulates the amount of precipitation better than if driven by the ECMWF global model, as revealed by the differing medians. The second

aspect corresponds to the fact that different LAMs (orange) driven by the same global model (ECMWF) perform differently. For the MM5 and COSMO models, the simulated amount of precipitation is on average underestimated, while for MESONH the amount is overestimated (MESONH is the only model using a two-way nesting method). The third aspect (purple) is the positive effect of the 4D-Var assimilation of GPS water vapor measurements in the MM5 model for the amplitude component of SAL. In contrast, both with and without assimilated GPS data, precipitation objects in the MM5 forecasts are too small and/or too peaked (as indicated by the negative median of S).

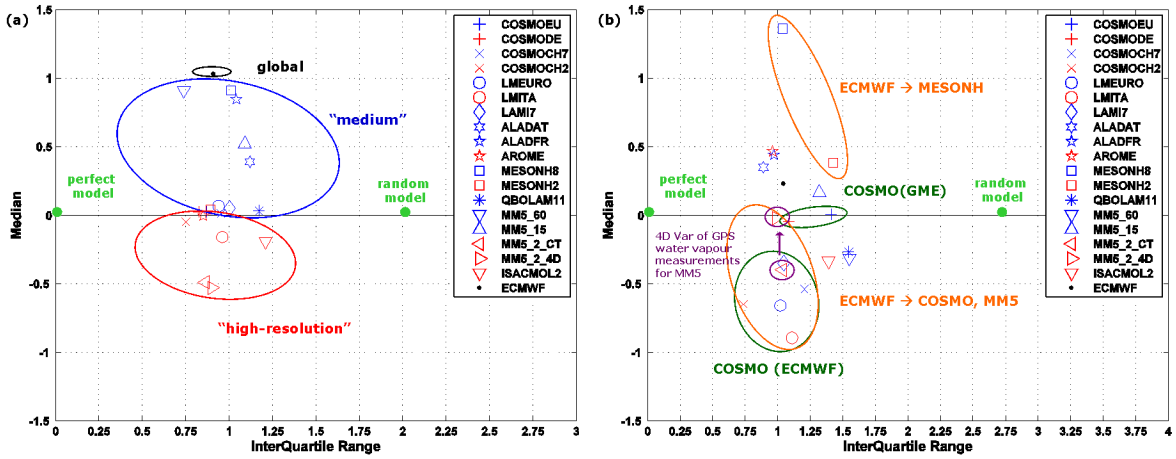

Figure 3.3: Interquartile range vs. median for the SAL components S (a) and A (b) for JJA 2007 in the COPS Germany domain. Black symbols denote global, blue medium-resolution and red high-resolution models, respectively.

Summary & Conclusions

Daily QPFs from a set of 19 models have been verified with the recently developed feature-based technique SAL in the German part of the COPS area during summer 2007. The investigation reveals some important differences between medium-resolution models with parameterized deep convection and high-resolution convection permitting models. On average, the high resolution models simulate the structure of the precipitation field more realistically than the medium-resolution models (as shown by the smaller IQR of S), however some of them show a systematic underestimation of the structure component (median of $S \leq 0$). The quality of the simulated precipitation amount is linked to the following three characteristics. The COSMO model driven by the GME (median of $A \simeq 0$) predicts the amount of precipitation better than if driven by the ECMWF (median of $A < 0$). The IQR of A is smaller for the high-resolution models. For the MM5 model, the use of 4D-Var assimilation of GPS water vapor measurements leads to a better estimation of the precipitation amount but not of the structure of the precipitation objects.

Probably for the first time such a large dataset of forecasts from different models has been

available for a thorough validation of QPF performance. It is interesting that systematic differences occur between models that parameterize deep convection (here referred to as medium-resolution models) and models that don't parameterize deep convection (here referred to as high-resolution models) - if using a feature-based verification measure like SAL. In particular when considering the structure of a precipitation field, the first results from the new generation of convection-permitting models are promising. However, one should keep in mind that this study focused on a relatively small mountaineous region in southwestern Germany during one particular summer season. Further work is required to assess the robustness of these results and to quantify the QPF quality of the different model categories in other regions and during other seasons. Also, the considered summer season in 2007 was characterized by strongly contrasting synoptic weather conditions (*Zimmer and Wernli 2008*) and it will be rewarding to compare the models' QPF performance for different weather regimes.

Acknowledgments: This work has been funded by the priority program "Quantitative Niederschlagsvorhersage" (SPP-1167) of the German Science Foundation (DFG). We are thankful to the German Weather Service (DWD) for providing the rain gauge data.

References

Casati, B., L. J. Wilson, D. B. Stephenson, P. Nurmi, A. Ghelli, M. Pocernich, U. Damrath, E. E. Ebert, B. G. Brown and S. Mason (2008). Forecast verification: current status and future directions. *Met. Apps.,* **15,** 3-18.

Frei, C. and C. Schär (1998). A precipitation climatology of the alps from high-resolution rain-gauge observations. *Int. J. Climatol.,* **18,** 873-900.

Paulat, M., C. Frei, M. Hagen and H. Wernli (2008). A gridded dataset of hourly precipitation in Germany: its construction, application and climatology. *Meteorol. Z.,* in press.

Wernli, H., M. Paulat, M. Hagen and C. Frei (2008). SAL – a novel quality measure for the verification of quantitative precipitation forecasts. *Mon. Wea. Rev.,* **1**36, 4470-4487.

Wulfmeyer, V., A. Behrendt, H.-S. Bauer, C. Kottmeier, U. Corsmeier, A. Blyth, G. Craig, U. Schumann, M. Hagen, S. Crewell, P. Di Girolamo, C. Flamant, M. Miller, A. Montani, S. Mobbs, E. Richard, M. W. Rotach, M. Arpagaus, H. Russchenberg, P. Schlüssel, M. König, V. Gärtner, R. Steinacker, M. Dorninger, D. D. Turner, T. Weckwerth, A. Hense and C. Simmer (2008). The Convective and Orographically-induced Precipitation Study: a research and development project of the World Weather Research Program for improving quantitative precipitation forecasting in low-mountain regions. *Bull. Amer. Meteor. Soc.,* **89,** 1477-1486.

Zimmer, M. and H. Wernli (2008). COPS Atlas – The meteorological situation from June 1 till August 31, 2007. Internal Report No. 1, Institut für Physik der Atmosphäre, Universität Mainz, 100 pp.

3.3 Automated CRA method

Mikołaj Sierżega (1) and Bogumił Jakubiak (2)
(1) University of Warwick, (2) University of Warsaw, ICM

Introduction

Among many approaches to the verification of output of numerical weather prediction (NWP) models the entity-based method proposed by E.E. Ebert and J.L. McBride in [Ebert & McBride] is arguably the most intuitive. The CRA technique mimics "eyeball" verification in order to rigorously quantify visual similarities of forecast and observed rain events. Assuming that we have forecast and observed rain entities mapped onto a common grid we may compare properties like location, size, mean and maximum intensity, volume, area and evaluate performance of a NWP model with respect to these variables. Object-based verification provides more information about model's performance than standard statistics so operational version of Ebert-McBride technique would be a helpful diagnostic tool. This technique, however, is not easily automated. The procedure requires some decision making which would usually be done by human. There is also an ambiguity when forecast and observed fields involve many separate rain systems or when forecast and observed entities don't overlap at all. In what follows we propose a systematic procedure that resolves these problems. In this framework entire forecast and observed fields are compared and differences between them are quantified in terms of entity-based verification method.

Method

In Fig.3.1 below, there is a particular case of forecast and observed fields mapped onto a common grid. Since grid of the radar system and model grid do not overlap and extent of radar scan is finite, part of the forecast field suitable for verification is cut from the original size. The classic pointwise verification severly punishes this forecast because rain systems almost don't overlap. There is, however, a similarity between those fields. There is an elongated, slightly bent, large rain system in both pictures at approximately the same location. There are also some smaller systems in the centre. Visual similarity is clear but under closer inspection significant differences emerge. The forecast field contains more rain events but they are apparently smaller and less intensive. In order to quantitatively compare the forecast and observed fields we need to look from two points of view. On the one hand if we observe a large rain system and a corresponding object in the forecast field we can concentrate on model's skill to predict this particular event and describe differences in terms

of location, size, shape, volume etc. This local viewpoint may be sufficient if we're interested in model's ability to reveal some specific types of events like severe storms or large rain systems. On the other hand we'd like to assign some measures to entire forecast fields often composed of many separate rain systems some of which may have no counterpart in observations or otherwise. From this viewpoint model's success in accurate prediction of one particular rain event may be insufficient to constitute a good forecast. Our method collect these local, "object-wise" measures and assign statistics to entire forecast fields. Procedure consists of a series of steps.

Step 0. Since we want to compare sub-regions of fields directly, observations and forecasts are mapped onto a common grid. It may be the case that forecast and observation grids do not overlap or that observations are incomplete e.g. finite extent of radar scan. Although it is possible to artificially extend incomplete observations and statistically incorporate their effect (see [Ebert & McBride]), we present a simplified approach where we accept only those rain systems which are fully enclosed within the common field i.e. they don't touch the boundary.

Step 1. The first step is extraction of "events" from both fields. Depending on the kind of data and specific features under investigation a minimal threshold is set. In Fig.3.1 the threshold is 5mm/3h. Now an algorithm is applied to find connected entities enclosed by the

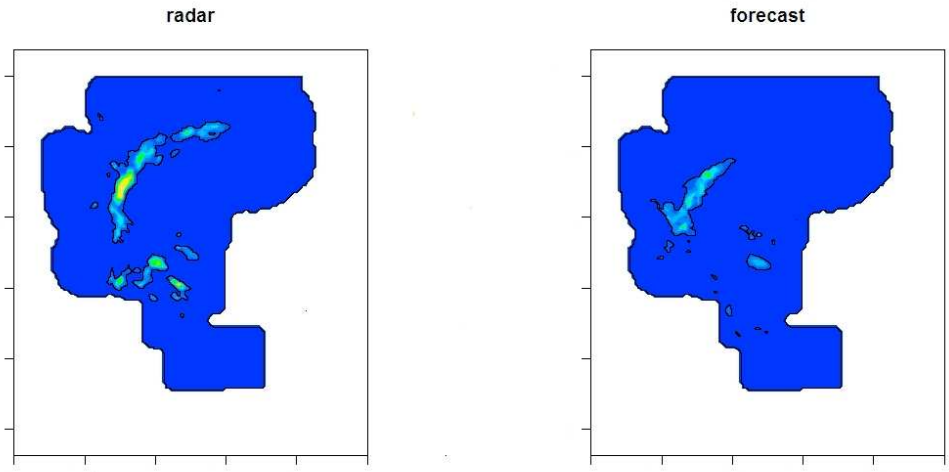

Figure 3.1: Threshold shows separate rain systems

threshold isohyet in both pictures. It is important to stress that entities are identified in both fields separately. They are not yet merged to define CRAs as in the case of classic Ebert-McBride technique. Those entities are treated individually. We can investigate attributes of any one event i.e. position, mean precipitation, maximum precipitation, area, volume.

Different events are identified by their unique locations. Those are just coordinates in the common grid. It is a matter of choice how we define the location. If model's ability to predict heavy rain events is under investigation we may choose to identify the location with the centre of mass of an object i.e. centre of mass of pixels that constitute an object, where their mass is given by intensity of rain. In our example location is defined as the centre of area of an object i.e. the centre of mass of pixels where each pixel has unit mass. This choice is more suitable when stress is put on geometric pattern rather than intensity. Fig.3.2 shows events extracted from their original fields.

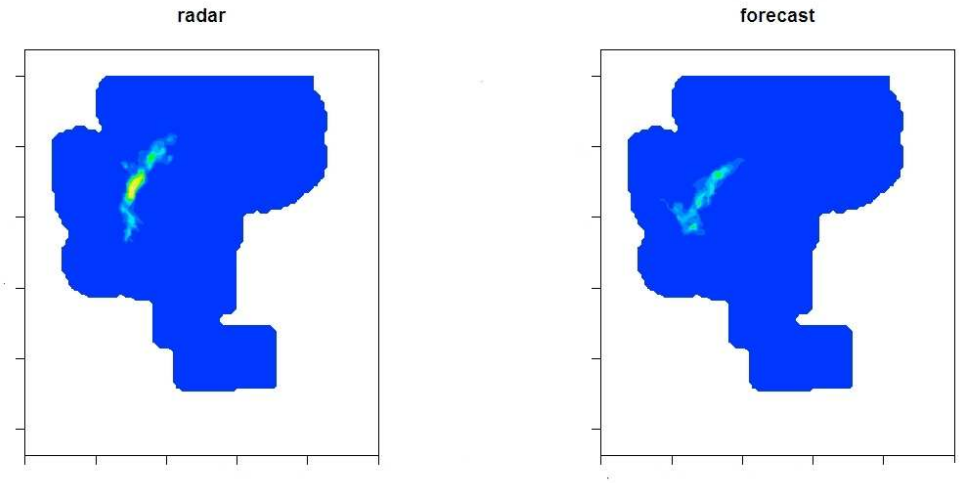

Figure 3.2: Individual rain entities

Step 3. Now we have two sets of well described entities. First set contains observed and the second forecast entities. We take an event from the set of observed events and we merge it into the forecast field. Depending on what is understood as acceptable displacement we define a search zone i.e. a circle centred at location of our observed event and radius of our choice. In our case study the radius is 200 km. All forecast entities whose location is inside the circle will be compared with the observed entity. At this stage Ebert-McBride technique is applied to each [observed event, forecast event] pair separately. One by one they are horizontally translated over the observed event and moved around until the best fit is obtained. Best fit may be defined in many ways. Here the total squared error is calculated. When all events are checked, the one that provides the minimal error is chosen and the matched pair is removed from sets of events. This is the local stage of the procedure. After the pair is removed we repeat the procedure with another observed event and so forth until we're left with no more observations. It has to be said here that not all forecast and observed pairs will be matched. There can be three cases:

1. there is a matched pair,

2. there is no forecast event in the search zone - observation without a pair,

3. there are forecast events left after all observed were used - forecast without a pair.

These cases will form a basis of dichotomous statistics later.

Step 4. Those events that are matched may be compared further. It is again a matter of choice what we understand as accurately forecast intensity. In our case study we follow the scheme proposed in [Ebert & McBride]. There is a sequence of categories 1-2, 2-5, 5-10, 10-25, 25-50, 50-100, 100-150, 150-200 and >200 mm/d. When the maximum intensity of observed and forecast event falls within the same category there is a "hit". Otherwise we may have an "underestimate" or "overestimate". In this way we can analyse such indicators like ratio of underestimated/overestimated/correct to total number of pairs and quantitatively describe model's skill to predict intensity.

Dichotomous statistics

We have two distinct sets of values suitable for dichotomous statistics. First comes from the matching step. After an algorithm has matched corresponding pairs we call them "hits". Those observed events that are left without a pair are called "misses" and those forecast events that are left when all "hits" and "misses" are removed are called "false alarms". Observe that "correct negatives" don't make any sense in this approach. However all the classical dichotomous statistics which make no use of "correct negatives" are well defined. Among those are e.g. *frequency bias*, *probability of detection*, *false alarm ratio* and *threat score*. Second set of dichotomous statistics comes from differences in intensity. We take only matched pairs i.e. "hits" from above statistics and count number of underestimate, correct and overestimate intensities. We refer to correct intensities "hits" like before but it shouldn't create misunderstanding.

Case Study

Our statistics describing the matching step are summarised on Fig.5.5 and Fig.3.4.

Four different statistics, each for a control run and the mean estimated from ensemble were averaged over the cases we have at our disposal. Threat score and the probability of detection decrease in time. Ensemble mean is better during the first 12 hours of the forecast, compensating the spin-up time of each individual run. In a period from 12 to 24 hours the statistics from control and ensemble runs are comparable. It is interesting to see that for the second day of the forecast the control case gives better results than ensemble while the ensemble is better than the control for the third day of the forecast (with minor exceptions).

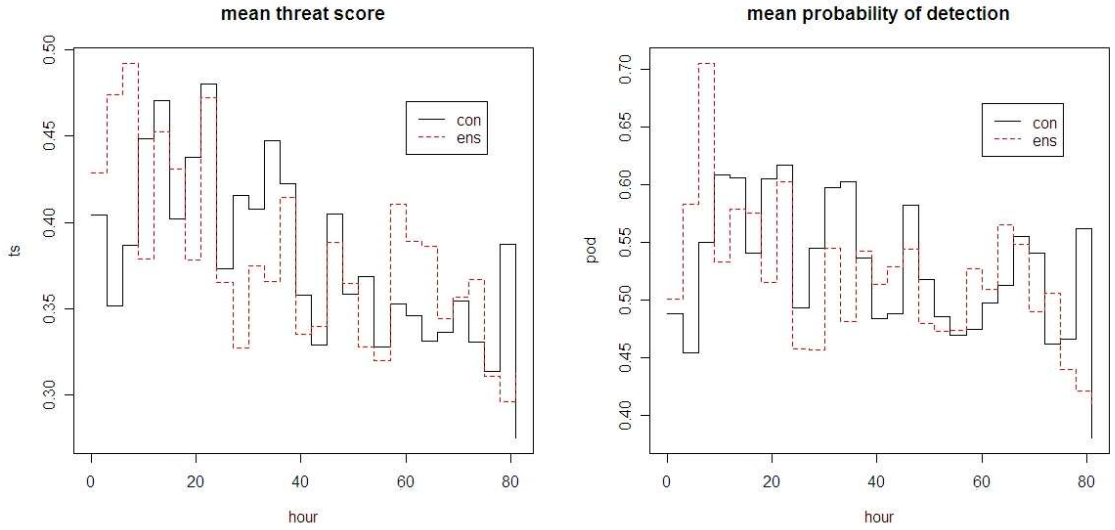

Figure 3.3: Statistics of matching events

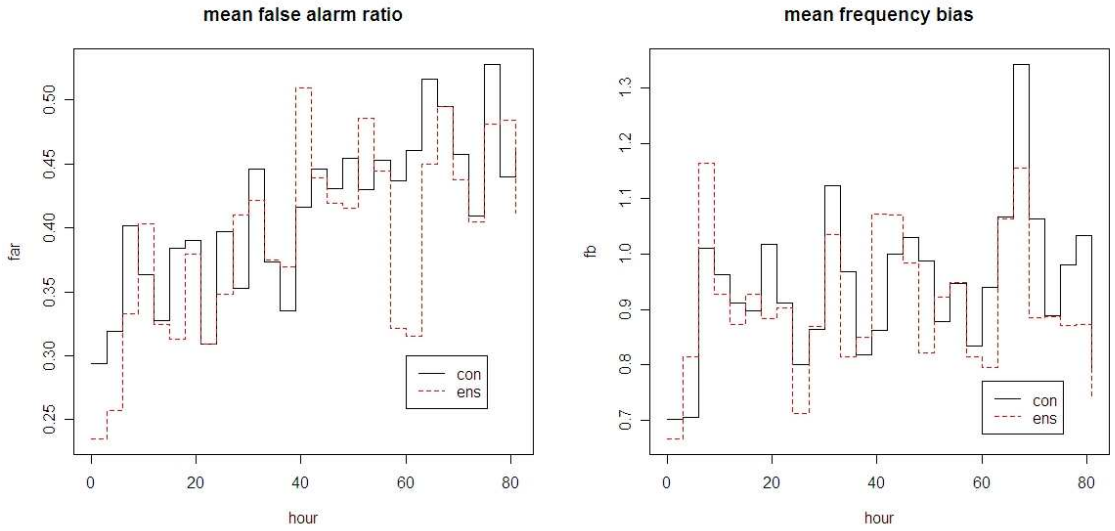

Figure 3.4: More statistics of matching events

At the end of the forecast period, the control forecasts are sufficiently better than ensemble mean, what could be explained by too narrow spread of the ensemble. The daily cycle is evident in all of four statistics, also the shift between control and ensemble statistics in daily cycle is observed. It is difficult to propose what is the cause of such behaviour, and it is very likely that our sample is to small to the obtain the correct answer.

Statistics describing differences in a rain intensity are illustrated in Fig. 3.5. Ensemble runs have smaller underestimates ratios and higher overestimates ratios comparing with the control runs. Hit ratios for control run are better for first two days of the forecast while hit ratios for ensemble mean are better for the third day of the forecast.

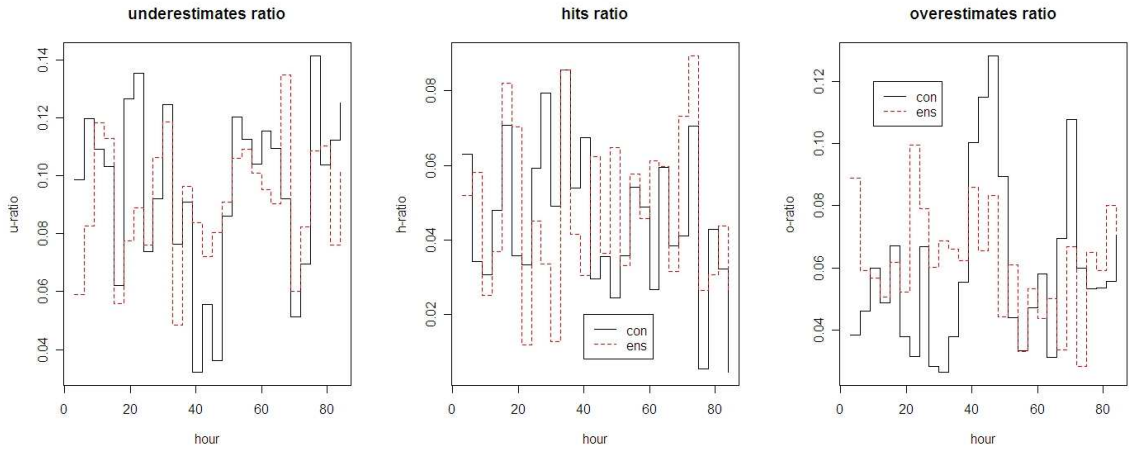

Figure 3.5: Statistics of intensity

Summary and Outlook

Object-based verification provides a deeper insight into nature of models' errors. While classical (grid) pointwise statistics don't discriminate between errors due to missed location or wrong intensity the Ebert-McBride technique helps to pinpoint particular flaws of a given forecasts and indicate which internal subroutines may be responsible for poor performance. This particular strength of CRA method is especially useful in determination of systematic errors. It is therefore of interest to perform this kind of verification on regular basis. The procedure presented above may prove helpful in designing an operational, fully automated, object-oriented verification method.

Acknowledgements: This research has been partly supported by the NICOP program under the grant N000140510673 and by the KBN grant COST/20/2006. We used computer resources of ICM, Warsaw University.

References

Ebert, E.E. and J.L. McBride, 2000: Verification of precipitation in weather systems: Determination of systematic errors. J. Hydrology, 239, 179-202.

4.1 Variationally derived extrapolation of radar echoes

Martin Ridal, Magnus Lindskog, Günther Haase and Nils Gustafsson

Swedish Meteorological and Hydrological Institute, S-601 76 Norrköping, Sweden

Background

The Swedish Meteorological and Hydrological Institute (SMHI) is developing a nowcasting system for generating short range precipitation forecasts. The general idea is to to advect the latest available structure of accumulated precipitation, as obtained from radar reflectivity composites, forward in time by applying 2-dimensional, semi-Lagrangean advection. The approach is similar the method used by Germann and Zawadzki (2003). The radar composites are derived using data from the NORDRAD network (Michelson, 2006), with a horizontal resolution of 2 (or optionally 4) km and a temporal resolution of 15 minutes. The advection field is variationally derived by utilising a time-sequence of radar reflectivity composites separated in time by 15 minutes. To catch non-developed convection there is a weighting towards a NWP forecast, in this case the SMHI operational HIRLAM forecast (11 km horizontal resolution). The geometry of the advection field is obtained from the same HIRLAM model domain, illustrated in Figure 4.1 together with the horizontal coverage of

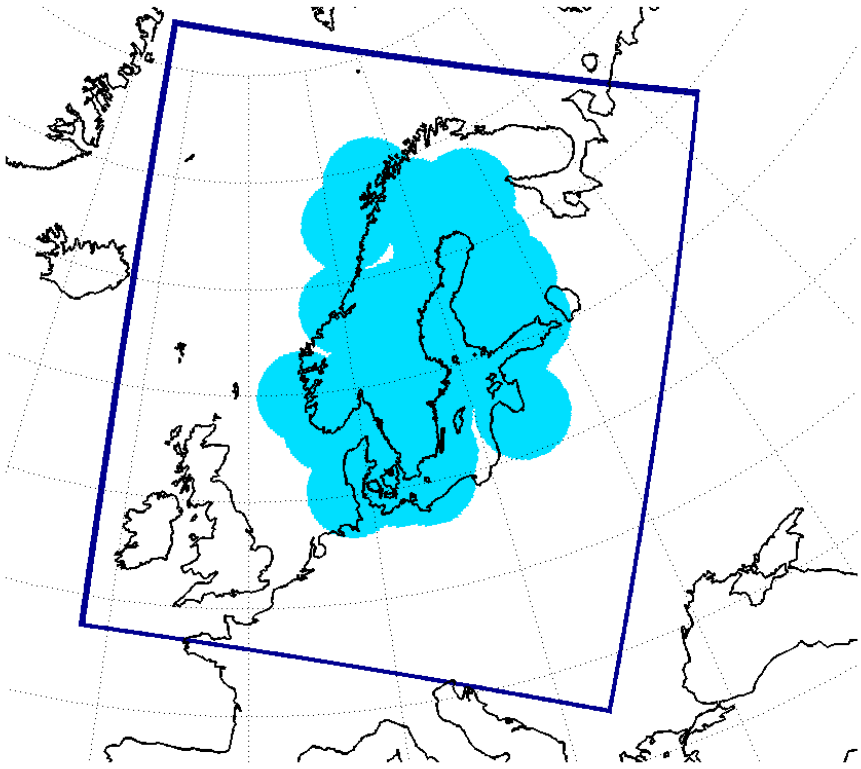

Figure 4.1: Illustration of advection field (frame) and horizontal coverage of NORDRAD radar composites utilised (circles).

Variational methodology

The variational methodology applied for deriving the advection field is based on the HIRLAM 4-dimensional variational data assimilation (Gustafsson et. al, 1999, Lindskog et. al, 2001). It consists in finding the model state vector, x_0, including a 2-dimensional advection field (u,v) and a reflectivity field ψ, at the start of an assimilation window, that minimizes the following cost function, J:

$$J(x_0) = J_b(x_0) + J_o(x_0) = \frac{1}{2} x_0^T B^{-1} x_0 + \frac{1}{2} (HMx_0 - \psi_{obs})^T R^{-1} (HMx_0 - \psi_{obs})$$

Here J_b measures the distance to a background model state, x_b, valid at the start of the assimilation window, and J_o measures the distance to the reflectivity observations, ψ_{obs}, which consist of 2-dimensional radar composites spread in time within a 90 minutes assimilation window. The background state is a first guess of the 2-dimensional advection field and reflectivity field at the beginning of the assimilation window (t_0). The background advection field is taken from the level 50 wind field of the latest available 6 hour SMHI operational HIRLAM forecast (11 km horizontal resolution). The background reflectivity field is set close to zero everywhere. Within the assimilation window, the advection field is assumed constant in time, while ψ has a time variation due to advection. M is the advection model that propagates ψ forward in time, to the time of the observations. H is the observation operator that in our case simply consists of horizontal interpolation of the model state reflectivity to the positions of the reflectivity observations, ψ_{obs}. B is the matrix containing the covariances of the background error field (u, v, and ψ) and R is the matrix containing the covariances of the reflectivity observation errors (ψ_{obs}. The denotation ^{T} indicates the transpose, or adjoint, of a matrix.

The cost function is minimized iteratively and for each iteration calculation of the gradient of the cost function is required. The minimization problem is not strictly quadratic, however, since the advection model Mx_0 depends non-linearly on the advection field (u and v included in M) and on the initial reflectivity field ψ. To avoid minimization divergence, we will solve this minimization problem by successive re-linearizations in an outer minimization loop and by solving a standard quadratic minimization problem in each such outer loop. The solution of the quadratic minimization problem may be referred to as the minimization inner loop. For each minimization inner loop, we will apply a tangent linear model Mx_0, obtained by linearization around the solution for the advection field (u,v) and the initial reflectivity (ψ) from the previous outer loop iteration. After convergence of the outer loop minimization, this means that the reflectivity observations have induced a reflectivity field and advection field that are most consistent with the 2-dimensional observed reflectivity pattern and its variation in time. That advection field should then later on be used to advect accumulated precipitation structures obtained from the latest available observed radar reflectivity composite three hours forward in time. To catch non-developed convection and advection of precipitation into the area, a weighting towards a NWP forecast is applied during this time.

Results

a. *Idealised example using simulated observations*

In an illustration of the functionality of the variational methodology the background advection field is set uniform all over the domain, having a speed of roughly 1.4 m/s towards north-east. The background reflectivity field is set to all small positive value close to zero

everywhere. Each 15 minutes two single simulated reflectivity observation are provided. The positions of the reflectivity observations is shifted more and more towards south-east, within the 75 minutes assimilation window, with a speed of roughly 25 m/s. The positions of the observations and the background advection field are illustrated in the upper panels of Figure 4.2.

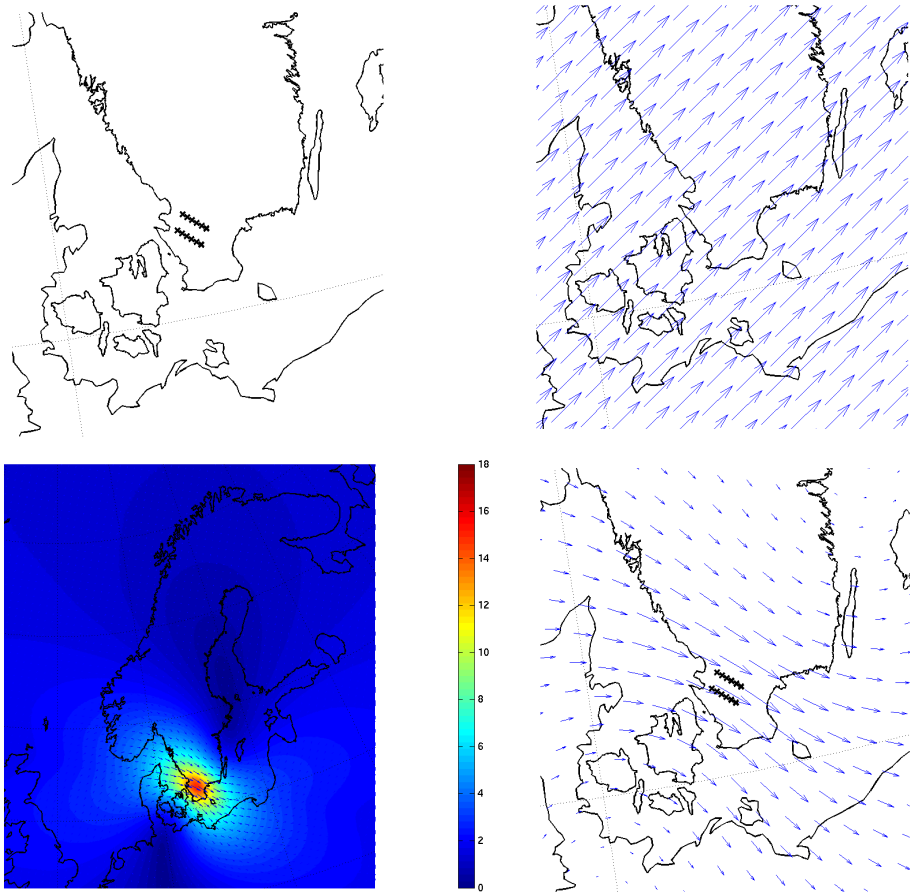

Figure 4.2: Horizontal position of observations at various times (1 to 90 minutes) within the assimilation window (upper left) and direction of background advection field (upper left) with a speed of approximately 1.4 m/s. Variationally derived advection speed (lower left) in m/s and direction (lower right).

Also shown is Figure 4.2 (lower panels) is the speed and direction of the variationally derived advection field. Close to the position of the observations it is roughly 18 m/s towards south east.

b. *Full scale illustration*

A full scale demonstration of the method is carried out for 20080326, 10.30-12.00, utilizing a time-sequence of radar composites. The resulting variationally derived advection field is presented in Figure 4.3, together with the background advection field, which is a HIRLAM low level wind forecast.

There are some significant differences between the background advection field and the variationally derived advection field. For example, over Northern Finland the variationally derived southward advection is significantly smaller, while in the south east and south of Finland in it larger.

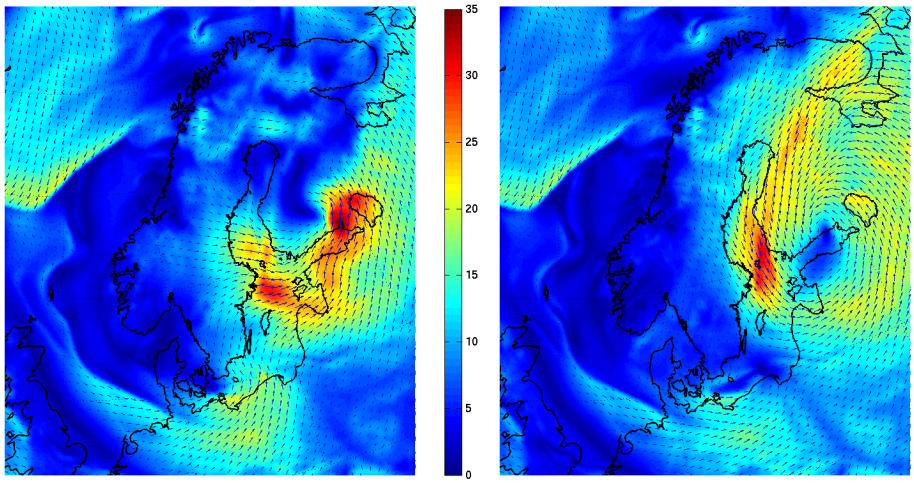

Figure 4.3: Variationally derived advection field for 20080326, 10.30-12.00 (left) and corresponding background advection field (right).Unit: m/s.

In Figure 4.4 the following 3h advection and resulting forecast of 3h accumulated precipitation is shown without weighting towards a NWP forecast. The left panel shows the result when the variationally derived advection field is used, the middle panel when the background advection field is used also for the advection and right panel shows the verifying observed 3h accumulated precipitation, as obtained from radar composites. Note that the position of the precipitation maxima is better predicted when variationally derived advection field is applied.

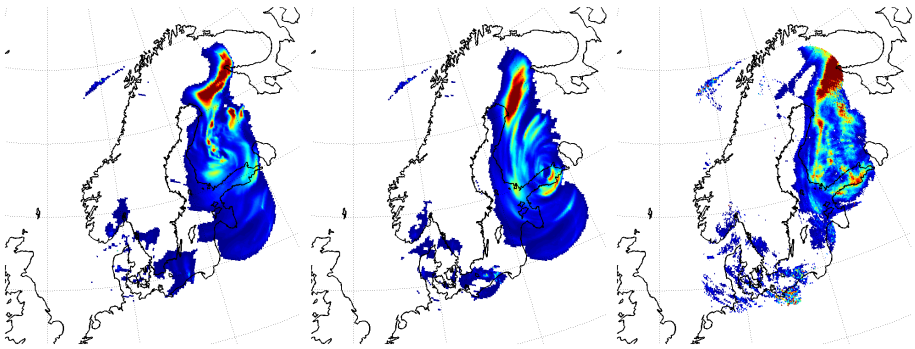

Figure 4.4: Three hour forecast of 3h accumulated precipitation(mm) for 20080326, 14.45-17.45. With variationally derived advection field (left), with background advection field (middle) and verifying radar based observations (right).

Conclusions

A variationally based method for extrapolation of radar based precipitation structures forward in time has been developed. It uses a time sequence of radar composites to derive an advection field which is then applied in a semi-Lagrangean advection of the latest available radar composite. The methodology has been demonstrated to work in idealised experiments using simulated observations and prescribed background fields as well as in full-scale frameworks using real radar composites and wind forecasts. The system is currently applied pre-operationally at the Swedish meteorological and Hydrological Institute. In the preoperational phase the system is evaluated for future improvements including improved quality control and tuning.

References

Germann, U. and Zawadzki, I.: Scale-dependence of the Predictability of Precipitation From Continental Radar Images. Part I: Description of the Methodology, Mon. Wea. Rev., 130, 2859- 2873, 2002.

Gustafsson, N., Berre, L., Hörnquist, S., Huang, X.-Y., Lindskog, M., Navascués, B., Mogensen, K. S. and Thorsteinsson, S. 2001. Three-dimensional variational data assimilation for a limited area model. Part I: General formulation and the background error constraint. Tellus, 53A, 425-446.

Lindskog, M., Gustafsson, N., Navascués, B., Mogensen, K. S., Huang, X.-Y., Yang, X., Andr, U., Berre, L., Thorsteinsson, S. and Rantakokko, J., 2001: Three-dimensional variational data assimilation for a limited area model. Part II: Observation handling and assimilation experiments. Tellus, 53A, 447-468.

Michelson, D., The Swedish weather radar production chain. Proc. ERAD (2006), 382-385, 2006.

4.2 Using numerically predicted and measured radar data for nowcasting

Á. Horváth[(1)], I. Geresdi[(2)], P. Németh[(3)]

[(1)] *Hungarian Meteorological Service Storm Warning Observatory Vitorlás u. 17, H-8600 Siófok, Hungary; E-mails: horvath.a@met.hu; csirmaz.k@met.hu*

[(2)] *University of Pécs, Institute of Environmental Sciences, Ifjúság u. 6, H-7624 Pécs, Hungary; E-mail: geresdi@gamma.ttk.pte.hu*

[(3)] *Hungarian Meteorological Service, Marcell György Observatory, P.O. Box 39, H-1675 Budapest, Hungary; E-mails: nemeth.p@met.hu; dombai.f@met.hu*

Introduction

Estimation and nowcasting of precipitation mainly based on appropriate usage of radar reflectivity data. Time series of radar images allows the calculation of radar motion vector fields. Once motion vector fields between two radar images is known, radar reflectivity can be interpolated to any time with high density (say 2 minutes), and the reflectivity-rain intensity (Z-R) relations can be used more exactly for quantitative precipitation estimation. Using motion vectors, extrapolation of radar images and nowcasting of precipitation is feasible for a limited time ahead. The problem with that method is that radar echoes and the radar motion vectors are evolving during the forecast time. High resolution numerical models can be applied to extend validity of motion vector fields. Using hydrometeors (mixing rates of rain, snow, graupel, hail etc) artificial radar reflectivity and motion vector fields can be calculated. Comparing and smoothing motion vector fields coming from radar measurement and NWP allows us to extend advection of precipitating system and upgrade nowcasting of precipitation. In the first section of this paper the precipitation estimation, in the second section the NWP artificial reflectivity calculation in the third part a radar assimilation method and in the forth part precipitation nowcasting method is presented.

Precipitation estimation using time series of radar reflectivity

The radar reflectivity allows us to estimate precipitation intensity. Lets suppose that reflectivity-intensity calculation is an errorless procedure (which is a rather strong assumption) and we integrate precipitation from reflectivity images with 15 minutes time resolution. The result is shown in Fig. 4.1 where unrealistic precipitation fields come from the error of echo advection and echo intensity changing.

To decrease the advection and evolution errors the first step is to calculate motion vector of radar echoes. There are several existing methods to do this calculation, here the TRAC (Tracking RAdar echoes using Correlation) procedure were applied. During TRAC procedure the radar grid was divided in macro grids and motion vectors were determined based on maximum correlations for the macro grids. After some quality control to filter out noisy vectors on macro grid fine resolution motion vectors were interpolated to all grid points of the original radar grid.

Once a motion vector field between two radar images belonging T2 and T1 are calculated by TRAC method, the radar reflectivity interpolation can be done at any time between T1 and

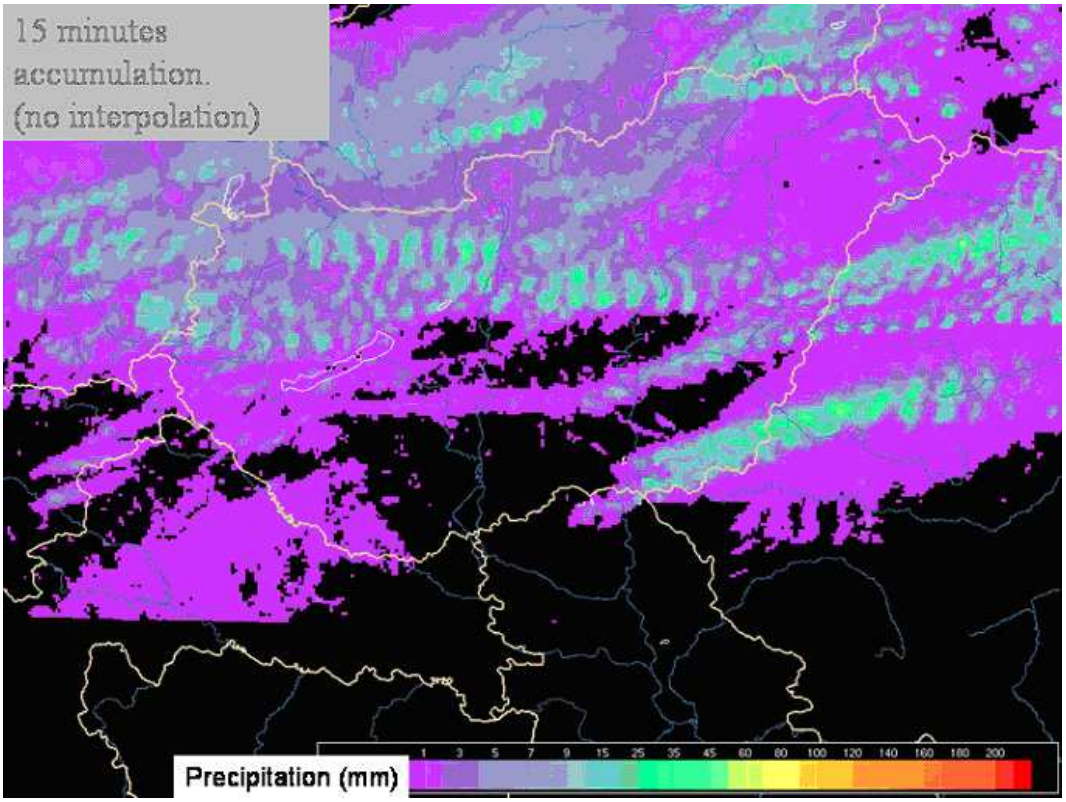

Figure 4.1: 2 Hours accumulated precipitation calculated by radar images with 15 minutes time resolution.

T2 by the following. Echoes from T1 moved forward and echoes from T2 moved backward by motion vectors and a reflectivity of a given pixel is interpolated between forward and backward moving reflectivity values as shown in Fig.4.2.

The methodology using interpolated radar images provides more realistic accumulated precipitation fields. The optimal time step of precipitation calculation was found 1 minute. The 12 hour precipitation field of Fig.4.3 is calculated from 15 minutes measurements interpolated to 1 minute.

Calculating motion vectors from NWP output

NWP provides hydrometeors as output. For radar reflectivity calculation the mixing rations of rain waters and solid precipitation elements such as graupel snow and hail are used.
Radar reflectivity of the precipitation elements was calculated by supposing Rayleigh scattering; that is the reflectivity depends on the sixth power of diameter of the particles. Using exponential size distribution the reflectivity of the rain drops is given by the following equation:

$$Z_R = n_{RO}\ exp(-\lambda_R D)dD = 720\ 10^{18} n_{RO}\ \lambda_R^{-7},$$

where n_{R0} $(8 \cdot 10^6\ m^{-4})$ is the interception parameter of the size distribution. The dimension of the reflectivity is $\mathrm{mm}^6\mathrm{m}^{-3}$. The λ_R parameter can be calculated from the rain mixing ratio (q_R):

$$\lambda_R = \frac{\pi \rho_w n_{RO}}{\rho_a q_R}^{0.25},$$

where ρ_a and ρ_w are the density of air and water, respectively. In the case of the solid precipitation elements (snow and graupel/hail) difference between dielectric factor of water

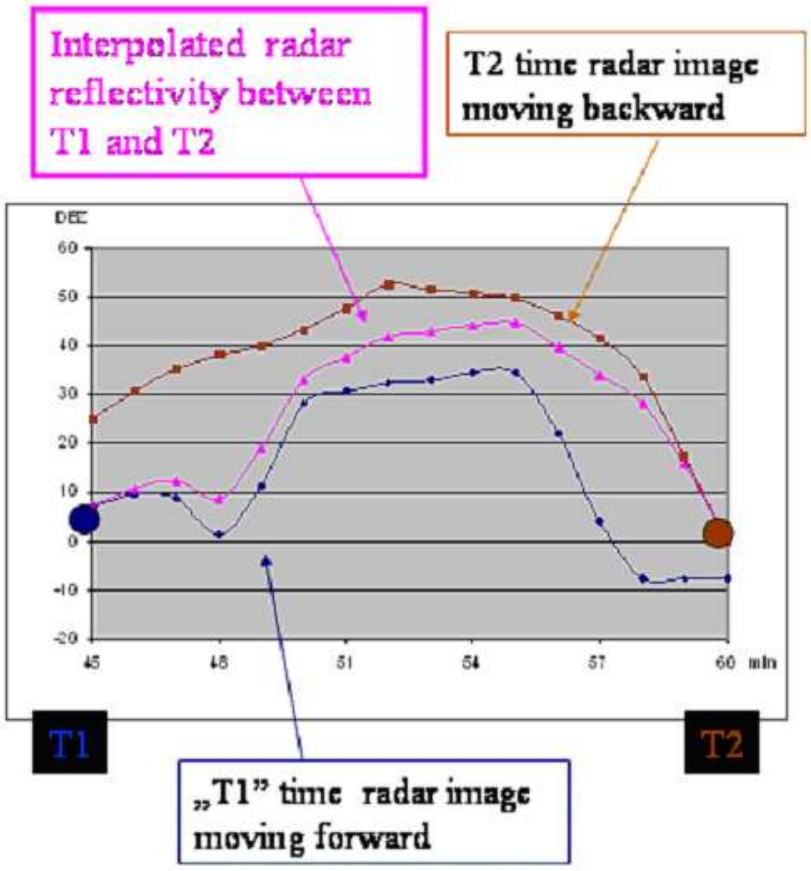

Figure 4.2: Interpolation of radar reflectivity using motion vector.

and that of ice was taken into consideration. The following equations give the reflectivity of the snow and garupel/hail particles. It was supposed that their size distributions, as in the case of the rain drops, are also exponential with fixed interception parameters of $n_{S0} = 3 \cdot 10^6 m^{-4}$ and of $n_{G0} = 4 \cdot 10^4 m^{-4}$ for the snow and hail and graupel particles, respectively.

$$Z_{SDRY} = 720\ 10^{18} \frac{|K_I|^2 \rho_s^2}{|K_w|^2 \rho_w^2} n_{SO} \lambda_S^{-7},$$

$$Z_{GDRY} = 720\ 10^{18} \frac{|K_I|^2 \rho_G^2}{|K_w|^2 \rho_w^2} n_{GO} \lambda_G^{-7},$$

where ρ_S and ρ_G are the density of the snow particles ($100 kg/m^3$) and graupel/hail particles ($800 kg/m^3$), respectively. The value of the dielectric factors ($|K_w|^2$ and $|K_I|^2$) are 0.93 and 0.21, respectively. The λ_S and λ_G parameter can be calculated from the snow and graupel/hail mixing ratios:

$$\lambda_S = \frac{\pi \rho_S n_{SO}}{\rho_a q_S}^{0.25}, \quad \lambda_G = \frac{\pi \rho_w n_{GO}}{\rho_a q_G}^{0.25}.$$

If the temperature is larger than 0^oC the solid precipitation elements start to melt. Due to the melting a water layer covers the snow and graupel/hail particles. The presence of the water layer modifies the reflectivity of these particles:

$$Z_{SDRY} = 720\ 10^{18} n_{SO} \lambda_S^{-7},$$

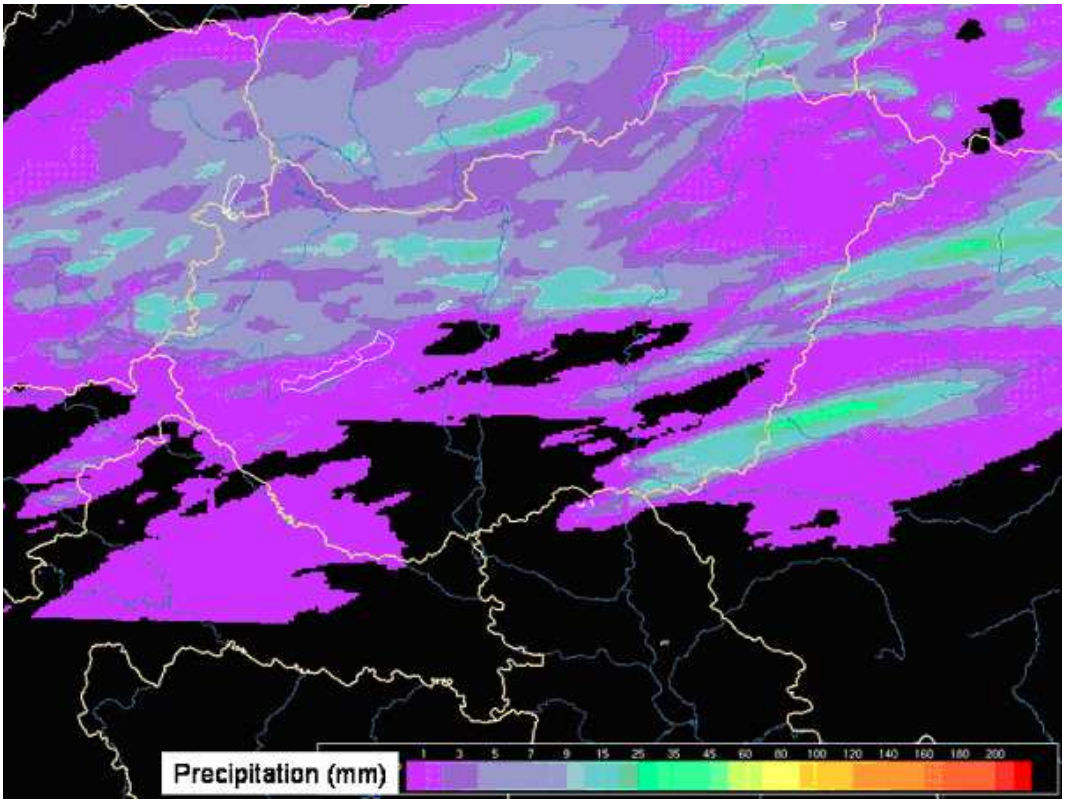

Figure 4.3: 12 Hours accumulated precipitation calculated by 1 minute interpolated radar images.

$$Z_{GDRY} = (720\ 10^{18} n_{GO} \lambda_G^{-7})^{0.95}.$$

Reflectivity values were calculated at all model grid points and the maximum value of vertical columns were chosen to create NWP radar image. Results of model integration were taken in every 15 minutes, and simulated radar motion vector fields were calculated in the chapter 1 described way.

Assimilation of convective storms in NWP

The numerical simulations were made by the MM5 (NCAR-PSU Mesoscale Model Version 3) showed that equivalent potential temperature (EPT) values are vertically near constants at severe thunderstorms (Fig.4.4). The mean EPT value of the lowest 1000 m can be considered as vertically constant value at grid points where thunderstorms are. The assimilation of thunderstorms works that at grid points where radar observation indicates thunderstorms the EPT profile is considered constant. Supposing the air column at thunderstorms are saturated (relative humidity is 100 %) a new vertical temperature profile (*T(pressure)*) can be recalculated. Thunderstorms appears as wet warm bubbles in the objective analysis and using built in nudging technique of MM5 these strong trigger effects can be introduced into the model.

Precipitation nowcasting

Considering the procedures described above four levels of precipitation estimation and forecast can be defined.

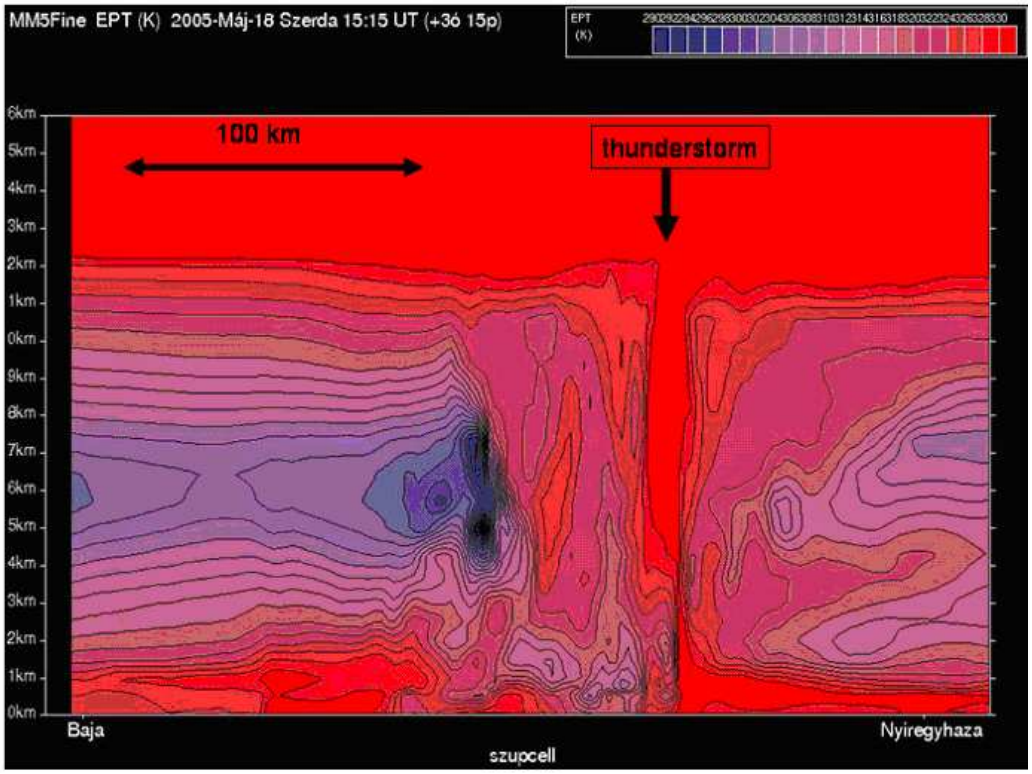

Figure 4.4: Cross section of equivalent potential temperature at the case of severe thunderstorm.

1. Estimation of measured precipitation can be done using time series of radar reflectivity using motion vector field calculation by the method described in section 2.

2. Very short range nowcasting of precipitation can be done using extrapolation of radar echoes in such a way that echoes are moved by the motion vector fields ahead and the precipitation is calculated from the present and the extrapolated radar field by the same method.

3. Longer forecast (1-2 hours) can be produced involving NWP. The procedure described in section 3 allows us to determine predicted motion vector fields. Measured and predicted vector fields can be smoothed allowing more precise forecast of radar reflectivity.

4. A more advanced method is the NWP triggering method described in section 4. Assimilating heavy thunderstorms into the model via triggering allows us to forecast not only motion vector fields but development of thunderstorms, too. At a successful assimilation continuity can be created between the real measured and numerically forecasted thunderstorms extending the forecast time of the precipitation.

The 1-3 levels are used in operative practice at the nowcasting system of Hungarian Meteorological Service. The 4^{th} level is only in experimental state.
The methods described above can be verified comparing forecasted radar echoes with real measured radar echoes. Case studies show that squall lines, supercells can be predicted for 2-2.5 hours ahead with good reliability. Nowcasting of local and isolated thunderstorms are much less successful.

Conclusion

Quality of precipitation estimation can be upgraded applying time series of radar images. Series of radar images also allow making very short range precipitation forecast using motion vector fields. More complex method is involving numerical model into calculation of radar motion vector field that extends the forecast time. Using a trigger method, severe thunderstorms indicated by radar reflectivity can be assimilated into a high resolution numerical model and it may establish continuity between measured and numerically predicted convective phenomena.

4.3 Rapid screening of flash flood impacted areas in Hungary

E. Pirkhoffer, S. Czigány, I. Geresdi

Department of Soil Sciences and Climatology, Institute of Environnmental Sciences, University of Pécs, Pécs, Hungary

Introduction

Despite the widespread publicity of the conventional floods of the rivers Danube and Tisza, the public awareness of flash flood events is limited in Hungary. However, large flash flood disasters are exceptions, as they were documented and published widely by several authors (e.g.: Horváth, 1999, Koris and Winter, 2000; Ely and Nagyváradi, 2001; Szlávik, 2003). Similarly, our scientific knowledge on flash floods is much more limited than on conventional riverine floods. The few studies, which discuss the hydrological problems of low-mountain watersheds; however, these studies only provide a broad but distant overview of the actual complexity of the phenomena. Undoubtedly, Hungary is not the typical location for flash flood generation; its lowland characteristics do not provide relief energy comparable to the mountains of the Alps or the Carpathians, and, similarly peak flood discharges are significantly less than those, which occur in Alpine environment (Ranzi et al., 2007). Nevertheless, several flash flood events have occurred and were documented in Hungary, e.g. on the B*ükkö*sdi–víz in SW Hungary (July 1, 1954 and June 27, 1987), on the Átalér (June 9, 1953), and the K*ö*vicses and Cs*örgö* Streams (on April 18, 2005) in Northern Hungary (e.g.: Eszéky, 1987; Eszéky, 1992; Vass, 1997, Horváth,2005). These flash floods were localized events; however, they caused widespread and considerable economic losses (Lóczy ando Juhász, 1996; Gyenizse et al., 2005).

Climate change is likely to affect the frequency of extreme weather (e.g.: intense convective rainfall) and weather associated phenomena, such as flash floods. However, in lack of substantial statistical data, the identification of trends of this type is challenging and likely to be misleading. Meteorological factors, on the other hand may have a subordinate role on flash flood generations. For instance, the increasing extension of surfaces under human influence (e.g. clear cuts and forest roads) in rural and non-urban environments may significantly enhance the impact of rainfall on surface runoff. In other words, primary triggering factors of conventional flash floods, occurring in natural environments, may be similar to pluvial and urban floods that occur on paved surfaces. Thus, such potentially flash flood triggering factors also needs to be considered prior to the prediction of flash floods and in risk management.

To prevent, or at least mitigate, extensive economic loss and fatalities, our objective, in collaboration with the Hungarian Meteorological Services, is to create a nationwide flash flood guidance (FFG) system for the hilly and mountainous regions of Hungary (approx. 36,000 km^2). Such forecasting system will be based on ultrashort weather forecasting, numerical models, radar measurements and site-specific precipitation/water discharge functions. In such cases, warning could be issued with a few-hour time lead prior to the occurrence of the flood, potentially preventing economic and life losses. The development of a nationwide flash flood guidance and warning system first requires the application of a rapid screening method to delineate the potentially flash flood affected watersheds. Rapid screening and

identification of flash flood impacted watersheds primarily involves topography (slope) but also considers other environmental factors, such as rainfall intensity and duration, soils, vegetation and land use.

The objective of the present study is to identify the most flash flood prone watersheds of Hungary and to analyze the spatial pattern of the potential environmental factors that may contribute to flash flood generation. Based on the identification and mapping of these environmental factors and documented flash flood events, in the present paper we present the development of a nationwide vulnerability model. This both statistically and historically based map (hereafter HiStaM) forms an initial, but integral part of the nationwide FFG system and is suitable for a decision support system.

Materials and methods

The most important environmental factors we analyzed include precipitation, topography, soils, land use and vegetation and surface rock types. In our initial approach we generated a watershed model for the hilly and low-mountain regions of Hungary by using the appropriate digital elevation (50 meter spatial resolution) and hydrographic models. Watersheds ranging from 10 km^2 to 60 km^2 were delineated with the Hydrogeographical module of ArcGIS 9.2 for the entire land area of Hungary.

The precipitation databases are founded on three datasets that depicts the spatial variance of rainfall patterns in Hungary. These three datasets include the highest measured rainfall intensities, highest cumulative rainfall per a single event, and return time of 40+ mm rainfall events. The applied rainfall data were measured at 99 standard automated weather stations operated by the Hungarian Meteorological Services (Országos Meteorológiai Szolgálat, OMSZ) and are roughly evenly distributed throughout the country. We also incorporated data to the HiStaM from non-automated, manually operated rain gages.

The slope angle map was created from the 50-meter resolution DEM of Hungary in ArcGIS 9.1 and the same software was used to calculate and map the inflection points of each individual watershed. Slopes were classified according to their steepness (slope inclination).

Obviously higher slope inclination and increasing precipitation directly enhance the probability of flood risk. Other environmental factors, such as land use and soils, on the other hand, may decrease flood risk. In terms of land use and land cover we considered bare rock surfaces, meadows, grasslands and other impervious layers as enhancing factors for surface runoff.

Soils were modeled with the $1 : 100,000$ resolution AGROTOPO database (see e.g. Várallyay a et al. 1979; Várallyay et al. 1980a; Várallyay et al. 1980b; Várallyay 1985) from which we a a a used soil physical properties (texture and hydraulic conductivity) and soil thickness.

We deselected limestone and dolomite areas from the geological database of Hungary as limestone and dolomite enhance infiltration along their vertical fractures forming preferential flowpaths. The above described databases were overlaid and processed with ArcGIS 9.2 and IDRISI for Windows 32 softwares to spatially visualize and compare the geographical difference and to identify the possible spatial correspondence among (i) topography, more precisely slope inclination (ii) rainfall pattern and (iii) past occurrence of flash floods . Spatial limitation of the studied environmental factors is primarily determined by precipitation data, as this factor has the poorest spatial resolution.

Historical data were based on literature (documented flash floods) and damage reported to insurance companies. The modeled location of flash flood impacted watersheds and historical

data was then spatially correlated and analyzed in ArcGIS 9.2.

Results

Until today, 835 flash flood, urban and pluvial flood associated damage was reported to insurance companies in Hungary (e.g. Horváth, 1999, Koris and Winter, 2000; Szlávik, 2003; a a Hizsák, 2005, Horváth, 2005; Kovács and Kovács, 2007). Purely based on topography (slope and elevation), potentially flash flood prone (PFFP) areas cover a total area of 36,152 km^2 , i.e. 38.86% of the land area of Hungary. These areas encompass 1,082 watersheds, with and average area of 33.41 km^2. However, in our case study smaller watersheds were delineated in order to spatially homogenize input environmental factors (e.g. soil and canopy) for the hydrological model.

Spatial rainfall patterns reflect only a limited topographically influenced effect. Although the three highest rainfall maxima per event are recorded in mountainous areas, other extreme peak values are located e.g. on the Little Hungarian Plain (LHP) and to a certain extent on the Great Hungarian Plain (GHP). The pronounced high intensity and high accumulated rainfall event in the NW corner of the country was caused by an abrupt convective rainfall event, hence the influence of topography here is unlikely as it is located in the Little Hungarian Plain. Since other high intensity precipitation events were also observed in the Great Hungarian Plain, such events cannot be exclusively associated with an orographic influence. The highest measured hourly rainfall intensities poorly correlate with either topography or the location of documented flash floods. With their relatively low spatial extent, their identification is problematic, at least at the available rain gage frequency. The highest value was recorded in the NW corner of the country (Mosonmagyaróvár, 82 mm h^{-1}). However, the second highest value was reported from the Mátra Mountains (Kékes–teto$''$, 65.5 mm h^{-1}), a typical location for flash flood generation (e.g. Horváth, 2005). A five-year return time of a 40+ mm rainfall per rainfall event seems to be certain over the entire land area of Hungary (based on the 1961-1990 meteorological data set). Correlation between the spatial distribution of flood-affected areas and rainfall pattern within the borders of Hungary is rather poor. Although the map of 40+ mm rainfall per rainfall even indicates a certain degree of orographic effect to explain the higher intense rainfall frequency, the higher rainfall intensity of the SW part of the country (caused by low pressure systems originating primarily from the Mediterranean region) is coupled only with a scarce number of documented flash floods (e.g. B*ü*kk*ö*sdi–víz). A second frequency maximum, due to orographic effects, is found in the two highest mountains of Hungary, the Mátra and the B*ü*kk.

Our former studies indicated that flash floods were not only affected by rainfall intensity and duration, but they are also extremely sensitive to other environmental factors, such as slope, soil type, soil thickness and rock type (Pirkhoffer et al., 2007; Czigány et al., 2008). Soil properties, such as physical soil type and topsoil thickness were also included in the generation of the HiStaM. The AGROTOPO's resolution was sufficient for the development of the HiStaM, although we used a better resolution soil map for our case study (Zalavári, a 2008). Unlike the Alpine region (Ranzi et al., 2007), soil properties considerably affect the rate of surface runoff and, although indirectly, significantly impact stream discharge in Hungary. Soil properties were classified according to hydraulic conductivity and topsoil thickness, i.e. enhancing or mitigating effects on surface runoff. The secondary porosity and macropores of limestones can significantly mitigate the on-site generation of flash floods, while at the perimeter of such areas interflow triggered outflow could significantly contribute to surface runoff. From this consideration, we included the potential effect of limestone rocks in the generation of the HistaM.

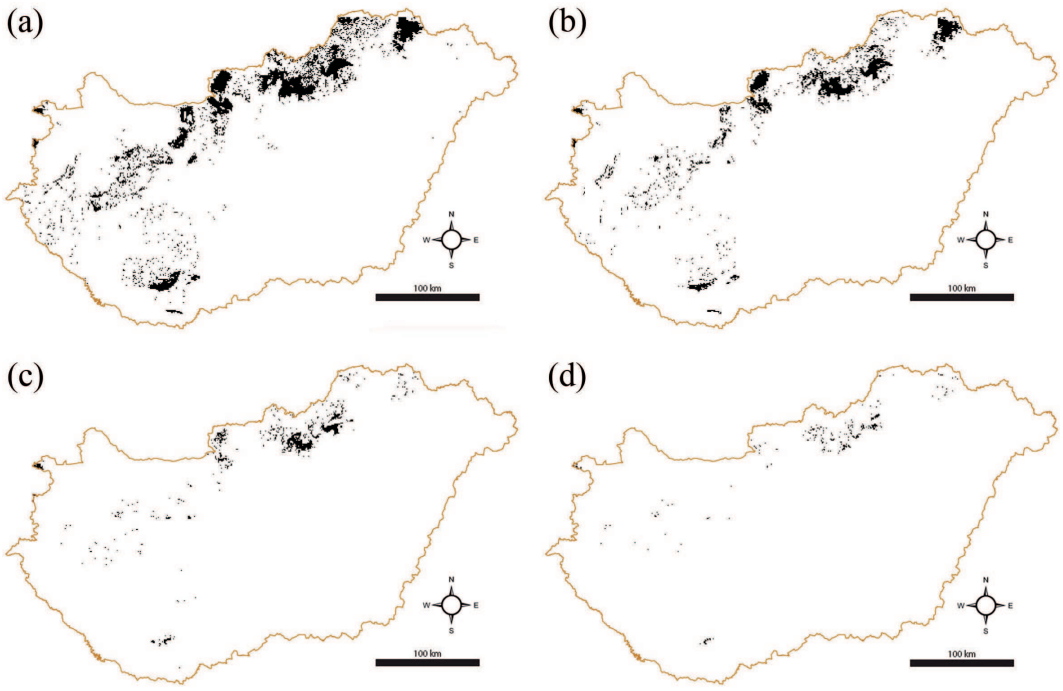

Figure 4.1: HiStaM based flash flood vulnerable locations in Hungary at (a) 1%, (b) 2%, (c)5% and (d) 10% level compared to the highest potential pixel value

When input datasets were overlaid we obtained the location of watersheds of high flash flood vulnerability of the entire country at 1%, 2%, 5% and 10% levels, compared to the potential maximum value of the HiStam (Fig. 4.1).
Observed and documented flash flood affected (ODFF hereafter) areas cover 5,926 km^2, while the HiStaM based modeled area encompasses 5,741 km^2 for all individual points. Our HiStaM overlaps with the ODFF areas on 1,819 km^2 that equals 30.70 per cent of the accumulated area of the ODFFs (Fig 4.2). Outliers were located along the Transdanubian Mountains (Bakony). Hitherto no flash floods have been reported from the Bakony, however topography and soil conditions would favor flash flood generation here. On the other hand, other limestone and dolomite covered areas, such as the Vértes Mountains, the Bükk Mountains and the Aggtelek region have been affected by flash floods several times over the past decades (e.g.: Szilágyi, 1954; Szlávik, 2003). It needs to be mentioned however, that in the latter cases, floods primarily occurred along the perimeter of the limestone areas. The foothill location of documented flash floods can be attributed to the contribution of subsurface runoff that triggers flash floods when water leaves the limestone zones. Another reason for the lack of documented flash floods in the Bakony can be explained by the low spatial density of operating stream gages here. Note that limestone areas could only eliminate in situ flash floods when uncovered i.e. lacking soil cover. In soils on limestones, infiltration obviously reduces and hence runoff increases.

Several severe flash, pluvial and urban floods have been reported from the headwaters of the River Kapos (e.g. Hizsák, 2005), although judging from our historical-statistical model this area is not affected by flash floods. A large flood event occurred here on August 21, 2005, initiated by a 105 mm rainfall event over a 3-hour period. A possible reason for lacking model predicted floods here is likely caused by the considerable anthropogenic influence (impervious layers) of the strongly urbanized area and the increasing extent of clear cuts in the watershed, not included in the CLC2000.

It is noteworthy, that none of the 1 by 1 km pixels reached the potentially highest value

in the HiStaM. This is explained by the high spatial heterogeneity of the observed and studied eight environmental factors. The impact of topography on the HiStaM is obvious. Note, that precipitation is important but not an exclusive factor according to our model. The large rainfall event on the LHP was eliminated by the model and does not appear on the HiStaM provided vulnerability maps (Fig 4.2). Even at 1% level, contiguous flood-influenced areas are only found in the B*ü*kk, Mátra, B*ö*rzs*ö*ny and Mecsek Mountains, hence these areas have the highest potential flash flood vulnerability, where operation of the FFG system is essential. Other hilly and low-mountain regions only show a discontinuous and scattered spatial vulnerability pattern where flash flood generation is less likely, however still expectable. Hence, the FFG system and the nationwide warning should be extended to these latter areas as well.

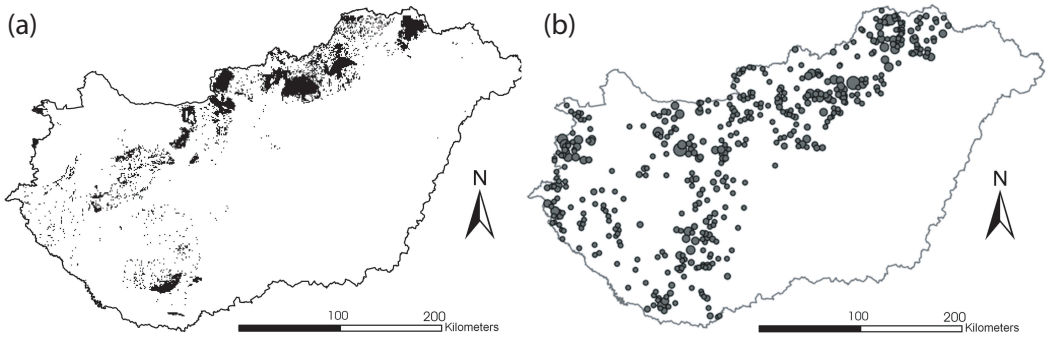

Figure 4.2: Watersheds with potentially flash flood-impacted (black dotted) areas simulated by our historical-statistical model (Figure A); Locations, from which flash, urban and pluvial flood associated damage and economic loss have been reported to insurance companies (Figure B) potential pixel value

Summary and Outlook

Model validation is carried out in a small low-mountain watershed in SW Hungary, the catchment of the B*ü*kk*ü*sd Valley, western Mecsek Mountains. This watershed lies in the flowpath of high convective storm cells, and rainfall intensity is usually further increased by orographic effects. The valley and the surrounding villages have been inundated by flash floods several times in the past (see above). This area was chosen as a typical low mountain watershed in Hungary which could be employed as a model (template) watershed representing the majority of flash flood influenced watersheds in Hungary. Here we monitor the temporally variable environmental factors, namely (i) precipitation, (ii) soil moisture, (iii) canopy cover, and (iv) stream discharge. By monitoring these environmental factors we study the proportion of each factors with which they individually contribute to flash flood generation. We presume that this preliminary monitoring data will increase the spatial accuracy of the watershed identification by the HiStaM. The conclusions derived from the monitored data are assumed to be successfully employed in the flowchart based nationwide FFG system.

References

Czigány, S., E. Pirkhoffer and I. Geresdi (2008): Environmental impacts of flash floods in Hungary in: Samuels, P., S. Huntington, W. Allsop and J. Harrop (eds.): Flood Risk Management: Research and Practice. Taylor and Francis Group, London, ISBN 978-0-415-

48507-4 pp. 1439-1447.

Ely, L. and L. Nagyváradi, 2001: Application of Paleofloods to Flood Hazard Assessment a in Hungary. In: Kovács, J. and Lóczy, D.(Ed.): A vizek és ember. PTE TTK Földrajzi Intézet, Pécs, pp. 189-195.

Eszky, O. 1987. A Bükkösdi-víz felsõ vízgyûjtõjé tervezhetõ árvízcsúcscsökkentõ tározók hidrológiai tanulmányterve. Initial plans for the development of a flood protection reservoir in the headwaters of the Bkksd Valley. Pcs, manuscript, (in Hungarian).

Eszéky, O. 1992. A Bükkösdi-víz vízhozamnyílvántartó állomásainak felülvizsgálata. (Overview of stream gages of the Bükkösd Valley) Pécs, manuscript (in Hungarian).

Gyenizse, P., Szabó-Kovács, B. and Sebõk, M. (2005): Hidrological impacts on the social and economic processes over the Dráva flood plain - Geographical Review (Földrajzi Közlemények) Vol. CXXIX. (LIII.) pp. 67-72.

Hizsák, I. 2005. A Kapos áradása. A Drávától a Balatonig. (Flooding of the River Kapos) A Dél-Dunántúli Környezetvédelmi és Vízügyi Igazgatóság, valamint a Dél-Dunántúli Környezetvédelmi, Természetvédelmi és Vízügyi Felügyelõség idõszaki lapja. 2:6-8. (in Hungarian).

Horváth, E. 1999. Szélsõséges hidrológiai események rekonstruálása feltáratlan kisvízgyûjtõkön. (Reconstruction of extreme hydrological events in poorly studied small watersheds) Vízügyi Közlemények. 81:486-497. (in Hungarian).

Horváth Á. 2005. A 2005. április 18.-i mátrakeresztesi árvíz meteorológiai háttere. (Meteorological aspects of the April 18, 2005 flood event of Mátrakeresztes) http://www.met.hu/pages/vihar20050418.html, last accessed: April 29, 2008. (in Hungarian).

Koris, K. and Winter, J. 2000. Az 1999. évi nyári rendkívüli árvizek a Mátra és a Bükk déli vízgyüjtöin. (Extreme summer flood events in the southern watersheds of the Bükk and Mátra Mountains in 1999) Vízügyi Közlemények, 82:199-219. (in Hungarian).

Kovács, A. and Kovács, P. 2007. Árvíz a Szinván: az orografikus csapadéktöbblet egy extrém esete. (Flood on the Szinva Creek: extreme case of orogrphically influenced precipitation) Légkör. 52:5-7. (in Hungarian).

Lóczy D. and Juhász, Á. 1996: Hungary. In: Geomorphological hazards of Europe. Ed. Embleton, C. and Embleton, Ch. Elsevier, Amsterdam. 243-262.

Pirkhoffer, E., Czigány S., Geresdi I. and Nagyváradi L. 2007. Effect of topography and rainfall pattern on the occurence of flash floods in Hungary. Carpatho-Balkan-Dinaric Conference on Geomorphology, October 24-28, 2007, Pcs, Hungary (poster presentation).

Ranzi, R., Zappa, M. and Bacchi, B. 2007. Hydrological aspects of the Mesoscale Alpine Programme: Findings from field experiments and simulations. Q. J. R. Meteorol. Soc. 133: 867-880.

Szlávik, L. 2003. Az ezredforduló árvizeinek és belvizeinek hidrológiai jellemzése. Hydrological characterization of floods drainage waters of the past 10 years. Vízügyi Közlemények 85:547-565. (in Hungarian).

Vass P. 1997. Árvizek a Bükkösdi-patak felsõ szakaszán. Floods in the headwaters of the Bükkösd Stream) in: Tésits, R. and Tóth J. (eds.): Földrajzi tanulmányok a pécsi doktoriskolából I. Bornus Nyomda, Pécs. P.261-285. (in Hungarian, English summary).

Várallyay G., Szücs L., Murányi A., Rajkai K. and Zilahy P. 1979. Magyarország termöhelyi adottságait meghatározó talajtani tényezk 1:100 000 arányú térképe. I. Agrokémia és Talajtan 28:363-384. (in Hungarian).

Várallyay G., Szücs L., Murányi A., Rajkai K. and Zilahy P. 1980. Magyarország termöhelyi adottságait meghatározó talajtani tényezök 1:100 000 arányú térképe. II. (Soil properties map of Hungary. II., resolution: 1: 100 000) Agrokémia és Talajtan 29:35-76. (in Hungarian).

Várallyay Gy., Szücs L., Rajkai K., Zilahy P., and Murányi A. 1980. Magyarországi talajok vízgazdálkodási tulajdonságainak kategóriarendszere és 1: 100 000 méretarányú térképe. (Soil hydrological properties map of Hungary III., resolution: 1: 100 000) Agrokémia és Talajtan 29:77-113. (in Hungarian).

Várallyay G. 1985. Magyarország 1: 100 000 méretarányú agrotopográfiai térképe. (Soil hydrological properties map of Hungary IV.: aspects of Hydrotopography, resolution: 1: 100 000) Agrokémia és Talajtan 34:243-248.

Zalavári, P. 2008. Térinformatikai módszerekkel segített talajtérkép és talajtani adatbázis kialakítása villámárvizek modellezéséhez. M.Sc. Thesis, University of Pécs, Dept. of Soil Sciences and Climatology (in Hungarian)/

4.4 On testing the stability and reliability of hydrometeor classification operational products

Miria Celano[1], Pier Paolo Alberoni[1,2]

[1] *ARPA - SIMC, Bologna (Italy);* [2] *ISAC - CNR, Bologna (Italy).*

Introduction

The use of polarimetric radar measurements allows to identify the prevailing hydrometeor type and its spatial distribution within a meteorological event. This information is particularly helpful in operational monitoring to characterise deep convection events (especially for hail presence) and winter stratiform snow episodes. Real-time hydrometeor classification maps, from the two polarimetric C-band radars located in the Po Valley and managed by ARPA Emilia-Romagna (S. Pietro Capofiume and Gattatico), are provided to operational meteorologists every 15' to support weather monitoring and nowcasting activities.

Previous studies (Celano et al., 2008) highlighted that hydrometeor classification maps are improved by using a sophisticated analysis method, instead of a simple averaging, to estimate surface temperature, but also that they are quite sensitive to small variations of the radar variables involved. As an example, pre-processing Z and ZDR data using various interpolation methods produces slightly different classification maps. This last consideration leads us to analyse the variability of hydrometeor identification maps resulting from different Z and ZDR field perturbations, in order to study the stability and the reliability of the classification product. Outcomes from this uncertainty study are presented.

The hydrometeor classification algorithm

The hydrometeor classification algorithm used refers to the scheme developed at the National Severe Storms Laboratory (Zrnic at al., 2001), with appropriate modifications to deal with C-band radar data (Marzano et al., 2006). The algorithm is based on a combination of weighting functions mapping the reflectivity Z and differential reflectivity ZDR space and associated with a particular type of hydrometeor.

The environmental temperature is used to remove further ambiguities by introducing the additional constraint that every class of hydrometeor can only be found within a prescribed range of temperatures. The summer version of the algorithm can discriminate the following classes: large drop (LD), light rain (LR), moderate rain (MR), heavy rain (HR), rain-hail mixture (RH), graupel and small hail (GSH), hail (HA), wet snow (WS), dry snow (DS) and ice crystal (IC), whereas the winter version discriminates a reduced set of hydrometeors (LR, MR, HR, WS, DS, IC), excluding classes related to convective events.

Radar fields perturbation and case studies analysed

In order to test the stability of the operational classification algorithm, different perturbations to Z and ZDR radar fields have been applied for two different case studies (a summer

severe storm and a winter snowfall) to investigate the algorithm behaviour in convective and stratiform events.

The summer event occurred in the early afternoon of August 3rd, 2006 and it was characterized by a supercell storm that developed in a frontal system after its interaction with a second convective line located over the Appennines and then swept over the Po Valley. The Doppler analysis detected the presence of the typical supercell vortex and the hydrometeor classification was limited by the strong attenuation phenomenon. This severe event caused many damages to a wide area of the Emilia Romagna Region. The winter episode occurred on January 3rd, 2008 and it led to a copious snowfall lasting over the Region for the whole day.

A first uncertainty study has been implemented by applying a "white noise" to Z and ZDR fields and then producing the resulting hydrometeor classification maps (1 hundred maps for each case study). Fields perturbation has been realized by adding random values Z' and ZDR', ranging from -1 to 1 dB and from -0.5 to 0.5 dB respectively, to Z and ZDR radar variables.

The second uncertainty evaluation has been performed by adding perturbations with different ranges, in order to investigate the stability of the classification maps even in large noise conditions and the different behaviours due to increasing perturbations.

Convective case (03-08-2006 12:34 UTC)

The San Pietro Capofiume operational classification map, displayed in Figure 4.1a, shows that typical convective classes are detected (i.e., LD in purple and GSH in dark green) together with LR, MR and HR classes (from light to dark blue). The HA pixels (light green), instead, refer to clutter areas, especially over the Appennine regions, and they appear as fixed-points when classification maps, collected at subsequent times, are analysed.

For this convective episode, about 5% of the classified pixels changes its assigned hydrometeor type when the "white noise" is applied. These pixels are shown in Figure 4.1b, where some stable areas (see empty light brown circles) and unstable areas (located close to the attenuation cone, see red circles filled with light blue points) are also highlighted. Larger range field perturbations produce appreciable variations (Figure 4.2a, b, c), with an increase of LD and GSH pixels providing a noisy structure to light rain areas (light blue). It is possible to note, anyway, that the main precipitation pattern is similar and maintained for all the maps (i.e., areas with heavy, ice or slighter precipitation), even when the applied noise is much higher than a realistic operational variation (up to -6÷6 dBZ for Z and -3÷3 for ZDR fields displayed in Figure 4.2c).

Histogram displayed in the top of Figure 4.3a represents the occurrence of the hydrometeor type (examining the 100 maps) averaging on all the pixels affected by the noise (ND means no data and NC not-classified pixels). It shows a general picture of the mean "perturbed" pixel, pointing out that the most involved class in perturbation is LR, followed by GSH. Histogram in Figure 4.3b, obtained normalizing the bars values of the previous histogram to the number of pixels of the not-perturbed operational map (for each class type, scaled $x10^4$), highlights that GSH (located close to the attenuation region) is the most "perturbed" class followed by LD, while the other classes present similar behaviours.

Finally, histograms of Figure 4.4 show, for each class of the map obtained assigning the more frequent class to each pixels, the occurrence of all the hydrometeor types in the 100 perturbation maps. RH (assigned to very few pixels) and HA classes (due to clutter phenomenon)

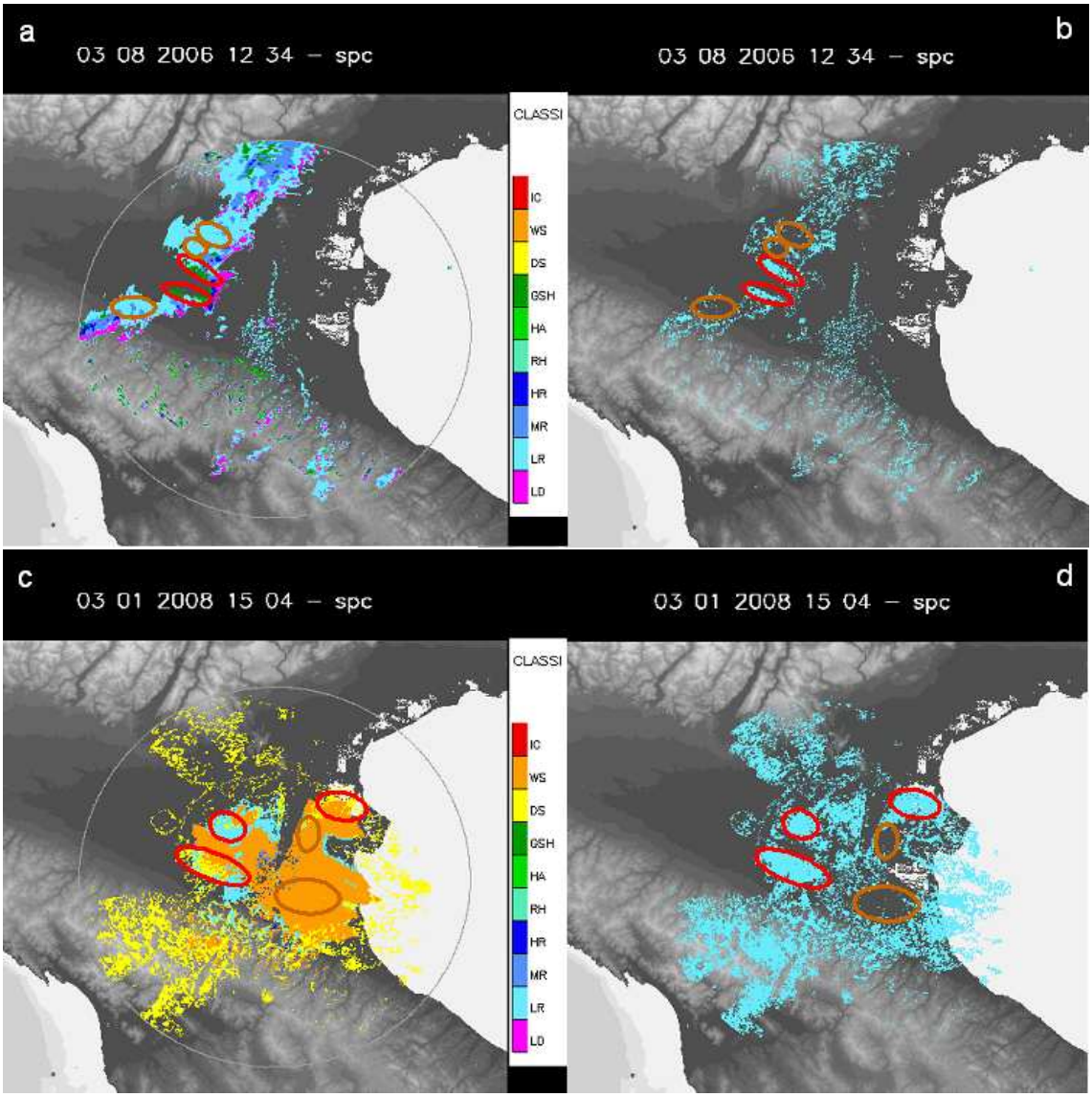

Figure 4.1: On the left: hydrometeor classification maps of 03-08-2006 at 12:34 UTC (a) and 03-01-2008 at 15:04 UTC (c). On the right: pixels changing their assigned hydrometeor type after the addition of "white noise" (b and d, respectively, for 03-08-2006 and 03-01-2008 case studies).

have been not displayed. As is possible to note, classes are quite stable, having the main occurrence higher or close to 80%, while the other assigned classes have quite low occurrence. Further, LR and GSH are the only classes involved in the NC pixels and the more frequent class instead of LD is LR (16.3 %, that is the highest), as can be expected from previous hydrometeor classification algorithm sensitivity analysis (Celano et al., 2005).

Stratiform case (03-01-2008 15:04 UTC)

Hydrometeors detected in the operational classification map (San Pietro Capofiume radar), displayed in Figure 4.1c, are WS (in orange), DS (in yellow), LR (and few HR and MR classes) and pixels affected by the perturbation are about 17%, much more than for the convective case. Figure 4.1d highlights that WS areas are quite stable (empty light brown circles), whereas the mixed regions (LR-DS-WS, red circles) are the most variable, followed

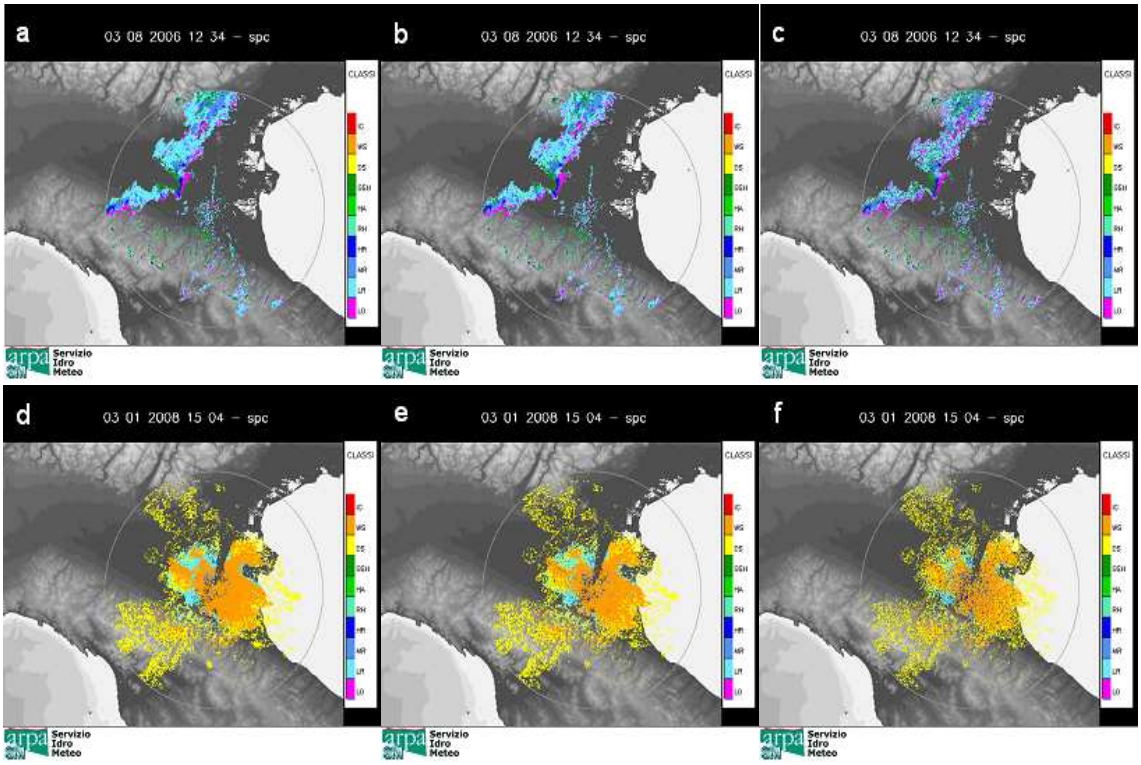

Figure 4.2: Hydrometeor classification maps of 03-08-2006 at 12:34 UTC (top panels) and 03-01-2008 at 15:04 UTC (bottom panels) obtained by adding three increasing perturbations to Z and ZDR fields (-2≤Z≤2, and -0.5≤ZDR≤0.5, a and d maps; -3≤Z≤3 and -1≤ZDR≤1, b and e maps; -6≤Z≤6 and -3≤ZDR≤3, c and f maps).

by the DS areas.

Considering the pixels affected by the "white noise", DS (with NC data) turns out to be the class most involved in the perturbation (histogram shown in Figure 4.3c), whereas when the occurrence is normalized to all the pixels, MR and LR appear to be quite unstable too (Figure 4.3d). Figure 4.5 displays the occurrence of hydrometeor types for each class of the more frequent classification map. Because the few MR and HR classes detected near the ground for the snowfall event are supposed to be mis-classified pixels, the statistical analysis for these types of hydrometeors has not been performed.

As in the previous convective case, all the classes turn out to be quite stable. DS is the class more involved in Not Classified pixels, the more frequent class instead of LR is DS (10.9%), of WS is DS (9.8%) and of DS is IC (13.8%).

Conclusions

In both case studies analysed, classification maps, resulting after the Z-ZDR field perturbations, maintained the main precipitation pattern, confirming a good stability and reliability of the hydrometeor classification algorithm used for operational activities.

The stratiform event presents stable WS areas, while DS and mixed regions are quite variable. For the convective episode, the areas most affected by the perturbation are those filled with GSH and LD classes.

Moreover, the severe convective case classification has shown a better stability respect of the stratiform one (5% varying pixels vs 17%), with the exception of the areas affected by strong

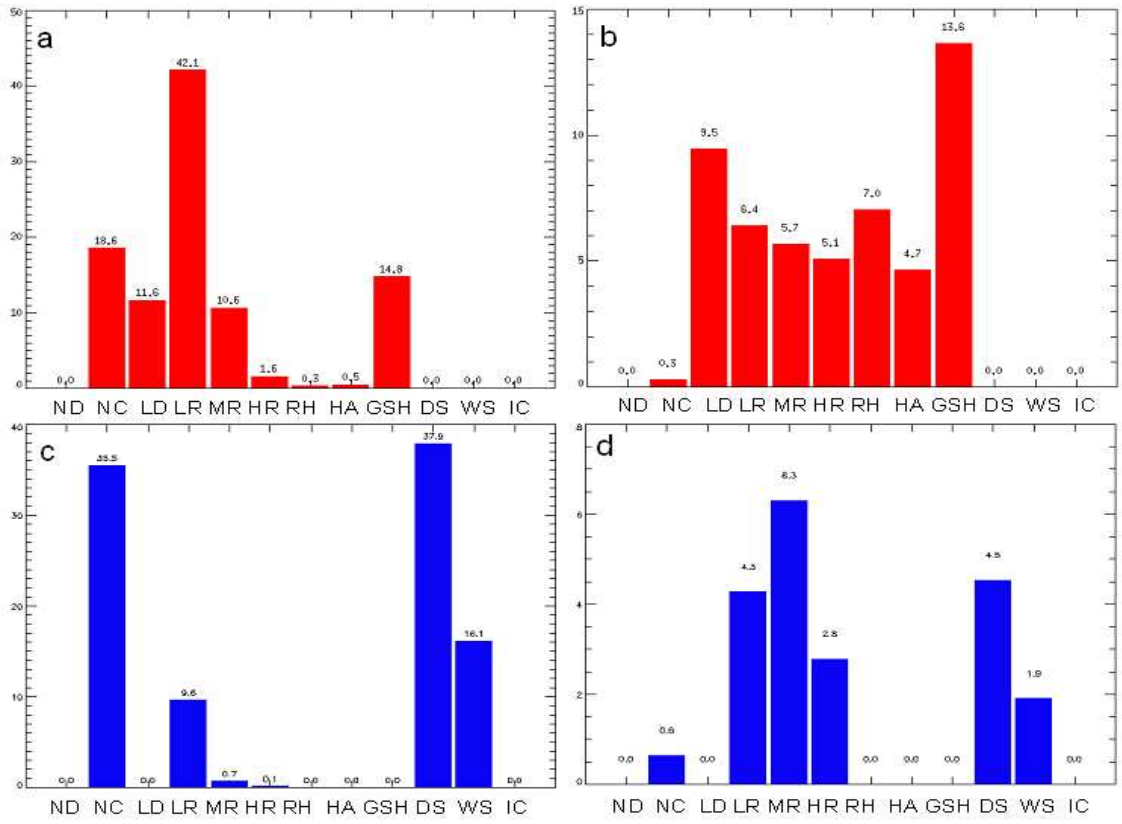

Figure 4.3: Left histograms: occurrence of the hydrometeor type averaged on the pixels affected by the noise for the 03-08-2006 (a) and the 03-01-2008 (c) case studies. Right histograms are obtained normalizing the bars values of left histograms to the pixel number of the not-perturbed operational map (for each class type, scaled x10^4), for the 03-08-2006 (b) and the 03-01-2008 (d) case studies .

attenuation (where especially GSH is detected).

References

Celano, M., P.P. Alberoni, V. Levizzani, and A. R. Holt, 2005: Analysis of severe con- vective events from two operational dual polarisation Doppler radars. Natural Hazards and Earth System Sciences (NHESS), 6, 397-405.

Celano, M., C. Govoni, P.P. Alberoni, 2008: Using a hydrometeor classification algorithm from two Doppler C-band radar data to infer snowfall areas in winter events. WRAH Conference, 10-15/03/2008, Grenoble, France.

Marzano, F. S., D. Scaranari, M. Celano, P.P. Alberoni, G. Vulpiani and M. Montopoli, 2006: Hydrometeor Classification from dual-polarized weather radar: extending fuzzy logic from S-band to C-band data. Adv. Geosci., 7, 109-114.

Zrnić, D. S., A. V. Ryzhkov, J. M. Straka, Y. Liu, and J. Vivekanandan, 2001: Testing a procedure for automatic classification of hydrometeor types. J. Atmos. Oceanic Technol., 18, 892-913.

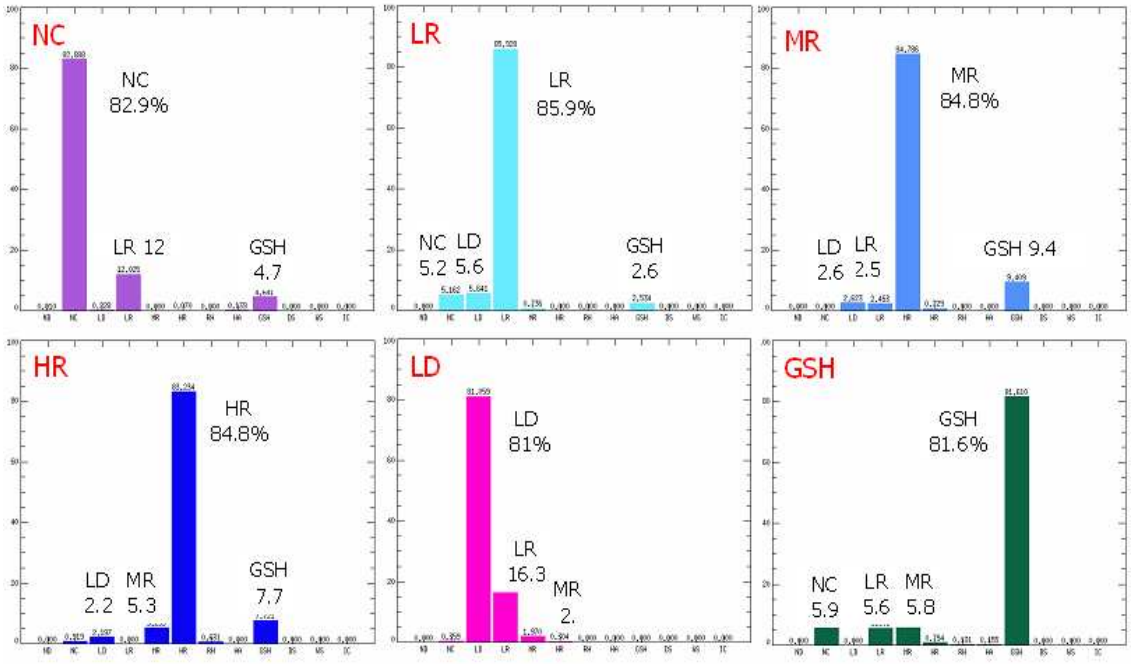

Figure 4.4: 03-08-2006 12:34 UTC; histograms of the occurrence of the hydrometeor types, for each class of the more frequent classification map.

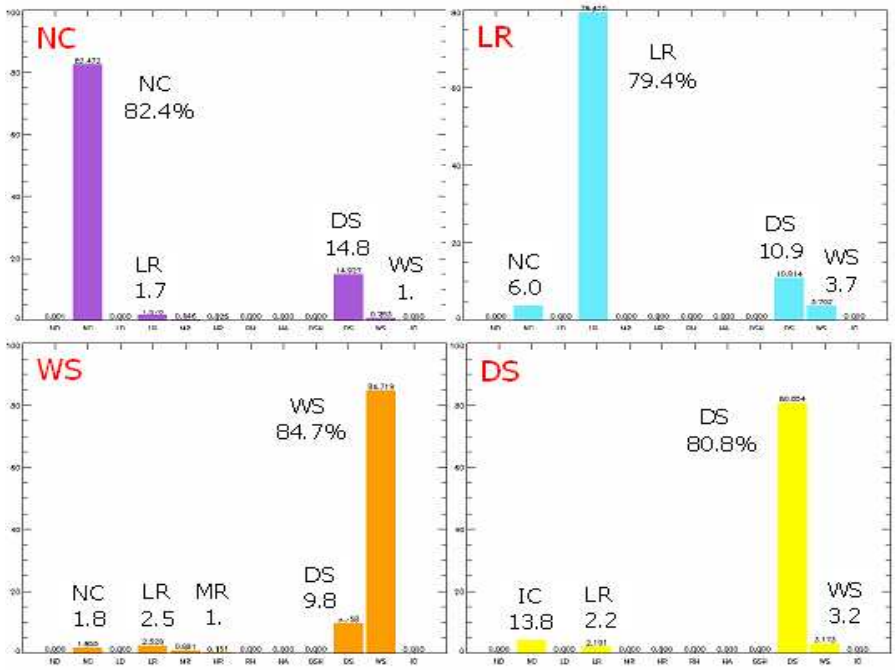

Figure 4.5: 03-01-2008 15:04 UTC; histograms of the occurrence of the hydrometeor types, for each class of the more frequent classification map.

Aknowledgments

This activity is carried on in the framework of projects PROSCENIO and "Mod-Met" supported by National civil Protection Dept.

5.1 Uncertainty assesment in the framework of radar quantitative precipitation estimate developed at ARPA-SIM

Anna Fornasiero [1,2], Pier Paolo Alberoni[1] and Roberta Amorati[1]

(1) ARPA-SIMC, Bologna, Italy, (2) CIMA foundation, Savona, Italy

Abstract

Uncertainty assessment in radar quantitative precipitation estimate (QPE) is one of the most challenging tasks in the radar hydrometeorology studies. Several sources of error affect the quality of radar data, like poor calibration, clutter, beam blocking, attenuation, anomalous propagation, variation of reflectivity with height etc. and their effects propagate along the data elaboration process up to the final product. In most cases well-constructed correction procedures are applied, which reduce the impact of these errors, but often the final reliability of the rainfall estimate is not described. The scope of this work is the validation of the framework developed at ARPA-SIM for its regional radar network which is consisting of two radars located in San Pietro Capofiume and Gattatico. Three versions of the QPE procedure are compared. The first one corrects the Doppler filtered reflectivity data for anomalous propagation and clutter; the second one adds beam blocking evaluation and correction and improves anomalous propagation detection using a beam trajectory model which accepts radiosounding data as input; the last one adds the reconstruction of the rainfall rate at the ground level by means of the identification of a mean Vertical Profile of Reflectivity. The radar products are evaluated by comparison with the measurements of a network of quality controlled raingauges; the mountains area is separated from the rest of the radars domain and the rainfall is cumulated during the whole event. The analysis is carried out on mainly stratiform cases: some statistical scores are calculated and the precipitation fields are observed to describe the reliability of the different radar QPE products.

Incidence of QPE error sources

Radar QPE accuracy is a strategic information for meteorological services, especially in order to monitor the areas where raingauges are absent, but it is still a field of investigation. In fact, the incidence of different uncertainty sources varies considerably depending on local climatology and topography and on radar systems types. The magnitude of different errors is a crucial point to define the best QPE strategy in each particular condition.

For non polarimetric radars it is possible to group the errors in three types: hardware dependent, related to reflectivity (Z) retrieval and to the conversion of Z in rain rate .

Hardware uncertaintes are caused by the poor knowledge of the instruments characteristic which can change in time due to substitution or deterioration of the components: antenna positioning, transmitting chain and receiving chain require therefore a constant monitoring, in other words, calibration. Reflectivity measurement are spoiled by clutter (due to ground, anomalous propagation, sea, birds and insects, clear air), attenuation (due to radome, gas, rain, hail), beam blocking, hail echoes, inhomogeneous beam filling. Finally, the conversion of reflectivity into rain rate (R) is subjected to errors due to vertical reflecivity variation,

overhanging precipitation, wind drift, Z-R relation. In fig. 5.1 is shown a summary table of the principal sources of error at midlatitudes (Fornasiero, 2006) filled considering a wide literature and the research works of Fabry et al. (2004) and Saltikhoff et al. (2004). The bars show the range of relative error in % units over a cell of 1km x 1km produced by different factors.

Ground clutter, vertical reflectivity variation, beam blockage and attenuation show the higest impact, and they are able to nullify the reliability of a rain rate estimate. The Table is useful to compare different errors but not sufficient to define the data correction priorities. Another information should be added about the errors frequency, which is dependent on the local conditions.

Figure 5.1: Range of relative errors (%) in radar QPE for a cell of 1 km x 1 km. Where the colours becomes darker are to be intended extreme values.

Po Valley region and errors localization

The two radar systems of San Pietro Capofiume and Gattatico managed by ARPA-SIM (hereinafter SPC and GAT) are located in the Po Valley, an area of Northern Italy limited in the Southern part by the Appennini mountains, in the Northern and West one by the Alps and in the East part by the Adriatic Sea. They monitor therefore a region which is partially flat and partially characterized by complex orography. The climat in the Valley is continental: wet and hot in summer, with cold winter.

Anomalous propagation incidence

At the interface between cold-humid and warm-dryer layers the refraction index of air decreases sharply causing a deviation of the radar beam from its standard trajectory toward the ground. This condition is called supperrefraction and the effect on the beam path is known as anomalous propagation (AP), and causes a huge increase of clutter echoes. The nocturnal radiative cooling, in presence of stability conditions, produces a type of atmospheric stratification having the mentioned characteristics (surface temperature inversions

and humidity trapped close to the ground) during the whole year. Nevertheless in Summer the anomalous propagation is more frequent and more marked because the absolute humidity and its gradient are higher; in fact the variables governig the phenomenon are temperature, pressure and vapor pressure.

The Po Valley presents the highest climatological values of humidity in Italy (APAT, 2005) and this is the main reason why the area is often characterized by superrefraction conditions. Moreover, sometimes cool and humid air is advected from the sea over land by the sea breeze. In the ECMWF report (Lopez, 2008) is represented the superrefraction occurrence frequency simulated by the global model: the Po Valley shows the highest incidence in Europe together with the south-western Spain and the Tirrenic central coast of Italy. Two previous studies in this area (Alberoni et al. 2001, and Fornasiero et al, 2006 (1)), showed how anomalous propagation conditions are very frequent, mostly in Summer during the night (80% of incidence). Therefore the first ARPA-SIM QPE framework handled the errors produced by mean and AP clutter.

Beam blocking effect

The shielding effect of mountains reduces the radar visibility at the lowest elevations in a variable measure, depending on the propagation conditions. Since SPC and GAT radars are scanning an area partially covered by mountains, this effect is not negligible. A large area beyond the Appennino mountains is totally screened at the first elevation, and partially at the sequents, for both radars. This justifies the introduction, in the QPE framework, of an algorithm to correct beam blockage rate, which simulates the beam propagation conditions through a model based on radiosounding data.

VPR impact

During the cold season the zero degree level is on the average about 1500 m above the ground in the Po valley. Precipitation patterns are mainly stratiform and also bright band and the vertical reflectivity variation affect the radar QPE. When the rain rate is accumulated over some hours the VPR impact on the QPE maps is evident and dramatic. On the contrary in Summer this effect is minor because the vertical reflectivity gradients are negligible during convective event (in the range of heigth sampled to retrieve the QPE). Therefore the last ARPA-SIM QPE framework is integrated by reflectivity reconstruction at the ground level.

Other uncertainty sources

Other uncertainty sources are not addressed here, for example attenuation, drop size distribution variability, secondary trips, precipitation type. Their impact on the QPE quality is not negligible but minor respect to the above mentioned sources, for magnitude and frequency in the considered area. They can be taken into account in the characterization of the QPE quality pixel by pixel; in the ARPA-SIM framework for example a raw index of attenuation contributes to define the quality value of the rain rate field (Fornasiero, 2006).

ARPA-SIM QPE framework evolution

During the years the radar QPE framework has undergone several improvements addressing the principal error sources in the Po valley. The first one (2001) extrapolated the precipita-

tion at the ground level considering the lowest available Z measure not affected by ground clutter and converting it into precipitation, after AP clutter removal. The first condition was satisfied by means of a static map, which recorded pixel by pixel the elevation not affected by clutter in normal propagation conditions and during not rainy weather; AP clutter was removed observing the vertical coherency of the signal (Alberoni et al. 2001).

The second QPE framework (2006) added beam blocking correction and improved anaprop reduction by means of trajectory simulation based on the radiosounding data and on a multy ray representation of the beam. Instead of a static map of elevations, a dynamic one was used (Fornasiero et al. 2006 (2)).

The third and more recent framework (2008) is integrated by VPR calculation based on the method described by Germann and Joss (2002); the VPR is then quality controlled, analyzed and used to reconstruct the precipitation at the ground level (Fornasiero, 2008).

Case studies

The change of accuracy in radar QPE, produced by the frameworks evolution, was analized comparing the radar estimate with respect to the accumulated rain rate measured by raingauges, in two different case studies and for GAT radar. The first one, occurred in March 2007, is stratiform with bright band close to the ground, the second one is a mixed convective-stratiform event occurred in May 2007. The radar precipitation field is calculated considering the 125-km range acquisition (PRF=1200 Hz) and a 4-elevations volume scan.

The quantitative comparison was performed separating the flat area and the mountains area. In fig. 5.2 are represented the scores calculated for different thresholds, using the three schemes in the event of 24-28 March 2007. In the flat area, since the beam blocking problem is absent, the difference between frameworks 2001 and 2006 is negligible. The VPR correction (2008) improves the bias score and the critical succes index whereas the number of false alarms shows a sligth variation. The absolute values of BIAS and RMSE are reduced.

Over the mountains the algorithms 2001 and 2006 are more different (fig. 5.3). The framework 2006 produces an improvement for low thresholds which is lost for higer thresholds. The reason is probably the elevation change behind the mountains induced by the beam blocking algorithm, which leads to sample the reflectivity far from the ground. The addition of VPR correction (2008) smooths the problem and corrects this behavior.

For the second event, the scores are represented in fig. 5.4 and in fig. 5.5; an appreciable difference is present in the mountains area and between the 2006 and 2001 frameworks, due to the visibility change produced by the introduction of the beam blocking algorithm. The difference respect to 2008 is slight and difficult to evaluate (even if a bit of accuracy seems to be gained), because the effect of VPR correction is limited to the instants where the mean VPR has a stratiform shape (when the behaviour is convective, no correction is applied).

Summary and Outlook

The progressive introduction of AP clutter detection, ray path-beam blocking simulation and VPR correction in the ARPA-SIM QPE framework has certainly increased the quality of the QPE product during the years. The rain rate maps are now less noisy, more continouous behind the mountains and bright band signatures are smoothed. Otherwise the local evaluation is particularly tricky especially for the 2008 framework. The application of an averaged VPR to the whole map is in fact able to increase locally the errors especially in mixed cases,

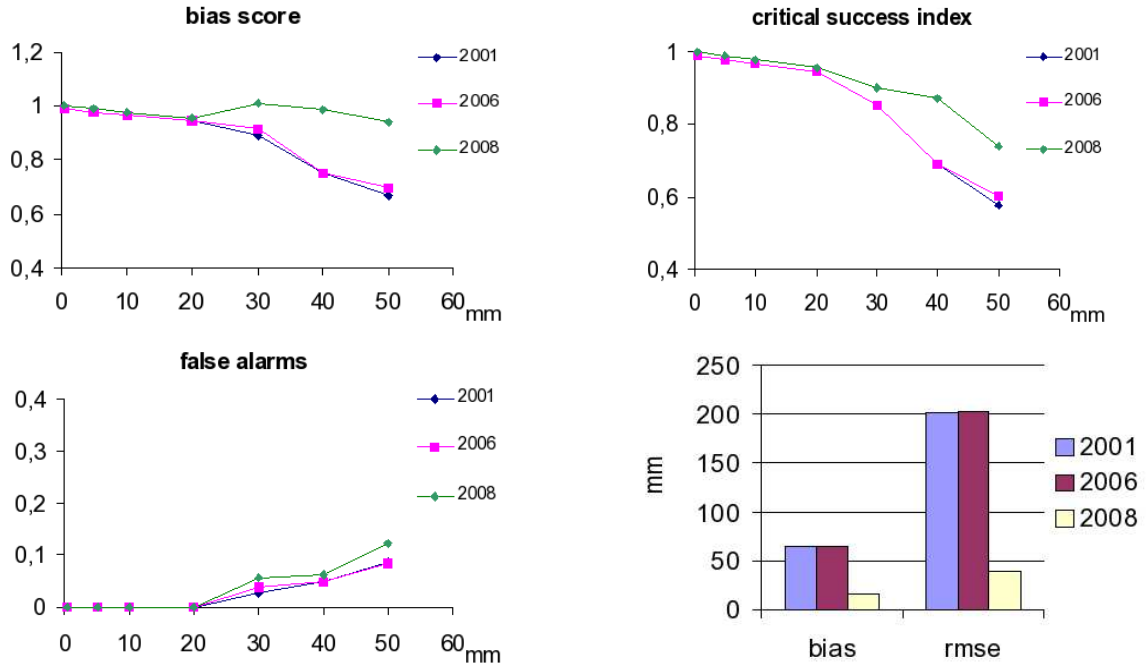

Figure 5.2: 24-28 March 2007, flat area: QPE scores for the three frameworks.

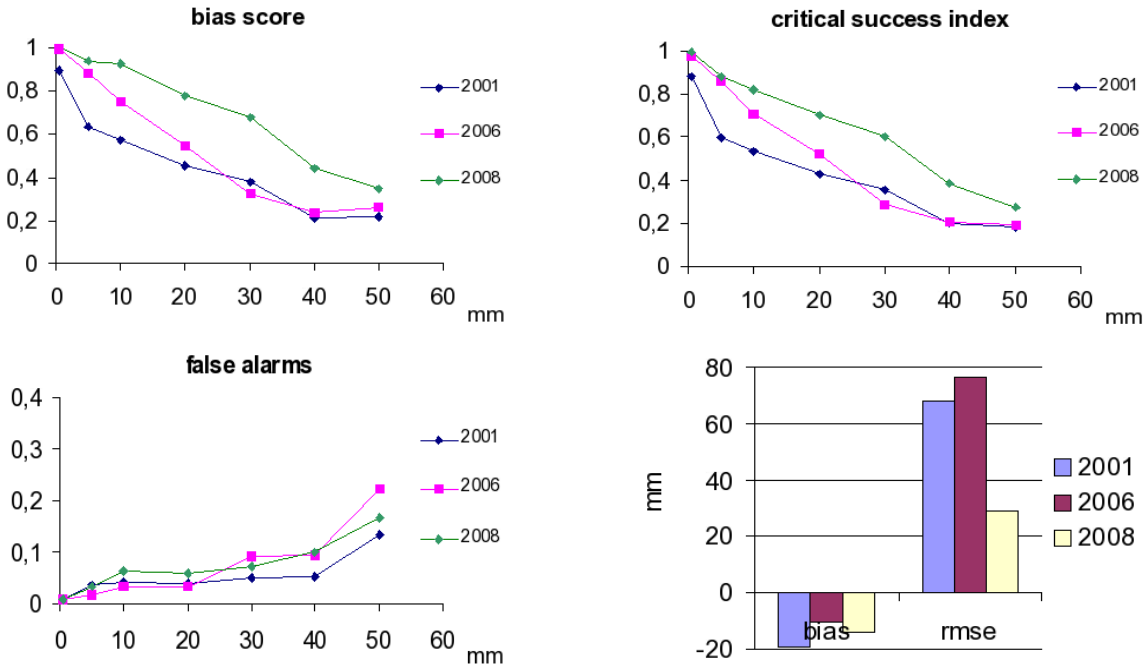

Figure 5.3: 24-28 March 2007, mountains area: QPE scores for the three frameworks.

even if on average it reduces BIAS and RMSE. Another point is the different efficacy of the frameworks in flat land and over the mountains: the performances are better over flat land due to the absence of beam blockage and to the minor impact of beam overshooting and VPR. In the mountains area the beam blocking correction improves the maps quality, but may increase VPR problems. In mainly convective cases the major effect on the scores is given by the beam blocking algorithm, whereas VPR correction produces small changes that are difficult to appraise. The results suggest to apply the VPR only in pure stratiform cases.

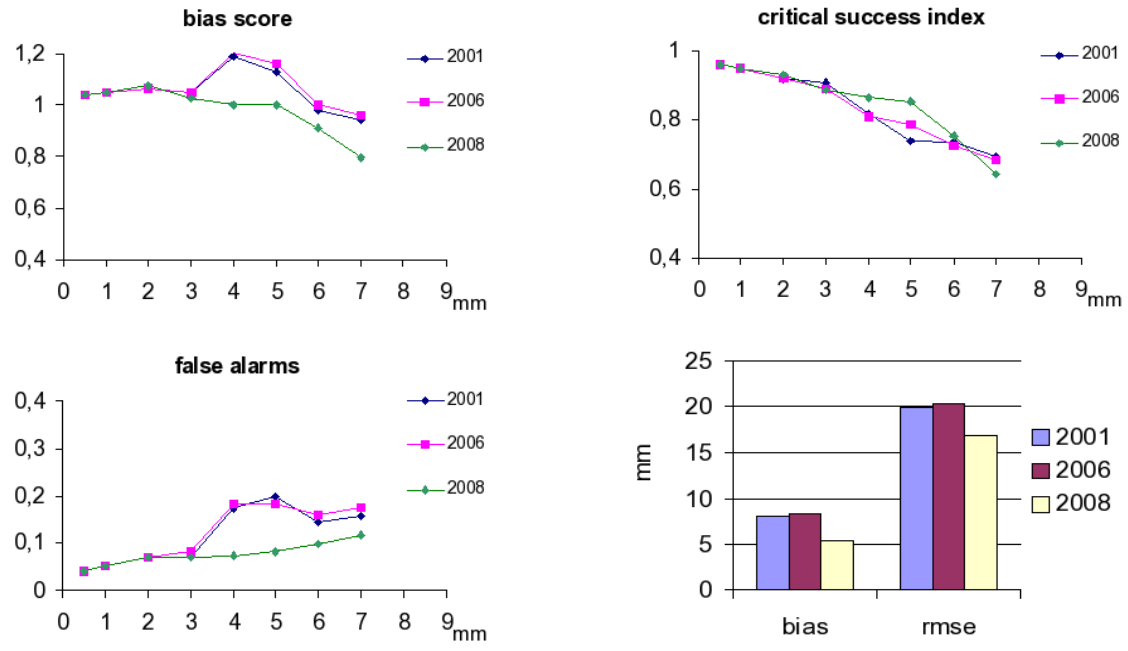

Figure 5.4: 4 May 2007, flat area: QPE scores for the three frameworks.

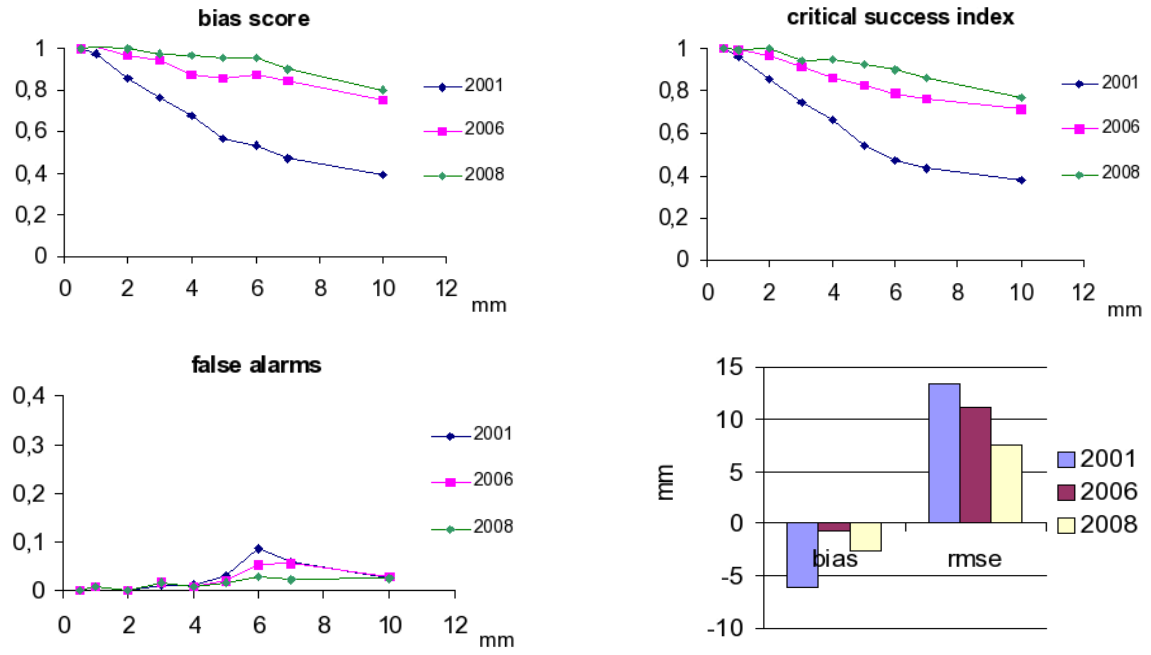

Figure 5.5: 4 May 2007, flat area: QPE scores for the three frameworks.

More work is also needed to improve radar QPE; a next interesting step could be the introduction of an algorithm of separation stratiform-convective to distinguish the two contributes in the VPR calculation and in the Z-R conversion. Moreover, in an optimal chain of QPE retrieval, the different behaviour of the correction procedures should be taken into account to define a decision tree able to track automaticly the more appropriate QPE path.

References

Alberoni, P. P., T. Anderson, P. Mezzasalma and D. B. Michelson and S. Nanni, 2001: Use

of the vertical reflectivity profile for identification of anomalous propagation. Meteorological Applications, No 8 , 257-266.

APAT, 2006: Gli indicatori del Clima in Italia nel 2005, anno I.

Fabry, F., 2004. Obstacles to the grater use of of weather radar observations. Preprints, 6th international symposium on hydrological applications of weather radar, Melbourne, Australia.

Fornasiero, A. 2006: On the uncertainty and quality of radar data. Phd Thesis. Universit degli Studi della Basilicata.

Fornasiero, A., Bech, J. B., Alberoni, P.P., 2006 (1): Statistical analysis and modelling of weather radar beam propagation conditions in the Po valley (Italy), NHESS No 6, 303-314.

Fornasiero, A., Bech, J. B., Alberoni, P.P., 2006 (2): Enhanced radar precipitation estimate using a combined clutter and beam blockage correction technique, NHESS No 6, 697-710.

Fornasiero, A. 2008: Radar quantitative precipitation estimation at ARPA-SIM: a critical approach to retrieve the rainfall rate at the ground level. 5th Eur. Rad. Conf. Helsinki, Finland.

Germann, U. and J. Joss,2002: Mesobeta profiles to extrapolate radar precipitation measurements above the Alps to the ground level, J. Appl. Met., 41, 542-557.

Lopez, 2008: a 5-year 40-km resolution global climatology of super-refraction for ground-based radar meteorology. ECMWF technichal memorandum No 549.

Saltikhoff, E. and the NORDRAD/BALTEX TEAM, 2004: Radar data quality issues in Northern Europe. 3rd Eur. Rad. Conf. Visby, Sweden.

5.2 Data assimilation experiments with ensemble Kalman filter

Bogumil Jakubiak

University of Warsaw, ICM, Pawińskiego 5A, 02-106 Warsaw, Poland

Introduction

Kalman filtering approach to data assimilation in meteorology and oceanography has more then twenty years of implementation. Introduced to oceanography by Evensen (2003), ensemble Kalman filtering approach has been extensively developed in US and results are presented in number of papers. First implementation of the ensemble Kalman filter to storm-scale events using simulated data was reported by Snyder and Zhang (2003), and later on by Tong and Xue (2005). Results of experiments with assimilation of real radar data were presented by Dowell at al. (2004). The progress in implementation of filtering methods to data assimilation was possible after the development of the square root filters concept (Anderson, 2001), an implementation of sequential analysis of observations (Anderson, 2003) and development of the DART - the modern software tools able to run experiments in efficient way. To learn the features of the filtering methods, from number of models available in DART environment we choose the simple one-dimensional Lorenz L96 model and two-layer isentropic primitive equation model.

Algorithm of the ensemble filtering approach

The ensemble Kalman filer is formulated as two-step procedure. First step is a forecast of the model state to the next observation time. The ensemble members are evolved independently, according to the nonlinear weather prediction model. The second step is the analysis, i.e. adjustment of the entire ensemble to the information available in new observations. Such update reflects both the new state estimate and the uncertainty included in observations. The input to the filter analysis are:

- the background (forecast) ensemble $\left\{\mathbf{x_b^i} : \mathbf{i} = \mathbf{1}, \mathbf{2}, ...\mathbf{k}\right\}$
- the observation operator $\mathbf{H} : \mathbf{R^m} \rightarrow \mathbf{R^s}$ that maps the model space to the observation space
- the observations $Y^o \in \mathbf{R^s}$
- the observation error covariance matrix $\mathbf{R} \in \mathbf{R^{sxs}}$

We assume that the best available estimate to the system state, before the observations are taken into account, is the background mean.

$$\bar{\mathbf{x}}_b = (k-1)\sum_{i=1}^{k} \mathbf{x_b^i} \tag{5.1}$$

Define the $m \times k$ matrix of background ensemble perturbations $\mathbf{X_b}$ whose i^{th} column is $\mathbf{X_b^i} = \mathbf{x_b^i} - \bar{\mathbf{x}}_\mathbf{b}$. Then the background uncertainty in this state estimate is described by the background error covariance matrix

$$\mathbf{P_b} = (\mathbf{k-1})^{-\mathbf{1}}\mathbf{X_b}(\mathbf{X_b})^\mathbf{T} \tag{5.2}$$

Sequential assimilation of the observations is easier to implement and finally it gives the same result as simultaneous processing of all observations. To compute the state variables ensemble we need to compute the prior ensemble estimate of observation k using state variable ensemble updated by all observations prior to k, compute update increments for each ensemble member, and finally update the estimate of the state variables for each ensemble member.

$$\begin{gathered} x_i^o, i = 1, ...N \\ y_{i,k}^p = h_k(x_i^{k-1}) \\ \Delta_{i,k}^{k-1} = y_{i,k}^p - y_k \\ x_{i,j}^k = x_{i,j}^{k-1} + \frac{cov_{xj,yk}^{k-1}}{var_{yk,yk}^{k-1}} \Delta_{i,j}^{k-1} \end{gathered} \tag{5.3}$$

In sequential filter algorithm the forward observation operator for the first observation is applied to the ensemble state vector x^1 to produce a prior ensemble approximation, y^1, of the observation. Observation increments, Δy^1, are computed using the observation value, $\widetilde{y}^1$ and error variance, $\sigma_{o,1}^2$, and regression is used to compute increments for the state. The state is updated by adding the increments to produce x^2 and the process is repeated for each observation in turn.

The output of the analysis are the analysis ensemble $\{\mathbf{x_i^a} : \mathbf{i} = \mathbf{1}, \mathbf{2}, ...\mathbf{k}\}$, the analysis mean and the analysis error covariance matrix. The analysis mean $\bar{\mathbf{x}}_a = (k-1)\sum_{i=1}^k \mathbf{x_a^i}$ represents the estimate of the system state after the observations are assimilated and the analysis error covariance matrix $\mathbf{P_a} = (\mathbf{k-1})^{-\mathbf{1}}\mathbf{X_a}(\mathbf{X_a})^\mathbf{T}$ represents the uncertainty of this estimate.

Ensemble Kalman Filter is based on the Monte Carlo integration of the Fokker-Planck equation and its convergence rate for linear Gaussian problems depends on the dimension of the phase space.

Experiments with L96 Lorenz model

The Lorenz L96 model represents an 'atmospheric variable' x at m-equally spaced points around a circle of constant latitude. The j^{th} component is propagated in time following the differential equation with the quadratic advection term that conserves the total energy and linear dissipation and external forcing terms. Our experiments with L96 model concentrated on testing the way of reducing the sampling errors due to noise. Model imperfections lead to erroneous prior distribution. Filter sampling errors lead to too little variance in priors. The common method in such cases is to implement covariance inflation. The method is based on the idea that the true is farther from ensemble mean than it is suggested by the prior sample. Covariance inflation avoids this by increasing the prior variance. After the model

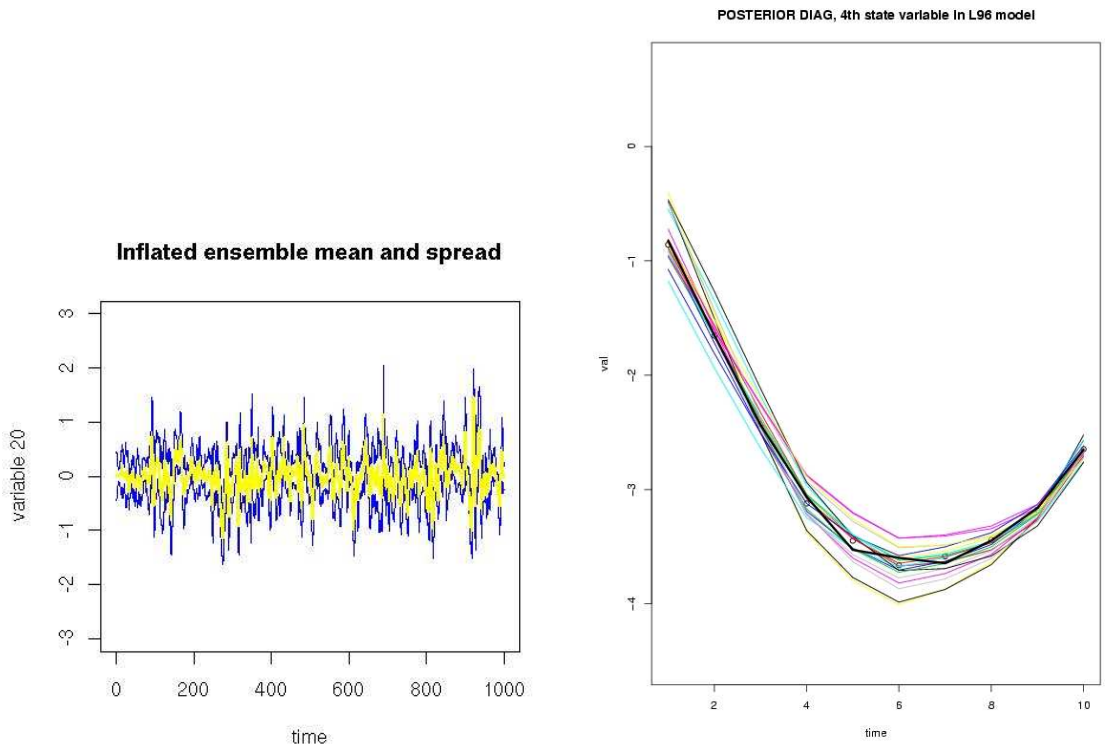

Figure 5.1: Experiments with covariance inflation in L96 model

is advanced in time, the prior sample variance of each model state variable is increased by linearly inflating the ensemble around its mean. Left panel of Fig. 5.1 shows the evolution in time the inflated ensemble mean and spread for the variable 20 of the L96 model. Right panel on that same figure shows posterior diagnosis of each realization form 20 member ensemble and the ensemble mean for the 4^{th} state variable

Experiments with isentropic primitive equations model

The more realistic, isentropic, primitive equations two-layer pe2lyr model was implemented to DART by Jeffrey Whitaker. We used the model in a standard configuration 71×36 points. We generated 100 day sequence to use in spinning up the model. After that we generate 50 day sequence to use it as the basis for 20 ensemble members tests. After these computations we run filter to generate 80 ensembles perturbed from single restart file. Examining the ensemble spread we found it not enough, so we rerun the model and the filter starting with the final states from the previous step.

The pe2lyr model has three variables: interface height, zonal and meridional wind components. In our experiments only wind components were assimilated, interface height was used for diagnostic purposes. On Fig. 5.2 both wind components are presented on upper and bottom layer respectively. This ensemble mean after 50 days of integration show well developed structures of the flow. The interface height on bottom and upper levels presented on Fig. 5.3 reflect the features of wind field assimilated by that model. The variability of the height is from -2242.55 to 13308.1 m.

More detailed inspection of the time series of wind components presented on Fig. 5.4 and Fig. 5.5 in selected point (in that case in Central Poland) shows stronger variability of both components during the first 30 days of data assimilation. These results are for 80 member

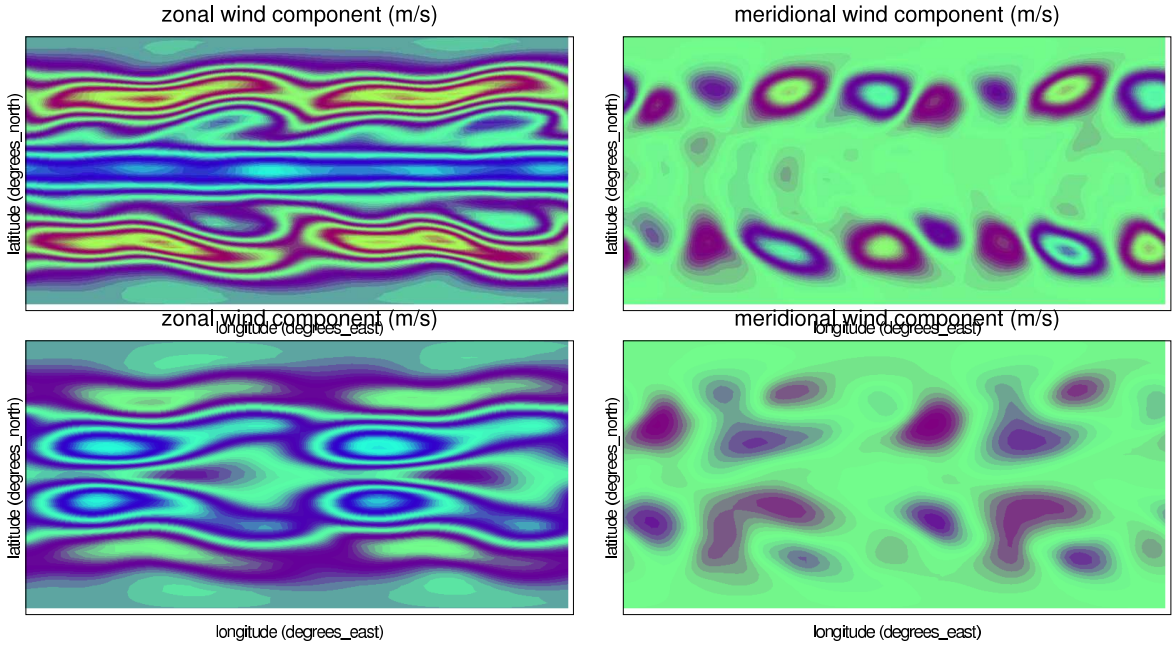

Figure 5.2: Zonal and meridional wind components after 50 days of integration

ensemble mean.

Summary and Outlook

The main purpose of these experiments was to familiarize ourselves with the modern data assimilation tools developed in a frame of the Data Assimilation Research Testbed (DART) initiative. We found this tool very efficient, well designed and programmed. We would like to use the DART for experiments with the numerical weather prediction model COAMPS. Square root ensemble filters available in DART are formulated in a such manner, than they could be used in real atmospheric applications. The statement that the data assimilation for high-dimensional nonlinear atmospheric models is a challenging task is true and will be valid in near future. The important issue in future implementation of DART to the the operational data assimilation schemes is a proper use of the uncertainties (sources of errors) in a manner similar to proposed by Jeffrey Anderson and his colleagues.

Acknowledgments:

This research has been partly supported by the NICOP program under the grant N000140510673 and by the KBN grant COST/20/2006. We used computer resources of ICM, Warsaw University. For assimilation experiments the DART software from NCAR was

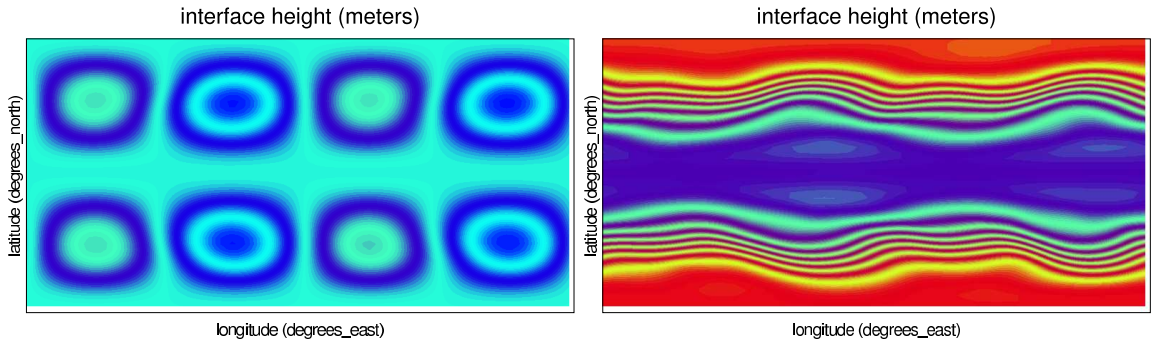

Figure 5.3: Posterior diagnostics: variable Z, levels 1 and 2, time=50 days

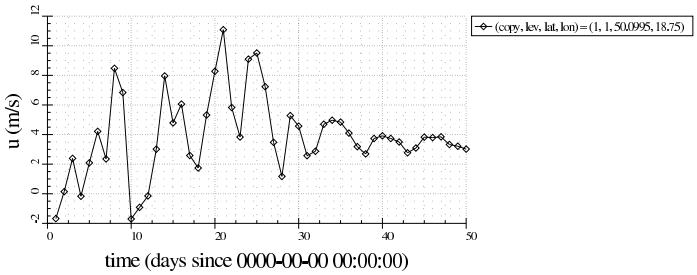

zonal wind component from posterior ensemble state

Figure 5.4: The zonal wind component for the point (50.1N, 18.75E), level 1

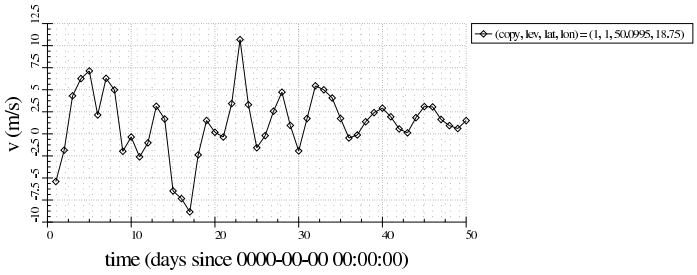

meridional wind component from posterior ensemble state

Figure 5.5: The meridional wind component for the point (50.1N, 18.75E), level 1

used. Pictures were printed using ncview facility.

References

L.J. Anderson, 2001: An ensemble adjustment Kalman filter for data assimilation. Mon. Wea. Rev., 129, 2884-2903.

L.J. Anderson, 2003: A local least square framework for ensemble filtering. Mon. Wea. Rev., 131, 634-642

C.D. Dowell, F. Zhang, L.J. Wicker, C. Snyder and N.A. Crook, 2004: Wind and temperature retrivals in the 17 May 1981 Arcadia, Oklahoma supercell: Ensemble Kalman filter experiments. Mon. Wea. Rev., 132, 1982-2005

G. Evensen, 2003: The ensemble Kalman filter: Theoretical formulation and practical implementation. Ocean Dynamics 53, 343-367.

C. Snyder and F. Zhang, 2003: Assimilation of simulated Doppler radar observations with an ensemble kalman filter. Mon. Wea. Rev., 131, 1663-1677

M. Tong and M. Xue, 2005: Ensemble Kalman filter assimilation of Doppler radar data with a compressible nonhydrostatic model: OSSE experiments. Mon. Wea. Rev., 133, 1789-1807.

5.3 Enhancing weather radar observations in complex topography using radio-propagation information

Joan Bech (1) and Günther Haase (2)

(1) jbech@meteo.cat, Meteorological Service of Catalonia, Barcelona, Spain.
(2) gunther.haase@smhi.se, Swedish Meteorological and Hydrological Service, Norrköping, Sweden.

Introduction

The common assumption of average atmospheric temperature and humidity vertical profiles (normal radio-propagation conditions) provides a convenient way to calculate echo heights for weather radar observations. However, it is a well known fact that in a number of cases this assumption is often violated, impacting seriously in the quality of weather radar observations under the so-called anomalous propagation conditions -typically bending of the radar beam to the surface more than usual, i.e. super-refraction. The classical effect of super-refraction, or its extreme case of ducting, is the increase of the number and intensity of ground and sea clutter echoes. Additional side-effects include errors in echo height assignments (including those clutter-free) or, in complex topography environments, variation of the degree of beam blockage due to sheltering by mountains.

In this presentation an overview of related work to this topic performed under the framework of the COST-731 Action is presented. This includes estimation of the variability of radio propagation conditions using radiosonde data sets, methodologies for correcting radar beam blockage corrections considering realistic radio-propagation conditions derived from Numerical Weather Prediction (NWP) data, a Bean Propagation Model (BPM) to calculate actual radar coverage and for correcting precipitation estimates in blocked radar bins, a specific application to a radar siting case or the development and implementation of a technique for assimilating blocked radar data into an NWP system.

Propagation conditions variability and radar beam blockage

Variations in the radio propagation conditions of the radar beam may produce unexpected echo heights errors if standard propagation is assumed. As noted previously (see among others Bech et al. 2003 or Fornasiero et al. 2006) this phenomenon may cause errors in radar beam blockage corrections, which are typically applied in complex topography environments to enhance quantitative precipitation estimates from beam shielding.

Modelling of radar beam blockage under different propagation conditions has been done trough the use of a Beam Propagation Model (BPM). BPM requires as input a high resolution digital elevation model, a description of the radar system (position, antenna beam width and elevation angle, etc.) and information about the radio propagation conditions (Bech et al. 2007a). The propagation conditions are typically described by a refractivity profile derived either from radiosonde observations or from NWP model output (see Bech et al. 2007b) used in a geometrical-optics approach though more sophisticated options are also possible considering for example hybrid parabolic equation methods as described by Bebbington et al. (2007).

Figure 5.1 illustrates the beam blockage problem with the Rst radar (Norway). The top picture shows a view of the radar and three nearby hills (labelled with the numbers 1, 2 and 3) which produce blockage, while the rest of the horizon is flat and unobstructed. An example of observed daily radar accumulated precipitation (bottom left) shows clearly the effect of the shielding by the three hills (plus other obstacles to the northeast). The BPM output (bottom right) simulates the blockage -in reasonable agreement with the observations- and allows quantifying the degree of shielding. This enables subsequent correction of the estimated precipitation field or analysis of the associated anaprop echo pattern (for example, additional sea clutter caused by anaprop which Doppler filtering does not remove correctly).

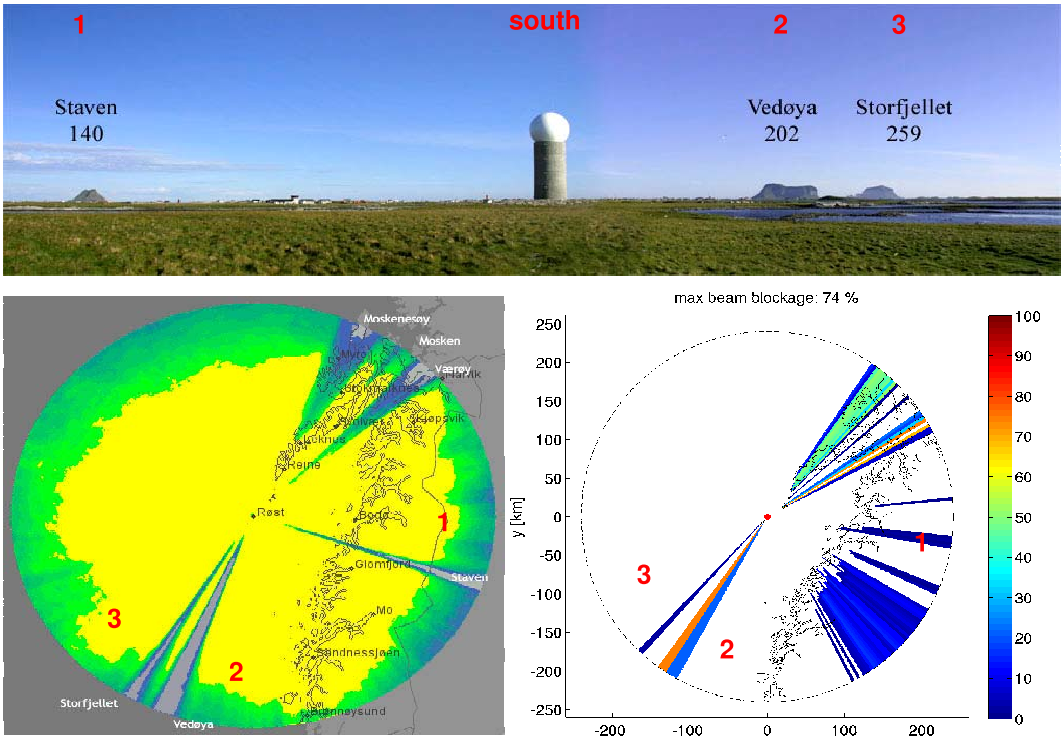

Figure 5.1: View of the Rst radar (Norway) looking south; three hills (numbered 1 to 3) cause partial beam blockage (top). Example of observed daily radar rainfall accumulation, showing the effects of blockage in the precipitation field (bottom left). BPM output showing the simulated blockage of the radar.

The use of the BPM corrections allowed the reduction of the bias between yearly radar precipitation estimates and gauge records by 1 dB for moderate blockages (1 to 50 per cent), and by up to 3 dB for intense blockages (50 to 70 per cent) as described in detail in Bech et al (2007a). Moreover, several case studies using HIRLAM 6-h forecasts suggested the potential of the BPM system to provide a general prediction of the radar coverage and the associated ground and sea-clutter patterns under anomalous propagation events.

Radar siting using BPM

Another application of the BPM is radar siting, allowing not only to take into account the influence of terrain on several possible sites but also super-refractive conditions experimented in the region which may have substantial effects on the radar coverage. This is illustrated with the Hemse radar in Gotland island, Sweden which had to be uninstalled in June 2007

because the agricultural silo over which was built had to be demolished (Haase et al. 2006).

The analysis of alternative locations where the radar could be moved took into account a number of issues, including property rights, technical infrastructure (road access, power supply, etc.), local vegetation, radio interferences (e.g. RLAN), the existence of nearby obstacles (churches, GSM towers, windmills,..) and topographical blockages. The last two items were assessed using the BPM model. Ten different new locations were evaluated considering both standard radio propagation conditions and HIRLAM NWP model output corresponding to intense super-refractive anaprop (ducting) events.

An example of the analysis is given in Figure 5.2, corresponding to a super refractive event (9 July 2005 00 UTC). The figure shows the modelling of the blockage and beam propagation at 90 degrees azimuth (East) considering different sources of the refractivity profile: radiosonde and HIRLAM output (from the 22 and 11 km grid length versions). The top row corresponds to the Hemse site (completed with actual observations) and the bottom row to one of the potential sites evaluated (G09). In this case the G09 simulation indicated that this site was not affected by beam blockage when using HIRLAM data as input. The analysis of several cases showed that using HIRLAM profiles corresponding to the radar site provided more accurate simulations than using radiosonde profiles, as the radiosonde -located at some distance- was not always representative of the radar site.

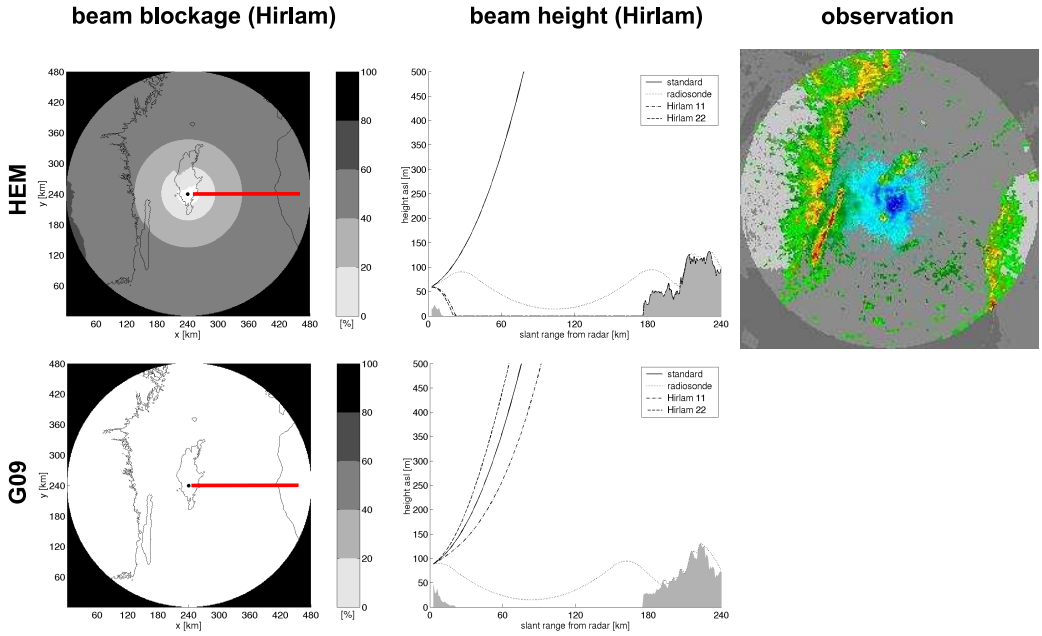

Figure 5.2: Anaprop event (9 July 2005 00 UTC) modelled for the Hemse radar site (top row) and the G09 site (bottom row) using refractivity profiles from both radiosonde and HIRLAM output (22 and 11 km grid length versions).

Assimilation of radar reflectivities considering topographical beam blockage

This section deals with the application of topographical radar beam blockage corrections to assimilated radar reflectivities based on the BPM system (Haase et al. 2007). This

was applied to AROME (Application de la Recherche l'Oprationel Mso-Echelle) an NWP system for the convective scale developed by Mto-France with 2.5 km horizontal resolution. It uses a three-dimensional variational (3dVar) data assimilation scheme and has an advanced representation of the water cycle with five hydrometeor classes (cloud water, rainwater, primary ice, snow and graupel) governed by a bulk microphysics parameterization.

The assimilation of radar reflectivities consists of three steps: 1) simulate reflectivities from the model hydrometeors using an observation operator (Caumont et al. 2006), 2) retrieve columns of pseudo-observations of humidity and other model prognostic variables from a reflectivity column, and 3) assimilate the pseudo-observations through the 3dVar assimilation scheme.

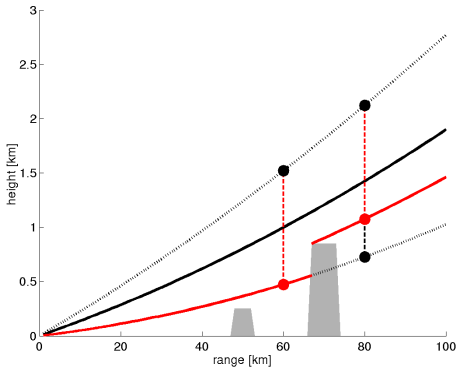

Figure 5.3: Vertical interpolation from model to radar space (along dashed lines). The black solid line corresponds to the beam center while the dotted lines mark the beam width of the unblocked beam. The red solid line defines the actual visibility at this elevation angle assuming atmospheric standard conditions. The circles indicate the integration limits used in the vertical interpolation for the blocked (red) and unblocked beam (black), respectively.

Figure 5.3 illustrates the vertical interpolation with and without beam blockage. Gauss-weights are computed for all model levels within the beam width (dotted lines). Currently, topographical shielding is not considered, i.e. the vertical interpolation (dashed lines) is always performed within the theoretical beam width (black circles). This is justified for flat regions (in Figure 5.3 at 60 km), but in mountainous regions the interpolation might consider model levels which are not visible by the radar (in Figure 5.3 at 80 km). By using BPM's visibility maps for standard propagation the vertical interpolation becomes more realistic where the radar beam is partly blocked (red solid line). In this case the lower integration limit is lifted to the lowest visible height at that azimuth and range (red circles) while the weights remain untouched.

This technique is demonstrated with a case study (14 May 2007 09 UTC) showing AROME simulations for three different French radars: Bollne, Nmes and Opoul (Figure 5.4). The effect of the AROME topography on the modelled visibility is clearly appreciated and in some cases also in the actual radar observations. The analysis of the results indicated a positive impact in using visibility maps producing less rejected pixels and also a decrease of the absolute mean departure. It was also noted that the resolution of AROME's topography may not be sufficient to generate proper visibility maps so higher resolution topographies are being considered.

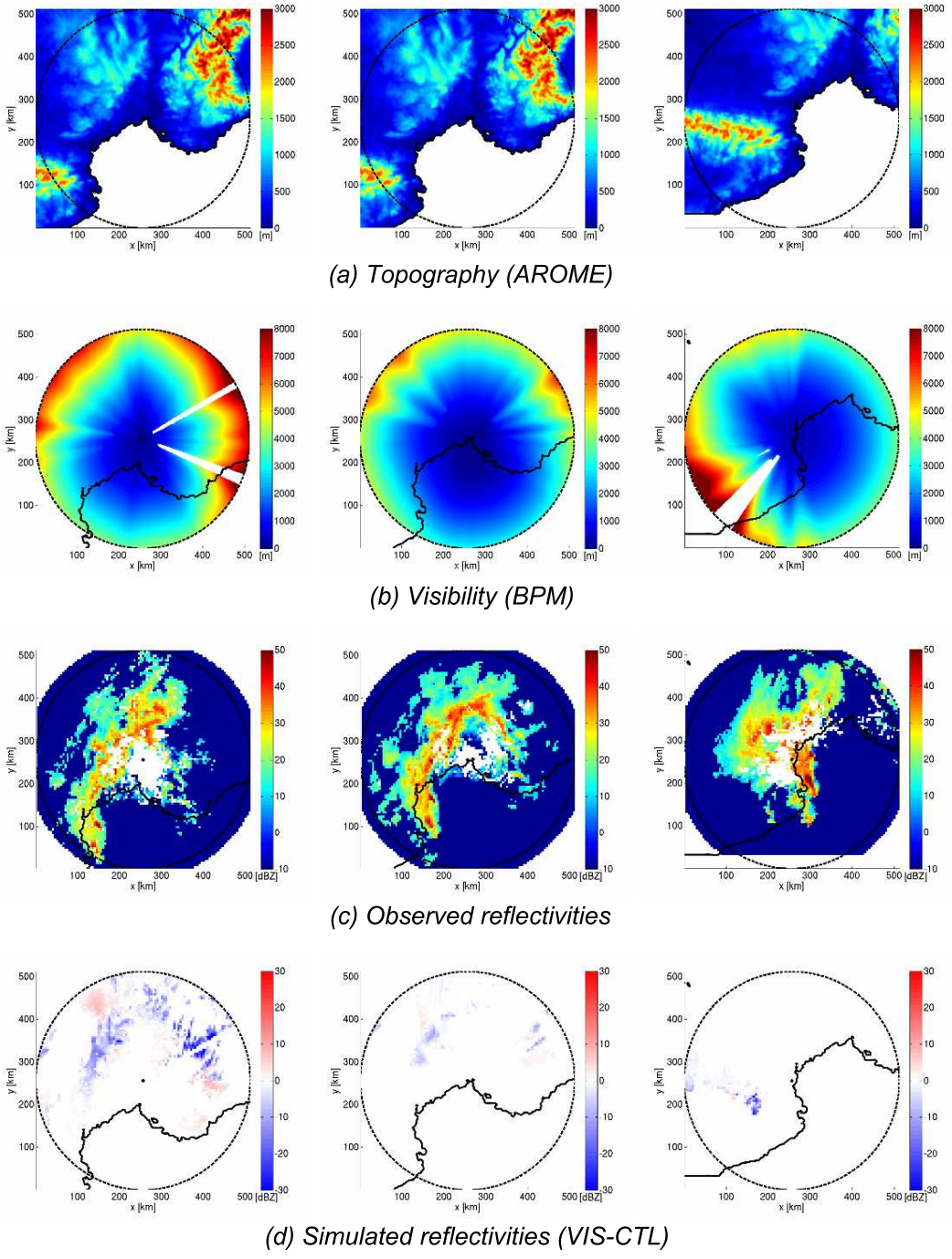

Figure 5.4: AROME simulations for 14 May 2007 09 UTC with (VIS) and without visibility maps (CTL) for Bollne (left), Nmes (center) and Opoul radar (right).

Final remarks

Different applications of modelling radar beam propagation in complex topography environments have been described in this paper. Two aspects, topographical beam blockage, and the use of realistic radio propagation conditions (i.e. not assuming standard refraction) are considered in a modelling system to enhance radar observations in order to provide improved high quality quantitative precipitation estimates or input to a high resolution NWP forecasting system. It should be emphasized that radar propagation conditions may present substantial variability (normal conditions assumed not always met) so echo height estimation

assuming normal conditions may be incorrect (potential impact in related products: blockage corrections, VPR, VVP, etc.). The BPM tool presented has been used to generate correction matrices for topographical beam blockage for standard propagation for NORDRAD sites, has shown good potential to detect AP using HIRLAM11 refractivity profiles in several case studies and also has been used in radar siting analysis. Complementary, considering topographical beam blockage in AROME's assimilation scheme has shown a positive impact on the simulation of radar reflectivities, thus improving the data assimilation process in an advanced high-resolution NWP forecasting system.

Acknowledgments

This study has been performed under the framework of the EU concerted research Action COST-731 "Propagation of Uncertainty in Advanced Hydrometeorological Forecasting Systems". As referenced in the text some of the results reported here were obtained in collaboration with Uta Gjertsen (formerly at met.no, Norway), Eric Wattrelot (Mto-France, France), and Marian Jurasek (Slovak Hydrometeorological Institute, Slovakia) to whom the authors are particularly thankful.

References

Bebbington, D., Rae, S., Bech, J., Codina, B., and Picanyol, M.: Modelling of weather radar echoes from anomalous propagation using a hybrid parabolic equation method and NWP model data, Nat. Hazards Earth Syst. Sci., 7, 391-398, 2007. http://www.nat-hazards-earth-syst-sci.net/7/391/2007

Bech, J., B. Codina, J. Lorente and D. Bebbington, 2003: The Sensitivity of Single Polarization Weather Radar Beam Blockage Correction to Variability in the Vertical Refractivity Gradient. J. Atmos. Oceanic Technol., 20, 845-855.
DOI: 10.1175/1520-0426(2003)020¡0845:TSOSPW¿2.0.CO;2

Bech J., U. Gjertsen, G. Haase, 2007a: Modelling weather radar beam propagation and topographical blockage at northern high latitudes. Quart. J. R. Meteorol. Soc., 133, 1191-1204. DOI:10.1002/qj.98

Bech, J., B. Codina, J. Lorente, 2007b: Forecasting weather radar propagation conditions. Meteorol. Atmos. Phys., 96, 229-243. DOI:10.1007/s00703-006-0211-x

Caumont, O., V. Ducrocq, G. Delrieu, M. Gosset, J.-P. Pinty, J. P. du Chatelet, H. Andrieu, Y. Lematre, and G. Scialom, 2006: A Radar Simulator for High-Resolution Nonhydrostatic Models. J. Atmos. Oceanic Technol., 23, 1049-1067.

Haase, G.; Gjertsen, U.; Bech, J.; Granstrm, ., 2006: Assessment of potential radar locations using a beam propagation model. 4th European Conf. Radar Meteorol. Hydrol., Barcelona, Spain.

Haase G., J. Bech, E. Wattrelot, U. Gjertsen, M. Jurasek, 2007: Towards the assimilation of radar reflectivities: improving the observation operator by applying beam blockage information, 33rd Conference on Radar Meteorology, AMS, Cairns, Australia. Proceeding

Fornasiero A., P. P. Alberoni, J. Bech, 2006: Statistical analysis and modelling of weather radar beam propagation conditions in the Po Valley (Italy). Nat. Hazards Earth Syst. Sci., 6, 303-314. http://www.nat-hazards-earth-syst-sci.net/6/303/2006

5.4 Exploitation of radar observations in HIRLAM

K. Salonen[1], G. Haase[2], S Niemelä[1] and H. Järvinen[1]

[1] *Finnish Meteorological Institute, P.O.Box 503, FI-00101 Helsinki.*
[2] *Swedish Meteorological and Hydrological Institute*
Correcponding author email: kirsti.salonen@fmi.fi

Introduction

The High Resolution Limited Area Model (HIRLAM; Undén et al., 2002) is developed as a cooperative effort among the national weather services of Denmark, Estonia, Finland, Iceland, Ireland, the Netherlands, Norway, Spain and Sweden. The analysis scheme used in the HIRLAM model is 3D/4D- variational data assimilation (Gustafsson et al., 2001; Lindskog et al., 2001). This article gives an overview of the use of radar observations in the HIRLAM framework. The HIRLAM reference code includes all the needed tools for radar radial wind data assimilation. The details are discussed in the following. An observation operator for radar reflectivity observations is not included in the HIRLAM data assimilation system at the moment. However, a radar simulation model (RSM) is used for real-time monitoring and validation of the model. An example of the use of RSM is shown. In the end, a short outlook is given.

Radial wind observations

The HIRLAM strategy is to generate spatial averages, so called superobservations, from the raw radial wind observations prior to data assimilation. This preprocessing step reduces random observation errors effectively and can also be used to decrease the impact of representativity errors. The desired resolution for the superobservation is defined with two free parameters, range bin spacing ($\overline{R}$), and azimuthal averaging ($\overline{\phi}$). Near the radar, the raw observations used in the averaging are selected from a circle area limited by the arc distance of the two adjacent output azimuth gates. After the arc distance exceeds the value of range bin spacing, the data selection area is defined by $\overline{R}$. With this approach fewer raw observations influence on superobservation near the radar than at longer measurement ranges. Each raw observation is allowed to influence one superobservation only. Model experiments indicate that the best fit between the superobservations and the model counterparts is obtained when values of the order of $\overline{R} \simeq 10$ km and $\overline{\phi} \simeq 2^\circ$ are used. In more general terms these parameter values correspond at 50 km measurement range approximately a 1.75 km $\times$ 1.75 km averaging area with a 10 km range spacing.

In variational data assimilation, a model counterpart for the observation is calculated with an observation operator. The radar radial wind observation operator implemented in the HIRLAM data assimilation system interpolates the model profiles of the horizontal wind components u and v to the observation location and projects them on the horizontal plane towards the radar and on the vertical plane to the slanted direction towards the radar (Salonen et al., 2003). The horizontal interpolation is done with bi-linear interpolation, and a Gaussian averaging kernel is used in the vertical interpolation. The Gaussian averaging kernel takes into account the broadening of the radar pulse volume as a function of measurement

range. The observation operator takes into account also the pulse path bending. Modelling the pulse path bending has two effects, the observation height at range d is different from the one obtained with the $\frac{4}{3}r$ -law, and the effective elevation angle of the radar pulse path is different from the antenna elevation angle.

Specific tools for radar radial wind data monitoring have been developed in the HIRLAM framework. Aggregation of the radar radial wind observation minus model counterpart (OmB) values for different azimuth directions in the bias calculation can result in a zero bias even in the presence of systematic differences in the observed and modelled wind speed and/or direction. This is due to the symmetric nature of the radial wind component as a function of azimuth angle. The bias estimation method introduced in Salonen et al. (2007) is applied in monitoring the OmB bias in the radar measurements in HIRLAM. Random errors do not have such an azimuthal dependence and thus the OmB standard deviation of the radial wind component can be studied directly.

Figure 5.1 shows an example of the cycle to cycle monitoring for radar Anjalankoski, Finland, 8th Feabruary 2008 06UTC. Upper panel of Fig. 5.1 shows a scatterplot of radial wind observations as a function of model counterparts. The observed wind varies between – 18...+12 ms^{-1} which is well inside the limits of the unambiguous velocity interval of ± 36 ms^{-1}. In an ideal case the observations would follow the one-to-one line shown with black solid line. In this case, the observations follow quite nicely the ideal case line. The middle panel of Fig. 5.1 shows the observations (black dots) and the model counterparts (red dots) as a function of azimuth angle. It can be concluded from the figure that the wind field has been nearly uniform, as the observations and their model counterparts have a clear indication of cosine form. The lower panel of Fig. 5.1 shows the OmB standard deviation as a function of measurement range (black solid line) and the number of observations at each range (grey bars). In this cycle, radar observations originate mainly from measurement ranges shorter than 65 km, and until that range the OmB standard deviation is low, varying between 1.5...2.5 ms^{-1}. For longer measurement ranges the number of observations decreases rapidly and the standard deviation increases close to 4 ms^{-1}. These observations originate from altitudes 3 – 6 km and they may represent isolated scatterers.

Reflectivity observations

A radar simulation model (RSM, Haase and Fortelius, 2001) has been implemented into HIRLAM for verification and monitoring purposes. RSM is a software package that simulates radar reflectivity measurements corresponding to the output of a NWP model. The assumed location, frequency and scan pattern can all be chosen to match any available radar data within the model domain. RSM then computes the local reflectivity at each grid point of the model, and generates a simulated measurement by taking into account the beam propagation and attenuation within the simulated atmosphere. The purpose of RSM is to make it possible to use radar measurements for forecast verification directly, without having to solve the difficult problem of linking the observed reflectivity to precipitation at the ground.

At the moment, RSM is not used with the HIRLAM model operationally, since the model treats the precipitation as a diagnostic process. The RSM approach is more useful if the model has a prognostic precipitation scheme. Therefore, RSM has been utilized mainly with the meso-scale NWP model AROME, which is part of the HARMONIE-system (Hirlam-ALADIN Research on Mesoscale Operational NWP In Europe).

Figure 5.2 shows a comparison of radar reflectivities on 9th October, 2008, at 18 UTC, simulated from AROME data by RSM (upper panel) and observed by radars located at

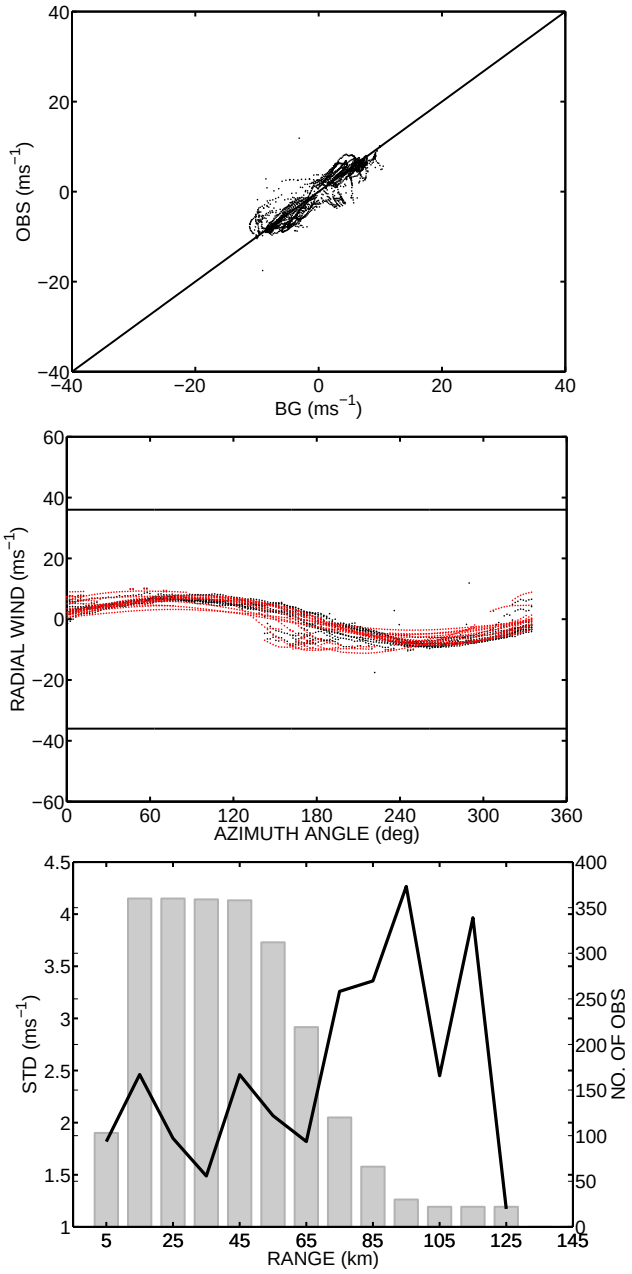

Figure 5.1: Upper panel: Scatterplot of radial wind observations as a function of model counterparts for cycle 29. The black solid line indicates the ideal fit. Middle panel: Observations (black dots) and model counterparts (red dots) as a function of azimuth angle. Lower panel: OmB standard deviation as a function of measurement range (black solid line). Grey bars show the number of radar radial wind observations at each range.

Anjalankoski, Ikaalinen, Korppoo, Kuopio, Vantaa, and Vimpeli with elevation angle 0.3°. A cold front was passing over Southern Finland at the time. The cold front moved faster than predicted and Fig. 5.2 reveals the phase difference at 18 UTC. The observed reflectivity pattern is also more scattered than the model prediction. RSM is a very effective tool for cycle to cycle monitoring of the NWP model predictions

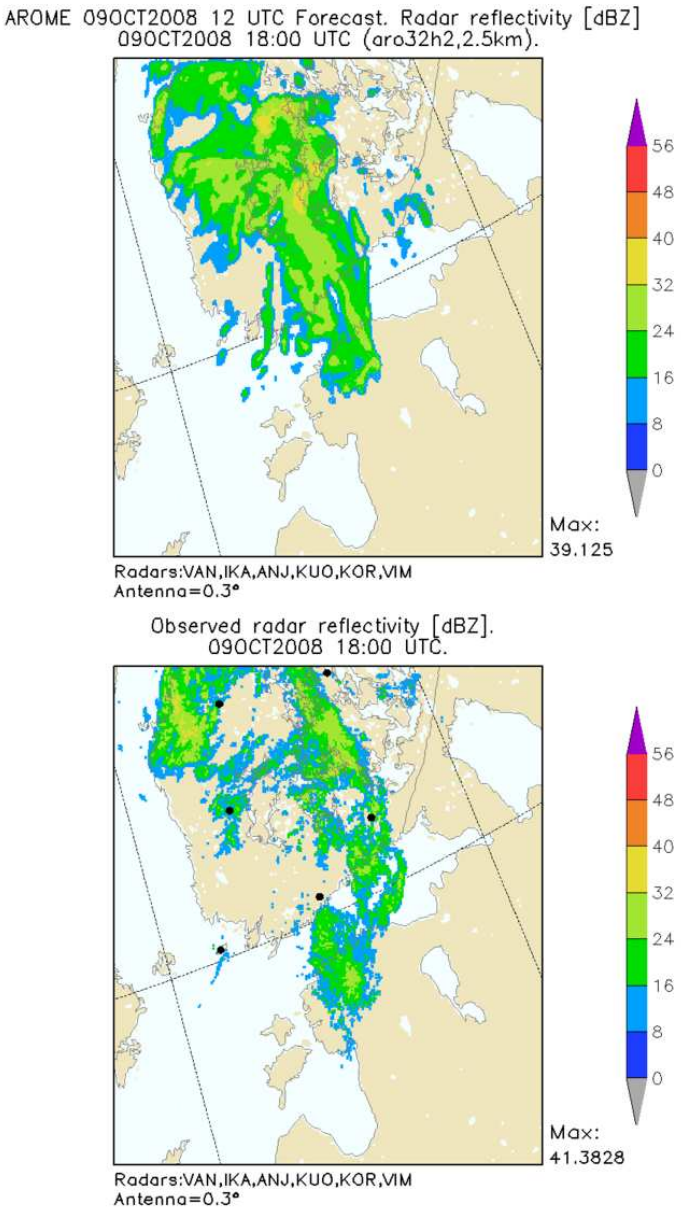

Figure 5.2: Comparison of radar reflectivities simulated with RSM (upper panel) and observed by the FMI radar network (lower panel).

Outlook

HIRLAM model includes all the needed components for operational data assimilation of Doppler radar radial wind observations. Preparations to start the operational use are ongoing. The measurement tasks in the Finnish radar network have been renewed during summer 2007. The special needs of the NWP community have been taken into account in the renewal process and a task designed for radial wind data assimilation purposes has been implemented. Radial wind data has been passively monitored against HIRLAM and operational use in data assimilation is in near future plans.

The impact of using radar radial wind observations in HIRLAM 4D-var is now investigated by performing comprehensive impact studies (CIS) in which the joint impact of a variety of observation types is studied. The focus in the CIS experiments including radial wind

observations is on summertime synoptic scale forecasting of convection. The experiments are carried out at $\sim$ 10 km horizontal resolution. Mesoscale CIS are planned to be performed after the synoptic scale studies have been completed.

In the future, the NWP model monitoring with RSM is planned to be extended to cover the dual-polarimetric features. This would enhance the knowledge on how the microphysics of the NWP model is able to handle the phase change processes in the atmosphere.

References

Gustafsson, N. and Coauthors, 2001: Three-dimensional variational data assimilation for a limited area model. Part I: General formulation and the background error constraint. Tellus, 53A, No. 4, 425-446.

Haase, G. and C. Fortelius, 2001: Simulation of radar reflectivities using HIRLAM forecasts. HIRLAM Technical Report, No. 51. Available online at http://hirlam.org/open/publications/TechReports/TR51.pdf.

Lindskog, M. and Coauthors, 2001: Three-dimensional variational data assimilation for a limited area model. Part II: Observation handling and assimilation experiments. Tellus, 53A, 447-468.

Salonen, K., Järvinen, H. and M. Lindskog, 2003: Model for Doppler radar radial winds. Pp. 142-145 in Proceedings of the 31st Conference on Radar Meteorology Volume 1, Seattle, 6-12 August 2003. American Meteorological Society, Seattle, Washington, USA.

Salonen, K., Järvinen, H., Eresmaa, R. and S. Niemelä, 2007: Bias estimation of Doppler-radar radial-wind observations. Quart. J. Roy. Meteor. Soc., 133, 1501-1507.

Unden, P., Rontu, L., Järvinen, H. and Coauthors, 2002: HIRLAM-5 Scientific Documentation. SMHI, 144 pp.

5.5 Sensitivity analysis of assimilation of radar derived surface rain rate into the regional COSMO model

Virginia Poli [1,2], Francesca Di Giuseppe [2], Tiziana Paccagnella [2] and Pier Paolo Alberoni [2,3]

[1] *CIMA Foundation, Savona, Italy,* [2] *ARPA-SIMC, Bologna, Italy,* [3] *ISAC-CNR, Bologna, Italy*

Introduction

Numerical Weather Prediction based on high resolution models, with grid resolution in the range of 1-4 km, undergoes intensive research and development especially to improve local weather predictions and the forecast of severe weather events.

At very high resolution the use of dense and highly frequent observations becomes crucial in assimilation systems. Radar derived surface rain rate could serve the scope of feeding rapidly updating cycle but the challenge remains to create an operational framework able to handle moist process necessary for rain assimilation. Here a variational approach is proposed in which the retrieval of temperature and humidity profiles from radar derived surface rain rate is performed by employing two linearised parametrizations of large-scale condensation and convection. The retrieved profiles are then used as pseudo observations into the nudging scheme of the COSMO model which ARPA-SIM run operationally to provide weather forecast for Italy.

The variational scheme was initially developed at ECMWF for active satellite observations and is now adapted for the Italian radar network. It has the advantage of tackling the difficult problem of how to vertically re-distribute in a coherent way the heat released by the rain formation process. Former works just assumed constant/climatological profile. Sensitivity studies of the variational scheme to input parameters are presented and the quality of the retrieved profiles are assessed by means of statistical analyses.

Methodology

1D-VAR algorithm

The goal of the 1D-Var retrieval system is to find the optimal model state x_a, that simultaneously minimises the distance to the observations, y_0, and the background model state, x_b. The model state consists of the vertical profiles of temperature and specific humidity, which are the control variables. A quasi-Newton algorithm is employed to minimise the following cost function

$$J = \frac{1}{2}(x - x_b)^T B^{-1}(x - x_b) + \frac{1}{2}(y_0 - H(x))^T R^{-1}(y_0 - H(x)) \tag{5.1}$$

Where B and R are the background and observation error covariance matrices and H is the observation operator which projects the model state into the observation space.

The proposed scheme tackles the unresolved question on how to vertically re-distribute the heat released by the rain formation process. Former works assumed constant/climatological profile. The proposed one performs the retrieval of temperature and humidity profiles from radar derived surface rain rate, employing two linearized parameterizations of large-scale condensation [Tompkins Janiskova 2004] and convection [Lopez Moreau 2005] firstly developed at ECMWF and now adapted for our regional radar network. In 1DVAR moist physical schemes are necessary to convert the model state into precipitation rates that can be compared with radar observations [Lopez Bauer 2007].

Data

The forecast model used in this work is the COSMO-I2 which is a non-hydrostatic model used operationally at ARPA-SIM with a grid resolution of 2.8 km. Forecasts with lead times of 15 minutes are used as input of the variational algorithm.

Radar data are from Emilia-Romagna composit. Reflectivity measures are acquired every 15 minutes on a range of 125 km with an horizontal resolution of 1 km and then are converted in rain rate. The use of very high spatial and temporal data resolution should guarantee improvements in the initial condition knowledge. Nevertheless, highly correlated observations could introduce unwanted correlation error into the analysis. Since this can create spurious structures an observation thinning has been performed. The error on rain rate observations has been estimated to 30% of the measured value as a first guess. An effort will be performed in the future to estimate a more space related error.

Radar data thinning

Data thinning is performed by an autocorrelation analysis of reflectivity radar fields. Using all data images acquired during the day under study a correlation histogram has been calculated as a function of distances between two variables data points. Smaller the distance higher the correlation between two points, being the correlation at zero distance equal to one by definition. Figure 5.1 shows the result of the analysis.

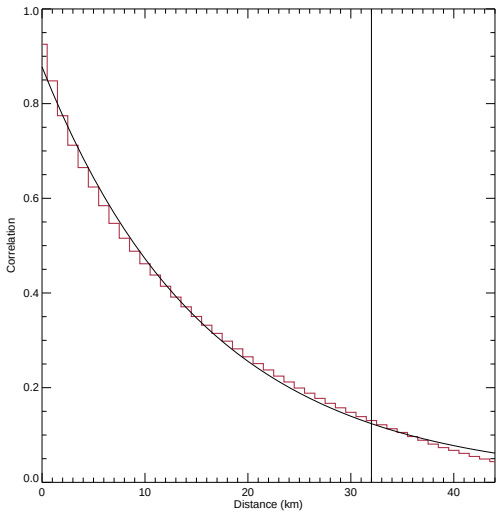

Figure 5.1: Correlation histogram as function of distances between two variables data points. Fitting function is displayed.

To fit the histogram a parametric function

$$f(x) = a_0 e^{a^1 x} \tag{5.2}$$

has been used with parameters a_0=0.87 and a_1=-0.03. The e-folding distance of 32 km is chosen as decorrelation (i.e. thinning length).

Off-line 1D-Var: test case

The selected case study is a convective event occurred in Northern Italy on 4-6 May 2007. It was characterized by intense precipitation. Figure 5.2 presents some of the stages of the event during the 4th of May as seen by the radar composit and predicted by the COSMO model. Both radar and model data are then bilinearly interpolated on a regular grid.

Figure 5.3 shows the profiles of different cloud parameters as computed by the 1D-Var package. In figure 5.3(a) the surface observed rain rate (black diamond) is displayed together with first-guess and analysis profiles.

Summary and Outlook

Examining the retrieved profiles it can be noticed that the 1D-Var algorithm is able to vertically redistribute heat released by the rain formation process in a coherent way. All cloud parameters are modified in a physically consistent fashion. The mean temperature and specific humidity increments (Fig. 5.4) provided by the 1D-Var package over the whole experiment are remarkably small signifying that the observations are not affected by large biases.

In the scatterplot of figure 5.5 model rain rate is plotted against observed rain rate for all of the points analysed in the whole event. As a zero order the analysed rain rate is closer to the observed rain rate when compared to the background as shown by the scatterplot. The 1D-Var package is therefore able to bring the model closer to the observed quantities.

In the future the impact on the assimilation technique on the COSMO 3D-integration will be analysed.

References

Tompkins A. M., and M. Janiskova, 2004: A cloud scheme for data assimilation: description and initial tests. Quart. J. Roy. Meteor. Soc., 130, 2495-2518.

Lopez P., and E. Moreau, 2005: A convection scheme for data assimilation: description and initial tests. Quart. J. Roy. Meteor. Soc., 131, 409-436.

Lopez P., and P. Bauer, 2007: "1D+4D-Var" assimilation of NCEP Stage IV radar and gauge hourly precipitation data at ECMWF. Mon. Weather Rev., 135, 2506-2524.

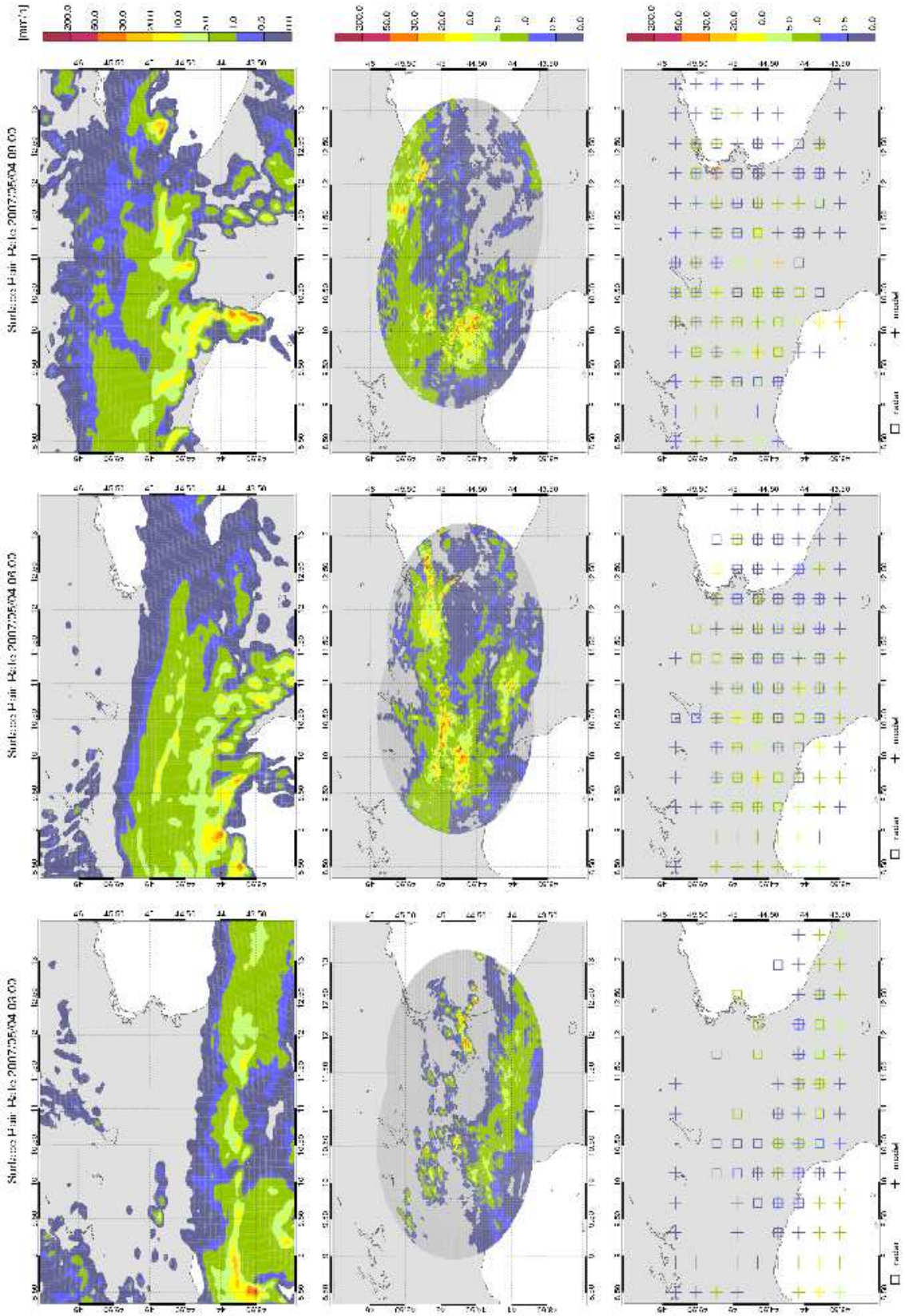

Figure 5.2: Surface rain rate at 03:00, 06:00 and 09:00 UTC of 4 May 2007 as forecasted by the model and seen by the radar. Images in the last row show model and radar data interpolated on the same regular grid.

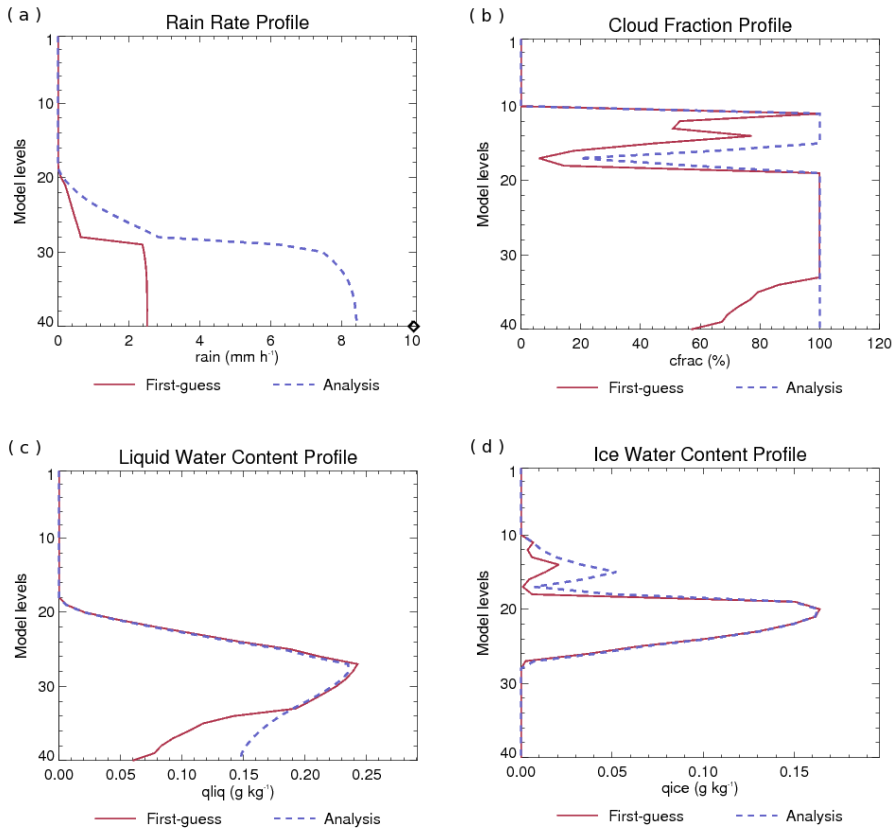

Figure 5.3: Vertical profiles of different cloud parameters for the first-guess (solid) and the analysis (dashed).

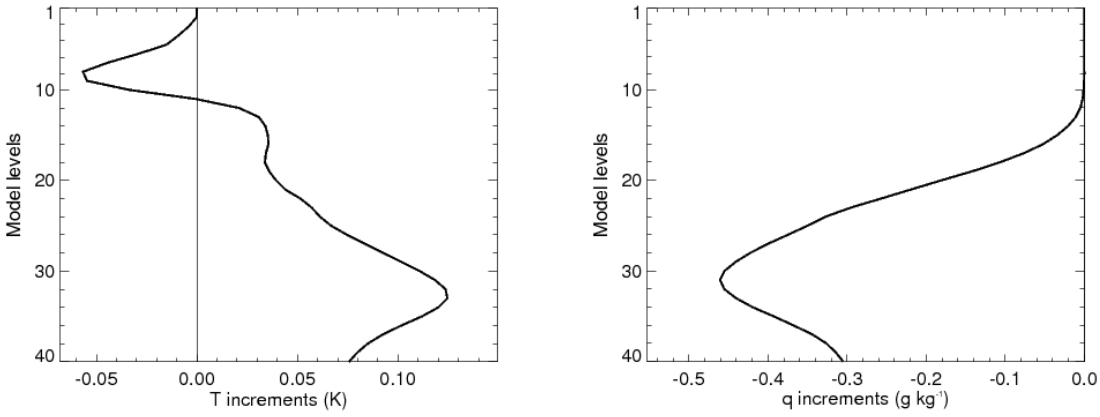

Figure 5.4: Mean temperature (left) and specific humidity increments (right).

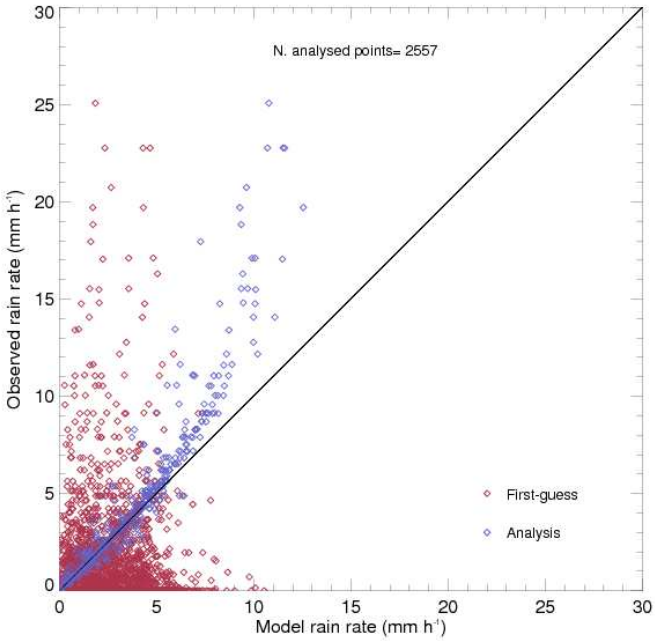

Figure 5.5: Model rain rate against observed rain rate for first-guess (red diamonds) and analysis (blue diamonds).

5.6 3DVAR implementation to evaluate the propagation of uncertainties in the Weather Research and Forecasting Model (WRF)

D. Charalambous[1,2], F. Tymvios[1], S. Michaelides[1] and P. Constantinides[1]

[1] *Cyprus Meterological Service, 1418 Nicosia, CYPRUS*
[2] *Department of Physics, University of Lancaster, Lancaster LA1 4YB, U.K.*

Abstract

The Cyprus Meteorological Service has recently migrated to the Weather Research and Forecasting Model (WRF), which is now being used as the primary forecasting tool for operational and research purposes. In order to check the forecast accuracy and better understand the propagation of uncertainties through the model, we have performed simulated data assimilation tests. In this preliminary study, we present model output as well as output following assimilation of artificial temperature data at 850 hPa. Following this preliminary study, further work is currently on the way to assimilate both radiosonde and radar data.

Introduction

The Weather Research and Forecasting Model (WRF) is a widely used atmospheric model for both research and operational weather forecasting applications. The Cyprus Meteorological Service has recently migrated to WRF, which is currently being used as the primary tool for research purposes as well as for day-to-day operational weather forecasting. *Preliminary* model verification has so far indicated that WRF performs relatively well in describing and forecasting the weather in the Cyprus area. Formal model verification procedures are currently being deployed in order to fully assess the performance of the model and determine various ways of improving it.

WRF also allows for three-dimensional variational data assimilation (3DVAR) which can be used to assimilate meteorological observations, radiosonde, radar and other data (Xiao *et al.*, 2008). The aim of the 3DVAR procedure is to calculate an optimal estimate of the true state of the atmosphere at a particular time. This is usually accomplished by the iterative extremisation of a prescribed cost-function—see Skamarock *et al.* (2005) and Kalnay (2003) for more details.

In an attempt to study the propagation of uncertainties and hence approximately assess the predictability of the model, we have used the 3DVAR procedure to assimilate simulated data into the model and study the effect of the assimilation on the forecast output. The various technical details of our study are presented in the next section followed by our results, conclusions and suggestions for further work.

Technical Details

As a first attempt at using the 3DVAR process to assimilate meteorological data into the model, we have generated artificial temperature values for all grid points used by WRF,

corresponding to the $p_0 = 850\,\mathrm{hPa}$ level. For simplificity, we have used a cylindrically-symmetric Gaussian distribution of temperature, that is of the form

$$T(x, y, p_0) = \langle T \rangle_0 + (T_\mathrm{p} - \langle T \rangle_0) \exp\Big\{ -\frac{1}{2\sigma^2} \big[(x - x_0)^2 + (y - y_0)^2 \big] \Big\}, \tag{1}$$

where $\langle T \rangle_0$ is average temperature over the p_0 surface corresponding to the $t + 0$ model output before performing data assimilation, *i.e.*

$$\langle T \rangle_0 \equiv \frac{1}{A} \iint_A \mathrm{d}x\, \mathrm{d}y\, T(x, y, p_0), \tag{2}$$

A being the area of the forecast domain. The centre of the Gaussian distribution is located at (x_0, y_0); its peak value is T_p and its full width at half maximum (FWHM) is approximately given by the parameter σ.

In our study, we have chosen $T_\mathrm{p} = 290\,\mathrm{K}$. The background average temperature was found to be $\langle T \rangle_0 = 274.42\,\mathrm{K}$, corresponding to the $t + 0$ model output for 17 February, 2008. The Gaussian temperature distribution was centred at 29.5°E and 35.5°N. The model resolution was 29 km, corresponding to 51 pixels in the E-W direction and 39 pixels in the N-S direction. The value of the parameter σ was set to an integral multiple of the model resolution; in particular, we have used σ values corresponding to 1, 2, 3, 4, 5 and 10 times the model resolution, labelled as S1, ..., S10 in our results. Thus, S1 corresponds to a very sharp temperature anomaly which falls off to the average value rather quickly, whereas S10 represents a rather broad distribution of temperature, affecting the whole domain. The model was initialised using meteorological data from the National Centres for Environmental Prediction (NCEP) every 6 hours and run for 72 hours, providing forecast output every 3 hours.

Results

The results both *with* and *without* artificial data assimilation are shown in Figs. 5.1–5.3. The temperature field resulting from the model after assimilating artificial data produced from eq. (1) is represented by solid contour lines; model output without any data assimilation is displayed with dotted contours. Also shown are colour plots indicating the numerical difference between the above mentioned temperature fields. Note that we only present results corresponding to S1, S5 and S10 since these are the most representative of our study, with S2, S3 and S4 exhibiting similar behaviour.

The temperature anomalies present over parts of Turkey are due to orography: the model assigns the special temperature value of $10^{35}\,\mathrm{K}$ to any points with pressure altitude less than 850 hPa and hence such points were ignored in our calculations. The corresponding numerical difference shown in our colour plots is solely due to the Gaussian-distributed temperature values of eq. (1).

We have also assimilated uniformly-distributed temperature values as opposed to Gaussian-distributed ones and have observed very similar overall behaviour but also certain differences, see Fig. 5.4.

Conclusions and Further Work

The results indicate that after approximately 36 hours, the two model runs appear to converge to a large degree; this behaviour is reproducible for all values of the FWHM of the assimilated Gaussian temperature distribution. We believe that this can be attributed to the fact that

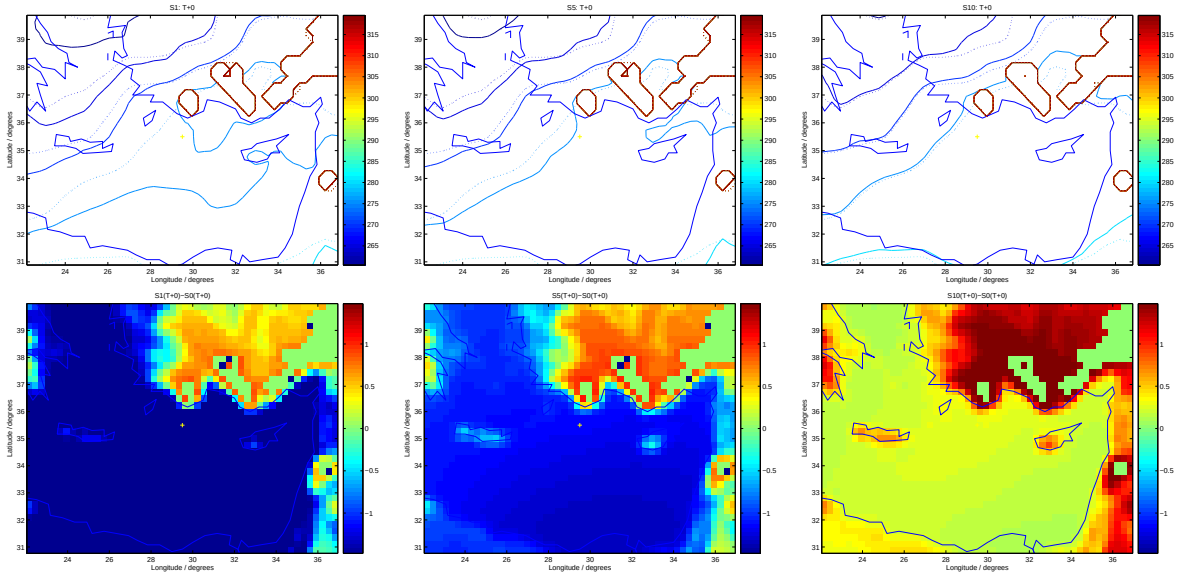

Figure 5.1: Model output for the temperature field at 850 hPa, on 17 February 2008, 00 UTC. The solid temperature contours (top row) correspond to model output following the assimilation of the artificial temperature data described by eq. (1). The dotted contours correspond to the model output without data assimilation. Shown along the bottom row is a colour plot of the difference between the data plotted along the top row.

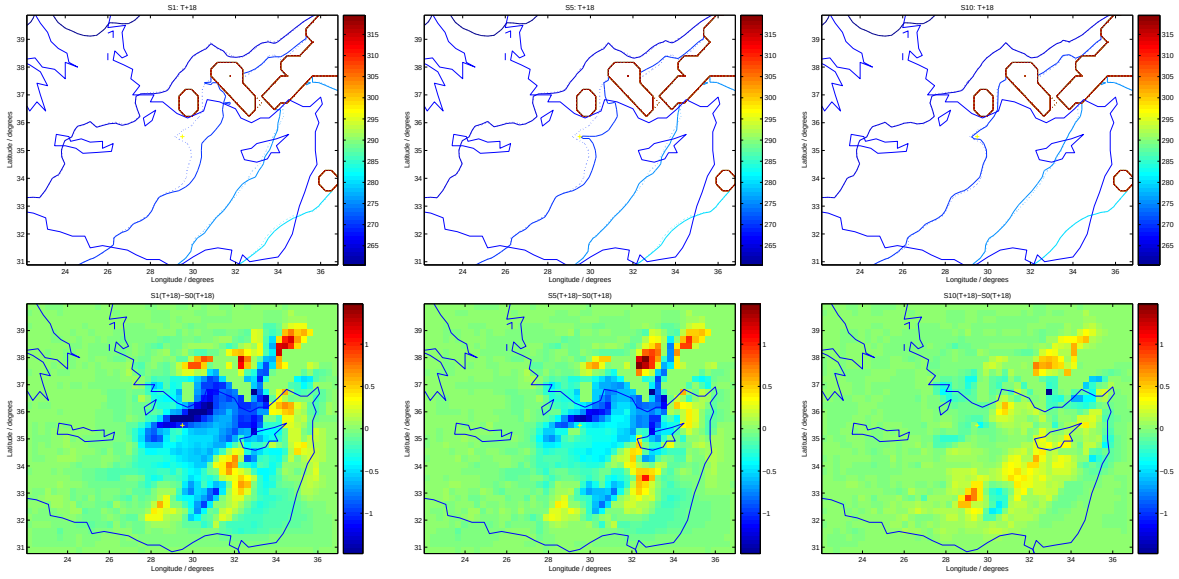

Figure 5.2: Corresponding model output for the temperature field at 850 hPa, on 17 February 2008, 18 UTC.

the model uses initial data every 6 hours and thus the forecast is "guided" by the initial conditions.

During the first few forecast times, there appears to be a significant difference between the two runs throughout the domain used for our study. However, after approximately 18 hours, the area where the two runs differ significantly appears to be concentrated around the point where the Gaussian temperature distribution was originally applied (marked by a cross sign), as one might naively expect. We would also like to draw attention to the rightmost pair of graphs of Fig. 5.4 in comparison with the corresponding pair of graphs shown in

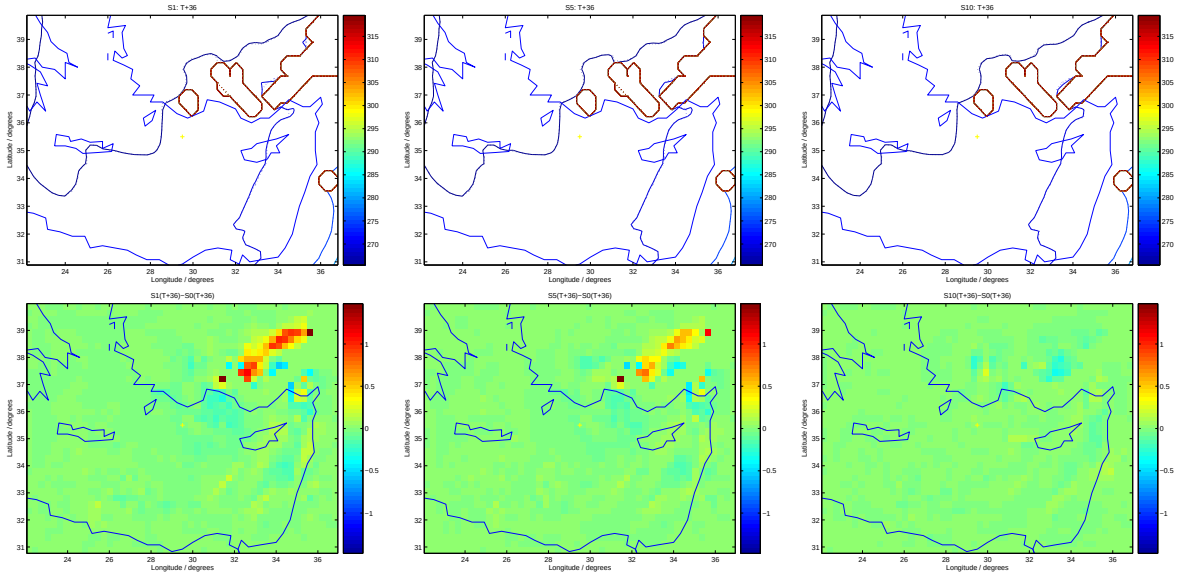

Figure 5.3: Corresponding model output for the temperature field at 850 hPa, on 18 February 2008, 12 UTC.

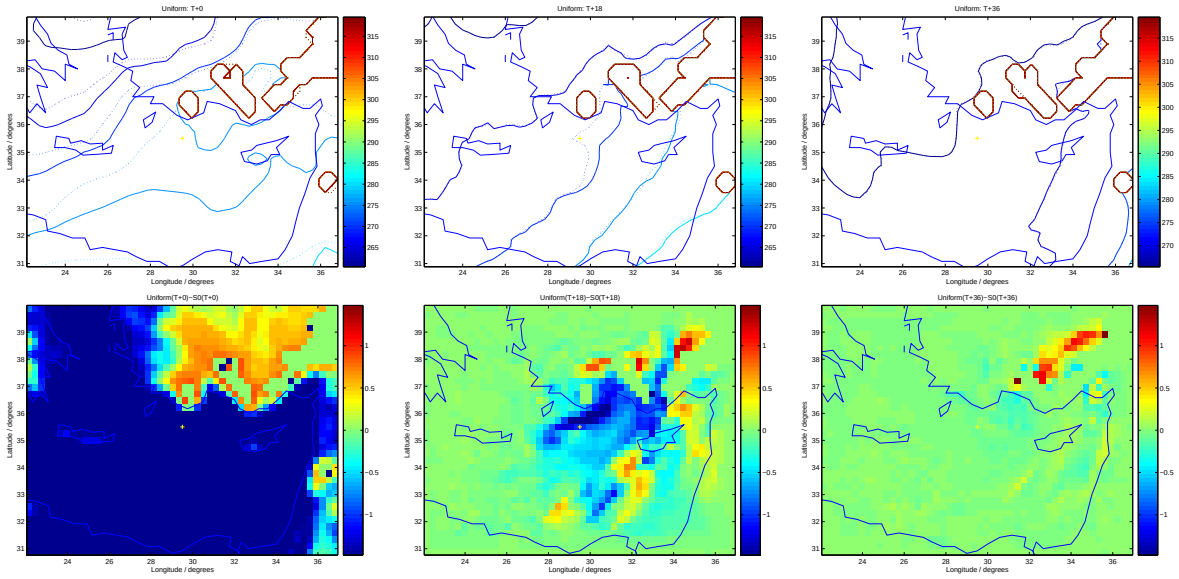

Figure 5.4: As for Figs. 5.1–5.3 but for uniformly distributed assimilated temperature values. Note that each pair of plots now corresponds to a different time instant: 17 Feb. 2008 at 00 UTC (leftmost), 18 UTC (middle) and 18 Feb. 2008 at 12 UTC (rightmost).

Fig. 5.3: there seems to be a significant difference between the model output following the assimilation of large FWHM-Gaussian-distributed data and uniformly distributed data at $t + 36$. In fact, we have found that the two runs (that is, with and without assimilation of uniformly distributed data) converge after $t + 51$, *i.e.* at a much later time than those corresponding to Gaussian-distributed data.

Further tests are currently being carried out to investigate both qualitatively and quantitatively the exact cause of the convergece described above as well as of the slight difference in behaviour between the two types of assimilated data (uniformly distributed vs Gaussian distributed). These tests involve running the model using initial conditions only for the $t+0$ frame as well as using different temperature distributions.

Finally, we would like to emphasize that this is a preliminary study. We are currently working on the assimilation of both radiosonde and radar data, using artificial and actual data sets and investigating the effect of the assimilation on model variables at various pressure levels.

References

Xiao, Q., Lim., E., Won, D-J., Sun, J., Lee, W-C., Lee, M-S., Lee, W-J., Cho, J-Y., Kuo, Y-H., Barker, D.M., Lee, D-K., Lee, H-S., 2008: Doppler Radar Data Assimilation in KMA's Operational Forecasting. Bull. Amer. Met. Soc., 89, 39–43.

Skamarock, W.C., Klemp, J.B., Dudhia, J., Gill, D.O., Barker, D.M., Wang, W. and Powers, J.G., 2005: A Description of the Advanced Research WRF Version 2. NCAR Technical Note TN-468+STR, Boulder, Colorado.

Kalnay, E., 2003: Atmospheric Modeling, Data Assimilation and Predictability. Cambridge University Press, Cambridge.

Employment of a Laser Disdrometer in Torino: data validation and comparison with Bric della Croce radar data

R. Cremonini , R. Bechini , V. Campana , L. Tomassone

ARPA Piemonte Area Previsione e Monitoraggio Ambientale, Torino, Italy

Abstract

The disdrometer is an instrument allowing the retrieval of some informations concerning raindrops characteristics. In particular it allows the reconstruction of the drop size distribution (DSD). It thus can be useful to calibrate meteorological radars, which measure reflectivity, function of the sixth power of the hydrometeors diameter. It is an important task to reconstruct the drop size distribution according to the precipitation type (such as stratiform rain or convective rain), with the aim to get better estimation of precipitation at ground. In this work the data registered by the disdrometer located in Torino have been analysed. We considered five precipitation events occurred in 2006: disdrometer data have been compared to rain registered at ground by raingauges located in Torino area, in order to evaluate the reliability of the instrument. Secondly the DSD parameters have been derived, averaging disdrometer data over 10 minutes intervals, and used to calculate theoretical reflectivity and differential reflectivity, under the hypotesis of drop shape model proposed by Andsager et al. in 1999. Such reflectivities have been compared to the reflectivities measured by the polarimetric weather radar located in Bric della Croce, 6 km far from the disdrometer.

Instruments description

Thies-Clima disdrometer

The Thies-Clima disdrometer, installed in Torino, Piedmont region, at a height of 270 m s.l.m., at the end of 2005 (Fig. 1), samples precipitation with one minute time resolution, using a laser beam having a 45 cm^2 surface, and a 0.75 mm thickness. In presence of hydrometeors the laser beam is partly hidden, and the receiving signal is reduced; the diameter of the particle is calculated from the amplitude of the reduction. The fall speed of the particle is calculated from the duration in time of the reduced signal. The instrument, for a minute of sampling, provides the following important informations:

- the total number N of identified hydrometeors, classified according to diameter (20 classes, 0.16 to > 8 mm diameter) and vertical velocities (20 classes, 0.2 to > 20 m/s). A matrix is given, with dimensions 20×20, resuming the characteristics of raindrops in the considered time interval (60 sec);
- precipitation intensity averaged on the last minute, calculated converting the total water volume through the sampling surface in 60 seconds, in millimetres per hour.
- precipitation intensity averaged on the last five minutes, calculated as the average of the last five single minute intensity.

Other characteristics, concerning the identified hydrometeors type, are very useful in case of solid precipitation, but were not considered in the present study, mainly oriented to the analysis of rain precipitation.

Fig. 1 – Thies-Clima disdrometer installed in Torino, C.so U.Sovietica 216

Figure 5.1: This–Clima disdrometer installed in Torino, C.so Unione Sovietica 216.

Other instruments

In this study were also used data retrieved by:

- a polarimetric doppler weather radar, located in Bric della Croce, at about 6.4 Km far from the disdrometer, at an altitude of 736 m s.l.m.
- Torino Vallere raingauge, located 3.7 Km far from the disdrometer.

Case study

Some rainfall events occurred in Piedmont region during the year 2006 (see Table 1), and involving Torino in particular, have been considered and selected:

- 08/05/2006, convective event in Torino area
- 10/05/2006, mainly stratiform event
- 14/09/2006, mainly stratiform, but characterised by intensity peaks during the night and the first morning
- 25/09/2006, mainly stratiform
- 06/12/2006, stratiform event without snow

	08/05/2006	10/05/2006	14/09/2006	25/09/2006	06/12/2006
MAX Intensity 24hTorino Vallere	28.8 mm/h	8.4 mm/h	14.4 mm/h	9.6 mm/h	6 mm/h
MEAN Intensity 24hTorino Vallere	5.9 mm/h	3.2 mm/h	4.3 mm/h	2.6 mm/h	1.6 mm/h

Table 1 – Rainfall events

Table 1: Rainfall events.

Disdrometer data validation

Comparison with raingauges

As a first step, in order to evaluate the reliability of data supplied by Thies-Clima disdrometer, rain rates averaged on 10 minutes intervals have been calculated and compared with data provided by Torino Vallere raingauge. In Fig.2a and Fig.2b are plotted data from the two instruments, during a convective and a stratiform event. It is possible to notice a good agreement in the measurements, with a general little underestimation by the disdrometer (blue lines). The rainfall intensity retrieved by the instrument has been calculated using intervals of 10 minutes, summing the volume of fallen drops on the considered interval.

Velocity field validation

In order to calculate DSD using reliable data, was carried on an analysis of the velocity field data. For all the considered events we compared velocity data from disdrometer with theoretical velocity associated to each diameter by the following formula

$$V(D) = 9.65 - 10.3\ e^{-0.6D}$$

proposed in 1973 by D. Atlas [1]. We obtained some unphysical velocities for the first three diameter classes (0.125÷0.250 mm, 0.250÷0.375 mm, and 0.375÷0.500), and for this reason we excluded all the drops having velocity V not lying between the two curves: (VATLAS(D) 2 m/s) and (VATLAS(D) + 2 m/s). Finally we decided to omit the last class of diameter and velocity, as the superior boundary is not known. An example is shown in Fig. 3.

DSD calculation

The drop size distribution varies spatially and temporally within a single rainfall event, furthermore it is influenced by other factors such as the storm type or the climatic regime. This variability causes important errors in rainfall estimation by meteorological radar, because the application of a fixed Marshall-Palmer equation ($Z = aR^b$, where Z is the radar reflectivity in dbZ, R the rain rate in mm/h and a, b two parameters associated to the DSD, fixed according to the pluviometric climatological regime) does not consider the variation in precipitation characteristics. The drop size distribution has been calculated averaging disdrometer data on 10 minutes of measurement, using the formula suggested by Kruger and Krajewski in 2001 [2], taking into account detected diameters and measured velocities as well:

$$N(D_i) = \frac{1}{\Delta t\ \Delta D_i} \sum_{j=1}^{M_i} \frac{1}{A\ v_j}.$$

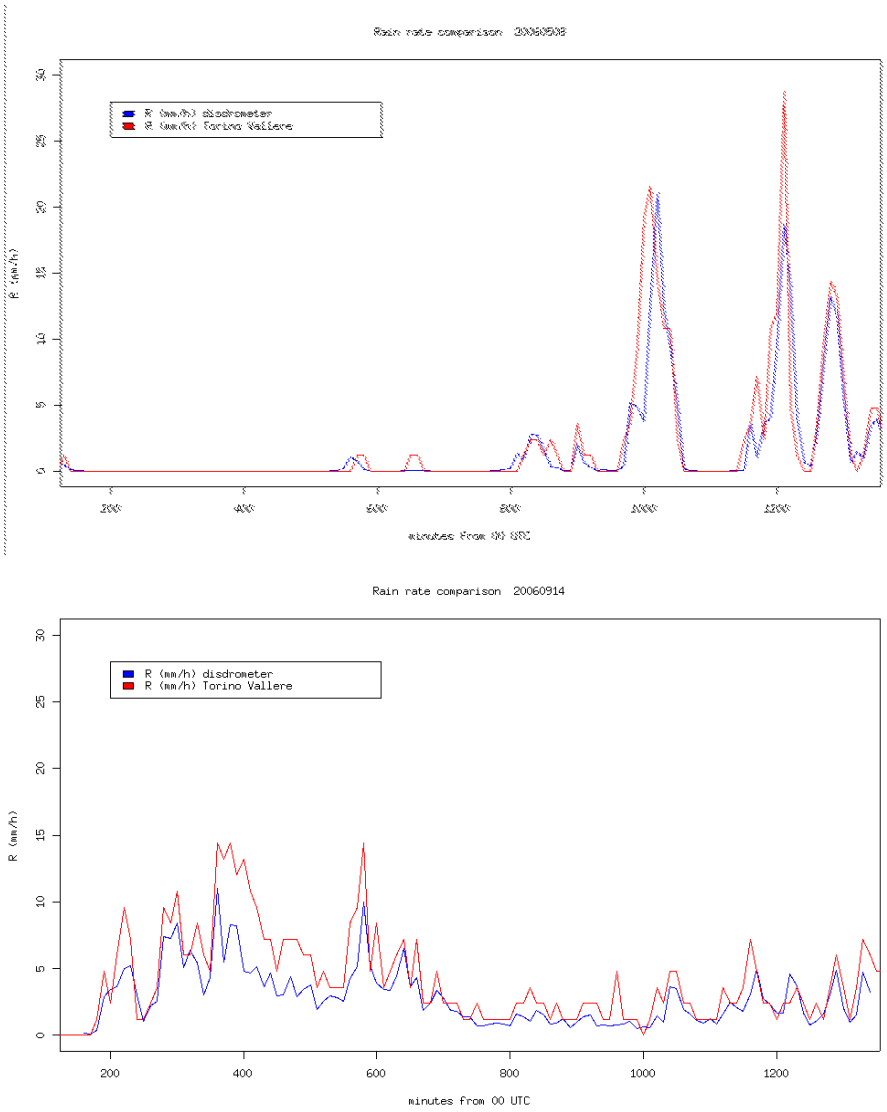

Fig. 2 – Comparison of rainfall intensity by disdrometer and raingauges
a) 08/05/2006 convective event
b) 14/09/2006 stratiform event

In this formula N(D_i) is the distribution of drops (in $m^{-3}m^{-1}$) characterised by a diameter in the interval $[D_i - \Delta D_i/2, D_i + \Delta D_i/2]$, M_i is the number of drops in size class i measured in Δt, which represents the sample time interval, A is the measuring area and v_j the vertical velocity of the j th drop with diameter D_j.

In this way we obtained a discrete DSD averaged each ten minutes, having one value of N(D) for every diameter classified by the disdrometer. In Fig. 4, are shown images of DSDs and associated precipitation percentages for two of the events listed before. A general good agreement with results in literature was found, as we obtained:

- distributions mostly characterised by bigger drops, in case of convective intense precipitation (Fig. 4a)
- distributions with smaller drops, in stratiform weak precipitation events (Fig. 4b)

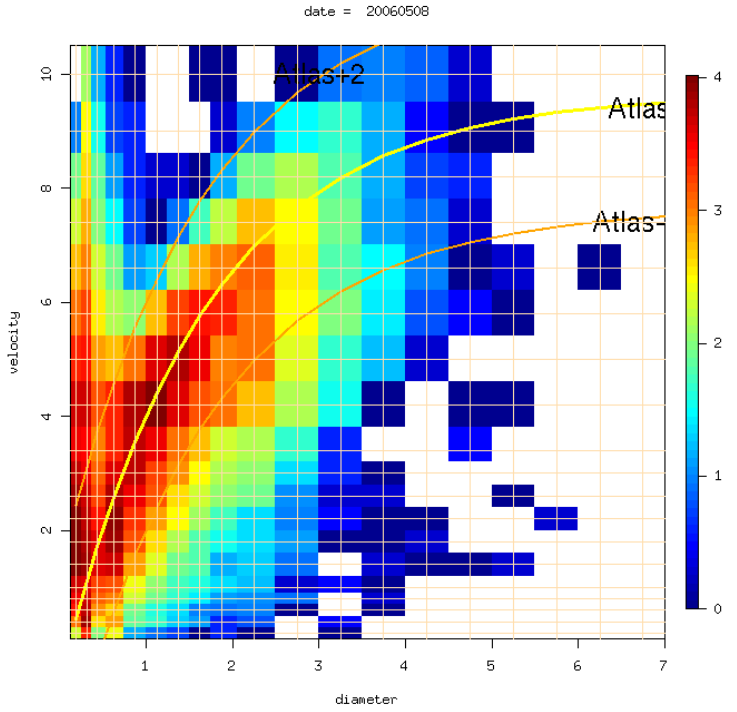

Fig. 3 – Diameter vs velocity logarithm for the 08/05/2006 convective event

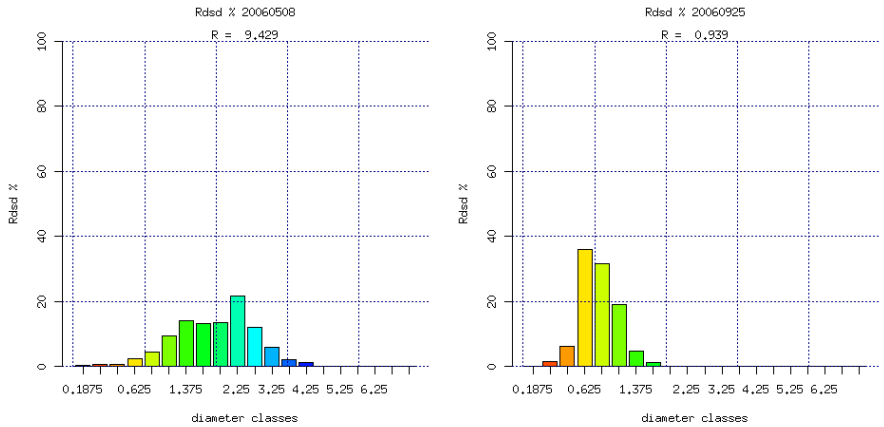

Fig. 4 - percentage precipitation due to different diameter drops
a) 08/05/2006 event at 21:10 UTC
b) 25/09/2006 event at 01:40 UTC

Reflectivity calculation and comparison with radar

Once the discrete DSD has been computed, it has been possible to recalculate the precipitation intensity according to the following formula presented in Doviak and Zrnic, 1993 [4]:

$$R = \frac{6\pi}{10^4} \sum_{i=1}^{n} N(D_i) D_i^3 \; v(D_i) \; \Delta D_i$$

At the same time, using the same distribution and formula, the horizontal reflectivity ZH referred to each 10 minutes interval has been computed. Then, for each considered case study, ZH and R have been fitted, and two coefficients a and b, linked to the precipita-

tion characteristics, have been extracted. Considering the variability of the precipitation character during the selected events, it makes sense to separate stratiform rain case studies from convective ones, and calculate distinctly parameters a and b. In Fig. 5a and 5b the classical parameters values (Marshall-Palmer M-P, and Joss-Waldvogel J-W) are compared with the ones obtained using disdrometer data for the 5 events, separated according to the precipitation character.

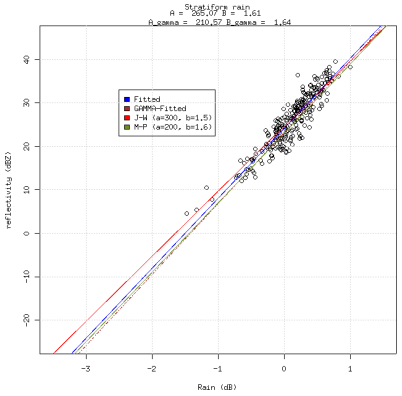

Fig. 5a – Graphical representation of rain rates (dB) vs horizontal reflectivities for stratiform precipitation

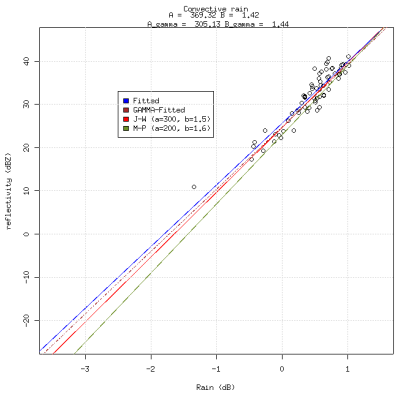

Fig. 5b – Graphical representation of rain rates (dB) vs horizontal reflectivities for convective precipitation

As a final verification, the results obtained for horizontal reflectivity by disdrometer have been compared to reflectivities measured by Bric della Croce radar, in the first radar cell exactly above the disdrometer. As evident in Fig. 6, we obtained a good agreement of the reflectivity trends by the two instruments, but a general heavy underestimation by the radar (of about 4 dBZ), that needs to be deeply investigated.

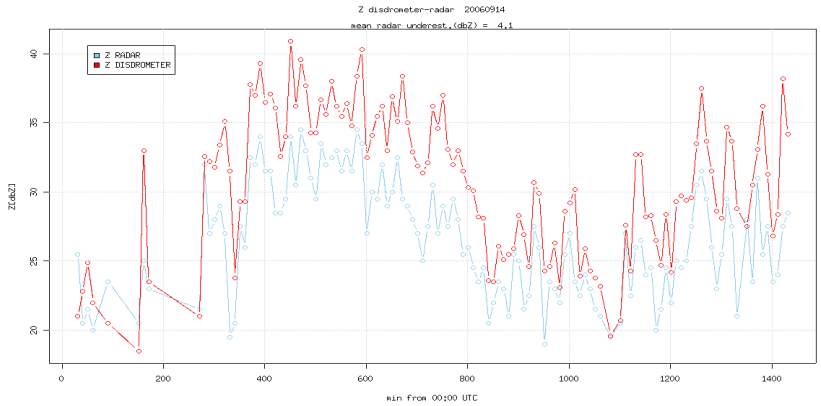

Fig. 6 – Comparison of horizontal reflectivities (dB) obtained by disdrometer (red), and measured by Bric della Croce radar (light blue) in the cell exactly above the disdrometer site (14/09/2006 event)

References

[1] Atlas D., Srivastava R., Sekhon R., Doppler radar characteristics of precipitation at vertical incidence, Rev. Geophys. Space Phys., 11, 135, 1973

[2] Kruger A., Krajewski W.F., Two-Dimensional Video Disdrometer. A Description, Journal of Atmospheric and Oceanic Technology, n. 19, 602-617, 2001

[3] Ulbrich C.W., Petitididier M., Campos E.F., Radar properties of maritime rain found

from disdrometer data at Arecibo, Puerto Rico. Preprints, 29th Int. Conf. on Radar Meteorology, Montreal, QC, Canada, Amer. Meteor. Soc., 676679, 1999

[4] Doviak R.J., Zrnic D.S., Doppler radar and weather observations, 2nd Ed. Academic Press, 1993

[5] Pruppacher H.R., Klett J.D., Microphysics of Clouds and Precipitation, 2nd Edition. Kluwer Academic Publishers, 1998

[6] Diss S., Rapport dvaluation du disdromtre implant sur le site du Ral Collobrier. Analyse des vnements pluvieux de mai dcembre 2005, Projet FRAMEA, 2006

[7] Andsager K., Beard K.V., Laird N.L., Laboratory Measurements of axis ratios for large Raindrops, J. Atmos. Sci., 56, 2673-2683, 1999